UNIVERSITY OF UDINE
Faculty of Mathematics, Physics & Natural Sciences
Department of Mathematics & Computer Science

Doctorate of Philosophy in Mathematics & Physics
Cycle XXIV

A new stereoscopic "Sum-Trigger-II" for the MAGIC Telescopes

Coordinator: Prof. Alessandro De Angelis
Supervisor: Dott. Barbara De Lotto
Assistant supervisor: Prof. Alessandro De Angelis

Candidate: Francesco Dazzi

Academic Year 2011–2012

To myself and
my family because
what you can is
what you want!
And to everybody
who believes
in justice...

Abstract

This thesis describes the work done in collaboration with the *MPI*[1] group during three years of Ph.D. at the University of Udine - Department of Physics and *INFN* Section of Padova, in 2009 – 11. The candidate is a member of the *MAGIC* (*Major Atmospheric Gamma-ray Imaging Čerenkov*) collaboration, which manages two IACT (*Imaging Air Čerenkov Telescopes*) telescopes for *VHE* γ–ray astrophysics.
MAGIC, located at the Observatory of Roque de Los Muchachos in the Canary Island of La Palma, is devoted to the detection of γ–rays of astrophysical origin in the energy domain above 25 GeV (Very High Energy).

Gamma-ray photons, the most energetic hence smallest wavelength form of electromagnetic radiation, travel incredible distances across the Universe. At such high energies the photon fluxes are extremely low and direct detection would require detector effective areas that are impractically large for current space-based instruments. Fortunately, such high energy photons produce extensive air showers of secondary particles in the atmosphere that can be observed on the ground, both directly by radiation counters and optically via the Čerenkov light emitted by the ultra-relativistic shower particles.
Gamma-ray astrophysics observations are still limited at lower energies by non-gamma-ray backgrounds, and, at higher energies, by the number of photons that can be detected. Larger area detectors and better background suppression are essential for progress in the field. Low energy threshold and excellent sensitivity are key parameters for a better understanding of γ–ray messengers in the GeV domain, and allow these telescopes to cover energies in good overlap with satellite experiments, thereby providing essential complementary information. The importance of this range of the electromagnetic spectrum is extremely relevant, because it probably hides the explanation of open and enigmatic questions. The main targets are very distant *AGNs* (*Active Galactic Nuclei*), *Pulsars* and *GRBs* (*Gamma-Ray Burst*).

This research is mainly focused on the design, the development, and the realization of a new stereoscopic *Sum-Trigger-II* for the *MAGIC* Telescopes, in order to increase the detection efficiency at very low energies (< 50 GeV). The *Sum-trigger-II* is an alternative to the current standard digital trigger, which has an energy threshold of about 50 GeV. This novel trigger concept is based on the analogue sum of signals coming from patches of the camera detector. A small prototype system, the so-called "Sum-Trigger", was already used in a single telescope operation mode, which led to the detection of pulsed γ–rays from the *Crab Pulsar* at 25 GeV. Soon, the old prototype analogue *Sum-Trigger* will be upgraded to a new system filling the whole trigger area in the camera, which will be mounted on both telescopes for stereo observations. The new system will contain new elements: a continuously adjustable analogue delay line, which allows a computer controlled timing flat-fielding of all trigger channels, a passive backplane for the signals distribution to the right patch and a differential high frequency cabling. The system will also have an automatic gain flat-fielding and an absolute trigger threshold calibration.

[1] *Max Planck Institute* for Physics in Munich, Germany.

Outline

This thesis presents the project of a novel stereoscopic *Sum-Trigger-II* for the *MAGIC* telescopes. It can be divided in the following two parts:

Part I: The physics case

In Chapter 1, an introduction to γ–ray astronomy and astrophysics is presented, starting from the historical point of view and finishing with modern research.
The beginning dates back some centuries before the common era. Chinese, Indians, Mayan, Egyptians, and Babylonians started to record the positions of celestial bodies and the cycles of Nature indispensable for agricultural activities. The first attempt to give a logical explanation to the stars came from the ancient Roman-Greek philosophers. They changed completely the purpose of science, moving it from farming and religion to pure knowledge.
For two millennia man was tied to geocentrism, until heliocentrism was introduced with the Copernican Revolution in the sixteenth century. This is the beginning of the Scientific Revolution, a period that saw a fundamental transformation in scientific ideas across many disciplines. A new scientific method was introduced and the discovery of new technologies, such as the telescope, eased the progress of knowledge.
Between the nineteenth and twentieth century, the development of spectroscopy and the subsequent rise of the new science of astrophysics created new activities for astronomers in the investigation of the physical and chemical nature of stars. Until then, the astronomers were bound by the relatively narrow frequency band of visible light, to which our eyes are sensitive and the Earth's atmosphere is transparent enough. The second part of the twentieth century saw rapid technological advances in astronomical instrumentation. Specific sensors able to detect radiation at different wavelengths were developed and new telescopes began observing the Universe in the infrared, ultraviolet, X–ray, and γ–ray parts of the electromagnetic spectrum, as well as observing cosmic rays.
The discovery of cosmic rays was a crucial moment for the growth of astrophysics, because it opened the access to new methods to study celestial bodies. The development of this new branch contributed also to the detection of γ–rays, energetic photons that travel through the Universe without being deflected by magnetic fields.
The main very high energy gamma sources studied by experiments as *MAGIC* are: *Supernova Remnants*, *Pulsar*, *Binary System*, *Active Galactic Nuclei* and *Gamma-Ray Bursts*. In addition, these new telescopes can perform studies related to fundamental physics and cosmology.

In Chapter 2, the theory of the extended atmospheric showers, the detection technique of VHE γ–rays and the subsequent data analysis are presented.
Elementary processes which occur both in our galaxy or in distant extragalactic sources can accelerate or even generate high energy particles. These particles are messengers

of the astrophysical emission phenomena and cross long distances up to the Earth's atmosphere. Gamma-rays, which are not deflected by the magnetic fields during their travel, follow a straight trajectory and indicate the position of the source.
Impinging the Earth's atmosphere, the cosmic particles initiate a cascade of secondary products that develops towards the ground. The spatial and the temporal evolution of the shower depends on the nature and the energy of the primary particle, which triggers different particle processes.
Relativistic charged particles in the shower may polarize the atmospheric medium that then emits Čerenkov photons. Ground-based telescopes collect the faint Čerenkov light, producing a two-dimensional projection of the three-dimensional shower. This technique, called *IACT*, allows one first to discriminate the background, imposing topological and temporal constraints, and then to reconstruct the event. In fact, the data recorded by the detector are treated by complex algorithms which parametrize the shower morphology in order to extrapolate information about the astrophysical source.

In Chapter 3, a study of the morphology of low energy showers is presented.
The *MAGIC* telescopes has been designed mainly for physics research at low energies in the GeV domain, with several motivations which range from fundamental physics to cosmology and astrophysics. Unfortunately, this portion of the spectrum lies between the lower limit of the *IACT* technique and the upper limit of satellite experiments. A good overlap between ground-based and space detectors is crucial to give continuity to research fields that are connected.
The intrinsic limitation of the detection technique and the available technology force one to use innovative methods, novel algorithms and upgraded systems. In this ambitious context, the attention to every detail, both physical and technological, is essential. In order to find the best solutions, the proprieties of the low energy electromagnetic shower, due to a γ–ray, are explained and the projection's morphology is analysed. Qualitative results and conclusions based on empiric and Monte Carlo studies are reported. Finally, the main features are linked to possible solutions that can improve the efficiency of a Čerenkov telescope.

Part II: The technological case

In Chapter 4, the MAGIC telescopes, operating at the Canary Island of La Palma, are introduced and the hardware components described, before and after the upgrade of *MAGIC–I*.
The telescopes are light tubular structures, which sustain a parabolic reflective surface, utilized to collect the Čerenkov photons emitted by the extended air showers. They can be orientated in azimuth and elevation to track a source in the sky with high angular resolution.
The Čerenkov light is focused on photosensors, which convert the optical signals into electrical ones. The pulses are then amplified and processed by a multi-level trigger system which performs a selection on which events should be recorded. In parallel, there is the data acquisition branch which registers the interesting signals every time it is activated by the trigger. All the subsystems are controlled by an central control.
Currently, the telescopes are being upgraded. A new readout and an improved trigger system are being commissioned. In the summer of next year, the camera of the older telescope will be renewed and a novel stereoscopic analogue trigger will be added in the electronic chain.

Chapter 5 is dedicated to the presentation of the novel stereoscopic analogue trigger.
In 2007, an innovative prototype trigger system, called *Sum-Trigger* was installed in the *MAGIC* electronic chain. The new concept is based on the analogue sum of adjacent pixels, which exceeds a fixed threshold when they are lit-up by an extended air shower. The success of this idea reached the apex with the publication on *Science* of the *Crab Pulsar* discovery at 25 GeV. Unfortunately, the trigger area was limited to a thin central ring of the camera and the stability, the maintenance and the equalization of the system were extremely difficult.
A new professional version, dubbed *Sum-Trigger-II*, is under construction. The basic concept is the same, but the system layout, the electronics controls, compactness and robustness are significantly improved. Monte Carlo simulations of the complete system predict very interesting achievements in the domain under 50 GeV.
Every subsystem that composes the *Sum-Trigger-II* is illustrated in detail and the current performance is presented.

In Chapter 6, the concept and the hardware of the stereoscopic trigger is described.
Since 2009, *MAGIC* is endowed with a second telescope which allows data-taking in the stereo mode. The stereoscopy gives the possibility to register the same event from two different points of view, improving the detection quality and the image reconstruction in the analysis framework. In a *IACT* array, the telescope layout determines the features and the performance of the experiment. *MAGIC* has built the second telescope 85 m far from the first one, ensuring a large common effective area, which consequently keeps a low energy threshold.
The telescopes operate synchronously when tracking the same source. A common trigger system (stereo trigger) alerts the data acquisition, when the same atmospheric shower hits both detectors generating local triggers. Obviously, the different light paths and the relative delays introduced by the electronics chains are taken into account and corrected in the selection logic.
The stereo trigger, which will also manage the outputs of the new analogue *Sum-Trigger-II*, will be upgraded with a new multi-purpose board, dubbed *MiniPulsar*. The main design and the performance of the first prototype are described in detail at the end of the chapter.

The last Chapter outlines the conclusions and the future perspectives of this work.

Contents

1

Introduction: γ-ray astrophysics

ASTROPHYSICS[a] deals with the physical properties of celestial objects that populate the Universe. This field of study is in strong progress and it is catching the attention of many physicists, because it is a very broad subject, full of unsolved questions. We can consider it a composite of many disciplines, as for instance electromagnetism, thermodynamics, relativity, cosmology and even fundamental physics.
Astrophysics represents the encounter between two very ancient branches of science: astronomy and physics. A historical overview and a description of the main aspects of this subject, which will be the starting point of this introduction, should provide a simple and logical explanation of the current research activity in astrophysical environments. This chapter is focused mainly on three topics: 1) history of astrophysics; 2) cosmic-rays; 3) current status of gamma astrophysics.

[a] In Greek means: nature of stars.

1.1 History of astrophysics

The Universe observation is one of the most ancient man's curiosity, originating in the elementary needs of mankind. The astronomers were instrumental in establishing the measurement of time, because people needed to know exactly when to plant and harvest. They followed the cycles of the seasons and lived close to the natural rhythms of the planet. The possibilities of antique science stopped at fixing the apparent positions of the objects on the sphere and collecting the visible properties. Any attempt to rationalize the observed facts was a failure, until Greeks laboriously built up a speculative system.
In the beginning the astrometry, which deals with the position and the motion of the heavenly bodies, was the only astronomy[1] branch developed. We have to wait many centuries to see the coming of a new discipline, called astrophysics, which treats the investigation of their chemical and physical nature. At the current time, astrophysics may be said to have absorbed the old descriptive astronomy, while the astrometry is based on the theory of gravitation, where mathematics keeps a central role.

[1] Astronomy is a natural science that deals with the study of celestial objects. It is divided into two main branches, distinguished as astrometry and astrophysics.

1.1.1 Prehistoric astronomy

The first astronomical knowledge was early established by the Chinese, Indians, Mayan, Egyptians, and Babylonians.
The Chinese were meticulous in keeping astronomical records, particularly the appearance of comets, novae and other transients. An impressive Chinese record in July 1054 is a guest star, that was bright enough to be seen during the daytime for nearly a month in the constellation, that we call *Taurus*. We believe this to be the supernova explosion that gave rise to the *Crab Nebula*, and our knowledge of the date of the explosion itself is a very important key in understanding the death of massive stars.
They used the circumpolar stars[2] as their reference point for the heavens, unlike the Indo-Europeans, who used observations based upon the rising and setting of celestial bodies on the ecliptic and the horizon. In order to mark the passage of time and the seasons, the Chinese primarily used the orientation of the *Big Dipper*[3] constellation relative to the pole star in early evening. The Chinese astronomers generated fantastically accurate measurements of time and charted unusual cosmological phenomena, and their ideas filtered down the *Silk Road* into the Middle East and Europe.

Indian astronomy was heavily tied to their religious and spiritual outlook of the world, but it contained many accurate observations of phenomena and some original elements, which were a catalyst for the growth of mathematics. It was mainly based upon the stars and the sidereal period, namely the time that takes an object to make one full orbit around the Sun. They used the stars and the planets to create astrological charts and read omens, devising sophisticated mathematical models and developing many interesting theories, many of which passed into the Islamic world and Europe.
In addition, Indian astronomers also proposed that the stars were exactly like the Sun, but much further away. They also understood that the Earth was spherical and attempted to calculate the circumference of the planet.

Figure 1.1: One of the most important Mayan calendar: the *Haab'*.

The observations of the Mayan priest-astronomers were entirely dedicated to astrology. Their incredibly accurate astronomical calculations and sophisticated mathematics were steeped in religion and omens.
It is not surprising that the Mayans observed the stars to chart the seasons and developed a calendar. The two main calendars were the *Tzolk' in*, a 260-day calendar of 13 numbers and 20 day names, and the *Haab'* (Fig. 1.1), of 365 days. This calendar had 18 months of 20 days, with a 5-day month added at the end of the year. The reason why they used 20 days for a month is largely based upon their numeric system, which is a base twenty.
The Mayans did not have complex instruments to estimate the positions of celestial objects, but they built some great temples,

[2] A circumpolar star is a star that, as viewed from a given latitude on Earth, never sets (that is, never disappears below the horizon), due to its proximity to one of the celestial poles. Circumpolar stars are therefore visible for the entire night on every night of the year.

[3] The *Big Dipper* is an asterism of seven stars, which are the seven brightest of the formal constellation *Ursa Major*.

which were aligned to the Sun, especially midsummer, midwinter and the equinoxes. They further refined their astronomical techniques, recording the positions of the planets, devising tables for long-term predictions of the movements of these planets, and creating tables to predict eclipses. Their predictions were so sophisticated that they included corrections, showing that they fully understood that the movement of the planets and precession were complex.

In Egypt, considerable technical skill was attained and a constellation system came in use [24]. For instance, the precise orientation of the pyramids, aligned towards the pole star, is a piece of evidence. Moreover, the evaluation of the site of the temple of *Amun-Re* at Karnak, taking into account the change over time of the obliquity of the ecliptic[4], has shown that the *Great Temple* was aligned on the rising of the midwinter Sun.

Figure 1.2: Circular megalith at Nabta. (Courtesy of Raymbetz)

Also the Egyptian calendar was always in close connection with the stars' evolution and it was the base of agriculture and predicting the seasons. The main example are the stone circles at Nabta Playa (Fig. 1.2), which show that they were accomplished at marking time and calculating the coming of the Nile's floods. The Egyptians were fully aware that the year was about 365 days plus the extra quarter day and they prepared a calendar based around the star *Sirius*, which arises highly on the sky in conjunction with the Nile's floods. The days were divided into 24 hours, using sundials to tell the time. For the night, 36 groups of stars, called *Decans* were considered. The most amazing example is the star map, also called star clock, on the ceiling of the *King Ramesses VI*'s tomb. This map may be used to map the journey of the stars for each hour of the night, through the whole year.
Whilst Egyptian civilization declined, it became absorbed by the Greek and Roman cultures and many aspects are still modern and in use.

The Babylonian astronomy was deeply influenced by Sumerians, which introduced the astrolatry[5] and the sexagesimal (base 60) place-value number system. This is a simplified method of recording very great and very small numbers and it is still the base of the modern practice of dividing a circle into 360 degrees, of 60 minutes each. By merging this new mathematical instrument and the skill to observe and study the sky, they have identified the ecliptic way of the Sun, which was divided in 360 parts, each one for one single day of the year. They have also identified, for the first time, the inner planet *Mercury* and the outer planets *Mars*, *Jupiter* and *Saturn*.
During the 8th and 7th centuries BCE, Babylonian astronomers developed a new empirical approach to astronomy. They began studying philosophy dealing with the ideal nature of the Universe and began employing an internal logic within their predictive planetary systems. In the 3rd century BCE, searching in the past reports for repeating occurrences of ominous phenomena for each planet, they created mathematical mod-

[4]It is the apparent path of the Sun, or the real path of the Earth as seen from the Sun.
[5]Astrolatry is the worship of stars and other heavenly bodies as deities, or the association of deities with heavenly bodies.

els that allowed them to predict these phenomena directly. This was an important contribution to the astronomy and the philosophy of science, and some scholars have thus referred to this new approach as the first scientific revolution. This new approach to astronomy was adopted and further developed in Greek and Hellenistic astronomy, where the dependency upon Cosmology starts.
More importantly, this period saw the transmission of ideas between the Indians, Babylonians, Greeks, and Persians. This exchange of theories and philosophy was extremely important to the development of astronomy.

1.1.2 Greek and Roman astronomy

The main fortune of Greeks was the strategic geographical position. They lay at the crossroads of many trade routes and were influenced by many other great cultures. The ancient Greek philosophers took in the knowledge of other populations and refined astronomy with an innovative approach. They moved from an observational science into a full-blown theoretical science. The Greeks kept the idea of Gods, but they were not satisfied with purely theological explanations for phenomena and began to model the structure of the Universe. This was the first real attempt to find a grand universal theory and to explain the origin of Universe, which is a machine that runs upon mechanical and mathematical principles, that could be deduced through logic and reasoning.

There are several important Greek astronomers, such as *Thales* (624 – 546 BCE), who recognized the importance of the star constellation *Ursa Minor* for the navigation, and *Anaximander* (610 – 546 BCE), who was the first to create a cosmological model. His major contribution was to imagine the Earth as hanging in space, with the other heavenly bodies describing circles around it. *Anaximander* believed that the Earth was cylindrical in shape and surrounded by air and then fire (Fig. 1.3). The inhabited portion lay on top of the cylinder, surrounded by an ocean. Another great contribution was the idea of infinity and the tantalizing possibility that the Universe could be unbounded.
Another one was *Pythagoras* (570 – 495 BCE), who postulated that the Earth was spher-

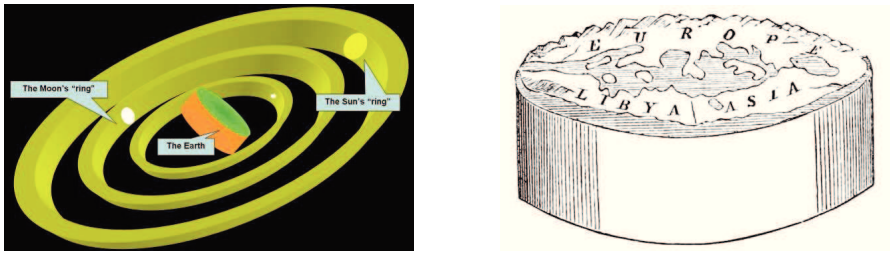

(a) Anaximander's Universe model (b) Anaximander's Earth model

Figure 1.3: *Left:* the *Anaximander*'s Universe model, in which the celestial bodies move around the Earth in circle. (Image credit: © Centre for Astrophysics and Supercomputing, Swinburne University of Technology)
Right: the *Anaximander*'s Earth model, which consists in a cylinder surrounded by air and fire.

ical, a huge departure from *Anaximander*'s model. Famously, he proposed this idea because he noticed that ships disappear below the horizon when they sail away, implying that the surface of the Earth is curved.
The milestone was put by *Plato* (427 – 347 BCE) and his pupil *Aristotle* (384 – 322

BCE). They believed that the entire cosmos was constructed with precision and that circles and spheres, as the most perfect objects, were the key to understand the Universe. In their models, the stars, Sun, and Moon were fixed to concentric crystalline spheres, rotating inside one another. The stars formed the outermost crystal sphere, followed by the planets, the Sun, the Moon, and the spherical Earth at the centre. Unfortunately, this image of the sky does not explain completely the motion of the Universe objects, both size and brightness variability and the different seasons' length. The problem was ostensibly solved by *Appollonius of Perga* (250 – 220 BCE) and his solution was applied by *Hipparchus* (190 – 120 BCE) to describe the movements of the Sun and Moon. He believed that the Earth did not lie at the very centre of the Universe, but lay slightly off-centre. *Ptolemy* (90 – 168 CE) took further this idea and expanded it to all the planets, proposing the famous theory of epicycles[6] (Fig. 1.4). Using trigonometry, *Hipparchus* and *Ptolemy* devised a model, where the Sun, Moon, and planets moved around the Earth in circles, but rotated in smaller circles within this cycle. This perfectly explained the sometimes retrograde motion of the Moon and planets, and elucidated why the Sun and Moon were sometimes closer to the Earth and, subsequently, larger [126].

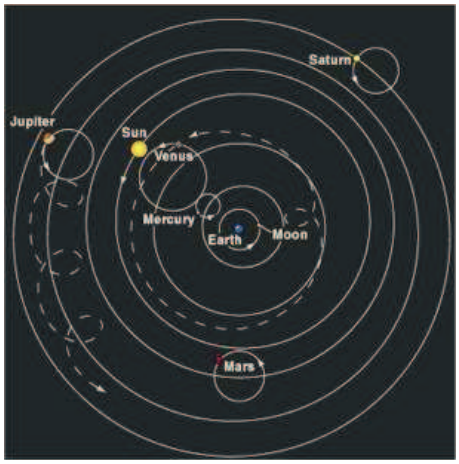

Figure 1.4: The *Ptolemy*'s geocentric model. (Image credit: Lola Judith Chaisson - Astronomy today, by E. Chaisson & S. McMillan)

Ptolemy was the apex of an important cycle in the history of astronomy. In this period the Romans conquered Egypt, which again became the centre of scientific activity. Obviously this is the end of an amazing cultural interchange, where the native Egyptian tradition of astronomy had merged with Greek astronomy as well as Babylonian astronomy.

The ancient Roman-Greek philosophers were both a blessing and a curse of science. On the one hand, they moved the idea of the structure of the Universe away from Gods and superstition, using geometry to create harmonic models which described the underlying motions of the Universe. On the other hand, the geocentric model and the epicycles of the ancient Greek astronomers persisted for long time, influencing later theoretical cosmologists to take the wrong path. In fact, the Ptolemaic astronomy became standard in medieval Western European and Islamic astronomy, until it was displaced by the heliocentric and Tychonic systems in the 16th century.

1.1.3 Sixteenth century

After the significant contributions of Greek sages, the astronomy entered into a relatively static period. For many centuries, the main astronomy's core was strongly tied to the old Roman-Greek philosophy. Many concepts remained immutable and they settled into the common social and religious life. There was no space for new original thoughts, because they were not considered innovative, but often something completely wrong, nasty and dangerous. In addition, the advanced astronomical treatises of classi-

[6] Circle in which a planet moves and which has a centre that is itself carried around at the same time on the circumference of a larger circle.

cal antiquity were written in Greek, and with the decline of knowledge of that language, only simplified summaries and practical texts were available for the study. This very long trend was disrupted by two daring astronomers, who met much resistance, not only from the Catholic Church and its reluctance to accept a theory not placing God's creation at the centre of the Universe, but also from those who saw geocentrism as a fact that could not be subverted by a new, weakly justified theory. These two are *Nicolaus Copernicus* and *Tycho Brahe*.

In 1543[7], *Copernicus* upset the historic geocentric model introducing the heliocentrism, where the Earth and planets revolved around a stationary Sun at the centre of the Solar System [45]. Now it is easier to explain the planets motion and there is no need to recourse to the sophisticated epicycles. *Copernicus* moved heliocentrism from philosophical speculation to predictive geometrical astronomy, elaborating the system in full geometrical detail and using selected astronomical observations to derive important numbers. His work was a consequence of a yearning for a greater mathematical harmony, without violating the principle of uniform circular motion[8] proposed by the Greek predecessors.
His theory stimulated further scientific investigations, becoming a landmark in the history of science that is often referred to as the *Copernican Revolution*.

The *Tycho Brahe*'s thinking was more conservative than *Copernicus*'s one. He combined the geometrical benefits of the Copernican system with some philosophical concepts of the Ptolemaic system. He proposed a geo-heliocentric model, in which the Sun, the Moon and the stars revolve around the Earth, and the other five planets orbited the Sun. The central topics of Thyconic theory were an unmoving Earth for reasons of physics, astronomical observations and religion.
Brahe was one of the greatest observer of the sky. He succeeded to measure, with a precision never reached, the ecliptic inclination, the eccentricity of Earth's orbit, the inclination of the lunar orbit and the retrograde lunar nodes[9]. Finally he drew up the first modern stars catalogue with more than 1000 star positions.

1.1.4 Recent astronomy

During the last four centuries and especially the twentieth one, the understanding of the cosmos is extraordinarily progressed thanks to the development of new instruments and methods. From then on, the dichotomy between science and technology became very strong, progressing more often in parallel. The beginning is 1609, when *Galileo Galilei* started to observe the stars using a small optical telescope[10] (Fig. 1.5). In the sea of these striking discoveries, there are the *Jupiter*'s satellites, the phases of *Venus*, the mountains of the Moon, the spots on the Sun, *Saturn*'s unique "appendages" and the perception of the stellar composition of the *Milky Way* [62].
However this was the century of theory, where many aspects of Nature were thus laid down with marvellous intuition; one above all, the geometrical plan of movement in the

[7] *Copernicus*' major theory was published in *De revolutionibus orbium coelestium*, in the year of his death, though he had formulated the theory several decades earlier.

[8] This principle asserts that the natural motion of a celestial body is around a circle, and the motion must be uniform when viewed from the centre of that same circle.

[9] The plane of the Moon's orbit is inclined with respect to the ecliptic. This angle varies due to the complexity of the Moon's orbit, but the average inclination is 5°. The intersection of these two orbital planes form an axis, or line, and the points of intersection are called the Moon's nodes.

[10] *Galileo Galilei* did not invent the telescope, but was the first to use it systematically to observe celestial objects and record his discoveries. The first telescope was created by *Hans Lippershey* in 1608, one year before.

(a) First *Galileo*'s telescope (b) The lens of first *Galileo*'s telescope

Figure 1.5: The first telescope built by *Galileo Galilei* (1609). The main tube is composed of wood lathes, covered by red-brown skin and gold friezes. The convex lens diameter is 37 mm and its focal length is 980 mm, while the eyepiece diameter is 22 mm with a focal length of -47,5 mm (a negative focal length means it is divergent). The telescope can magnify the objects by a factor of 21 times with a field of view of 15'. (Courtesy of Museo Galileo Firenze - photo Franca Principe)

Solar System. *Johannes Kepler* was the first to attempt to derive mathematical predictions of celestial motions from assumed physical causes. In 1609, he elaborated the first two of the "Three Laws" of planetary motion [81] and the third in 1619 [82]. The first rule eliminates the circular motion, which had been fashionable for two millennia. The second replaces the idea that planets move at uniform speed around their orbits, with the empirical observation that the planets move more rapidly when they are close to the Sun and more slowly when they are farther away. The third rule is a harbinger of the law of gravitation, which would be developed by *Newton*.
Subsequently *Isaac Newton* discovered the *Universal Gravitational Law* (1687), showing that the same uniformly acting force regulates celestial revolutions and compels heavy bodies to fall towards the Earth's surface. Every particle of matter attracts every other with a force directly proportional to their masses, and inversely proportional to the squares of their distances apart. This was a further bond between physics and astronomy. He also found out the three laws of motion [103], which dominated the scientific view of the physical Universe for the next three centuries. Finally, *Newton* demonstrated the consistency between *Kepler*'s laws and his gravitation theory verifying the discordance between the Sun and the centre of gravity of the Solar System, thus removing the last doubts about heliocentrism and advancing the *Scientific Revolution*. This period rose a deep transformation in scientific ideas across physics, astronomy, and many other disciplines, which heavily influenced modern sciences. The core of this new kind of thinking is the concept of a systematic, mathematical interpretation of experiments and empirical facts: the scientific method. The way in which scientists worked was radically changed.

By comparing modern with antique observations, in 1718 *Edmund Halley* (1656 – 1742) understood the stars' movement, which is far from being fixed, each star having its own path across the sky. The stellar motions became a wide and expansive field of research and a preliminary attempt to regularize them was made by *Herschel*'s determination.
In fact, the extraordinary improvement of reflecting telescopes (Fig. 1.6) by means of Sir *William Herschel* (1738 – 1822) opened a fresh epoch of discoveries, mainly in the Solar System environment. He got a high notoriety for the discovery of *Uranus* and two of its major moons, *Titania* and *Oberon*, but probably his most important contribution came

from the search for visually very close pairs of stars. In that period, the astronomers tried to explain the proper motion of stars looking at the changes over time in their apparent separation due to parallax shift. He announced the hypothesis that the two stars might be a binary system, orbiting under mutual gravitational attraction [70].
The following step was pursued by *Friederich Bessel*, *Wilhelm Struve* and *Thomas Henderson* in 1838. Continuing to use the parallax method[11], they measured the star distances. The first stars accurately measured by them were *61 Cygni*, *Vega* and *Alpha Centauri*.

Figure 1.6: Model of telescope, exhibited in the *William Herschel* museum in Bath, which he discovered *Uranus* with. The power and magnification of his telescope was the secret of his success. It is 7 foot long and 6 inch diameter. Both mirrors, the main at the bottom of the tube and the secondary mirror near the top, were made of speculum metal.

The missing element to form the recent astrophysics is given by *William Huggins* in 1864. After reading the *Kirchhoff* and *Bunsen*'s report about the identification of chemical elements (spectrum analysis) by means of spectrograph[12], he decided to take advantage of this new technology and started to extract the composition of celestial objects [75]. In fact, he was the first to take the spectrum of a planetary nebula analysing *NGC 6543* and he identified the gaseous nature (mainly hydrogen) of many other diffuse and planetary nebulae [76]. In such a way, he began the study of novae physical mechanisms.
The investigation about the elementary constituents of the Universe became fundamental. This was the original stepping stone towards the traditional aspect of astrophysics, where the main interest was focused on the physical properties, such as density, temperature, chemical and nuclear composition of matter, luminosity and emitted spectrum of stars, galaxies, interstellar and intergalactic medium and everything that populates the Universe.

Another pioneer of stellar spectroscopy was *Pietro Angelo Secchi*, who was the first to adopt spectroscopy for the stellar classification. Using a visual spectroscope on the *Roman College Observatory*'s telescope, he completed a study of the spectra of about 4000 stars [117, 118, 119]. His scheme, subdivided in four spectral types, paved the way to future classifications, such as the *Harvard classification system* compiled at the *Harvard College Observatory* in the 1880s. This system was based on the *Henry Draper Catalogue*, which was a listing of the positions, magnitudes, and spectral types of stars in all parts of the sky. The first version[13] of the catalogue contained 10351 stars, designated by letter in alphabetic sequence according to the strength of their hydrogen spectral lines. At the beginning of the twentieth century and in the same observatory, *Henrietta Swan Leavitt* began to measure the brightness of many stars, noting that in the *Magellanic Clouds* several of them were variable and showed a pattern. In 1912, she confirmed

[11] It consists to estimate the apparent changes of position between stars, when seen from different points of view.

[12] A spectrograph is an instrument which separates an incoming wave into a frequency spectrum.

[13] The *Draper*'s work was followed through by *Annie Jump Cannon*. A new catalogue containing 225300 stars was published between 1918 and 1924.

that the brighter variable stars (*Cepheid variables*) had longer periods [89]. This relation between the luminosity and the stars' period is known as the *period-luminosity relationship* and it opened the possibility of measuring distances in the Universe.
The *Leavitt*'s method was well calibrated by *Harlow Shapley* some years later. By determining the distances of many globular clusters, for the first time he estimated the size of the *Milky Way*, which was much larger than previously believed [120]. He also concluded that the position of the Sun lay in the periphery of our own galaxy, far away from its centre. The belief of a small Universe was abandoned and its geometry was transformed from heliocentric to off-centre, dwindling the anthropocentric world view.

In the same period, around 1910, *Ejnar Hertzsprung* and *Henry Norris Russell* independently developed a procedure to classify the stars with the same spectrum, according to some features as the luminosity, temperature and mass. The final result for the stellar luminosity was the *H-R diagram* (Fig. 1.7). Nevertheless, the diagram clarified the stars' topology and some peculiar behaviour, but nothing related to their evolutionary mechanism and their internal engine. To know about that, we have to wait the marvellous insights of *Arthur Eddington*.

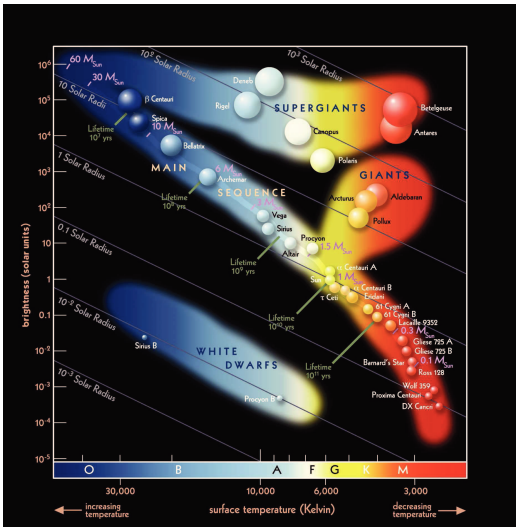

Figure 1.7: The *H-R diagram* is a graph of stars showing the relationship between the stars' absolute magnitudes or luminosities versus their spectral types or classifications and effective temperatures. (Courtesy of *ESO*)

Arthur Eddington studied the internal star equilibrium, he tried to discern all the forces at stake and developed the first true understanding of stellar processes [51]. His model was correctly based on the balance between the gravitational and radiant force, where any variation could change the main mechanism. The model treated a star as a sphere of gas held up against gravity by internal thermal pressure, and one of his chief additions was to show that radiation pressure was necessary to prevent collapse of the sphere. Moreover, he grasped the sub-nuclear origin of the immense generated stellar energy, overturning current thinking. He said that the energy was produced by some nuclear reactions which broke the nuclei of elements, located in the star's core. In 1920, *Eddington* considered the hydrogen as the most important fuel of these reactions, triggered by very high pressure and temperature. This is a typical exothermic[14] process, called nuclear fusion, which can self-feed.
This marvellous intuition was completed twenty years later by *Hans Bethe*, who proposed the *proton-proton chain* and *carbon-nitrogen-oxygen cycle* as the two main fusion

[14]Nuclear fusion can be either exothermic or endothermic, but here we're simply talking about exothermic kind, when stars release immense quantities of energy. The endothermic nuclear fusion is the mechanism by which all the elements heavier than iron are created in a supernova.

reactions, by which stars convert hydrogen to helium [11].
At the same time, *Eddington* was one of the first to receive several papers regarding *Einstein*'s theory of general relativity. Thanks to his mathematical skills, he understood the general relativity and in 1919 he organized two expeditions to observe a solar eclipse to make the first empirical test of *Einstein*'s theory: the measurement of the deflection of light by the Sun's gravitational field.

The relativity theory was concluded by *Albert Einstein* in 1916, but this was a very long and complex work, started more than ten years before. It was in the year 1905, when *Einstein* published the special theory of relativity [52], changing radically the basis of classic physics, finding a brilliant solution on how to reconcile the laws of classical mechanics with the laws of the electromagnetic field.
The peak of that study was just the general relativity theory [53], according to which the gravity of a body can modify the properties of the space, introducing the curvature of the space-time. Hence, he applied this theory to model the structure of the Universe as a whole. This new physics provides the foundation for several current understandings, as the black holes, regions of space where gravitational attraction is so strong that not even light can escape.

One of the most attracted contemporary by *Einstein*'s theory, was the German *Karl Schwarzschild*. He was the first to provide the exact solution to the Einstein field equations of general relativity, for the limited case of a single spherical non-rotating mass. The choice of the right approximations and the use of an elegant polar-like spherical coordinate system, secured that admirable result, appreciated directly by *Einstein* himself. That solution contains a coordinate singularity, which lies on the sphere of points at a particular radius, called the *Schwarzschild* radius[15]. If the radius of the central body is less than the *Schwarzschild* radius, all the massive bodies and even photons, located inside this region, must inevitably fall into the central body. When the mass density of this central body exceeds a particular limit, it triggers a gravitational collapse and produces a black hole.

In the first quarter of the twentieth century the knowledge of the Universe's structure notably increased, but its size was still unclear. This topic originated an important debate between the astronomers *H. Shapley* and *H. Curtis*, called the *Great Debate* [121]. *Shapley* argued that the *Milky Way* was the entirety of the Universe, containing all the spiral nebulae, such as *Andromeda*. On the other side, *Curtis* asserted that such nebulae were separate galaxies, thereby extragalactic objects. The debate was resolved only using larger telescopes. Fundamental was the *Edwin Hubble*'s work, in which he measured the great distance (greater than the *Milky Way* size calculated by *Shapley*) of some *Cepheid variable* stars located in spiral nebulae, confirming that spiral nebulae are independent galaxies.
Stimulated by the innovative *De Sitter*'s theory, in 1929 *Hubble* added another amazing feature of the Universe: the expansion. Observing the light spectra from galaxies beyond the *Milky Way*, he discovered a shift of light to red. This effect was a clear demonstration that the galaxies were drifted away. *Hubble* quoted in a plot the galaxies' speed and the distance, carried out the linear trend, namely increasing the galaxies distance their speed also increased (*Hubble*'s law[16]) [74].
Assuming a homogeneous, isotropic and expanding Universe, the law was theoretically derived from general relativity equations and afterwards *Hubble* confirmed it empiri-

[15] *Schwarzschild* radius is defined as: $R_s = 2GM/c^2$, where G is the gravitational constant, M is the mass of the central body, and c is the speed of light in a vacuum.

[16] The *Hubble*'s law is defined as: $z = H_0 D/c$, where z is the redshift of the galaxy, D the distance, c the light speed and H_0 the *Hubble*'s constant, whose value is 74 km/s per mega parsec.

cally. Already back in 1922, *Alexander Friedmann* had published a set of a possible mathematical solutions to the field equations that argued for an expanding Universe. In 1927, also the astrophysicist *Georges Lemaitre* had published a model of an expanding Universe, but their works were accepted only few years later [90].
An expanding Universe means that long ago it must have been far denser. In 1931 *Lemaitre* proposed that the Universe might have been originated by a primeval cosmic explosion, later on dubbed *Big Bang*[17] [91]. This hypothesis was challenged by a new theory, in which the Universe might be in a steady state. In this cosmological model, proposed by *F. Hoyle*, *H. Bondi* and *T. Gold*, new matter is continuously created as the Universe expands without changing its appearance over time. New stars and galaxies are formed at the same rate that old ones become unobservable as a consequence of the expansion [19].
The *Steady-State* theory started to be in decline in the late 1960s, when observations demonstrated that the Universe was evolving. From then on, the *Big Bang* is implicitly accepted in most astrophysical publications.

Another important scientist was *Walter Baade*. Between the two *World Wars*, he extensively studied the *Crab Nebula* and advanced the idea that *Supernovae* could produce cosmic rays and neutron stars. Moreover, he discovered two kinds of *Cepheid variable* stars, observing the central region of the *Andromeda* galaxy [6]. Considering this new population of stars, the *period-luminosity relationship* was corrected and the scale of the Universe became double [7].

As consequence of these new well-grounded theories and the advent of accelerators, scientists realized that the important cosmological features could be explained as natural and inevitable effect of elementary particle physics. Moreover, all of this pushed to another great change in the backgrounds of astronomers and their activities followed from observations beyond visual light.
In 1931, the American radio engineer *Karl Jansky* detected a radio emission from the centre of *Milky Way* [77] and opened the way for radio astronomy. Also X–ray astronomy took off after the war, thanks to physicists with expertise in designing and building instruments to detect high-energy particles. Finally γ–rays, infrared and ultraviolet light provided further means of non-optical discoveries in the space age. Currently, some particle physicists are turning to cosmology extrapolating information regarding the behaviour of matter under extreme conditions, beyond the limits of particle accelerators.

1.1.5 Modern astrophysics

The junction between astronomy and physics was provided by *Newton*, which derived the gravitation from the laws of *Kepler*. From then on, this bond became always more strong and after the novel concepts promoted by illustrious scientists in the nineteenth and twentieth centuries, as *Einstein*, *Maxwell*, *Stokes*, *Boltzmann* and many others, it matured into something indissoluble and inseparable. This is the birth of modern astrophysics, a branch of astronomy that studies the physical properties of celestial objects. Because it is a very broad field, astrophysicists typically apply many scientific disciplines, including relativistic, quantum and statistical mechanics, electromagnetism, thermodynamics, relativity, nuclear and sub nuclear physics. In practice, modern astronomical research involves a substantial amount of physics. Astrophysics can be divided in three different sections: 1) the theoretical astrophysics that prepares models and simulations to describe the phenomena in the Universe; 2) the observational

[17] The name *Big Bang* was invented by *Hoyle* in 1950.

astrophysics that records the radiation coming from space; 3) the fundamental space physics that uses cosmos like a laboratory to investigate particular particle properties and exotic physics, inaccessible in the common accelerators.

Theorists endeavour to create mathematical models and figure out the observational consequences of those models. They combine computational expertise with complex mathematics and detailed physics to solve surprising astrophysical problems and predict natural processes. It's then a matter of experimental observers to look for data that can refute a model or help in choosing between several alternate or conflicting proposals. In fact the advancement of science depends on the interplay between experimental research and theory. Some current classical subjects of theoretical astrophysics are stellar evolution and stellar endpoints, galaxy formation, magnetohydrodynamics[18], origin of cosmic rays[19] and physical cosmology[20].

The astrophysical observations are established on the reception from space of electromagnetic radiation, charged cosmic rays and neutrinos. The electromagnetic radiation sweeps over a large range of wavelengths (Fig. 1.8), which need specific techniques and detectors, as explained in the following list:

- **The radio astronomy** treats the radiation with a wavelength greater than some millimetres. There are two kinds of source emitting in this range of the spectrum: a) very cold ($< 1000\,\mathrm{K}$) objects as interstellar gas and molecular clouds; b) relativistic electrons in a weak magnetic field. Furthermore, there are some non thermal sources, which emit at these frequencies. The most important are pulsars and AGNs (*Active Galactic Nuclei*). At the wavelength of about one millimetre there is another relevant and appealing emission, the cosmic microwave background radiation[21] (*CMBR*). The study of these waves requires very large radio telescopes, to increase the signal-to-noise ratio and the angular resolution. The technological solutions lead to interferometric arrays like *Very Large Array* (*VLA*) or huge single structure like the *RATAN-600*, which consists of a 576 m diameter circle of rectangular radio reflectors.

- **The infrared astronomy** studies the radiation with a wavelength between millimetre fraction and 780 nm, close to the visible limit. Here, cold stars and non thermal *AGNs* are detectable. In addition, the interstellar dust emits in this range. Infrared observations are usually made with telescopes similar to the familiar optical telescopes, but new discoveries have been obtained by infrared satellite missions, where the most representative was *IRAS* (*Infrared Astronomical Satellite*). It has detected about 350000 infrared sources, increasing the number of catalogued astronomical sources by about 70%.

- **The optical astronomy** is the oldest and the only one in use until last century, because originally the astronomers could exclusively use the nuked eyes. In any case, this is not the real justification of the current success of this branch. The reasons are first the high atmosphere transparency in the visible domain, second the emission wavelength of most of the objects that populate the Universe and third the application of that radiation range to verify some physical and chemical properties as temperature, luminosity and matter composition. The main observed

[18] Magnetohydrodynamics is the discipline which studies the dynamics of electrically conducting fluids.

[19] Cosmic rays are energetic particles, originating from outer space.

[20] Physical cosmology is the study of the largest-scale structures and dynamics of the Universe.

[21] Cosmic microwave background is thermal radiation filling the observable Universe almost isotropically. It is the remnant heat left over from the *Big Bang*.

sources are stars, galaxies and nebulae. Currently, both optical telescopes and satellites are available for this research field. *Gran Telescopio Canarias* (GTC) is the world's largest single-aperture optical telescope.

- **The ultraviolet astronomy** deals with the radiation between 300 and 10 nm. Many emissions occur in this interval and they are a signature of hotter objects, typically in the early and late stages of their evolution. Unfortunately ultraviolet emissions are strongly absorbed in the interstellar space or by ozone in the atmosphere. This means that the observations at these wavelengths must be performed from the upper atmosphere or from space. For example, the *Hubble Space Telescope* and *FUSE* have been the most recent major space telescopes to view the near and far UV spectrum of the sky.

- **The X-astronomy** works from a wavelength of 0.01 to 10 nm, corresponding to the energies in the range 120 eV to 120 keV. Typically, X–rays from about 0.12 to 12 keV are classified as "soft" X–rays, while from about 12 to 120 keV "hard" X–rays, due to their penetrating abilities. The X–ray emission is coming from sources that contain an extremely hot gas at temperatures of many million degrees kelvin. Often the material is heated by the fall in the strong gravitational field, produced for instance by a nearby black hole. The first X–ray source dates back to 1962, when *Sco X-1* was discovered by a rocket designed by *Riccardo Giacconi*. Unfortunately X–rays are absorbed by the Earth's atmosphere, so the detectors must be taken to high altitude by balloons, sounding rockets[22] or satellites as *BeppoSAX*.

- **The gamma astronomy** handles the most energetic radiation, above 120 keV. At this high frequencies, the main sources are extreme and non thermal and can generate almost inconceivable amounts of energy. *Pulsars*, *AGNs*, *Supernovae remnants*, *Gamma-Ray Bursts* and *Micro-quasars* are the most detectable. In the first part of the gamma spectrum, space observatories as *FERMI* (*Gamma-ray Space Telescope*) are preferred, because the particles energy is too low to flow through the atmosphere. In the second part, the flux of high energy photons falls dramatically and the poor statistic imposes very large sensitive surface, which can be only built on ground. As shown in figure 1.8, the opacity of the atmosphere should prevent usual direct detection on the Earth's surface, however the interaction of γ–rays with atomic nuclei provides an alternative method. *MAGIC* (*Major Atmospheric Gamma-ray Imaging Čerenkov Telescope*) is an example of ground-based gamma telescope that uses this innovative approach.

Besides the photons, the Earth is hit by different showers of charged particles, called cosmic rays. These are basically protons, electrons and heavy nuclei that are deflected by magnetic fields, so they don't arrive directly from the origin along straight lines. It is impossible to determine the provenance of cosmic rays and the relation between detected particles and sources' properties. Nevertheless, these particles play often a central role in the generation of electromagnetic radiation very close to the source. The photons travel straightforward and can be recorded to study that process and the matter emitting not thermally.

The last kind of particles that are revealed on ground are neutrinos. They are not deflected by magnetic field being neutral and can be linked to the place of creation.

[22] A sounding rocket is an instrument-carrying rocket designed to take measurements and perform scientific experiments during its sub-orbital flight.

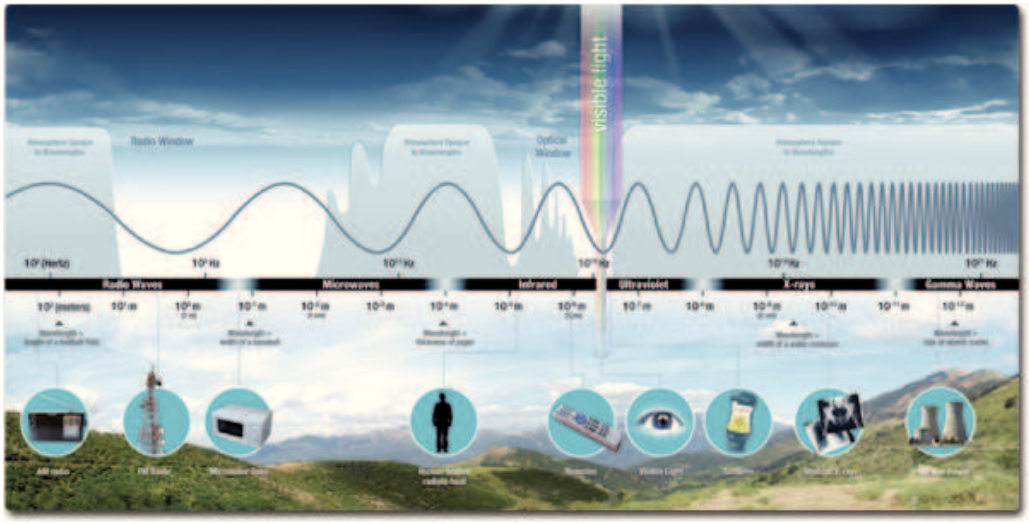

Figure 1.8: A sketch of the electromagnetic radiation absorption passing across the Earth's atmosphere. (From *NASA* website: http://missionscience.nasa.gov/ems/01_intro.html)

The problem here is the weak interactive power of neutrino. It is able to pass through ordinary matter almost unaffected, increasing extremely the difficulty to detect it. On the other side, this is a nice peculiarity of neutrino, because it is not significantly attenuated by its travel through the interstellar medium and it can probe very far astrophysical sources. Right now only two neutrino sources have been detected for certain: the Sun and the supernova *1987A* by the water-based detectors *Kamiokande II*.

Fundamental physics in space can provide the knowledge needed to address outstanding questions at the intersection of physics and astronomy. With laboratory energies necessarily limited, the Universe provides a fantastic range of extraterrestrial particle accelerators. The aim is to study signals from remote and energetic astrophysical objects to find out plausible answers to some unsolved important questions related to fundamental laws of Nature. The main items are driven by the necessity to find an evidence of a unified theory and investigate matter under exceptional conditions. Exploring the extreme Universe, scientists hope to probe the deepest laws of gravity and nuclear physics. These are exciting and potentially important topics that challenge astrophysicists for an explanation.
Important fields of research are the relativistic gravity and physics beyond the Standard Model[23]. An example is the *LISA* (*Laser Interferometer Space Antenna*) project, a system of three identical spacecrafts arranged in an equilateral triangle formation and separated by about 5 million km. Its objective is to measure gravitational waves expected from massive black holes, and galactic binaries.

1.2 Cosmic rays

As explained in sub section 1.1.5, cosmic rays are energetic charged particles, originating from outer space. The name is misleading, because for some time it was believed that

[23]The Standard Model is the name given to the current theory of fundamental particles and how they interact. It is a theory concerning the electromagnetic, weak, and strong nuclear interactions, which mediate the dynamics of the known subatomic particles.

the radiation was electromagnetic in nature. Contrarily, most cosmic rays are nuclei of atoms, ranging from the lightest to the heaviest elements in the periodic table. In addition, they also include high energy subatomic particles. They strongly interact with matter, but they are able to travel from their distant emitters to the Earth, because of the low matter density in space. Then, they collide with atoms in the air atmosphere and produce other secondary particles that shower down to the Earth.
There are still many open questions mainly regarding the origin of cosmic rays, but it is evident that the knowledge of quantity and type of these particles, helps us to understand the acceleration processes involved and to measure the composition of the Sun and many other distant sources.
In the history of particle physics, cosmic rays are a milestone, because after their recent discovery, just last century, positron, muon and pion had been studied. In fact, before the particle accelerators reached very high energies, cosmic rays served as a source of particles for high energy physics investigations.

1.2.1 History of cosmic rays

In 1785 *Coulomb* found that electroscopes[24] can spontaneously loose electricity in a certain time period, either by contact with less humid air or in the insulating supports [48]. One century after, *Henri Becquerel* made known the spontaneous radioactivity from elements in the ground. It was generally believed that the radioactivity caused air ionization and could be the most plausible explanation of the electroscopes' discharge. Moreover, further measurements, at the beginning of the twentieth century, demonstrated that such discharge was due to ionizing agents coming from outside the electroscope's vessel. Radiation from radioactive elements penetrated the container, producing ions in the air close the leaves and caused them to drop. Considering that the radioactivity originated from material in the crust, scientists started to calculate how much the consequent radiation should decrease with height. Bringing an electroscope at the top of *Eiffel Tower* in Paris (300 m above ground), the ionization rate due to the foreseen radiation was measured. Actually the measurement showed a diminution, but too small to confirm the previous estimation. Nevertheless the terrestrial origin of the unknown radiation continued to be the most common assumption, but the situation was so uncertain to keep alive both the idea of an extra-terrestrial and atmospheric origin.

The turning point was marked by *Domenico Pacini* (Fig. 1.9). In 1911 he observed a reduction ($\sim 20\%$) of the ionization rate at a depth of three meters underwater from the surface. *Pacini* concluded that not all the radiation could come from the radioactivity of Earth's mantle, but a part must be emanated from outside [106]. The radiation's decrease in underwater environment seemed to be in contrast with the weakening at the top of *Eiffel Tower*. The mystery was sorted out measuring the effect at some kilometres of altitude, thanks to balloons.
In fact the natural radioactivity was generated

Figure 1.9: *Domenico Pacini* during a measurement in May 1910. (Courtesy of Pacini family)

[24] An electroscope consists of two leaves of gold foil suspended from an insulated electrode in a metal box with glass window. When the electrode collects an electric charge, the leaves spring apart due to the electric repulsion.

by cosmic rays ($\sim 18\%$), by sources from nature ($\sim 23\%$) and by sources in the atmosphere ($\sim 59\%$), such as the radon gas (now we have to add the contribution from human-caused background radiation). Close to the Earth's surface, the terrestrial and cosmic contributions slightly balanced each other and it was difficult to see an evident difference, moving for some dozens of metres. Therefore appealing results were obtained flying up with special balloons.

In 1912 *Victor Hess* found that the ionization increased more rapidly as he ascended in a balloon (Fig. 1.10(a)). The outcome of the experiment showed that the ionization diminished just above the ground, it had a minimum around 1 km and then it grew slightly until ~ 4 km. In the last part of the flight (from 4 km to 5.2 km), the penetrating radiation became very strong and higher than on the ground (Fig. 1.10(b)). The solidity of this appraisal was guaranteed by the scientific apparatus consisting of three ionization chambers[25]. This was the confirmation that part of radiation entered the atmosphere from above [71]. Besides, he executed many balloon ascensions with different conditions: during the night, the day and even a Sun's eclipse. It was obvious that the radiation origin was related to something extraterrestrial, but not presumably the Sun.
The name given to this radiation was *cosmic ray*, because it was thought it might

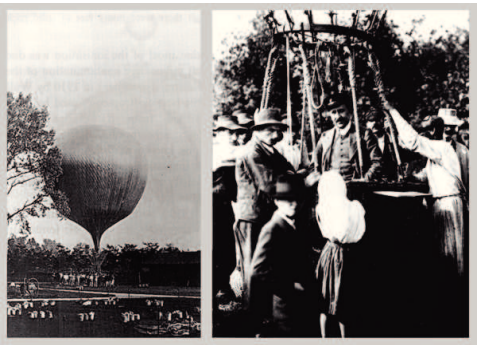

(a) *Hess* before the successful balloon flight

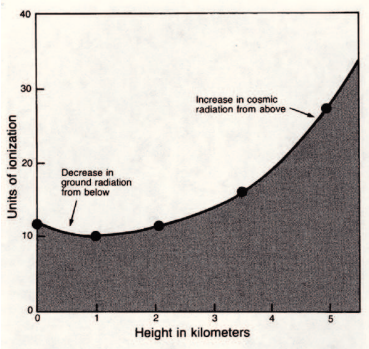

(b) The ionization variation as a function of the altitude

Figure 1.10: On the left photo, *Victor Hess* was preparing the balloon flight, in which he discovered the cosmic rays. On the right, the recorded points by *Hess*' ionization chambers, installed on the balloon. The presence of cosmic rays is evident only above 4 km. (From [85])

be a very penetrating electromagnetic wave. Only subsequently it was shown to be composed of material particles. In fact, the *Pacini* and *Hess*' investigations were only the beginning of the cosmic rays comprehension. Neither the composition nor the origin were unravelled at that period and some aspects are still now unsolved.

Another important step was obtained in 1928 by a lucky chance, when *Jacob Clay* recorded an ionization's dependence with the latitude during two trips [25]. The event spurred to measure the cosmic ray intensity changing the geomagnetic latitude. In 1932 *Compton* confirmed that there was a latitude correlation, corroborating that cosmic rays were charged particles, because such variation should not happen in case of gamma photons. *Compton* did not stop here, but furthermore he proved that most of the cosmic rays are positive. He counted the number of particles coming from west than from east close to the equator. Because of interaction with the Earth's magnetic field,

[25]The ionization chamber is a gas-filled radiation detectors, and is used for the measurement of ionizing radiation.

the west flux, constituted by positive particles, was higher.

The cosmic rays discovery opened a new way to understand the constituents of matter. In 1932, analysing the cloud chamber's tracks released by cosmic rays, *Carl Anderson* detected particles that acted like electrons, but with opposite charge [3]. The positron, so coined by *Anderson*, was the first evidence of antimatter and the experimental proof of the *Dirac equation*[26], which was the first theory fully to account for relativity in the context of quantum mechanics. Some years after it is the turn of the subatomic particle muon, always by hand of *Anderson* in collaboration with *Neddermeyer* [4]. The method is repeatedly the same: to distinguish the track curve's dimension and direction produced by cosmic radiation, when it passed through a chamber dipped in a magnetic field.
It was already clear that the particles observed presumably were not the primary cosmic rays, but secondary products from the interaction with the atmospheric nuclei. Only in 1941 the first primary proton was proved, when *Schein* and co-workers carried out complex *Geiger-Müller*[27] counter arrangements in balloon experiments [116].
Unfortunately the *World War II* slowed down the activity in this sector and the last detection is dated 1947, when the quartet *Powell*, *Muirhead*, *Lattes* and *Occhialini* placed for long time some photographic emulsions[28] at high altitude mountains, under the bombardment of cosmic particles. Subsequently, the photographic plates were developed and the microscopic inspection of the emulsions revealed the tracks of another charged element: the pion [88].

From then on, the accelerators started to take off and the cosmic rays, which have the drawback to be out of human control, were ousted. Anyhow this is not the end of cosmic rays history, rather they strongly came back in the last decade in order to compensate to the limited energy the man can produce in the scientific facilities. Nowadays, cosmic rays are one of the most meaningful argument of astro-particle physics and they are studied to better understand very energetic astronomical processes.

1.2.2 Cosmic ray features

The composition, the flux and the energy range are important topics of cosmic rays, because they are a direct sample of matter from Cosmos. This discernment allows us also to provide an exhaustive illustration of the Universe structural evolution, because they concur to the formation of some metals.
Cosmic rays include practically all the elements in the periodic table and many subatomic particles. They are constituted by 99% of atomic nuclei and by 1% of electrons and positron. Considering the nuclei's fraction, about 89% are nuclei of hydrogen (protons), 10% of helium (alpha particle), and the remaining 1% of heavier elements, which are the end products of stars' nuclear synthesis. We are talking about the primary cosmic rays, namely the original charged particle before the interaction with the interstellar matter or the Earth's atmosphere. When the primary ray bangs into other matter, secondary particles are created. This process is called cosmic ray spallation and it is the beginning of nuclear fission and nucleosynthesis. The result of the collision is the expulsion of large numbers of nucleons from the object hit and consequently lighter and rare metals, as lithium, are produced. Differently, when the cosmic rays approach

[26] The *Dirac equation* is a relativistic quantum mechanical wave equation that provides a description of elementary spin-½ particles, such as electrons.

[27] A Geiger counter is a particle detector that measures ionizing radiation produced in a low-pressure gas tube. Each particle revealed produces a pulse of current, where the energy is not distinguished.

[28] The photographic emulsion is based on silver-gelatin process, consisted of silver halide crystals suspended in gelatin, and the substrate of glass, plastic film or paper.

Earth, they collide with the nuclei of atmospheric gases. In these collisions pions, kaons and muons are generated.

The upper layer of the atmosphere is not hit by a constant flux of cosmic rays. The Sun's solar wind and the Earth's magnetic field are the causes of this variability. The solar wind, which is modulated by the solar activity, diffuses magnetized plasma. The cosmic rays, which interact with the plasma, are decelerated and sometime stopped, if their energy is low. On the other side, charged particles are deflected by Earth's magnetic field, which is dependent on latitude and longitude[29]. First, the cosmic flux, charged both positively and negatively, differs from East to West due to the geomagnetic field polarity. Moreover the charged particles tend to move along the magnetic lines, hence the radiation intensity is lower at the Equator than at the poles, where the lines are concentrated and perpendicular to the surface.

The energy spectrum of the primary cosmic rays (Fig. 1.11) covers many decades and it is now known to extend beyond 10^{20} eV. This upper limit is fixed by the very poor statistics due to the extremely low flux intensity, around one particle every century in an area of $1\,\mathrm{km}^2$. Ultra-energetic particles interact with photons of *CMBR* and cause a drastic lowering of the flux, called *GZK*[30] cut-off. The lower energy limit is bound to the motion of the solar magnetic wind, which blocks the low energy galactic cosmic rays.

The curve's profile is not constant and in some selected regions it is compatible with

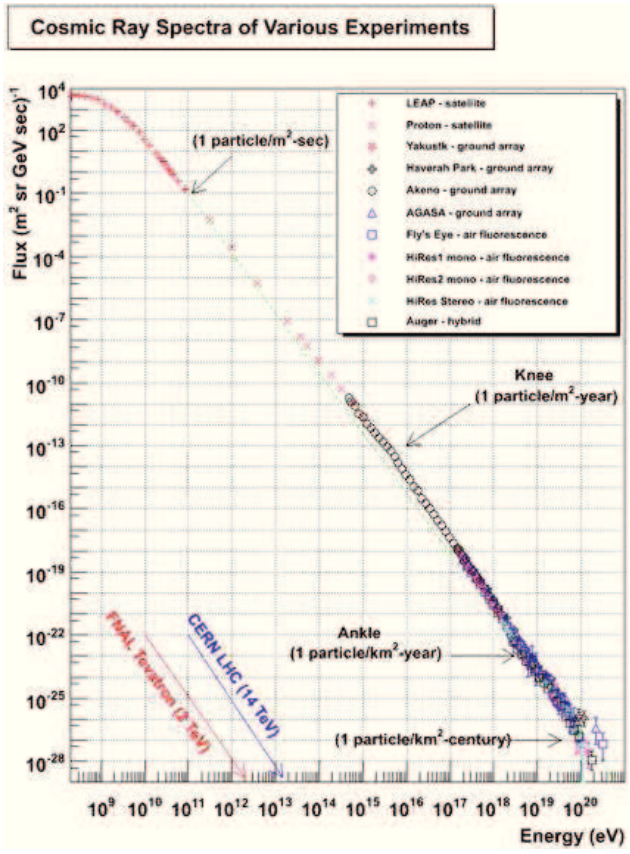

Figure 1.11: The experimental data of the cosmic rays energy spectrum in the wide range from $\sim 300\,\mathrm{MeV}$ to more than 10^{20} eV. As explained in the end of previous section (1.1.5), the current most powerful particle accelerators stop at energies of $\sim 10^{13}$ eV, very far from the most energetic cosmic ray, ever recorded by man. (From [66])

[29] The longitude dependence is a consequence of the misalignment between the geomagnetic dipole axis and the Earth's rotation axis.

[30] The *GZK* (from inventors *Greisen - Zatsepin - Kuzmin*) is a theoretical upper limit on the energy of cosmic rays from distant sources.

different power law functions:

$$\frac{\mathrm{d}\Phi}{\mathrm{d}E} \propto E^{-\alpha} \tag{1.1}$$

where α is the differential spectral index, which suggests a non-thermal origin of cosmic rays. Two particular portions can be easy distinguished: the so called "knee" around 10^{15} eV and the "ankle" around 10^{18} eV. Below the knee and beyond the ankle the dependence of cosmic ray intensity on particle energy is close to $\mathrm{E}^{-2.7}$, while between them is almost $\mathrm{E}^{-3.1}$. The vast energy spectrum indicates that there is a considerable amount of sources, which require different techniques to be detected.

There are many different and complementary techniques employed in this physics area. Some of them have the intent to examine primary cosmic ray, other the secondary products. These detectors can be sorted into:

- **Ground experiments**: *AGASA*, *HiRes Fly's Eye* and *Pierre AUGER* Observatory. They are designed to detect the ultra high energy cosmic rays. *AGASA* and *AUGER* are very large surface arrays, respectively of 100 km^2 and 3000 km^2. Differently *HiRes* utilizes the atmospheric fluorescence technique.

- **Satellite experiments**: *AMS-02* and *PAMELA*. They want to catch the antimatter content of the Universe, measuring the composition of cosmic particles.

- **Balloon experiments**: *ATIC*, *BESS-Polar*, *CREAM* and *TRACER*. They are been utilized for the study of medium energy cosmic rays, flying in Antarctica sky. The *ATIC* detector used the principle of ionization calorimetry, while the central device of *BESS-Polar* was a magnetic spectrometer. *CREAM* housed different systems capable of precise measurements of elemental spectra (for Z=1÷26) nuclei over the energy range $\sim 10^{11}$ to $\sim 10^{15}$ eV. *TRACER* has worked in the domain from $\sim 10^{13}$ to $\sim 10^{15}$ eV, for nuclei with Z between 5 and 26.

1.2.3 Cosmic ray origin

The cosmic rays, being electrically charged, are deflected by several magnetic fields throughout the galaxy and in the intergalactic space. This means that they don't travel straight from their sources, but their directions have been randomized, excluding the possibility to easily analyse them.
Actually the origin of cosmic rays is doubtful, but it is presumed to be in great measure associated to violent events, such as stellar explosions in our own galaxy. This is the most probable explanation, but not the only one, since the extension of the energy spectrum points to a variety of sources. In fact the first part of the spectrum, below $\sim 10^{15}$ eV, should be dominated by the galactic component of cosmic rays, while the last part, above the "ankle", by the extragalactic one.
In case of galactic cosmic rays, their energy derives from supernova explosions, which are very rare events (one every 50 years in our own galaxy). To justify the long term constancy of cosmic rays intensity, a not negligible part of the energy, released by such exceptionally high burst ($\sim 10^{51}$ ergs), must be converted to produce them. It is commonly accepted that cosmic rays are accelerated in the resulting explosion shock waves, which pass through the surrounding interstellar gas. The mechanism is called *Fermi acceleration mechanism*[31] and it provides an illustration on how to accelerate particles

[31] Charged particles gain energy travelling through the shock wave front, produced by a star explosion. The particles undergo multiple reflections, due to moving variable magnetic field, between the upstream and the downstream zone. In every reflection they increase the velocity.

up to 10^{15} eV. For higher energies an incontrovertible demonstration is still missing. Finally, most of the cosmic rays remain confined to the disk of the galaxy, trapped by its magnetic field.
A direct information of their place of production is lost, but the electromagnetic radiation they provoke can be studied. An important example is the *Crab Nebula*, a supernova remnant that emits radio synchrotron radiation due to primary electrons spiralling in the magnetic field. Also γ–rays, generated from the collision with interstellar gas, are observable.

The high-end spectrum in figure 1.11 indicates that the cosmic rays direction might be correlated to an extragalactic origin. According to the *GZK* limit, at these very high energies ($\gtrsim 5 \cdot 10^{19}$ eV) the particles interact with the photons of the *CMBR*. The favourite branch is:

$$\gamma_{CMBR} + p \rightarrow \Delta^{+} \rightarrow p + \pi^{0} \tag{1.2}$$

or

$$\gamma_{CMBR} + p \rightarrow \Delta^{+} \rightarrow n + \pi^{+} \tag{1.3}$$

where pions are produced through the Δ baryon resonance. This process continues until the cosmic ray energy falls below the pion production threshold and the mean attenuation length is of the order of several Mpc, incomparable with the small dimension of our own galaxy (15 kpc). Assuming a galactic origin for these ultra energetic protons, the absorption would be insignificant and the cut-off should not be present. On the contrary the flux drop seems to be an evidence as reported by the *AUGER*[32] collaboration in the plot 1.12, supporting the extragalactic scenario with a suppression at 10^{20} eV. Moreover the cross section of this process and the *CMBR* photons density fix

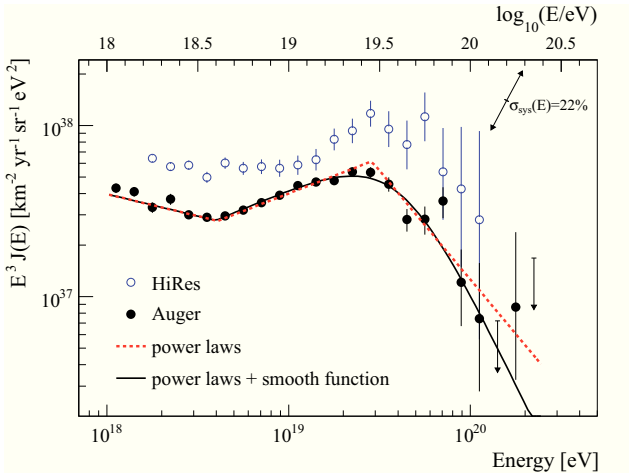

Figure 1.12: The *GZK* cut-off measured by the *Pierre AUGER* Observatory (filled points) and by *HiRes* instrument (open points). (From [42])

the maximum travel distance, that can be covered by particles with an energy higher than pion production threshold. These extragalactic cosmic rays, travelling over 50 Mpc, should never be observed on Earth. This remoteness is known as *GZK* horizon.
A further validation is given by the acceleration models, which predict that particles of energy larger than 10^{18} eV have to be addressed to the extragalactic space. Preliminary experimental data come from the *AUGER* project. It seems that the highest energy events, which are not deflected much by the weak magnetic fields in our own galaxy,

[32]The *Pierre AUGER* Observatory is an international cosmic ray observatory designed to detect ultra-high-energy cosmic rays.

present a direction effectively correlated with *AGNs*[33] [41]. Here the protons could be accelerated by the strong magnetic field associated by the central black hole. Unfortunately there is nothing certain, because these data are affected by poor statistics and large errors. An example, which marks the unresolved situation, comes from the controversial data of *AGASA* experiment.

1.3 γ–rays

The cosmic rays are not the only messengers from the unreachable celestial bodies: a substantial contribution is furnished by the electromagnetic radiation. Only a small part of this light is visible, the rest spreads in all the electromagnetic spectrum. The main feature of these photons is to be neutral, so they are not deflected by the magnetic fields in the outer space. They point back directly to the production source, providing stunning elements for the comprehension of the astrophysical and fundamental processes under extreme conditions.
A brief overview of the electromagnetic radiation spectrum and the associated detectors has been already presented in subsection 1.1.5. Here the attention is focussed on the very energetic light: γ–rays. Typically they manifest the presence of a high energy phenomena in the Universe, often related to *AGNs*, *Pulsars*, *Microquasar* or *Supernova remnants*. These processes include cosmic ray impacts with interstellar gas, stars explosions, and interactions of energetic electrons with magnetic fields.

1.3.1 History of γ–rays

The presence of gamma emission in the Universe was foreseen by theoreticians many years before the advent of the suitable instruments [58, 68, 100]. Initially, experiments were carried out with the help of spacecraft or special balloons in the 1960s, because γ–rays are mostly absorbed by the Earth's atmosphere. Some detectors were foreseen to catch X and γ–rays flashes from nuclear bomb blasts: the most famous case was the *Vela* program [34]. The first gamma telescope, sensitive to energies greater than 50 MeV, was put into orbit with the satellite *Explorer-11* away back in 1961, recording only 22 gamma photons. A problem to the power system compromised soon the data-taking, but not the publication of the article, which marked the beginning of the experimental gamma discipline [86]. Six years later, *OSO-3* improved that result with 621 events attributable to cosmic γ–rays.
In 1972, it is the turn of *SAS-2*, a satellite completely dedicated to the gamma astronomy. Unhappily, it stopped to work only after seven months owing to a serious technical problem. The European Space Agency was more lucky: between 1975 and 1982 a similar detector called *COS-B* operated very well reporting a complete map of the *Milky Way* up to 5 GeV. However the main limit was the poor spatial and temporal resolution. Only in 1991 the *CGRO* (*Compton Gamma-Ray Observatory*) started its mission, transmitting very explicative data on the most energetic electromagnetic radiation. Its energy domain swept from 20 keV, in the hard X–rays upper limit, to 30 GeV, thanks to four main telescopes on board. One of these four telescopes was *EGRET* (*Energetic Gamma-Ray Experiment Telescope*), which measured high energy (20 MeV to 30 GeV) γ–ray source positions to a fraction of a degree and photon energy within 15%. Initially it was validated that a considerable amount of γ–rays came from the

[33] An *AGN* (*Active Galactic Nucleus*) is a compact region at the centre of a galaxy.
[34] The program was run by the Department of Defence to keep watching clandestine nuclear tests. During a scan, *Vela* satellites detected for the first time a γ–ray burst

galactic plane, but subsequently the *NASA*'s jewel revealed some special extragalactic gamma sources, that now we call *Blazars*[35]. *CGRO* was a success and opened the way to the development of new instruments.
The following satellite, *HETE-2* (*High Energy Transient Explorer 2*), was lunched on October 2000. In that period, most of the attention was dedicated to the understanding of *GRBs* (*Gamma-Ray Burst*), the most luminous and sudden γ–ray flashes, likely associated with extremely energetic explosions of massive stars (hypernovae) in distant galaxies. The coordinates of *GRBs* detected were distributed to several ground-based telescopes within few seconds, thereby allowing multiwavelength observations of the initial phases of the afterglow. In fact, this satellite did not house simply the gamma detector, but even X–ray and UV instruments.
The last two gamma space missions started in 2002 with *INTEGRAL* (*INTErnational Gamma-Ray Astrophysics Laboratory*) and in 2004 with *Swift*. *INTEGRAL* is dedicated to the fine spectroscopy ($E/\Delta E = 500$) and imaging (angular resolution of 12 arcmin) of objects in the energy interval 15 keV to 10 MeV. *Swift* is composed by three main instruments, which work in tandem to assure rapid identification of *GRBs*. One runs in the optical domain 170 to 600 nm, another in the X–rays energies 0.3 to 10 keV, while the third in the hard X and soft gamma range 15 to 150 keV. Both satellites are still operating, after many years of activity. *INTEGRAL* has detected more than 700 gamma sources, as reported in the fourth *IBIS/ISGRI* soft γ–ray survey catalogue, while *Swift* has already recorded more than 500 *GRBs*. They are constantly providing new insights, helping us to understand processes such as the formation of new chemical elements and the mysterious *GRBs*.

The balloons should not be forgotten, because they were and are a fruitful alternative for γ–rays study. Often they have been also used for the development of new technologies and payloads for space flight missions. The history of gamma balloon-borne experiments is quite recent, but it was immediately stimulating. The extraordinary flights of the gamma imaging telescope *GRIS* in 1988 allowed to record the first cobalt-decay (^{56}Co) γ–ray image from the spectacular supernova *SN 1987A* and the positron annihilation line at 511 keV from the galactic centre [123, 92]. The obtained result, observing the newborn supernova, was an important brick for the investigation of stars' nucleosynthesis of elements beyond helium. *GRIS* continued his marvellous activity with other three flights in 1995, mainly analysing the galactic γ–ray spectrum and reporting new interesting conclusions about the formation of ^{26}Al, an isotope that is formed in massive stars near the end of their lives [102].
Further balloon experiments pursued the research in the hard X–rays and soft γ–rays regions. In 1992 and a second time in 1995, *HIREGS* flew over the Antarctica sky in order to observe solar flares and examine the flare acceleration processes, unresolved by scintillators that have been used in spacecrafts. The *High Resolution Gamma-Ray and Hard X-Ray Spectrometer* was conceived to operate from 20 keV to 18 MeV with an energy resolution of 1.5 keV, and up to 160 MeV with 0.5 MeV resolution. It confirmed and in addition improved the spectroscopic measurements of *GRIS* related to the electron-positron annihilation line and the ^{26}Al nucleosynthesis line.
The balloon-borne telescope *TIGRE* is very recent (2007 & 2010). A completely different technology, based on multi-layers of thin silicon detectors, was used to measure the energy losses of Compton recoil electrons in the MeV range. This new technique facilitated the background rejection, the sensitivity improvement and a clear image reconstruction. Moreover, the *Tracking and Imaging Gamma-Ray Experiment* acted as

[35] Blazar is a member of the wide group of *AGNs*

both a Compton telescope and a pair detector, guaranteeing a good efficiency over the entire interval 0.3 to 100 MeV and a wide field of view. Some black holes and *Pulsars* in the galactic neighbourhood were the main targets.

For energies higher than some hundreds GeV, the gamma flux is so weak that the small effective area of satellite experiments is insufficient. The history of ground-based telescopes started away back in 1968 with the *Whipple* observatory in southern Arizona[36]. It was the pioneer of atmospheric Čerenkov imaging technique in the very high energy (*VHE*) range 100 GeV to 10 TeV. *Whipple* was a 10 m telescope designed to collect the faint light of the Čerenkov radiation produced in the interaction between a γ–ray and the atmosphere. Analysing the properties of the collected blue Čerenkov light, it was possible to trace back to the original γ–ray. The main discovery occurred after twenty years of continuous progress, in 1989, when *Whipple* detected the first γ–rays from the *Crab* nebula [56]. The measured flux was steady and *Crab* became the standard candle in the *VHE* γ astronomy.
The astonishing result of the *Whipple* collaboration pushed the construction of new instruments in the beginning of 1990s. *HEGRA* (*High Energy Gamma-Ray Astronomy*) made use of the same principle of its precursor, introducing the stereoscopy, arranging four telescopes on a square of 100 m side length with two additional telescopes centred. This innovative approach to operate simultaneously with several telescopes improved the angular resolution, the spectral reconstruction of the primary particle and the background rejection efficiency. All of this could be translated in a sensitivity to very weak γ–ray sources, less than 1% of the *Crab* nebula flux in 100 h of data-taking. On the other side, this system was able to observe the most energetic photon (16 TeV) for that period from the Blazar *Markarian 501*.
Another air shower competitor experiment in the very high energy domain was *CLUE* (*Čerenkov Light Ultraviolet Experiment*). However, it should be considered complementary, because it was based on a different working method, which allowed to operate with Moon and to point luminous regions. The detector was sensitive in the *UV* range ($190 \div 230$ nm) preventing the use of the classical *IACT*[37] algorithms. *CLUE* did not achieve important results, but it was an additional sign that this new astrophysical branch provoked high interest.

1.3.2 Current γ–rays detectors

Currently the main and powerful satellite-borne gamma detector is the originally called *GLAST* (*Gamma-Ray Large Area Space Telescope*), renamed *FERMI* in honour of the famous Italian physicist *Enrico Fermi*. Another important instrument is *AGILE* (*Astrorivelatore Gamma ad Immagini ultra LEggero*), realized by the *Italian Space Agency* (*ASI*). As written in the subsection 1.3.1, *INTEGRAL* and *Swift* are still well operating satellites.

The core of the *FERMI* space observatory is the *LAT* (*Large Area Telescope*), an imaging high energy γ–ray telescope sensitive in the energy interval from ~ 20 MeV to ~ 300 GeV and able to cover the entire sky in only three hours, providing a continuous and efficient scan. The angular resolution is of the order of 1 degree, strongly

[36] Before *Whipple*, there were some precursors, which followed the Stuart Blackett's intuition about the Čerenkov light production in air [16]. The first discovery was made in 1953 by J. V. Jelley and W. Galbraith [79]. Then, some rudimentary prototype detectors were build in Crimea (1959–65), in Ireland (1962–66) and Massachusetts (1965–66) [134].

[37] *Imaging Atmospheric Čerenkov Technique* is a technique utilized by the telescopes that collect and analyse the Čerenkov light produced by extended air shower initiated by a cosmic ray. Usually they are sensitive to the blue light ($300 \div 400$ nm) and apply imaging algorithms.

dependent on energy. Point-like emissions are well determined up to few GeV, while going to higher energies, the poor statistics allows only a long integrative study of diffuse sources. These features show a superior performance compared to its predecessor *EGRET* (Table 1.1). The improvement in sensitivity is of a factor 30.
LAT is composed of four subsystems, which have specific rules in the detection mech-

Comparison between *FERMI/LAT* & *EGRET*		
PARAMETERS	**FERMI/LAT**	**EGRET**
Energy range	$20\,\text{MeV} \div 300\,\text{GeV}$	$20\,\text{MeV} \div 30\,\text{GeV}$
Peak effective area after background rejection	$> 8000\,\text{cm}^{\,2}$	$1500\,\text{cm}^{\,2}$
Field of view	> 2 sr	0.5 sr
Angular resolution of single photon on-axis	$< 3.5^\circ$ (100 MeV) $< 0.15^\circ (> 10\,\text{GeV})$	5.8° (100 MeV)
Energy resolution	$< 10\%$	10%
Dead-time per event	$< 100\,\mu\text{s}$	100 ms
Source location determination	< 0.5'	15'
Point source sensitivity	$< 6{\cdot}10^{-9}\,\text{cm}^{-2}\,\text{s}^{-1}$	$\sim 10^{-7}\,\text{cm}^{-2}\,\text{s}^{-1}$

Table 1.1: Main characteristics of the *FERMI/LAT* detector in comparison with his predecessor *EGRET*.

anism based on pair production effect[38]. The tracker reconstructs the path of the electron and positron pair, produced by the initial γ–ray. The calorimeter measures the complete amount of energy released by the particles. The anti-coincidence detector, placed on the outermost layer of the tracker, is a shield to block the unwanted charged cosmic rays. The data acquisition system is an electronic system that processes all the information coming from the previous substructures, selecting only the events of interest. The typical γ–ray evidence is underlined by no signal in the anti-coincidence shield, two joined tracks in the tracker and an electromagnetic shower in the calorimeter.
FERMI is equipped of a second important instrument, the *GBM* (*Gamma-ray Burst Monitor*), which extends down the detectable energy domain to 8 keV. The *GBM* field of view is several times larger than *LAT*, therefore very soft gammas and hard X–rays are caught by his 14 scintillation detectors to localize sudden bursts.

AGILE is a small *FERMI* observatory competitor, which consists of two instruments: *AGILE-GRID* and *SuperAGILE*. This combination sustains simultaneous detection photons in the 30 MeV $\div$50 GeV and in the 18$\div$60 keV energy ranges. The detector is very compact and light, it weights only ~ 130 kg[39], allowing a fast monitoring of the sky. This is an important peculiarity, which helps the rapid repositioning and imaging recording, after an alert of a strong gamma transient from a variable source.
The *AGILE* instrument, based on the advanced technology of the solid state silicon detectors, is quite powerful and cost-effective. The design concept is very similar to the previously described in the *FERMI* paragraph. *AGILE-GRID* contains a silicon-tungsten tracker followed by a caesium iodide calorimeter, everything covered by an anti-coincidence system. It is characterized by a large field of view of 2.5 sr, a good angular resolution of 15', a fine spatial resolution and a small dead-time less than 200 μs. The *SuperAGILE* is not thought to be a simple *GRB* monitor, but it offers in addition the possibility of analysing γ–ray and hard X–ray sources with a good angular

[38] The primary interaction of photons in the *LAT* energy range with matter is pair conversion.
[39] The total satellite mass is equal to 350 kg. For comparison the *LAT*'s weight is 2789 kg.

resolution of 6 arcmin and a sensitivity of ~ 10 mCrab for one day integration.

Very high energy photons (> 300 GeV) can be only revealed with ground-based telescopes. The extremely low particle flux requires detectors with extensive collective area, too huge and heavy for space missions. The detection technique on the ground is completely different, because the calorimeter is provided by the atmosphere. Primary γ–ray interacts with an air nucleus, producing a wide secondary particle shower. The *EAS* (*Extended Air Shower*) can be observed using arrays of counter detectors and through the Čerenkov light caused by his ultra relativistic part. This technique is called *IACT*.
These *IACT* telescopes, such as *HESS*, *MAGIC* and *VERITAS*, complement the capabilities of the previously described satellite-borne experiments. They have larger effective areas ($> 10^4$ m^2), but small fields of view ($3 \div 5^\circ$) and limited duty cycles relative to space observatories. However, the current Čerenkov telescopes extend a good sensitivity well below 300 GeV, furnishing a useful overlap with *FERMI*, in a formerly unexplored region of the electromagnetic spectrum. They can reach such a low energy threshold, because they use very large reflective surfaces to collect more photons and they are located at high altitudes, where the Čerenkov light density is higher. The main parameters of these three gamma telescopes are reported in table 1.2.

Name	**Location**	**Nr.**$_{Tel}$	**Reflective surface** $\varnothing$	**E**$_{th}$	**FoV**
HESS	S	4	12 m	100 GeV	5°
MAGIC	N	2	17 m	55 GeV (*)	3.5°
VERITAS	N	4	12 m	100 GeV	3.5°

Table 1.2: Some important characteristics of the three main IACTs in the world. (*) In *Sum-Trigger* mode, see section 5.1, the threshold is 25 GeV.

HESS (*High Energy Stereoscopic System*) is a system of 4 *IACT* telescopes located in Namibia (Africa) at an altitude of 1800 m, that operates from 2003 in the 100 GeV to 100 TeV energy range [61] (Fig. 1.13(a)). The telescopes, which have a single reflective surface of 107 m ^{2}, are arranged on a square with 120 m sides. This spacing represents a compromise between the large base length required for good stereoscopic viewing and the requirement that two or more telescopes are hit by the same shower. The collected light is focused by 382 glass mirrors, disposed in the *Davies-Cotton* design for $f/d \simeq 1.2$. At the focal plane, the photo detector, called camera, is equipped with 960 *PMTs* (*PhotoMultiplier Tubes*), covering a 5° field of view with a pixel size of 0.16°. The telescope' structure uses an alt-azimuth mount, which rotates on a 15 m diameter rail. It is made up of steel tubes, designed for high mechanical rigidity. Both azimuth and elevation are driven by friction drives acting on auxiliary drive rails, providing a positioning speed of 100°/min. *HESS* is perfectly indicated to observe the galactic centre region, because it is situated in the southern hemisphere and has a large FoV.

VERITAS is another similar array of four telescopes, located in southern Arizona, each with a 12 m optical *Davies-Cotton* reflector made of 350 hexagonal glass mirrors for a total area of 110 m^2 [132] (Fig. 1.13(b)). The Čerenkov radiation is reflected into a 499 pixels camera mounted on each telescope. Each pixel is a circular *PMT XP2970* from *Photonis* with a quantum efficiency of $\sim 20\%$ at 320 nm. The single telescope has a field of view of 3.5° and operates in the energy domain between 100 GeV and 50 TeV. The mechanical structure is similar to that of the *Whipple* 10 m telescope. The custom-designed tubular steel optical support is propped and orientated by an alt-azimuth commercial positioner (RPM PG-4003) with a maximum speed of 1 degree per second

and a pointing accuracy of $\pm 0.01°$.

(a) HESS (b) VERITAS (c) MAGIC

Figure 1.13: *Left:* the 4 *HESS* telescopes. (From Sciencephoto webpage)
Centre: the 4 *VERITAS* telescopes. (Courtesy of N. Galante)
Right: the 2 *MAGIC* telescopes. (Courtesy of R. Wagner)

MAGIC (Major Atmospheric Gamma-ray Imaging Čerenkov Telescope) is a system of two telescopes situated at the Roque de Los Muchachos observatory in La Palma, one of the Canary Islands, at about 2200 m above sea level (Fig. 1.13(c)). With a dish diameter of 17 m, it is the largest optical surface in the world. The first telescope started to be operative in 2004, while the second one, at a distance of 85 m from the first, started taking data in fall 2009. Mainly due to the large reflective surface (236 m^2), MAGIC is sensitive to cosmic γ–rays with energies between 50 GeV (25 GeV in *Sum-Trigger* mode) and 30 TeV. The lightweight carbon fibre frame allows a fast complete rotation of the telescope in less than 20 s. This rapid repositioning is an important feature especially when a *GRB* alert arrives from satellite monitoring systems. More details will be described in chapter 4.

1.3.3 γ–rays characteristics

In general the radiation propagating in the Universe is generated by hot objects, such as stars, and presents a thermal nature, where the frequency is proportional to their temperature. This radiation can reach the keV domain, but hardly there is something so hot to justify an higher thermal energy. Hence, in the case of high energy cosmic and γ–rays, the non-thermal processes are the most plausible explanation. Their power-law spectrum (Fig. 1.11) shows no indication of a characteristic temperature dependency, promoting an emission from the most extreme conditions, by particles moving very near the speed of light. Environments as stellar explosions and giant black holes at the centre of active galaxies are the best candidates for γ–rays generation.
The accelerator mechanisms probably stimulate primarily charged particles, such as electrons and protons, by means of powerful electromagnetic fields. Sometimes the acceleration occurs in a typical one-shot process, but very often the process is fed by a different continuous increasing in particle energy. For instance, in Supernova shock waves the particles gain energy for a long time, even more than 10000 years, bouncing between magnetic fields. Only after this initial stage, γ–rays appear as secondary products of accelerated charged particles. There are different ways to generate γ–rays, and hereafter the fundamental processes are described.

The first is due to the decay of π^0, produced when an accelerated proton interacts with nuclei of the ambient medium, into two gammas (Fig. 1.14(a)). This is the main hadronic channel for γ–ray production. A protons population interacts through inelastic scattering with nuclei and other protons of the ambient material, creating charged and neutral pions (Eq. 1.4). The neutral pions have a short lifetime and they decay in

gammas. The reaction can only take place when the protons energy exceeds a minimum value of two times the pion rest mass ($\sim 280\,\mathrm{MeV}$). It is interesting to note that charged pions decay leptonically emitting neutrinos. Therefore the hadronic channel should be correlated to a neutrino emissions.

$$\begin{aligned} p + p &\rightarrow \pi^0 + \pi^+ + \pi^- \\ \pi^0 &\rightarrow \gamma\gamma \\ \pi^+ &\rightarrow \mu^+ + \nu_\mu \\ \pi^- &\rightarrow \mu^- + \overline{\nu}_\mu \end{aligned} \tag{1.4}$$

The second one, which is called leptonic channel, is driven by electrons. When the accelerated particles are electrons, they may undergo *bremsstrahlung* in the ambient medium (Fig. 1.14(b)), may suffer *synchrotron* radiation losses in local magnetic fields (Fig. 1.14(c)), or may transfer a significant part of their energy to photons via the *Inverse Compton* scattering process.
When an high speed electron is deflected by the electrostatic field, generated by a

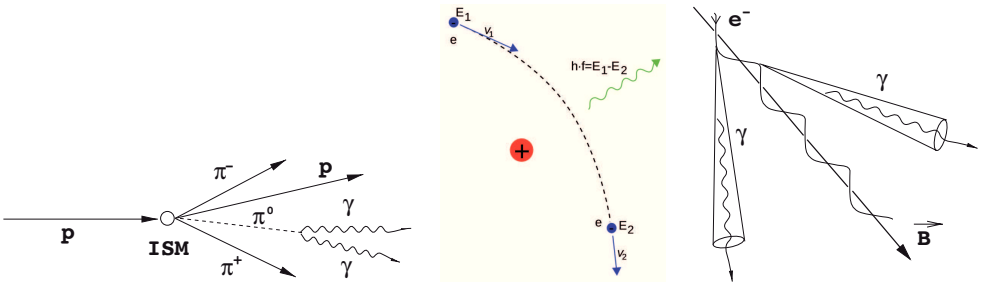

(a) Neutral pion decay (b) Bremsstrahlung (c) Synchrotron radiation

Figure 1.14: Some sketches of the main γ–ray production mechanisms. On the left, the neutral pion decay into two gammas, from the scattering between a proton and the interstellar medium. In the centre, the *Bremsstrahlung* produced by a high energy electron deflected in the electric field of an atomic nucleus. On the right, the *Synchrotron* radiation generated when a relativistic electron passes through a strong magnetic field.

charged atomic nucleus, it radiates an electromagnetic wave due to *bremsstrahlung*[40]. The electron loses kinetic energy, which is transferred into a photon. The characteristic *bremsstrahlung* spectrum is continuous and proportional to 1/E, where E is the energy of the photon. The released amount of energy is contingent on target's density and the crossing distance (Eq. 1.5), while the obtainable frequency range swaps from zero to the electron kinetic energy.

$$\Delta E = E_e(1 - e^{\frac{d}{X_0}}) \tag{1.5}$$

The parameter d is the distance and X_0 is the radiation length, inversely proportional to the target density.
When a relativistic electron passes through a strong magnetic field, it radiates an electromagnetic wave due to the *synchrotron* radiation. This emission is polarized and the spectrum is characterized by non-thermal power law with a peak proportional to the transverse component of the magnetic field. The maximum possible energy of irradiated photons is shown in equation 1.6: γ_e is the Lorentz factor of the electron

[40] *Bremsstrahlung* radiation becomes noticeable when the energy of the particle is very high compared to its self-energy. This constraint favours mainly electrons.

$(1/\sqrt{1-\beta^2})$, q_e the electron charge, m_e the electron mass and B the magnetic field.

$$E_{max} = \gamma_e^2 \frac{q_e B}{2\pi m_e} \tag{1.6}$$

High energy *synchrotron* radiation can be produced where a strong magnetic field is present, as close to a neutron star surface. This process is responsible for the radio emission from galaxy, from Supernova remnants and extragalactic radio sources, but it cannot exceed TeV limit. The limit's enhancement is provided by *Inverse Compton* scattering of these photons.
The *Inverse Compton* process occurs when relativistic electrons scatter off low energy photons, so that the photons gain and the electrons lose energy. It is probably the main gamma production mechanism in the Universe. On the basis of the original electron and photon energy, two regimes should be distinguished because the cross-section differs a lot: the *Thomson* and the *Klein-Nishina* limit.

$$E_{(\gamma,f)} \approx \begin{cases} \frac{4}{3} E_{(\gamma,i)} \cdot \gamma_e^2 & \text{if} \quad E_e E_{(\gamma,i)} \ll m_e^2 c^4 \\ \frac{1}{2} E_e & \text{if} \quad E_e E_{(\gamma,i)} \gg m_e^2 c^4 \end{cases} \tag{1.7}$$

In the *Thomson* regime, the emitted photons present a spectrum similar to the original photons, while in the *Klein-Nishina* regime, the result trend is steeper and is determined by the maximum energy of the participating electrons.

Both channels, hadronic and leptonic, generate a flux which is ruled by the density their charged parent particles and of the target involved. In the π^0 decay the external parameter is the ambient medium, in the *synchrotron* process is the strength of magnetic fields, while in the *Inverse Compton* process is the starting energy of target photons. All of this may be translated in a gamma energy spectrum closely related to the spectrum of the parent particles, which can be tracked back and studied.

In the *SSC* (*Synchrotron Self-Compton*) model [80] of astrophysical environments, where the gamma production follows a gravitational collapse, the leptonic channel is stimulated by a relation between the *synchrotron* radiation and the *Inverse Compton* mechanism. High energy γ–rays result from *Inverse-Compton* up-scattering of *synchrotron* radiation, peaked in the infrared or X–ray range, by the same relativistic electrons that produced the *synchrotron* radiation (Fig. 1.15).

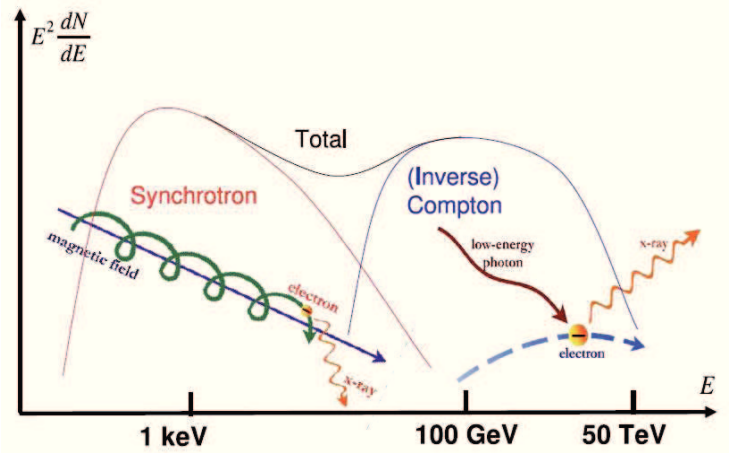

Figure 1.15: Differential energy spectrum of photons in the *SSC* model. (Courtesy of A. De Angelis)

Once generated, γ–rays propagate on straight lines through the Universe bringing precise information about the original source. The crossing matter during the travel is not irrelevant as in the case of the weak interactive particle neutrino. The native gamma flux decreases, absorbed before reaching the detectors. The cause resides in two fundamental processes: photon-matter and photon-photon pair production.
In the first case, γ–rays are absorbed in the interaction with hadronic or leptonic matter, as the interstellar and intergalactic medium. However the cross section is very low and the contribution is really trifling. Conversely, it is influential the main photon-photon pair production (Eq. 1.8).

$$\gamma + \gamma_{EBL} \rightarrow e^+ + e^- \tag{1.8}$$

For γ–rays with energy higher than 100 GeV, the target is provided by the optical and infrared part of the *Extragalactic Background Light* (*EBL*), produced by stars and reprocessed by cosmic dust (Fig. 1.16). When the γ–ray energy is sufficiently high to crate an electron-positron pair, converting energy into matter, the spectrum is heavily modified. For this reason it is important to know the *EBL*, in order to extrapolate the intrinsic spectrum of a source.
The photon absorption along its path is a function of the original photon energy and the

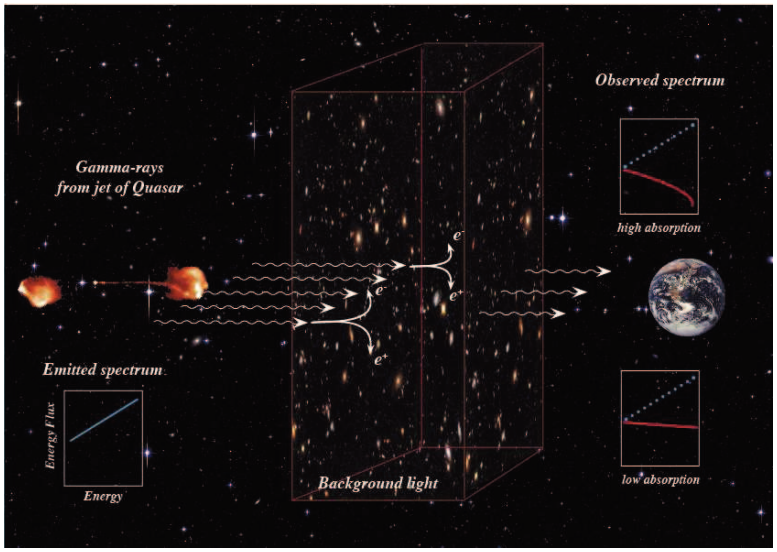

Figure 1.16: A cartoon of the effect of *EBL* on the γ–ray emission from a distant object. If the density of *EBL* photons is high (upper right graph), absorption is high and the highest energy γ–rays are lost. So the distribution of measured energies (spectrum) is strongly depleted. If instead the density is low (lower right graph), absorption is less and the spectrum is not changed as much.

redshift of the progenitor source. The light intensity decreases following the expression:

$$I = I_0 \cdot e^{-\tau(E,z)} \tag{1.9}$$

where τ is the optical depth.
Approaching the Earth, cosmic γ–rays are difficult to detect, because the noise is many orders of magnitude ($\sim 10^8 \div 10^9$) stronger. Charged cosmic particles are the primary source of background. Interacting with the Earth's atmosphere, they produce secondary particles and gammas. The experimental identification of primary gamma events is technologically very challenging and essential for the localization and the comprehen-

sion of the collective acceleration mechanisms, currently subject of a broad theoretical work. The energy range from 10 GeV to 50 GeV has not yet been experimentally well investigated. Lowering the energy threshold and the systematics is one of the major challenges of IACTs. For more details on the argument, read chapter 3.

1.4 Very high energy gamma sources

In the last ten years, the advent of new satellite and ground-based detectors for high energy γ–rays has impressively raised the scientific knowledge of the most violent phenomena in the Universe. To get an idea of the achieved detection progress, in figures 1.17(a) & 1.17(b) the sky maps of the third *EGRET* and the second *Fermi* source catalogues are shown. The *EGRET* catalogue contains only 271 sources, the *Fermi* one 1873, detected in 24 months. An interesting aspect of the last *Fermi* catalogue is the presence of still a lot of not associated sources, which stimulates a wide range of astrophysical research. In the catalogue, 127 sources are considered to be identified, while plausible associations are proposed for 917 *AGNs*.

Gamma-ray sources may be distinguished in galactic and extragalactic. Both the satellite and the ground-based data show respectively that the flux and the number of emitters of γ–rays decrease with the distance from the galactic centre, where they are produced by the collision between cosmic rays and the diffuse galactic gas (Fig. 1.18(a) & Fig. 1.18(b)). However a large variety of extragalactic sources, such as *AGNs*, have been discovered to emit non-thermal γ–rays.
In subsections 1.4.1, 1.4.2, 1.4.3 and 1.4.4 the main galactic sources are described, whereas in subsections 1.4.5 and 1.4.6 the extragalactic ones.

1.4.1 Supernova remnants

A *Supernova remnant* (*SNR*) is the structure resulting from the explosion of a star in a Supernova. It is characterized by an expanding shock wave of ejected material. The shock wave consequent the collapse of a star, at the end of his cycle, can efficiently accelerate particles up to more than 10% of the kinetic energy of the explosion. Most of the galactic cosmic rays below energy of 10^{15} eV are the progenitors of γ–rays from *Supernova remnants*. Consequently the measured *VHE* radiation is explained both with leptonic and hadronic models.
The first to be detected, assumed as standard candle in gamma astronomy, is the *Crab* nebula. In the MeV÷TeV domain its flux is considered quite stable and used for the experiments calibration. However, in September 2010 and April 2011 the *AGILE* and *Fermi* satellites have reported an increased γ–ray intensity above 100 MeV [28, 31, 27, 104], not confirmed in the TeV region[41]. The uncommonly rapid flux variation, one order of magnitude higher than the standard value, has reached the peak of $(26\pm5)\cdot10^{-6}$ ph cm^{-2} s^{-1} on a 12 hour time-scale (Fig. 1.19). It seems that particle acceleration mechanisms in inner nebular shock regions are more efficient than expected from classical theoretical models [129].

Often the Supernova spectra contain a pulsed emission from the central neutron star, which is the argument of subsection 1.4.2. When a *SNR* contains a *Pulsar* object in the centre, it is called *Pulsar Wind Nebulae*. The pulsed radiation emitted from the

[41] The *ARGO-YBJ* experiment has reported an enhanced TeV emission in September 2010, but this claim was not supported by the simultaneous observations of *MAGIC* and *VERITAS*.

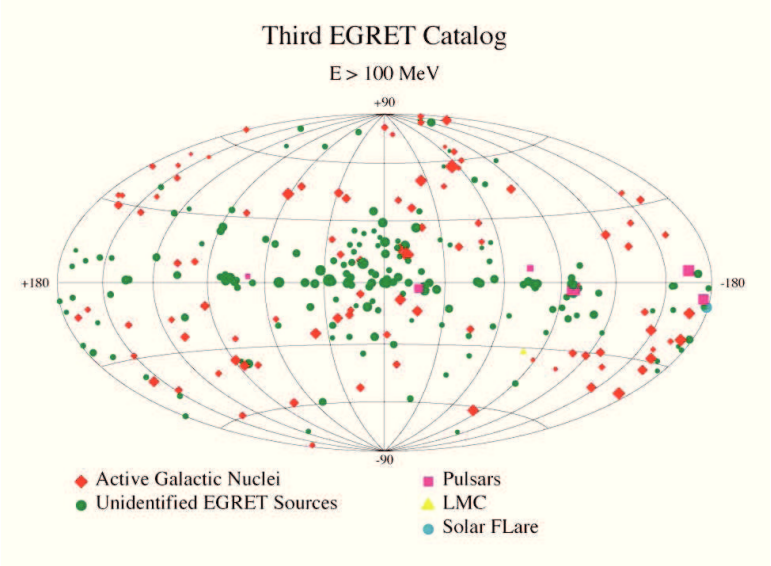

(a) *3rd EGRET* catalogue

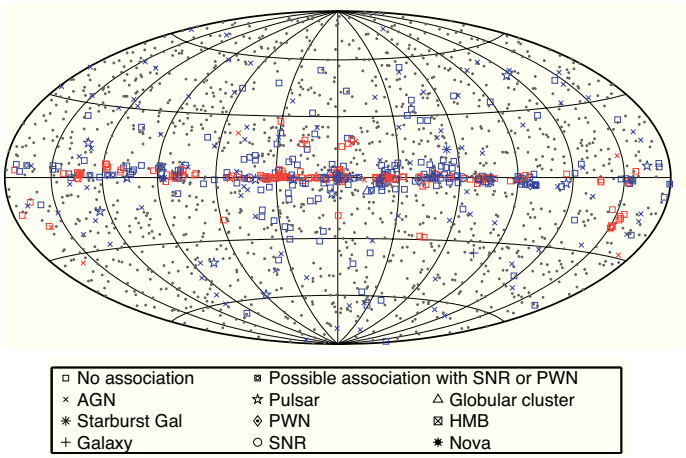

(b) 2nd *Fermi* catalogue

Figure 1.17: On the top the 3rd *EGRET* catalogue, which consists of 271 sources: 5 Pulsars, 1 solar flare, 93 Blazars associations, 1 likely Radio galaxy, 1 normal galaxy and 170 unidentified sources. (From [54])
On bottom the *Fermi LAT* full sky map showing 1873 flagged sources by source class. Sources potentially confused with diffuse emission are shown in red. Those with any other flag set are shown in blue. Sources with no flag set are shown as small dots. (From [30])

jets, can undergo *Inverse Compton* scattering with remnant material, engendering high energy γ–rays.

The essential elements for these phenomena are the star explosions and the interstellar medium. Prolific regions, in this sense, are star-burst galaxies and clusters of galaxies. Star-burst galaxies are characterized by a high frequency of Supernova explosions, becoming efficient acceleration sites and a powerful γ–ray sources. On the other side, clusters of galaxies are characterized by a dense inter-cluster medium. Cosmic rays, generated during the cluster evolution, are entrapped inside and cannot escape. The history and the progress of the cluster may be deduced by γ–rays resulting from

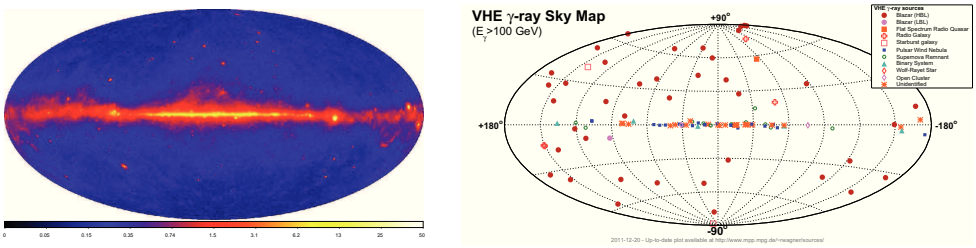

(a) *Fermi LAT* γ flux sky map (b) *VHE sky map*

Figure 1.18: *Left:* the sky map of the energy flux derived from the *Fermi LAT* data of the 2nd catalogue. The image shows γ–ray energy flux in the domain between 100 MeV and 10 GeV, in units of $10^{-7}\,\mathrm{erg\,cm^2\,s^{-1}\,sr^{-1}}$. (From [30])
Right: the map of all γ–ray sources detected above 100 GeV. (Image credit: R. Wagner)

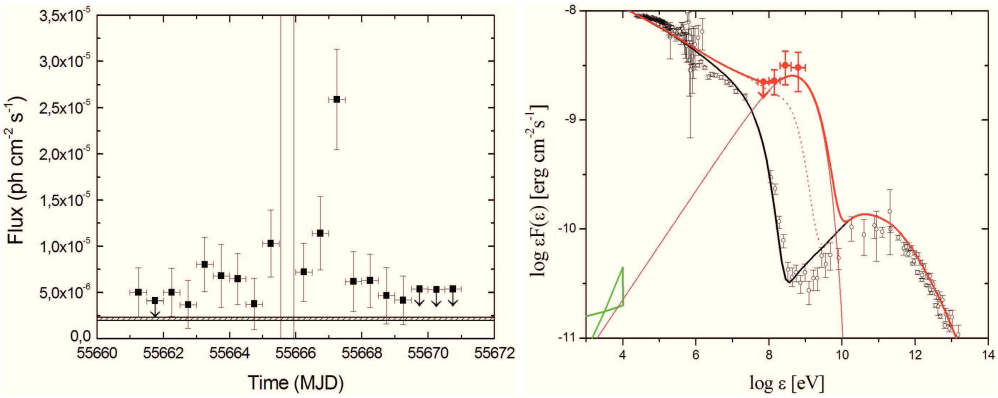

Figure 1.19: *Left:* the *Crab* γ–ray light curve above 100 MeV detected by *AGILE-GRID* in April 2011. The gray thin horizontal band shows the typical average flux ($(2.2\pm0.1)\cdot10^{-6}$ ph $\mathrm{cm^{-2}\ s^{-1}}$), and the gray vertical lines mark the time period without data caused by a communication problem. *Right:* the γ–ray pulsar-subtracted spectrum of the *Crab* nebula flare. The *AGILE* flaring spectral data (marked in red) were obtained for a 1-day integration during the interval 2011/04/15 09:40 UT – 2011/04/16 0.9:40 UT. Data points marked in black colour show the average nebular spectrum. The red curve is the result a possible theoretical model discussed by *AGILE* collaboration. The spectral region marked in green shows the X–ray spectrum of an inner region of nebula. This is indicative of an X–ray upper bound expected from the flare. (From [27])

the interaction between primordial cosmic rays and intra-cluster gas.

1.4.2 Pulsars

After a supernova explosion, a dense and fast rotating neutron star is formed in the centre, surrounded by the expanding remnants (Fig. 1.20). Inhomogeneities during the gravitational collapse, cause the neutron star's angular momentum, which increases the rotation speed in relation to its progressive compaction. The particles' acceleration is favoured in this area affected by intense fields, causing beamed electromagnetic radiation, regularly visible only when the beam is pointing towards the Earth. From here the name *Pulsar*. The radiation's direction is fixed by the magnetic axis of the *Pulsar*, which does not necessarily coincide with the position of the rotational axis. Without this misalignment, it is impossible for a stationary observer to see the pulsed feature. The pulsed irradiated emission is due to the interaction of the intermittent pulsar wind

outflow with the neighbouring ambient medium.

The experimental spectrum is still under study. Different models predict power law trend with different cut-off in the interval 1÷100 GeV. The most quoted ones are the *Outer gap* and the *Polar cap* models (Fig. 1.21).

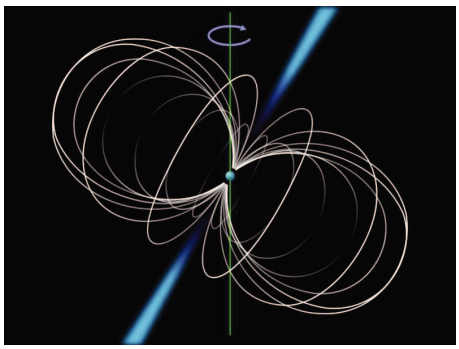

Figure 1.20: Schematic view of a *Pulsar*. The sphere in the middle represents the neutron star, the curves indicate the magnetic field lines and the protruding cones represent the emission zones. (Creative Commons licenses)

In the *Polar cap* model electrons are accelerated in the open field region near the magnetic poles, radiating γ–rays via *synchro-curvature*[42] radiation. A component of these high energy photons are subjected to pair production, but the rest, with lower energy, can survive and escape to infinity. The relevant feature of the *Polar cap* is a steep cut-off in the spectrum, which follows a super exponential trend [67].

In the *Outer gap* model the acceleration mechanism is considered to take place in the outer magnetosphere, far away the neutron stellar surface [23]. The γ–ray production is determined by photon-photon pair production, which is less energy dependent compared to the previous model. The resultant spectrum is smoother and the cut-off appears at higher energies.

Crab is one of the few known Pulsar TeV emitters. *MAGIC* is the only *IACT* telescope

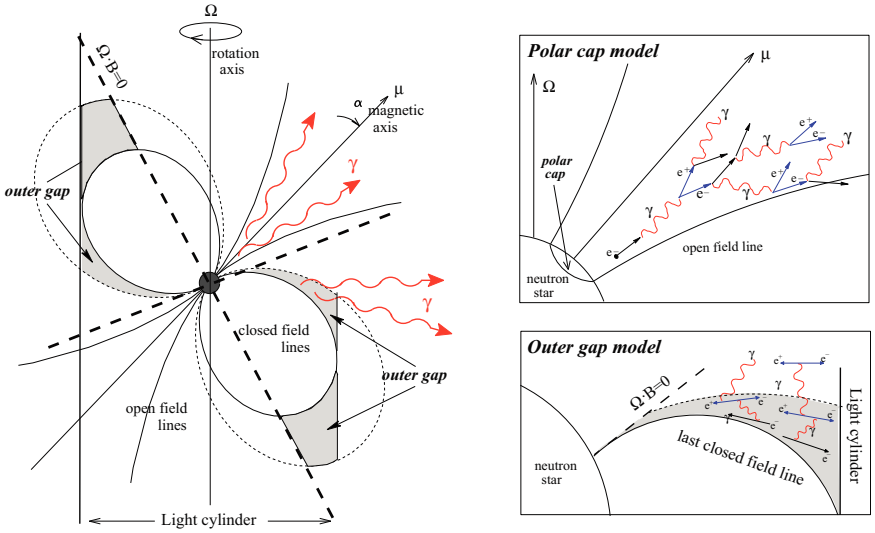

Figure 1.21: An illustration of *Pulsar*'s magnetosphere (left) and the most popular γ–ray emission mechanisms from a *Pulsar* (right). On the right top, the *Polar cap* and on the right bottom the *Outer gap* model. (From [96])

able to extend the detection limit to the never reached low energy threshold of 25 GeV. More details are presented in chapter 5.

[42] The *synchro-curvature* mechanism unifies the ordinary *synchrotron* and *curvature* radiation. In fact, *synchrotron* radiation is independent of the curvature radius of magnetic field, while *curvature* one is caused by particles moving along the curved field lines.

1.4.3 Binary systems

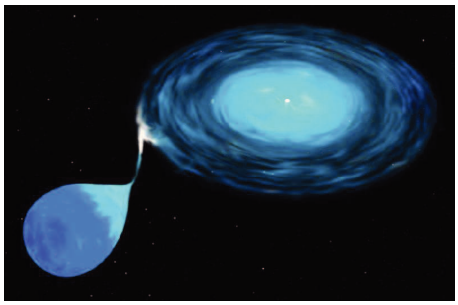

Figure 1.22: An artistic view of the accretion disk formation in a binary system.

The common definition of a *Binary* system indicates two stars that are orbiting around their common centre of mass. Often the distance between the two stars is such that there is no mutual effect and they essentially evolve separately. Sometimes it happens that the stars are close enough to influence each other gravitationally or even exchange mass, modifying their evolution. The more massive object, typically a white dwarf, a neutron star or a black hole of few solar masses, accumulates matter from its companion, forming an accretion disk (Fig. 1.22). In case both the system's components fill their *Roche* lobes[43], they give rise to an envelope that surrounds both stars. The accumulated gas in the accretion disk rotates in the external shell, heats up, and in a second stage can falls onto the compact star. Here the in-falling gas meets extreme conditions, which feed the generation of X–ray and γ–rays.

1.4.4 Giant molecular clouds

The molecular clouds represent a passive source of γ–rays. They don't produce any primary cosmic ray useful for an internal active gamma creation. They are simply a relatively dense barrier for the travelling high energy cosmic rays. The collision can be a localized sources of γ–rays. Generally the flux is not very high, but it may be enhanced if cosmic rays are trapped in cloud magnetic fields. At the present time, they are observed to study the cosmic-ray propagation. The technique is based on the measurement of the gamma flux from molecular clouds located at different distances along the path of an ultra high energy cosmic ray.

1.4.5 Active galactic nuclei

AGNs are galaxies with super massive ($\gtrsim 10^6\,M_\odot$) black holes in the centre. The observed radiation is characterized by different aspects, which may be unified in a single model that explains the different spectral categories of *AGNs*. At the centre of this system there is the engine, a massive black hole, surrounded by an accretion disk with fast moving clouds. Sometimes the falling matter to the central object stimulates powerful and narrow jets, perpendicular to the galactic plane (Fig. 1.23). The observer's view angle respect to the jet determinates the spectral energy distribution of the emitted radiation.
AGNs may be divided into two main classes, *radio-loud* and *radio-quiet*. In the first one, the emission contribution from jets is dominant and so it cannot be correlated to a stellar origin, namely from the stars that compose the galaxy. In the second case, the jets are simply missing or their emission is negligible. Several subclasses are related to the observational conditions.

[43] The *Roche* lobe is the spatial region around a star, within which orbiting material is gravitationally bound to that star.

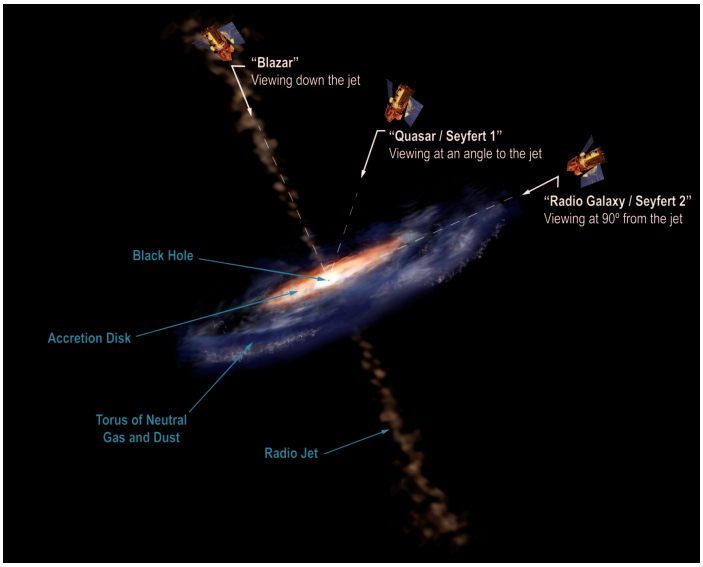

Figure 1.23: The *AGN* unified model. (Image credit: Aurore Simonnet, Sonoma State University)

- **Seyfert I & II**: the unified model proposes that in *Seyfert* the line of sight points directly to the active nucleus. They show narrow emission lines of hydrogen, helium, nitrogen, and oxygen from the accretion disk surface and a strong nuclear X–ray radiation. The optical continuum emission, originated closer to the black hole, is present only in the *Seyfert I*, because the *Seyfert II* are observed through an obscuring structure, which prevent the detection. The common host for these *AGNs* is a spiral galaxy.

- **Quasars**: it represents an intermediate position of the observer, where the central body, just outside the black hole horizon events, is directly seen. It is an extremely luminous object, more than the host galaxy. Its spectrum covers almost all the bands, mainly in the optical and X one. Some *Quasars* are also strong sources of radio and γ–rays. The host galaxies can be spirals, irregulars or ellipticals. The *Quasar*'s luminosity is proportional to the host galaxy mass, so that the most luminous *Quasars* inhabit in the elliptical galaxies.

- **Radio galaxies**: with the Radio galaxies the observer is moving towards the jet line. They typically manifest two lobes of radio emission, nearly aligned with the jets. These radio waves are very intense and due to the *synchrotron* processes. The ordinary radio galaxies host is elliptical, because it contain the most massive black holes.

- **Blazars**: when the line of sight points to the relativistic jet, the active galaxy is called *Blazar*. The special alignment with the jet explains some peculiar features, such as very high luminosity, very rapid variation and high polarization. Inside the jet, where a strong magnetic field is present, different particles interact producing a variety of observed non-thermal energy. The radiation spans from low radio frequencies to extremely energetic γ–rays. The involved processes are *synchrotron* radiation and *Inverse Compton*. The jets in *Blazars* are the favoured site of GeV$\div$TeV photons production.

Depending on the emission properties, *Blazars* are divided into two classes: *Flat Spectrum Radio Quasars* (*FSRQ*) and *BL Lac* objects (*BL Lacs*). The *FSQR* sources show strong and broad emission lines, while *BL Lac* objects show no optical emission lines. In both cases the host galaxies are giant ellipticals.

The relativistic jets, emerging from the central black hole, are likely the right place where the particles are accelerated. The mainstream interpretation of the acceleration mechanism in the jets is the *Synchrotron Self-Compton* ejection from ultra relativistic electrons. Only *radio-loud AGNs* can generate *VHE* γ–rays, detectable by the *IACT* telescopes. Moreover, when a clear correlations between TeV γ–rays and non-thermal X–rays exists, the leptonic population is considered to be the main channel of production.
The best-known TeV *AGNs* are *Markarian 421* and *501*, highly variable and often powerful gamma sources.

1.4.6 Gamma-ray bursts

GRBs (*Gamma-ray bursts*) are mysterious and powerful bursts of γ–rays, appearing to be distributed uniformly in the sky. They are the most luminous events in the Universe, normally linked to exceptionally energetic explosions of extragalactic origin. Even if the *GRB*'s light curves are extremely diverse and complex, the distribution of the observed duration shows a clear bimodal trend. In agreement with this peculiarity, they are divided in two groups: short bursts, lasting fractions of second, and long bursts (Fig. 1.24).
Long *GRBs* are affiliated to super massive stars ($> 40\,M_{\odot}$) core collapse and the sub-

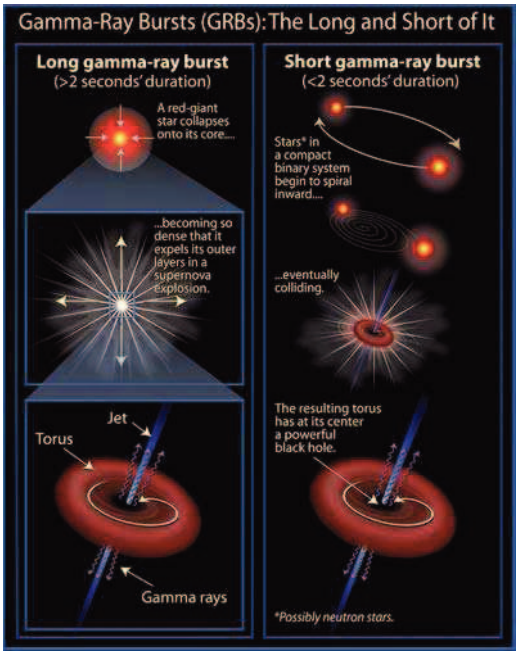

Figure 1.24: A sketch that simplifies the *GRB* formation in two main different scenarios. (From David Darling webpage)

sequent rapid formation of a black hole. Short *GRBs* have not a clear origin. They are likely associated to a fusion of two neutron stars into a black hole or directly a merging

of a black hole and a neutron star. The knowledge discrepancy between the two classes is fed by the presence of bright afterglows in the long *GRBs*, which have have been studied in greater detail than their short counterparts.
So far, *GRBs* have only been observed by satellites, while no evidence has been recorded in the *VHE* band. The main obstacle could be the *EBL* gamma absorption, not negligible due to their huge distance.

2

Atmospheric showers & IACT technique

PARTICLES originating in astrophysical processes are meaningful messengers of physics laws in the Universe. They cover long distances, sometimes travelling straight in line if they do not carry electric charge, or otherwise deflected by magnetic fields. Once arrived on the Earth, they may interact with atmospheric atoms, initiating extended air showers. Their evolution mainly depends on the nature of the primary particle and the atmosphere conditions. If the particle gets absorbed, the atmosphere can be considered a sort of natural calorimeter. The secondary products are the main targets of most of the ground-based *VHE* experiments, which can use different detection methods. The first part of this chapter is focused on the physics of the extended air showers. Then, the *IACT* technique and the analysis procedure, which takes advantage of that, are described.

2.1 The atmospheric showers

The extended atmospheric shower is the result of the interaction, in the high atmosphere, between the air atoms and a high energy cosmic particle, the so-called primary particle. The shower properties depend especially on the kind of the primary particle. It can be a proton, a nucleus, an electron, a photon, or rarely a positron.
The layouts of the experiments are adapted to the energy and the typology of the radiation under study. As mentioned in sub-section 1.2.2, there are vast arrays of detectors (e.g. the *Pierre Auger* observatory) intended to observe showers initiated by ultra and extreme high energy ($E \gtrsim 10^{15}$ eV) cosmic rays. Others, like the *MAGIC* telescope, that take advantage of the secondary products to get information on a very high energy (10^{10} eV $\lesssim E \lesssim 10^{14}$ eV) primary γ–ray.
The ground-based telescopes cannot detect directly the primary cosmic ray, but they can collect its secondary products. Hence, the comprehension of the *EASs* is essential to develop new strategies for the γ–rays selection and the background rejection in the new generation *IACT* telescopes. Thus, scientists can draw new conclusions on the origin and the unknown properties of the primitive cosmic rays.

2.1.1 EAS history

The *EAS* history is tightly related to the discovery of cosmic rays and its further consequent deepening. In 1934, *Bruno Rossi* noticed the observation of near-simultaneous discharges of two separated and distant Geiger counters, located in a horizontal plane,

during the preparation of a measurement of the so-called East-West effect. He hypothesized that the counters were struck by very extensive showers of particle, but unfortunately he had not time to study this phenomenon more closely [114]. However, this was one of the most meaningful findings in early cosmic-ray investigations.
In 1937, *Pierre Auger*, unaware of *Rossi*'s report, recorded independently that the cosmic radiation events were coincident in time, so associated to the same event. Further investigations, placing one of the counters in a different building more than 115 m away, revealed the correctness of the *Rossi*'s hypothesis: a new branch of atmospheric physics was opened. *Auger* pursued this work at high altitudes and succeeded in explaining the origin of the *EAS* and in quantifying the size distribution. He carried out a systematic identification of its constituent elements, as electrons, protons, and muons, that reached ground level spreading over a large area up to hundreds of squared meters [5]. Moreover, he declared to have observed showers up to 10^{15} eV, an energy domain still unknown at that time. This method allowed to register only particles that reached the ground level, but it did not explain the *EAS* development in the atmosphere.
Not much later, *Homi J. Bhabha* and *Walter Heitler* published a mathematical model, based on an expression for the probability of scattering positrons by electrons, which describes how primary cosmic rays interact with the upper atmosphere [12]. In their model, *EASs* are generated by the cascade production of γ–rays and $e^{\pm}$ pairs.

It must be pointed out that such measurements were made possible by the use of coincidence electronic circuits, which are able to warn the simultaneous (within a small time gate) passage of ionizing particles in far-between detectors. The inventor was *Rossi* in the 1930, who employed several triode vacuum tubes ([113]). The circuit was immediately adopted by many experimenters and the same concept is nowadays used in particle physics and in other areas of technology. It can be considered as the first primordial AND circuit, precursor of the logic ports in the modern computers.

2.1.2 Showers description

Primary cosmic rays typically approach the Earth's atmosphere at relativistic speed. They collide mainly with oxygen and nitrogen atoms, and generate fragments that tend to move in the same direction of the primary. In turn, the fragments decay or crash into more air molecules, creating a falling cascade that also spreads slightly sidewise. Therefore, the primary energy is shared out among millions and more secondary particles.

Two kind of showers can be distinguished. The first one, so-called *hadronic shower*, is initiated by a proton or a nucleus (Fig. 2.1(a)). The products of the first interaction are mainly pions ($\sim 90\%$), kaons and other nuclei, which constitute the hadronic core. The cascade is divided into three components, associated to the nature of the following secondary particles:

- **Electromagnetic**: this component derives mainly by the neutral pions decay.

$$\pi^0 \rightarrow \gamma + \gamma \tag{2.1}$$

  The produced photons are so energetic that can be converted in $e^{\pm}$ via pair-production. Further photons are then created by bremsstrahlung in a repetitive cycle, which generates new secondary particles with lower energy. Typically, one third of the primary energy is found in this component, because almost 30% of the secondary products are neutral pions.

- **Hadronic**: this component comprises the charged fragments of the first and subsequent collisions, which can hit other atmospheric atoms. Even the secondary charged pions can strike new nuclei, starting again the cycle. The hadronic interactions can continue as long as the available energy is higher than the pion critical energy ($\sim$ GeV).

- **Muonic**: this component is fed by the decay of the charged pions.

$$\pi^+ \rightarrow \mu^+ + \nu_\mu \tag{2.2a}$$
$$\pi^- \rightarrow \mu^- + \overline{\nu}_\mu \tag{2.2b}$$

The weak interacting neutrinos travel undisturbed, while some of the unstable muons can further decay, through the reactions:

$$\mu^+ \rightarrow e^+ + \nu_e + \overline{\nu}_\mu \tag{2.3a}$$
$$\mu^- \rightarrow e^- + \overline{\nu}_e + \nu_\mu \tag{2.3b}$$

At this point, the new born $e^\pm$ can start another electromagnetic component.
In addition, also charged kaons can directly contribute to the muonic component, according to the processes:

$$K^+ \rightarrow \mu^+ + \nu_\mu \tag{2.4a}$$
$$K^- \rightarrow \mu^- + \overline{\nu}_\mu \tag{2.4b}$$
$$K^+ \rightarrow \pi^+ + \pi^0 \tag{2.4c}$$
$$K^- \rightarrow \pi^- + \pi^0 \tag{2.4d}$$

The latter two relations (2.4c & 2.4d), which have a branching ratio of 63.4%, supply again the hadronic shower.

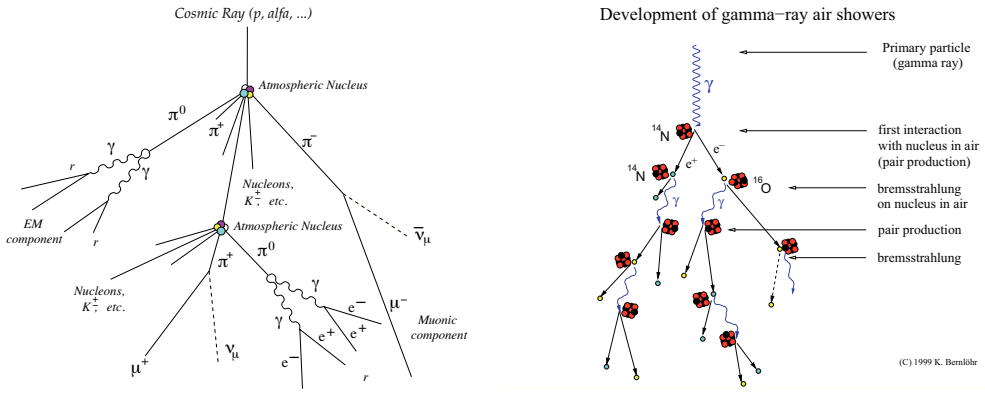

(a) Hadronic shower (b) Electromagnetic shower

Figure 2.1: *Left:* an hadronic shower generated by a cosmic ray. The three components, electromagnetic, hadronic and muonic, are illustrated. *Right:* an *EAS* initiated by a γ–ray. It is a continuous repetition of $e^\pm$ pair-production and bremsstrahlung. (Courtesy of Konrad Bernlöehr)

In the previous considerations, it has been exposed the general case of hadronic showers. It is possible to simplify substantially the scenario, assuming that cascades, originated

by heavy nuclei with mass number A, can be handle as the superimposition of A proton sub-cascades with energy E/A.

The second kind of showers, the so-called *electromagnetic shower*, is induced by a high energy photon[1] (Fig. 2.1(b)). A secondary $e^{\pm}$ pair is formed by electron pair-production. Subsequently, the electrons and positrons radiate new photons via bremsstrahlung, as in the electromagnetic component of the hadronic shower. The growth continues in a recursive way, until the shower particles reach the critical energy[2] ($E_c = \sim 83\,\mathrm{MeV/Q}$, where Q is the particle charge in electronic units) and cannot trigger so frequently the electron pair-production. Hereafter, the ionization of atmospheric atoms becomes the dominant process, the electrons rapidly cool off through the thermalisation and the shower quickly dies out. The whole process lasts about 10^{-4} seconds.
The electron's radiation length[3] (X_0) is approximately $36.7\,\mathrm{g/cm^2}$. After a distance of $\frac{9}{7}X_0$ from the first collision, approximately the mean free path, 63% of all incident cosmic γ–rays are converted in $e^{\pm}$. The maximum development of the cascade, namely the maximum number of electrons, is closely proportional to the primary energy. The higher the original photon energy, the larger the number of permitted electron pair-production processes. Also the position of the maximum[4] is logarithmically correlated to its energy. For primary γ–rays of 20 GeV to 20 TeV, it spreads in the range of 250 to $450\,\mathrm{g/cm^2}$, corresponding to a height of about 7 to 12 km above the sea level.

In 1954, *Heitler* proposed a relatively simple model to describe in first approximation the development of an electromagnetic shower [69]. Assuming that the primary energy

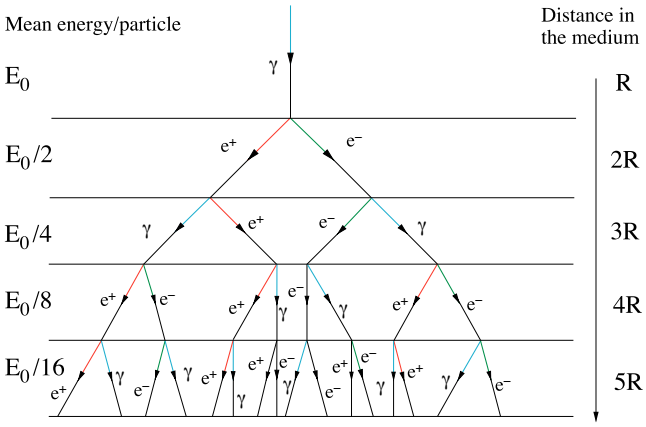

Figure 2.2: The *Heitler* model for an electromagnetic shower. Every segment corresponds to the mean free path of secondary particles.

is equally split into the secondary products, every collision halves it. The mean free path (λ) between two interactions is indicated with a segment in figure 2.2. At an atmospheric depth X, every path counts n ($n = X/\lambda$) branches, forming a shower of 2^n particles with a single energy of $E_0 \cdot 2^{-n}$. The maximum atmospheric depth (X_{max}) is achieved when the particles energy approaches E_c.

$$E(X_{max}) = E_0 \cdot 2^{-n_{max}} = E_0 \cdot 2^{-\frac{X_{max}}{\lambda}} \cong E_c \tag{2.5}$$

[1] The electromagnetic showers can be also originated by $e^{\pm}$.
[2] The photon E_c is $\approx 5\,\mathrm{MeV}$, when the Compton radiation dominates over pair creation.
[3] It can be defined as the material thickness, which reduces the mean energy of a radiation by a factor e.
[4] It is measured in terms of atmospheric depth, that is how much atmosphere the shower can pass through.

From the previous equation the maximum shower depth can be obtained:

$$X_{max} \cong \lambda \log_2 \frac{E_0}{E_c} \tag{2.6}$$

Changing the logarithm base

$$X_{max} \cong \lambda \frac{\ln \frac{E_0}{E_c}}{ln2} \tag{2.7}$$

An improved *Heitler* model, proposed by *Rossi* and *Greisen*, predicts precisely the longitudinal development of an electromagnetic shower, hence the total number of $e^{\pm}$ as a function of the atmospheric depth [115]. Some curves are illustrated in figure 2.3, where the parameter "s" specifies the first interaction point (s = 0), the shower maximum (s = 1) and the its extinction (s = 2).

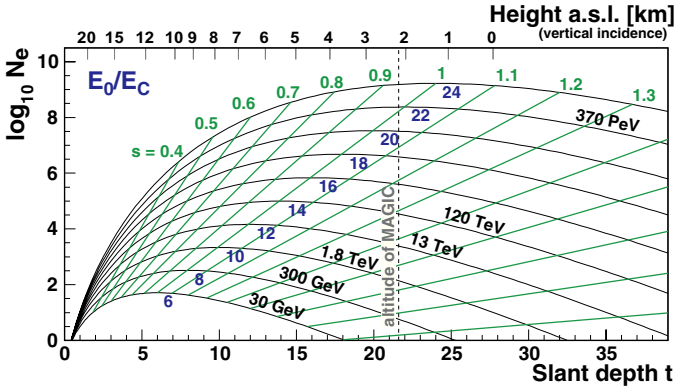

Figure 2.3: The longitudinal development of an electromagnetic shower in the atmosphere. The dotted vertical line indicates the altitude of the *MAGIC* site. (From [131])

The most distinctive characteristic between hadronic and electromagnetic showers is their lateral extension (Fig. 2.4). This property is due to the considerable transverse

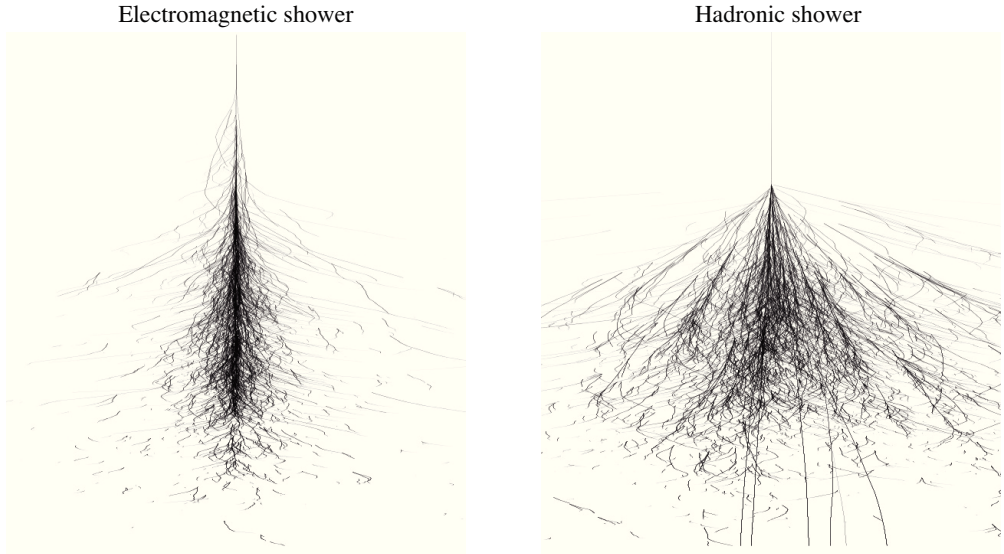

Figure 2.4: The different spatial distribution of gamma and hadronic showers. The first is slim and loosely concentrated along the direction of the primary. The second one is irregular and spread out containing several electromagnetic sub-showers with divergent directions. (Adapted from [130])

momentum in hadronic interactions. The difference is evident above 100 GeV, where it represents one of the most powerful discriminator factors in the distinction between gammas and hadrons.

2.1.3 The Čerenkov light

Charged particles in electromagnetic cascades emit Čerenkov[5] photons, if their energy exceeds the threshold value. The energy must be greater than $m_0c^2/\sqrt{1-n^2}$, where m_0 is the particle mass and n is the refractive index. For an electron, which is the main Čerenkov emitter due to its low energy threshold, the minimum energy corresponds to ~ 21 MeV in air at sea level[6]. When the charged particles pass close to the air atoms, they can temporally polarize it in distinct modes tied to their speed, as illustrated in figure 2.5. The following reorientation of the electric dipoles induces light emission.
As for the shock sound wave in the domain beyond Mach's number, the light wave front

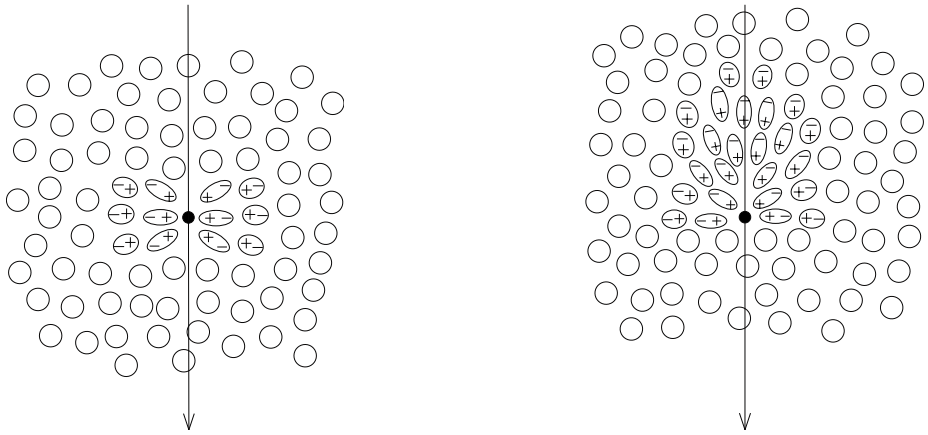

(a) Slow particle (b) Fast particle

Figure 2.5: *Left:* the air polarization induced by a slow moving charged particle. *Right:* the same effect due to a high speed particle.

propagates on a cone with the opening angle θ. The angle is a function of the particle speed and the local atmospheric refraction index:

$$\cos\theta = \frac{1}{\beta n} \tag{2.8}$$

where $\beta = v_{particle}/c$. Only particles that move with a velocity faster than the speed of light in the medium can radiate ($v_{particle} > c/n$). In figure 2.6, a graphical explanation of the angle θ is given. The light emission is described by the superposition of spherical waves using *Huygens*'s principle. Only when the particle is faster than the electromagnetic wave induced by the polarization, a constant phase wave comes out.
In the atmosphere, the refraction index is not constant, but it changes due to the air density variation, decreasing with altitude (h). Applying the isothermal atmosphere approximation model, both pressure and density decrease exponentially with increasing

[5]The name is due to the Russian discoverer P. A. Čerenkov, who recorded the radiation for the first time in the 1934.

[6]At the altitude of 10 km, close to the shower maximum development, this limit is double because n diminishes.

the altitude [135]. Consequently, the refractive index becomes:

$$n(h) = 1 + n_0 e^{-\frac{h}{h_0}} \tag{2.9}$$

where the fluctuations due to the air temperature and the wavelength of the radiation are neglected. According to equation 2.8, β changes along the shower's path, but continuously produces θ values inside an upper limit, which is a little more than 1° in the lower atmosphere. The emitted electromagnetic waves generate a front that can be schematized in a disc, with a thickness of only few meters. This also explains the arrival time distribution at the telescope level, which is contained in 10 ns[7].

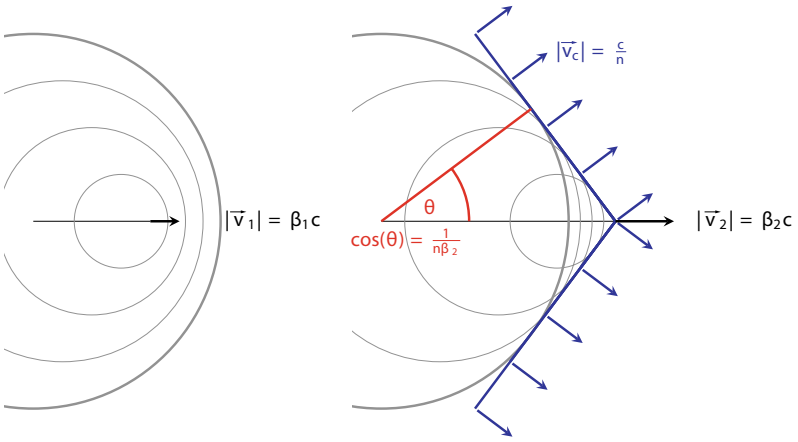

Figure 2.6: Simple sketch of the Čerenkov effect. When a charged particle moves slower than the speed of light in the medium, the electromagnetic waves, initiated along its trajectory, are not superimposed (left side). Differently, when its velocity exceeds the local speed of light, a surface of constructive interference appears. This effect causes the light to be emitted under an angle θ (right side). (Courtesy of C. Fruck)

Considering the largest shower expansion point at 10 km, the light spreads mainly in an area of around $50000 \div 100000\,\mathrm{m}^2$ at the ground level. As for the shower development, even the generated Čerenkov light is roughly proportional to the primary energy. However, the flash is very faint, counting only $\approx 4000 \div 5000$ photons per GeV, so a density of 10 particles in a square meter for a primary 100 GeV γ–ray.
Another parameter that influences the photons density is the the zenith angle of observation. For high values, the atmosphere thickness along the primary photon path increases substantially. This changes the relative distance between the maximum development of the shower and the ground, spreading the light in a greater area (Fig. 2.7).

The original light spectrum is altered by the mediums transparency (Fig. 2.8). In fact, photons are attenuated by scattering and absorption proportionally to the crossed atmosphere. For instance, photons can be deflected by small air atoms, in a process called *Rayleigh* scattering. The photon intensity reduction can be expressed by the following equation [18]:

$$\frac{dI}{dx} = -I \cdot \frac{32\pi^3}{3N\lambda^4}(n-1)^2 \tag{2.10}$$

where N is density of scattering particle and λ is the Čerenkov photon wavelength.

[7] 10 ns is a conservative value. The contribution after 6 ns could be considered negligible.

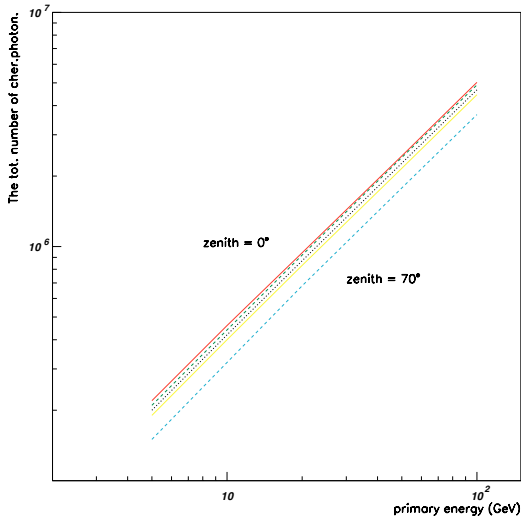

Figure 2.7: The total number of Čerenkov photons as a function of γ–rays' primary energy for several zenith angles (0°, 25°, 40°, 50° and 70°). The La Palma observation level, with its magnetic field, was chosen. The average total number of photons depends on zenith angle and increases with the primary energy. (Image credit: D. Sobczyńska)

The UV range is the most affected, because the cross section is tied to the mutual wavelength ($1/\lambda^4$). Another important scattering is called *Mie* scattering and it is due to the dispersion on aerosols and clouds. Typically its contribution is modest, but can become important during poor atmospheric conditions. On the other side, the absorption processes act below ∼300 nm with the ozone (O_3), the oxygen (O_2) and the nitrogen[8] (N_2). In the infrared region, the absorption is mainly due to the rotational and vibrational transitions of water (H_2O) and carbon dioxide (CO_2) molecules.
In air, the spectrum peaks around 330 nm, rather close to the ultraviolet and blue region. Consequently, one attempts to maximise the Čerenkov light sensitivity of detectors in the interval between 300 and 450 nm.

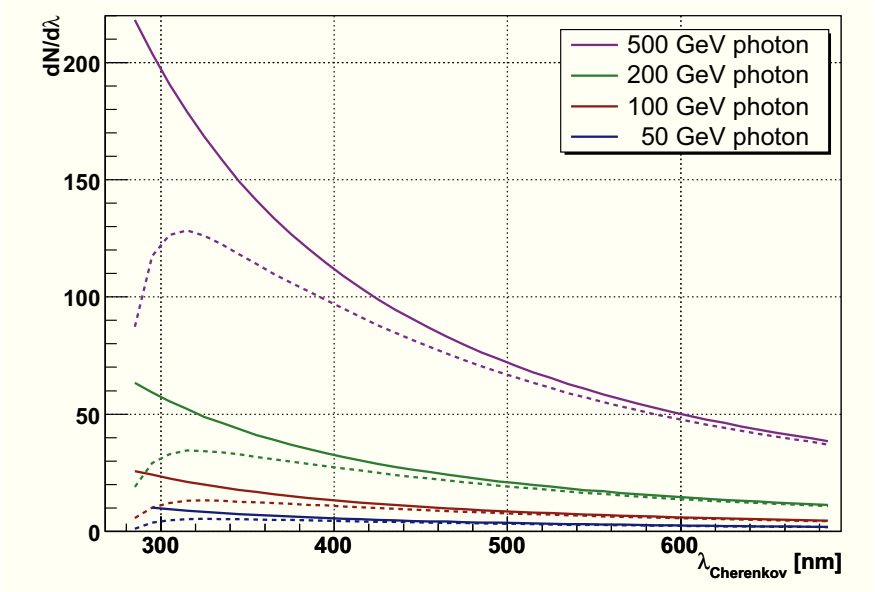

Figure 2.8: The differential spectrum of Čerenkov photons, calculated for different energies, before (continuous lines) and after (dotted lines) atmospheric absorption as a function of wavelength. (From [131])

[8]The oxygen and the nitrogen constitute the 99% of the atmosphere.

2.2 The IACT technique

The *IACT* telescopes are furnished with a large reflective surface, which focuses the Čerenkov light into a camera covered by photosensors. The photons, yielded at different heights, hit the mirrors with various angles, ending their travel in diverse *PMTs*. Hence, the light, converted in electrical signals, forms an image of the *EAS* in the camera plane. The conversion of a real three dimensional air shower into a projection on a flat surface is the base of the *IACT* technique (Fig. 2.9). Then the technique studies the reconstructed images of the *EASs*.
Photons emitted at the upper part of the shower have small Čerenkov angles, so they

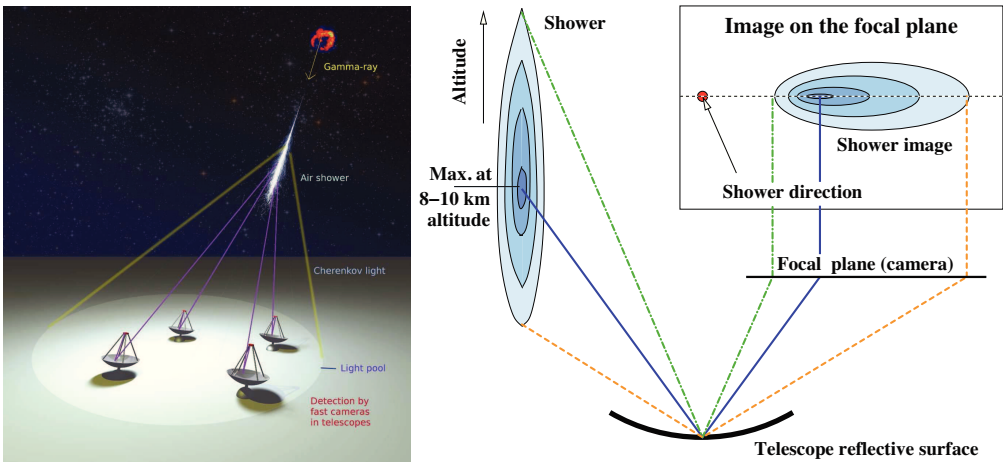

Figure 2.9: *Left:* an illustration of the Čerenkov light pool, initiated by a primary γ–ray coming from an astronomical source (e.g. a *Supernova remnant*), which illuminates an array of telescopes. *Right:* the subsequent creation of the shower imaging in one telescope (bluish ellipse). Along the shower longitudinal propagation, the light is emitted with different angles (coloured lines) and afterwards focussed in distinct photosensors. In the particular presented case of an electromagnetic shower, the shape is elliptical, but in general it could be irregular. The contour lines indicate the light intensity. (Adapted from [130])

are focused onto a region close to the camera centre. The others, generated at the end, have a large angles and are therefore mapped further away from the camera centre.

This method allows to study the main features of particles that do not reach the ground level, through the information that is carried by the Čerenkov light. The morphology of the images is used first to distinguish between electromagnetic, hadronic or muonic showers, then to characterize the event. Considering the particle cascades in the space-time[9] mathematical description, they appear with various geometries due to the internal processes involved. The main differences and how they affect the image parametrization are listed below.

- The hadronic showers have the broadest lateral distribution due to the high transverse momentum of the secondary interactions. This results in a wider ***width*** parameter, which is the half width of the minor axis of the shower projection. Moreover, they are also subject to considerable fluctuations in the shower development, generating a lot of irregularities.

[9]Space-time is usually interpreted with space as being three-dimensional and time playing the role of a fourth dimension.

- The hadronic showers are the most extended. In fact, the air radiation length of hadronic particles is higher than the photons one. The longitudinal evolution is calculated with the variable ***length***, which is the second moment of the charge distribution along the major axis of the shower image.

- Cosmic rays from the same source, deflected by the magnetic fields they have traversed, hit the atmosphere at different angles. The induced Čerenkov photons reach the telescope isotropically from everywhere, while gammas travel along the pointing direction. This property is transferred to the image orientation. The angle between the image major axis and the line passing through its core and the source nominal position on the camera is called ***alpha***. For events induced by γ–rays from the source the telescope points at, it is close to zero: i.e. the major axis of the camera image points to the camera centre, where photons coming parallel to the telescope axis are focused.

- The spread arrival time of the photons, in the camera plane, changes depending on the nature of the shower component: $1 \div 2$ ns for the muonic component, $2 \div 3$ ns for the electromagnetic one and $10 \div 20$ ns for the hadronic one. The root mean square of the arrival times, taken for all the pixels associated to the shower projection, is calculated (***time RMS***).

- Another important timing parameter is ***time gradient***, which estimates how much the arrival time varies along the major image axis. For an electromagnetic cascade the timing gradient is related to the longitudinal development, while it is not so evident for hadrons, which suffer larger shifts due to to the lateral expansion.

These parameters are used in the *gamma-hadron separation*[10] procedure. This technique is crucial to reduce the huge hadronic background (for weak sources roughly one good event every ten thousand) and to extract the characteristics of the primary γ–rays.
There are still other parameters that are utilized for the event reconstruction.

- A preliminary estimation of the primary particle energy is calculated with ***size***. It is the total number of photoelectrons counted in the shower image. For the same energy, the Čerenkov light emitted by hadron-induced showers is smaller compared to that produced in a gamma air showers. As explained in subsection 2.1.2, only a fraction of the original primary hadron energy is converted into the electromagnetic component.

- The image concentration is dug out of the variable ***conc(n)***[11]. It is defined as the ratio between the charge contained in the n brightest pixels and the total image size.

- The events that occur at very high impact parameters (distance between the shower axis and the point of detection) could be only partially recorded. The ***leakage*** is the portion of equivalent photoelectrons contained in the outermost ring of the camera per total image size. This parameter is important, because it estimates the fraction of signal lost because of too large impact parameter.

[10] It is the method utilized to distinguish gamma from hadronic events, analysing the shower images.
[11] n is the number of pixels that must be considered. For instance conc3 checks the 3 brightest channels.

- The shower maximum and its impact parameter is obtained by mean of the ***dist*** parameter. It is the distance between the image centre of gravity (the weighted average position of charge in the image) and the position of the source in the camera plane.

Most of these parameters, except the timing ones introduced recently by the *MAGIC* collaboration [37], are commonly used in the *IACT* experiments. They are called *Hillas parameters*, from the name of its inventor Anthony M. Hillas [72]. Some of them are illustrated in figure 2.10

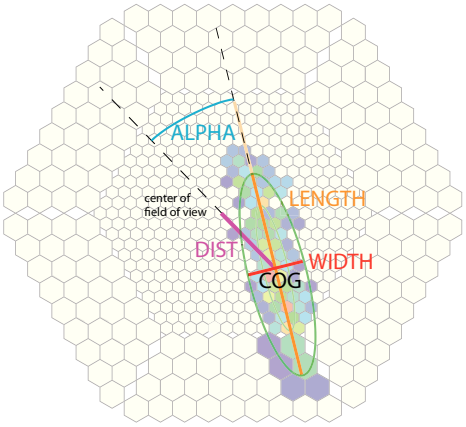

Figure 2.10: Representation of the *Hillas parameters* ***width***, ***length***, ***dist*** and ***alpha*** in a recorded event. (Adapted from [111])

The air shower image induced by an electron is similar to that of a photon. Only the orientation respect to the pointed source could change. This should be considered as an isotropic background, which is not possible to eliminate at very low energies.

2.3 The MAGIC analysis

The recorded shower projections are examined by the *MAGIC* analysis software tools. The main framework is called *MARS* (*MAGIC Analysis and Reconstruction Software*), an object oriented program written in C++ and developed in the ROOT environment [99]. It is composed of several sub executables, each realized for a specific commitment in the analysis chain (Fig. 2.11). The logical flow of data is seen in:

- ***Callisto***: the pulses generated by the *PMTs* are calibrated and converted in photoelectrons (2.3.1).
- ***Star***: in each telescope the shower image is first cleaned by the noise and afterwards parametrized by image parameters (2.3.2).
- ***SuperStar***: the information from both telescopes are merged and the stereo parameters are extrapolated (2.3.2).
- ***Melibea***: the γ/hadron separation is performed with the help of the random forest algorithm[12] outputs. The energy is estimated in the selected events (2.3.3).
- ***Odie***: the signal excesses are estimated and the significance is determined in a specific source position (2.3.4).
- ***Fluxlc***: the differential energy spectrum and the light curve are produced (2.3.4).

[12]It is a multi-dimensional classification system structured on decisional trees. It runs in a dedicated program.

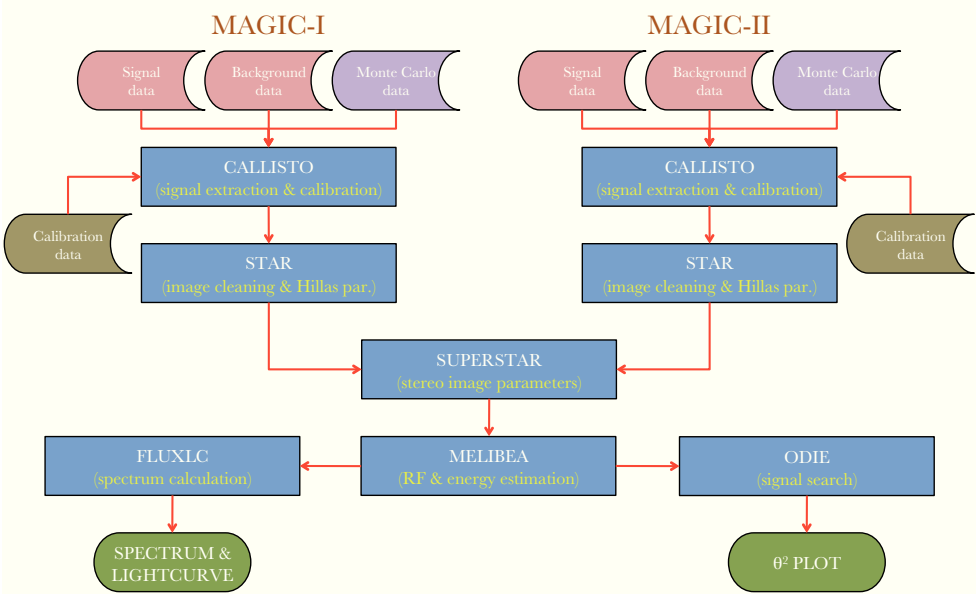

Figure 2.11: Flow diagram of the *MAGIC* standard analysis chain. (© F. Dazzi)

2.3.1 Signal extraction and calibration

The two telescopes use different readout electronics (4.6) and consequently distinct algorithms to extract the signal. The extraction procedure provides essential quantities, as charge, amplitude and signal arrival time, after the pedestal[13] subtraction. *MAGIC–I* applies a cubic spline extractor in a sampled range of 50 time slices[14], whereas *MAGIC–II* a sliding window algorithm in 80 slices.
The first one interpolates the pulse with a cubic spline curve [33]. The maximum of the obtained function represents the amplitude, while the charge is calculated performing the integral in a fixed window centred around the signal peak. The arrival time is defined at the rising edge at the voltage level of half maximum.
In the sliding window extractor, a routine searches the time range with a predefined dimension of 4 ns, where the signal integral is maximized. The peak inside the selected interval provides the amplitude, while its weighted average corresponds to the arrival time. The pedestal is estimated from the first 16 time slices of the readout window.

The Čerenkov light, collected by the *PMTs*, is converted into electrical signals that can be characterized by voltage measurements. A conversion factor is mandatory to connect the two quantities, photons and charge. Both telescopes are equipped with a calibration box in the middle of the reflector dish, which can emit known light pulses (4.7). Dedicated runs, so-called calibration runs, trigger only light flashes generated by the calibration system. These short flashes illuminate the whole camera with a constant intensity, so it is possible to study the behaviour of every single photosensor and calculate the proper conversion factor. Its value is constantly updated during data-taking through interleaved calibration events[15], activated at a frequency of 25 Hz. This allows to keep under control the fluctuations of the electronic chain.

[13] The pedestal is an estimation of electronic noise in the electronic chain.
[14] The time slice is related to the readout sampling speed. Here it corresponds to 0.5 ns.
[15] The interleaved calibration events have not not to be confused with calibration runs. During data runs, in which the telescope is triggered by cosmic events, some calibration pulses are included to update the calibration factors.

The first step is to move from incident photons to photoelectrons, by mean of the *PMT* quantum efficiency. Then, the method called ***F-Factor*** is applied to correlate the charge. It is based on the fact that the photoelectrons flux excess noise, introduced by the *PMT*, is proportional to the generated photoelectrons [98]. In general it can be expressed as:

$$F = \frac{(Signal/Noise)\ |_{input}}{(Signal/Noise)\ |_{output}} \tag{2.11}$$

namely a quantification of the additional noise introduced by the device under test. Assuming that the original photoelectrons distribution is Poissonian with mean N, the measured output charge, in *FADC* counts multiplied time (proportional to the voltage multiplied time) returns a mean $\langle Q \rangle$ with a spread σ. The equation 2.11 becomes

$$F = \sqrt{N}\frac{\sigma}{\langle Q \rangle} \tag{2.12}$$

where F is an intrinsic feature of each *PMT* measurable in the laboratory before the final installation. On the other side, $\langle$Q$\rangle$ and σ are computed from the calibration runs, hence the conversion factor is

$$C = \frac{N}{\langle Q \rangle} = F^2\frac{\langle Q \rangle}{\sigma^2} \tag{2.13}$$

where the relation 2.12 is used. Once the parameters to equalize the electronics are available, the recorded event can be nicely extracted and calibrated.

2.3.2 Image cleaning

The cleaning stage reconstructs the shower projection, rejecting all the pixels that do not contain information about the shower itself. All the pixels, whose charge is related to fluctuations, *NSB* (*Night Sky Background*) or stars, are excluded.
It is fundamental to optimize this procedure as much as possible to intercept the all spurious events that can be confused with good data. This field is improving constantly, mainly at the very low energies, where the shower projection shape is not well defined, because it involves few pixels as well as the *NSB* or star images. There are several cleaning tools, but the most utilized are currently two: the ***standard image cleaning*** and the ***sum image cleaning***.

In the *standard image cleaning*, an image generated by an *EAS* is assumed to be composed of a central part, in which a considerable fraction of the charge is concentrated, and an adjacent ring with typically less photoelectrons. Two charge thresholds are required to sort out the image core and the boundary pixels. The core must be formed by at least two neighbour pixels above the first threshold (Th_{core}). Boundary pixels have first to be in contact with a core pixel, then to exceed the second threshold ($Th_{boundary}$), which is smaller than Th_{core}.
The arrival time information allows to relax the charge thresholds and to reconstruct dim Čerenkov flashes, without loosing in sensitivity (Fig. 2.12). Two new constraints are implemented: a) the arrival time spread of core pixels must stay inside a restricted window, called ***TimeOffset***; b) the time difference between a boundary pixel and its neighbour one must be smaller than a fixed variable, called ***TimeDifference*** [37].

Besides the *standard image cleaning*, there is the innovative *sum image cleaning*, which improves the sensitivity by 15% below 150 GeV. It relies on the same concept of core and boundary pixel, but further constraints are added, forcing to a stringent

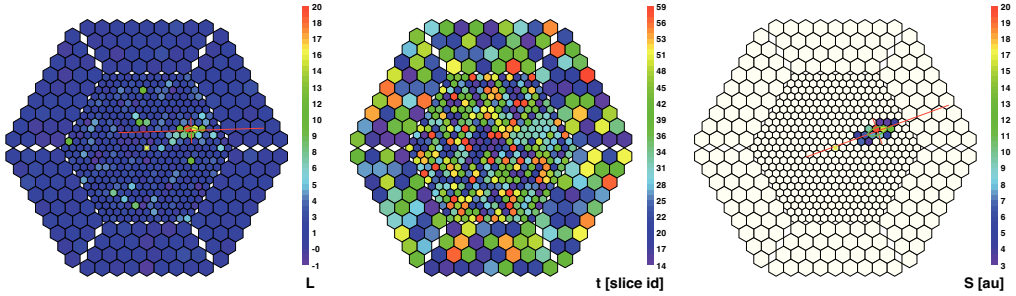

(a) Raw event (b) Event arrival time (c) Event after timing cleaning

Figure 2.12: *Left:* the event before the cleaning. *Centre:* the event arrival time expressed in time slices. *Right:* the same event after the standard timing cleaning. The ellipse and the associated lines represent some image parameters.

timing and new topological rules. Core pixels must be arranged in a close compact configuration of x units (xNN, where x is $2 \div 4$). The charge of each core pixel is clamped at a certain level (Th_{clip}) to get rid of the effect of the *PMT* afterpulses[16], and then the total charge of the xNN group is calculated. The second selection step is fulfilled if the sum exceeds another threshold (Th_{sum}). The new constraints are expressed as a functions of Th_{core},

$$Th_{sum} = S_{sum} \cdot x \cdot Th_{core} \tag{2.14}$$

$$Th_{clip} = C_{clip} \cdot \frac{Th_{sum}}{x} \tag{2.15}$$

where S_{sum} and C_{clip} are new parameters telescope independent.
Also in this case the timing constraints are considered and well tuned for each multiplicity. They are even a factor 5 more stringent than the limits imposed in the standard cleaning.

In table 2.1 the used values in both methods are listed. The choice of the parameters is driven by the compromise between the efficiency detection of low energy events and the introduction of noise, which can degrades the image parametrization and the subsequent reconstruction.

The graphical event representation is then parametrized with the *Hillas parameters*, explained in the previous section (2.2). Up to this stage the analysis chain runs independently for each telescope. When pairs of events recorded by the two telescopes are matched, the three dimensional stereo parameters are computed. In this way, the same shower is traced by two projections obtained from different points of view.
One of the most important is ***MaxHeight***, namely the height of the shower maximum, which depends on the primary energy. *MaxHeight* is indeed very helpful in the following γ/hadron discrimination at low energies.

2.3.3 Event classification

From this moment on, a *Random Forest* (*RF*) algorithm is executed in a dedicated program, called *Coach*. By analysing the position of the event in multi-dimensional space, the *RF* estimates the hadronness variable, which represents how much the primary particle is hadron-like [34]. The algorithm learns how to classify events depending on

[16] Afterpulses are spurious signals that appear after the main pulse of a *PMT*.

STANDARD IMAGE CLEANING				
Telescope (name)	**Th_{core}** (phe)	**$Th_{boundary}$** (phe)	**TimeOffset** (ns)	**TimeDifference** (ns)
MAGIC–I	6	3	4.5	1.5
MAGIC–II	9	4.5	4.5	1.5

SUM IMAGE CLEANING							
Tel. (name)	**xNN** (Nr.)	**Th_{core}** (phe)	**$Th_{boundary}$** (phe)	**C_{clip}**	**S_{sum}**	**TimeOff.** (ns)	**TimeDiff.** (ns)
	2NN	4	3	2.20	1.8	0.9	1.5
M-I	3NN	4	3	1.05	1.3	1.2	1.5
	4NN	4	3	1.05	0.7	1.9	1.5
	2NN	7	4	2.20	1.8	0.9	1.5
M-II	3NN	7	4	1.05	1.3	1.2	1.5
	4NN	7	4	1.05	0.7	1.9	1.5

Table 2.1: The parameters for the *standard* and the *sum image cleaning*.

their nature, by training on Monte Carlo and real data samples. The hadronness spans between 0 and 1, representing a γ-like or a hadron-like event respectively (Fig. 2.13(a)). *Melibea* applies the resulting *RF* matrices to the recorded data with the aim to reject the hadronic component of the background. A typical hadronness cut, used to reject most of the hadrons (mainly protons), is 0.1 (Fig. 2.13(b)). This cut is optimized by

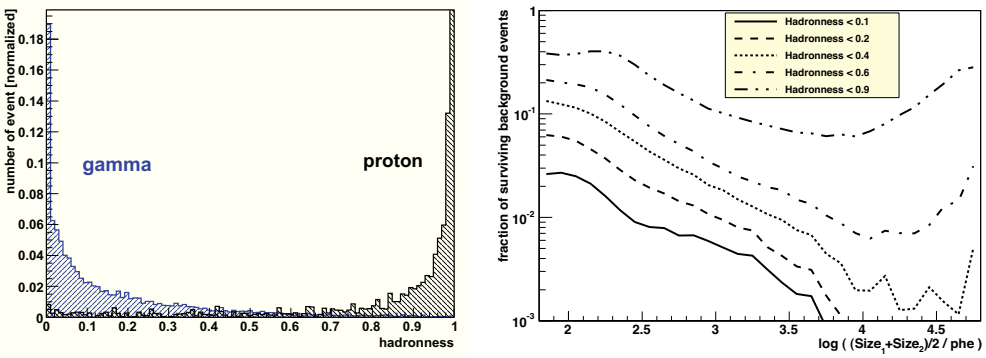

(a) *Hadronness* example (b) *Hadronness* rejection efficiency

Figure 2.13: *Left:* the classical output plot from the random forest algorithm. Gamma-ray events (blue area) are peaked around zero, whereas the hadronic ones (black area) increase the rate approaching the unit. In this distribution the reconstructed energy is above 100 GeV. (From [26])
Right: the fraction of surviving background events with different cuts in the *hadronness* parameter performed in the stereo analysis of *Crab Nebula*. (Adapted from [40])

using the quality factor, which is expressed by the relation

$$Q_{factor} = \frac{N_\gamma}{\sqrt{N_p}} \tag{2.16}$$

where N_γ and N_p are respectively the fraction of gammas and protons passing the selection cut.

Once γ-like events are selected, their energy is currently[17] estimated by using look-up tables based on Monte Carlo simulations. The creation of the look-up tables assumes that, at a given zenith angle, the light distribution at the ground is correlated with the parameters *size*, *impact parameter* and *MaxHeight*. The look-up tables are prepared independently for each telescope, then the final energy value is found as their weighted average.
It must be underlined that the estimated energy (E_{est}) is not equal to the real energy (E_{true}). Their discrepancy is determined by the relation 2.17.

$$D(E_{est}) = \frac{E_{est} - E_{true}}{E_{true}} \tag{2.17}$$

The $D(E_{est})$ distribution can be fitted with a Gaussian function, whose σ represents the energy resolution. The position of the peak is the energy bias, which should be as close as possible to zero.

The source position in the camera plane can be calculated in two ways: a) as crossing point of the main axes of the two single telescope images; b) in terms of a new parameter called ***Disp***, defined as the angular distance between the image centre of gravity and the reconstructed source position along the major axis. *Disp* is calculated by means of a parametrization of the shower elongation ($width/length$). Currently this method is enhanced by taking advantage of the *RF* algorithm in the computation of the space parameters. In the analysis of mono data, this updated method is called ***Disp RF***.
For stereo observations, if the *Disp RF* values, estimated in each telescope separately, agree inside a certain threshold, then the event is accepted and the final direction will be the weighted average of all of them, otherwise it is rejected. This procedure is called ***stereo Disp RF***.

The *Disp RF* method allows to introduce a new important image parameter, so called θ^2. It is defined as the square of the angular distance between the reconstructed and the catalogue position of the source on the camera plane. For γ-like events, its distribution is concentrated at small values, whereas it is flat for hadron-like images.

2.3.4 Source detection and characterization

This is the final step of a basic analysis. After the calibration, the cleaning and the classification of the recorded data sample, the γ–ray events are accumulated to achieve sufficient statistics to characterize the observed source. There are several tools to compute the celestial object properties. The principal ones are *Odie*, which calculates the parameter θ^2, and *Fluxlc* for the energy and intensity spectrum.

The estimation of the γ–ray signal from the reconstructed source position is done through the distribution of *alpha* and θ^2 parameters, which should peak at very small values (Fig. 2.14(a)). Hence, they indicate the place where there is the γ–ray emission, defining the signal region. The *alpha* analysis is typically applied for mono data of point-like sources with known positions, whereas in the case of stereo data the θ^2 computation shows better performance. Most of its power, comes from the utilization of parameters, which do not depend on an a priori known source position.

The θ^2 distribution is shaped by the overlap of γ–rays, peaked around zero, and the flat spectrum of the surviving hadrons[18]. In the signal region the number of events (N_{ON}) that have passed the cut selections are counted. There are still some hadron-like

[17] This method has been introduced with the stereo analysis. Before the energy was measured using the random forest algorithm, trained with events of known energy.
[18] The electrons contribution is not treated in this simplified description.

events that have survived the previous discriminating stages, and must be accounted. The same analysis, applied to the off data sample[19], allows to get a good approximation of the background events (N_{OFF}) in the signal region. The estimated number of γ–rays excesses is:

$$N_\gamma = N_{ON} - \alpha N_{OFF} \tag{2.18}$$

where α is a time normalization factor. In order to exclude that the signal excess is due to background fluctuations, the significance (S) is compute by using the Li & Ma formula [93]:

$$S = \sqrt{2}\left\{ N_{ON} \cdot \ln\left[\frac{1+\alpha}{\alpha}\left(\frac{N_{ON}}{N_{ON}-N_{OFF}}\right)\right] + N_{OFF} \cdot \ln\left[(1+\alpha)\left(\frac{N_{OFF}}{N_{ON}-N_{OFF}}\right)\right]\right\}^{\frac{1}{2}} \tag{2.19}$$

It is commonly assumed that a detection to be publishable should have at least a significance of 5σ.
An important index of the telescope performance is expressed by the sensitivity, defined as the minimum γ–rays flux, which returns 5σ significance in 50 h of observation. Using a Gaussian approximation of the equation 2.20, it can be expressed as:

$$Sensitivity(t) = \sqrt{\frac{t}{50}}\frac{N_\gamma}{\sqrt{N_{OFF}}} \tag{2.20}$$

where t is the time of observation.

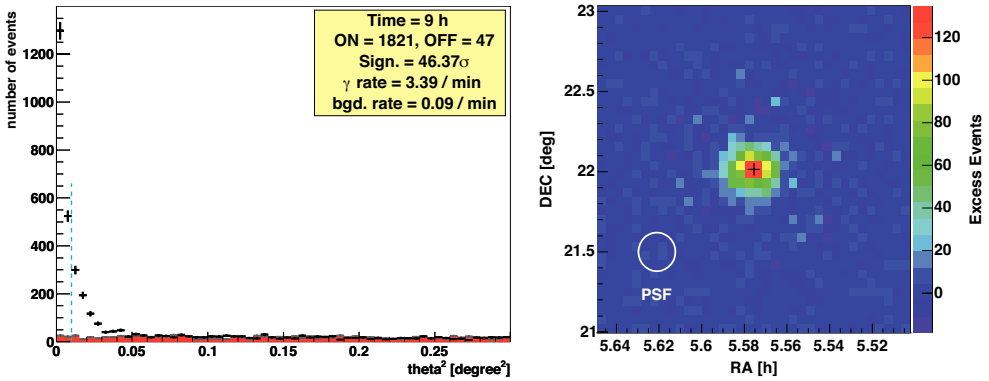

(a) θ^2 plot (b) Sky map example

Figure 2.14: *Left:* an example of θ^2 plot obtained from *Crab Nebula* observed in stereo mode. The signal is marked with black points, while the background area is coloured in red. The θ^2 cut is shown with the dashed blue vertical lines. (Adapted from [40])
Right: an example of sky map of the *Crab Nebula*. The position of the *Pulsar Wind Nebula* is marked by the black plus sign and the angular resolution is indicated by the circle. (Adapted from [32])

Once a gamma signal is detected, the source morphology can be studied by producing sky maps, which show the arrival directions in sky coordinates (RA & DEC) (Fig. 2.14(b)). To take into account the pointing uncertainty, the sky map is smoothed with a Gaussian function with σ equal to the angular resolution.

[19] It is a data sample recorded tracking a dark region of the sky close to the source.

The differential energy spectrum is calculated in *Fluxlc* with the following formula

$$E_{\gamma}^{diff} = \frac{dN_{\gamma}}{dE_{est} \cdot A_{eff} \cdot dT_{eff}} \tag{2.21}$$

where A_{eff} is the effective collection area and T_{eff} is the effective observation time. The effective area represents the geometrical region, corrected by the detection efficiency, in which a γ–ray triggers the telescope. The effective observation time is the temporal interval, during which the telescope is recording data, excluding the dead time of the detector.

Finally, the true energy is derived by the estimated one through an unfolding procedure. Assuming to know the telescope response function, it is possible to extract the true energy from the measured one by mean of a conversion matrix.
In addition, *Fluxlc* allows to produce light curves, namely the integral γ–ray flux as a function of time for energies larger than a certain value.

2.3.5 Data-taking modes

The *MAGIC* experiment is composed of two telescopes that can operate independently (***mono data-taking***) or synchronously (***stereo data-taking***). The first mode is typically used either when a telescope is under maintenance, while the other can take normal data, or when the performance of both detectors must be compared. The tracking of two distinct sources at the same time is never enforced, because the main target of *MAGIC* is the study of astronomical processes at very low energies, where the stereoscopic data-taking shows higher performance. In fact, the primary particle direction, the energy and in general the event reconstruction are more precise, because the same shower is registered from different point of views. Also the efficiency of the background rejection is much better. This theory is presented in detail in chapter 6.

In *MAGIC* there are two observation modes, which determinate the estimation procedure of the surviving background. To be sure that the observed region of the sky emits a signal, the number of recorded events is compared with the one extracted tracking a dark zone, where no signal is expected. The data set is accumulated in different moments, first pointing to the source and subsequently to a nearby darkpatch[20], trying to match the same outline conditions. This mode is called ***ON/OFF mode***.
Currently, the standard observations are performed in the so-called ***wobble mode***. The pointing source position is set 0.4° away from the camera centre. This allows to get simultaneously the signal and the background estimations. As show in figure 2.15, the background is estimated at symmetrical offsets from the telescope pointing direction. In order to avoid systematic bias due to detector inhomogeneities, every 20 minutes the wobble position is swapped.

The *MAGIC* telescopes can operate only during dark nights, when the faint Čerenkov flashes are not dominated by other sources of photons in the optical wavelengths. In addition, the photosensors are so sensible, that the full moon is enough to saturate them. Nevertheless, the electronics amplification has been conceived to take data even with moderate moon light.
Another essential condition for data tacking is good weather. The camera electronic cannot be exposed to high humidity and the telescope structure cannot be moved under strong wind. Finally, the presence of clouds or calima[21] in the sky increases the *Mie*

[20] A darkpatch is a region of the sky where there are not bright sources.
[21] The sand from the *Sahara* desert.

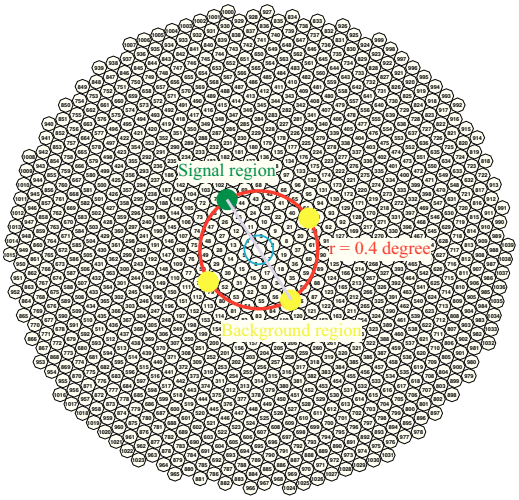

Figure 2.15: Representation of *wobble mode* observation in *MAGIC–II*. The source is placed at the green circle, whereas the yellow ones indicate the background regions. The gray line connects the source and the anti-source, which are swapped every 20 minutes. Differently, the blue circle shows the source position when the *ON/OFF mode* is activated. (© F. Dazzi)

scattering and affects the light collection.

3
Low size events morphology

In the energy domain between a few GeV and 50 GeV, gamma astrophysics is still full of uncertainties, so it needs the development of new strategies. A high sensitivity and a low energy threshold are key parameters to operate in a spectral region where the overlapping with satellite experiments is essential. *MAGIC* has been designed with this clear objective in mind and nowadays further investigations are still ongoing.
Technological innovations in the field of light collection and light conversion can favour the performance of the telescope, but it is also important to study the main features of the Čerenkov radiation generated by low energy particles and its interaction with the detector. The event's morphology and its charge distribution at the camera level should be understood to optimize the selection algorithms and the shower reconstruction. In this chapter, a general and basic introduction to this problem area is presented.

3.1 Physics motivations

There are strong scientific motivations to cover the gap between the space-based and ground-based observations, extending the *IACT* technique down to 10 GeV.

Gamma-rays, emitted by extragalactic sources, can interact with diffuse low energy photons of the *EBL* (*Extragalactic Background Light*), which is an evolving isotropic radiation due to stars and dust that fills the entire intergalactic space. Electron pairs are produced in the interaction, so the original gammas disappear. The interaction probability increases with distance and energy, so the observed spectrum of distant sources at high energies is depleted respect the original one [57]. Assuming to know the *EBL* spectral density, the attenuation factor represents a direct estimation of the source distance. However, sources at very high redshift are only accessible at low energies, where the flux suppression in not dominating. This effect strongly limits the study of a large amount of *AGNs*, which lie at high redshift. At low energies, below 50 GeV, the Universe is expected to become more transparent and distant sources can be detected. This opens an important window to a further understanding of the so-called γ–ray horizon.
In addition, the analysis of many distant sources allows to reduce the substantial uncertainties of the current *EBL* models, providing a better understanding of the stars and galaxies formation and their evolution [83].

It is commonly assumed that about 23% of the energy density in the Universe consists of an unknown, non-luminous, and non-baryonic matter called dark matter (DM). According with particle physics theories beyond the *Standard Model*, as *Supersymmetry*[1] ($SUSY$) and multidimentional models, the best candidates for the DM are the *WIMPs* (*Weakly Interactive Massive Particle*) [10]. These particles are supposed to be massive (between some GeV to 1 TeV), electrically neutral, stable[2] and could annihilate or decay into γ–rays. Among them, a good candidate is the supersymmetric neutralino (χ), which is the lightest supersimmetric particle.
Since the expected annihilation flux of γ–rays is proportional to the DM density, the $IACT$ telescopes can search signatures of the DM particle existence observing regions of the sky with foreseen high DM density as the Galactic Centre, Dwarf spheroidal satellite galaxies of the *Milky Way*, and galaxy clusters.

Some models predict an energy dependence of the speed of photons due to quantum gravity fluctuations of vacuum [87]. Cosmological γ–rays emitted simultaneously, but of different energy, should arrive at the Earth's atmosphere in different moments.
In order to be sensitive to this infinitesimal effect in the GeV domain, two ingredients are absolutely mandatory: a considerable distance to cover and a strong energy variability. Obviously the main candidates are rapidly flaring distant $AGNs$ and $GRBs$ that appear typically at large redshift [22]. Unfortunately, only detectors with a low energy threshold have the chance to reveal them, because of the energy cut-off caused by the EBL absorption.

Another argument that engenders interest are the *Blazar* jets, very powerful non-thermal emissions of $AGNs$ that expand in the surrounding medium. The emitted electromagnetic radiation spreads over a huge interval of the energy spectrum, so it is a matter of study for many experiments with different detectors. How the energy of the jet is converted into radiation and which is the working of the central engine are still not fully understood. There are controversial models that predict a pure leptonic or hadronic γ–ray emission and even some innovative hybrid explanations. Disentangling the various flux contributions to the emission will help to understand the production and acceleration mechanisms [20].
By lowering the $IACT$ energy threshold, it is possible to extend the spectrum of the detectable γ–rays emitted by *Blazars* and to measure the emission evolution in a wider redshift range.

In the GeV$\div$TeV range, *Supernova Remnants* are likely the main sites for the cosmic ray acceleration [17]. It is quite evident that the electrons are accelerated to TeV energies, but the proton case is still not so obvious, as much as the answer to the origin of the cosmic rays in this domain is unresolved. More sensitive measurements would open the activity to search the two components of the γ–ray spectrum, one linked to the leptonic channel and the other to the hadronic one.

A special attention is dedicated to *Pulsar* physics in the GeV domain. The best qualified models propose different cut-off energies to describe the emission from the neutron star. These breakpoints are, again, in the energy range that is presently difficult to access.
A low energy threshold is crucial to have an overlap with satellite detectors, which allows to compare the measurements of the tail of the *Pulsar* spectra. Some important studies are just now in progress, as reported in more detail in subsection 5.1.3.

[1] It is an extension of the *Standard Model*, in which a special symmetry puts in correspondence fermions and bosons.
[2] Stable means even with a lifetime greater than the age of the Universe.

3.2 Low energy atmospheric air showers

The physics principles, that describe the extended air shower at very low energies (10÷50 GeV), still remain the same as for higher energies. The difference lies in the available amount of energy that gets converted crossing the atmosphere. The cascades die out relatively soon[3], reaching their maximum development around a depth of 180÷240 g/cm^2 (11÷12 km a.s.l.), thus very far away from telescopes as *MAGIC*, installed at ∼2000 m of altitude. Adding the fact that the energy threshold for the Čerenkov photons production is double in the upper layers of atmosphere (35÷40 MeV for electrons), the number of emitted photons is very small. Furthermore, the higher is the altitude, the lower is the refraction index and the smaller is the Čerenkov angle, so the generated photons are strongly collimated along the charged particles trajectory.
In the case of showers initiated by γ–rays, which have a modest transversal development, the main consequences are small shower projections (small size) and a limited number of triggered events at large impact parameters.

These three parameters, energy, size and impact parameter, have been studied to reveal their correlation in low energy γ–rays, simulating the *MAGIC–II* telescope with the following conditions: mono ON/OFF data, standard trigger 4NN[4] and size < 250 phe. Up to 200 GeV, the energy and the size are linearly proportional, while beyond this value some Čerenkov light components with large emission angles with respect to the pointing direction, are focused outside the camera and hence lost (Fig. 3.1(a)). The curve's trend starts to become flatter.
Figure 3.1(b) shows that the mean impact parameter as a function of energy lies at a

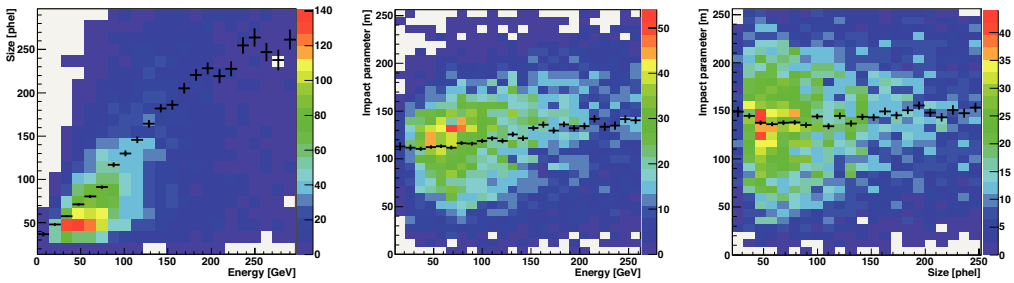

(a) Energy vs size (b) Energy vs impact parameter (c) Size vs impact parameter

Figure 3.1: *Left:* the correlation between the energy of simulated γ–rays and the size of the projections in the camera plane. The black crosses show the average points. *Centre:* dependency of the gamma energy with the impact parameter. *Right:* the size as a function of the impact parameter. (Images credit: E. Prandini)

constant value of 120 m up to 100 GeV. This corresponds to the Čerenkov pool border, a thin ring where the photons are concentrated, because a fraction of the light emitted at the beginning of the cascade with small angles meets the following emissions at larger angles. The whole blob spans between 50 m and 150 m and only at higher energies the contribution close to the shower axis (50 m < impact parameter < 100 m) disappears, giving way to some very distant events. This is due to the long longitudinal development of energetic showers.
The last illustration, size versus impact parameter, confirms again what has been explained previously (Fig. 3.1(c)). The blob is slightly more smeared, still in agreement

[3] Relatively to the development of a more energetic shower.
[4] For technical detail on these configurations read section 4.6.

with the size spread presented in figure 3.1(a).
The *CoG* (*Centre of Gravity*) plot, obtained with the same set of Monte Carlo data, shows an interesting structure (Fig. 3.2), which is a consequence of the plots 3.1. There is a hot ring around the camera centre, which points out that most of the events at low energies are concentrated in a thin doughnut shaped region. This suggests some interesting technical conclusions: a) it is fundamental the maintenance of this portion of both camera and trigger; b) the trigger design and its algorithm should be optimized at least for this region; c) in case the trigger area could not be large (limitations due to the cost, space, weight, etc...), it has to be restricted to this ring.

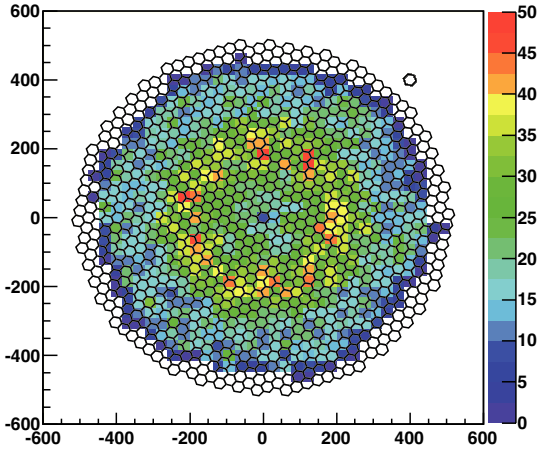

Figure 3.2: The *CoG* of events with size less than 250 phe. The simulated conditions are: ON/OFF mono data set using the *MAGIC–II* camera and standard trigger multiplicity 4NN. (Image credit: E. Prandini)

The thickness of the *CoG* ring indicates that in average the amount of angles involved in the light emission is limited, as expected by the fact that both the lateral and the longitudinal shower developments are relatively narrow. Even the spread of the Čerenkov light angle, due to the refractive index variation, extends in a tiny interval because most of the production occurs in a quite thin layer of the atmosphere. The recorded image size is small, containing typically less than 70÷80 phe distributed in few pixels. The projection's reconstruction becomes problematic and the event selection inefficient. The orientation and the concentration of the images are degraded and the parametrization described in sections 2.2 and 2.3 is no longer an effective tool. Finally, the energy and the angular resolution deteriorate, being dominated by statistical fluctuations, as it happens in a calorimeter[5].
In this energy domain it is crucial to consider the photon arrival time on neighbouring pixels and benefit from its small dispersion. The typical difference is less than 2 ns, so the reflective surface, the photosensors and the electronic chain of an *IACT* telescope should be designed to keep the isochronism well under this limit.

Another influential factor, in the regime of few GeV, is given by the background scenario. The cosmic hadrons, which are the main background source above 100 GeV, are less influential, because the momentum of the hadronic and muonic components approach the Čerenkov production threshold. Below 30 GeV the hadronic contribution is negligible and in turn the cosmic electrons continue to play an important role.
Unfortunately, there is a physical limit in the *IACT* technique. The electromagnetic showers initiated by primary electrons are similar to those due to γ–rays, independently of the energy. Even the electromagnetic component, generated by the neutral pion decay in the proton-nucleon interaction, presents the same characteristics. This kind of *EAS* cannot be distinguished by the current *IACT* telescopes and in principle it cannot be removed, contributing to limiting the flux sensitivity. However, for point-like sources and telescopes with a good angular resolution, a fraction of this background can be

[5]The combination of atmosphere and telescope forms a sort of calorimeter.

rejected reducing the timing gate of stereo trigger (see subsection 6.2.1). Nevertheless, simulation studies predict an electron trigger rate of few Hertz, for a telescope as *MAGIC* that can operate at 30 GeV, which is only one order higher than the gamma one [46].

Another intrinsic limitation is due to the action of the geomagnetic field on low energy showers. Sometimes charged particles get trapped in the atmosphere, because the *Lorentz* force deflects them in the East-West direction [47]. Therefore, the information provided at the telescope level is further reduced.

3.3 Event features at camera level

For a successful event detection and a subsequent image analysis, one needs to measure a minimum number of signal photoelectrons in at least some camera pixels. The number of photoelectrons produced in the *PMTs* photo-cathode, is proportional to the number of collected photons. Considering again the theory presented in subsection 2.1.2, it is possible to calculate approximately the number of photons involved, for instance, in a γ–ray of ~ 20 GeV. An electromagnetic shower generates 2^n particles with a single energy of $E_0 \cdot 2^{-n}$, until they reach the critical energy of ~ 83 MeV (Eq. 3.1).

$$\begin{aligned} E_0 \cdot 2^{-n} &= E_c \\ 20 \cdot 10^9\,\text{eV} &= 2^n \cdot 83 \cdot 10^6\,\text{eV} \\ n &= \log_2 241 = 7.91 \end{aligned} \tag{3.1}$$

The cascade consists of ~ 241 particles and it propagates to a depth equivalent to 7.91[6] interactions. One third of these particles are photons, whereas the rest are electrons and positrons. Only the latter, roughly 160 relativistic charged particles, can produce Čerenkov light.
Assuming to be in saturation[7], roughly 4000÷5000 Čerenkov photons are produced per GeV, so a γ–ray of 20 GeV emits roughly 100000 photons [78]. This light spreads at the telescope level in a huge area of $\sim 100000\,\text{m}^2$, namely one photon every square metre. For instance, a telescope like *MAGIC*, with a reflective area of $\sim 236\,\text{m}^2$ and a local reflectivity around 80%, can collect something like 190 photons. In case the light is not well focused or some mirrors are damaged, the counting could be even smaller. In average, for every charged particle generated in the electromagnetic shower, one photon is collected by the telescope.

Monte Carlo studies of low energy gamma showers confirm these important features concerning the photon distribution in the camera plane (*MAGIC–I*), after the reflector focusing. In figure 3.3, three exhaustive examples are illustrated.
Although the primary shower energy is very low, the photons (200÷250 units) span a wide region, over the border of the trigger area. However, most of them are isolated or their density in a single pixel is very low. Considering that the conversion factor of a *PMT* is around 30%, often no photoelectrons, or only one, are produced in that channels (violet and blue pixels). There are then few compact pixels (green, yellow and red) that present a sufficient amount of photons (> 10), which can be detected. These hot pixels are typically arranged in a compact area of 3, 4 or 5 units. There is always one core pixel which contains most of the light (20÷40 photons) and others which are

[6] This is also the number of stages in the *Heitler* model, namely the number of interaction along each path starting from the primary interaction.

[7] Above ~150 MeV the Čerenkov emission due to an electron is in saturation.

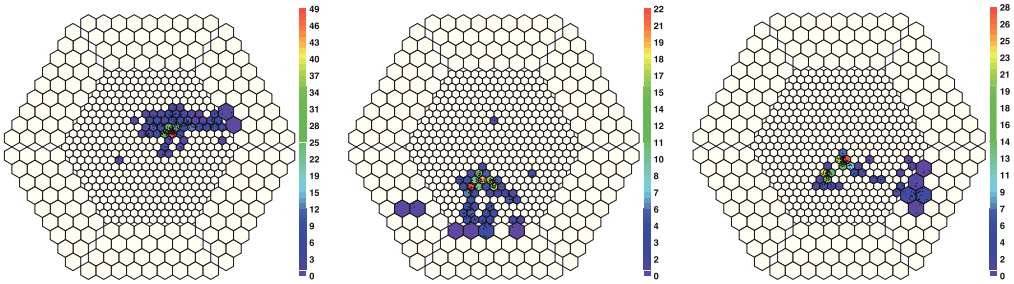

(a) Gamma event of 21 GeV (b) Gamma event of 22 GeV (c) Gamma event of 24 GeV

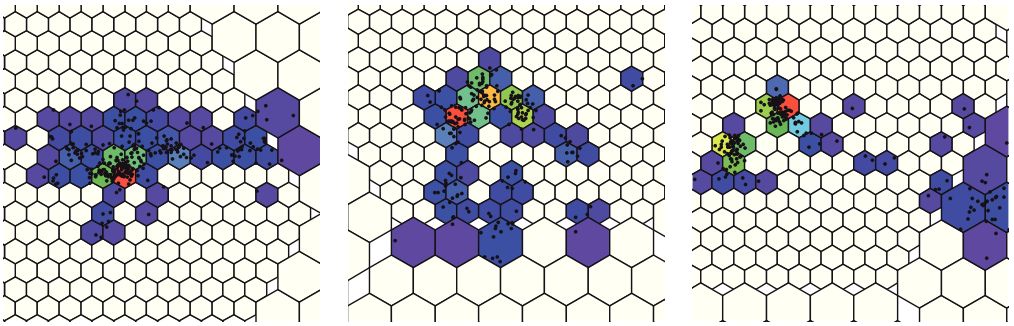

(d) Zoom of event at 21 GeV (e) Zoom of event at 22 GeV (f) Zoom of event at 24 GeV

Figure 3.3: The distribution of Čerenkov photons (black dots) of simulated γ–rays in the camera of the *MAGIC–I* telescope. The programs used for the simulation are *Corsika* and *Reflector*. The figure (d) is a zoom of figure (a), (e) is a zoom of (b) and (f) is a zoom of (c). Note that the Čerenkov photons cover a large area containing several pixels within the camera plane, but only few pixels count enough photons to trigger the detector. (Adapted from [111])

close to the detection limit of around 10÷15 photons, namely 3÷5 phe, typical threshold for the *MAGIC* experiment.
Often, as in the example at 24 GeV, additional concentrated packets of photons appear. It seems that the number of small hot bunches increases with energy, so that at a certain point, their density is so high that the images become uniform and well defined by a single block. To check this behaviour, γ–rays at different energies from $\sim 10 \div 60$ GeV have been recorded (Fig. 3.4). Actually, up to ~ 25 GeV it is common to see 2 or three bunches. For very low energies, around 10 GeV, the packets are well noticeable, because only one or two pixels are involved in each of them. Then, they become larger and so frequent that they start to overlap (25÷40 GeV) and finally they form a single huge blob ($E_0 \gtrsim 40$ GeV). The core pixels are always located in the apex of the image which is closest to the camera centre. This part of the projection, called head, represents the upper part of the shower, hence the first interactions. In this phase, the electrons are very energetic and practically undeflected by *bremsstrahlung* scattering. They are so collimated that the produced Čerenkov light is concentrated in only few pixels. Approaching the critical energy, the angular dispersion increases.
Considering the relativistic beaming effect, the angular dispersion is approximately inversely proportional to the *Lorentz factor*, hence it changes as a function of the interaction number (Eq. 3.2).

$$\alpha_{scattering}(n) \simeq \frac{1}{\gamma} = \frac{m_e c^2}{E(n)} \tag{3.2}$$

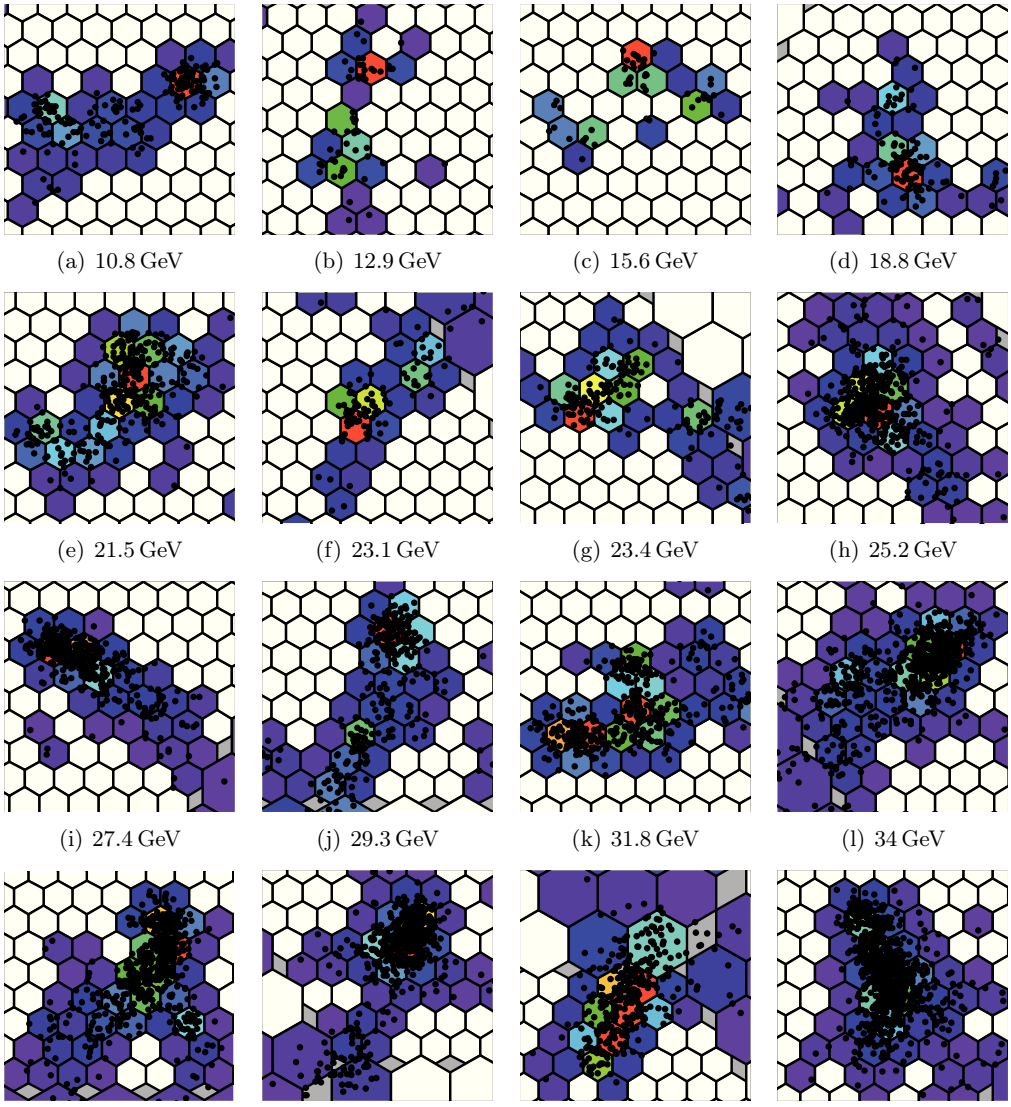

(a) 10.8 GeV (b) 12.9 GeV (c) 15.6 GeV (d) 18.8 GeV

(e) 21.5 GeV (f) 23.1 GeV (g) 23.4 GeV (h) 25.2 GeV

(i) 27.4 GeV (j) 29.3 GeV (k) 31.8 GeV (l) 34 GeV

(m) 36 GeV (n) 42.2 GeV (o) 48.3 GeV (p) 58.6 GeV

Figure 3.4: The distribution at the camera plane of Čerenkov photons due to γ–rays of different energies, from 10.8 GeV to 58.6 GeV. The main properties of the primary γ–rays and the number of recorded photons in the core pixels are reported in table 3.1.

Up to the critical energy, the electron deflections are reported in table 3.2 as a function of some energy values. Assuming that at every collision the electron energy is halved, it is possible to associate the deflection with the interaction number. The deflections undergone by the electrons are negligible up to the interaction n-4. Their Čerenkov projections are still contained inside a single pixel or at maximum shared between two pixels, if the edge effect is taken into account. In the last interactions, the angular dispersion becomes important and some electrons can be scattered more than 6 equivalent pixels away from the original trajectory. However, a consistent fraction continues to feed the central core around the earlier collimated electrons.
It must be added that even the Čerenkov angle variation contributes. Photons produced near the first interaction (~ 20 km) have an angle up to 0.3° smaller than the

Event (Name)	**Energy** (GeV)	**Impact parameter** (m)	**Total photons** (ph)	**Bunches** (Nr.)
a	10.8	124.8	171	2
b	12.9	125.1	57	2
c	15.6	130.9	95	3
d	18.8	135.8	116	2
e	21.5	54.5	340	2
f	23.1	179.1	113	2
g	23.4	176.4	200	2
h	25.2	67.8	460	1
i	27.4	90	408	1
j	29.3	129.2	440	2
k	31.8	53.7	459	3
l	34.0	96.7	662	1
m	36	128.3	630	1
n	42.2	166.4	590	1
o	48.3	192.6	436	1
p	58.6	151.3	869	1

Event (Name)	**Pix. core** (ph.)	**Pix. 1** (ph.)	**Pix. 2** (ph.)	**Pix. 3** (ph.)	**Pix. 4** (ph.)	**Pix. 5** (ph.)	**Pix. 6** (ph.)
a	43	1	5	11	5	5	4
b	11	0	1	3	2	0	3
c	11	1	5	5	0	0	0
d	28	7	3	6	12	8	5
e	39	20	11	22	33	10	29
f	20	2	0	11	16	4	1
g	23	0	4	10	19	8	0
h	76	11	60	62	37	19	28
i	102	15	13	91	23	4	12
j	52	17	18	18	12	6	7
k	43	24	6	14	16	22	20
l	95	23	9	10	71	57	29
m	72	63	19	2	5	47	34
n	132	11	29	25	36	48	32
o	32	33	21	29	33	10	5
p	149	87	30	38	95	59	29

Table 3.1: The main proprieties of the events displayed in figure 3.4. In the upper table, the bunches are the well recognized photon clusters. In the lower table, the monitored pixels are the six ones around the core pixel. The numeration starts from the pixel closest to the camera centre and moves clockwise.

photons generated in the last cascade development [78]. This is another factor that enlarges the dispersion of 3 equivalent pixels, but it is important at the analysis level because it empathizes the elongated shape.
A γ–ray of 40 GeV is initially submitted by 4÷5 strongly collimated interactions, where most of the Čerenkov photons are collected in few pixels, then the last scatterings smear the image, creating a uniform blob. Differently, a low energy event of 10 GeV

Interaction (Nr.)	**Energy** (GeV)	$\alpha_{scattering}$ (^{o})	**Equivalent pixel** (Nr.)
n	0.083	0.34	3.4
n-1	0.166	0.17	1.7
n-2	0.332	0.08	0.8
n-3	0.664	0.04	0.4
n-4	1.3	0.02	0.2
n-5	2.7	0.01	0.1
n-6	5.3	0.005	0.05
n-7	10.6	0.003	0.03
n-8	21.2	0.001	0.01
n-9	42.4	0.0007	0.007

Table 3.2: The angular deflections of a relativistic electron due to *bremsstrahlung* scattering, as a function of some energy values. Starting from the critical energy, the value is doubled, because it is assumed that the electron energy is halved every interaction, as in the *Heitler* model. The equivalent pixel is the number of *MAGIC–I* camera pixels (0.1°) contained in the angle $\alpha_{scattering}$.

is subjected only to 2÷3 collimated interactions, whereas the rest, which is dominant, is scattered significantly. This is the explanation of the multiple small, well separated bunches.
Finally, it is evident that most of the core pixels distribute in a ring around the centre, at not very large impact parameters. The main points can be summarized as:

- The camera region hit by the Čerenkov light is extended, but the light density is concentrated in few pixels.
- At very low energies the projections contain several small separated bunches of hot pixels.
- Most of the Čerenkov light is distributed within a ring around to the relative source position.
- Most of the Čerenkov light arrival time, in the camera plane, is contained inside a window of around 2 ns.

It is interesting to observe that by a full analysis of the light distribution, even if there is only one single photon in a pixel, it is possible to obtain an indication of the shower's orientation. On the contrary, taking into account only the dense small packets of photons, it is impossible to extrapolate the classical *Hillas* parameters. This feature suggests that there is still room for the classical *Hillas* imaging reconstruction. Obviously the photosensors size must be reduced to define perfectly the projection contour and the quantum efficiency should be at least higher than 50%.

The time is another component, which plays a crucial role in the low energy domain. To detect a faint event, the acceptance threshold should be very low, close to the noise typically dominated by *NSB*. For the current *IACT* telescopes, the *NSB* rate in a single pixel could reach several MHz with a low threshold of 3÷4 phe. The contamination due to this noise can be partially removed imposing a narrow time gate in the event selection and special algorithms in the reconstruction. However, a tight gate also causes the loss of some Čerenkov photons, deleting part of the image (more details in subsection 3.4.1). In figure 3.5, the arrival time simulation in the camera plane of an event of 10 GeV [84]

is presented. Most of the photons arrive within 2 ns, forming an image that initially is

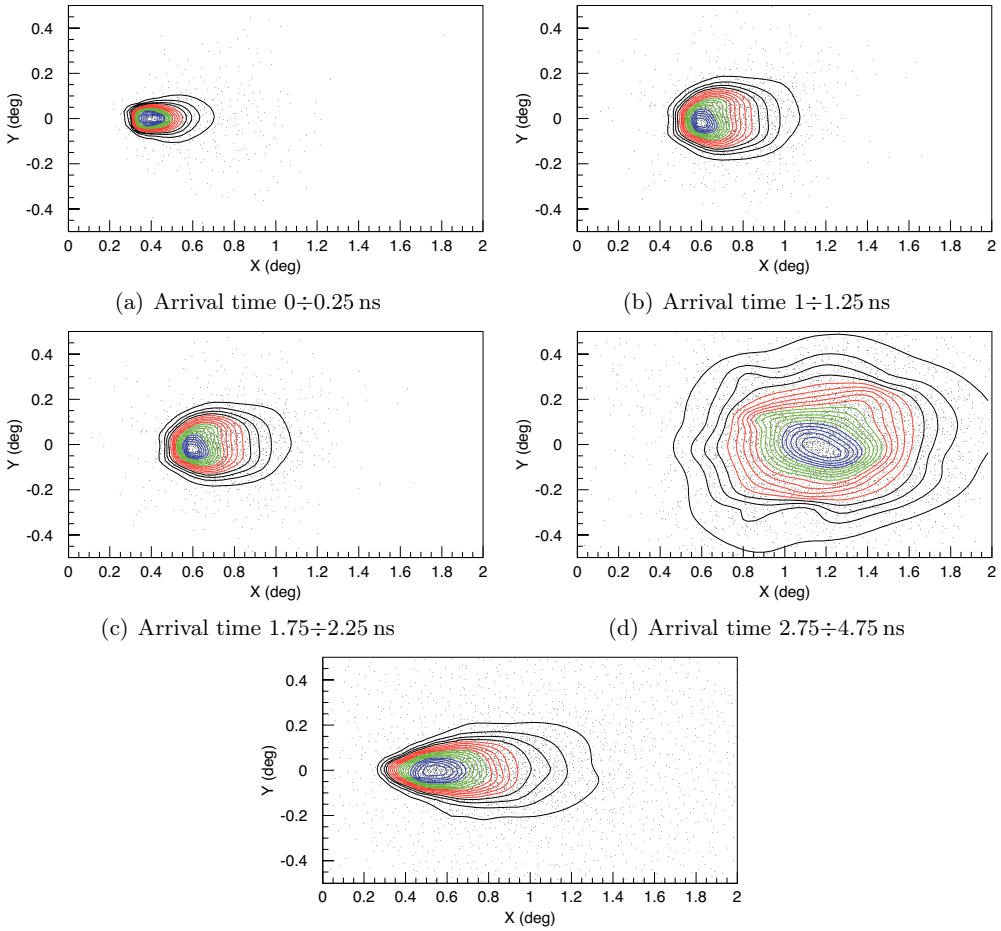

(a) Arrival time 0÷0.25 ns

(b) Arrival time 1÷1.25 ns

(c) Arrival time 1.75÷2.25 ns

(d) Arrival time 2.75÷4.75 ns

(e) Original event (0÷14 ns)

Figure 3.5: The projection of Čerenkov light emitted by a γ–ray of 10 GeV and an impact parameter of 150 m. The simulated photons are collected by a telescope of 30 m located at 2 km a.s.l.. The last figure (bottom) illustrates the original event without any particular arrival time cut. The first four figures show the projection in distinct temporal intervals. The arrival time windows are not equal because every image contains approximately the same number of photoelectrons. (Adapted from [84])

very concentrated, then spreads as a tail of a comet. The light emitted at the beginning of the shower development forms the head-on part of the image, while the delayed one is caused by the shower electrons that propagate further into the atmosphere. In fact, this component of light has larger Čerenkov angles and hits the camera further away from the nominal source position. The image profile becomes broad and the photon density somewhat lower. The large fluctuations are due to the multiple scattering of relatively slow electrons close to the critical energy.
The images in figure 3.5 demonstrate that a tight temporal constraint could be very useful in the selection algorithm to discriminate the *NSB*, but it affects the event reconstruction. Considering only a small duration of the image evolution, we obtain rather symmetric shapes, without an evident direction. Conversely, as already written during the comment of figure 3.3, the entire projection points out an orientation with

the classical elliptical shape. Anyhow, one should not be fooled by the nice appearance of the simulated photons. Introducing the camera pixelization and the correct reflector area, it becomes worse, with one or two pixels hot and the rest very faint.

Concluding, it seems that the time information could be applied with a tight threshold during the trigger phase in order to reject the background, but the threshold should be relaxed in the analysis reconstruction to form the complete image. Maybe the evolution of the arrival time could be used to extrapolate additional information.

3.4 Technical strategies at low energies

On the base of what has been described in the previous section, the performance of an *IACT* detector, at very low energies, is essentially determined by three conditions.

- The light detection efficiency has to be maximized. The quality of the information in the recorded event depends critically on the number of detected photons respect to the original quantity. Faint Čerenkov flashes contain a small amount of photons, which must not be lost. Even the leak of a small fraction of light could prevent either the detection of the event at the trigger level, or its reconstruction in the analysis. There are three important parameters that should be considered to improve this aspect: a) the telescope altitude; b) the light collection; c) the light focusing and its conversion.
  At higher altitudes, the photons density of an *EAS* increases, because the light pool covers a smaller area. Comparing the *MAGIC* altitude with a site at 5 km a.s.l., the photon density is a factor 2.5 lower, for an impact parameter below 100 m. Beyond 125 m where the low energy events are less concentrated, it becomes identical [84]. Moreover, the absorption of light crossing the atmosphere is reduced by $\sim 15\%$ for a telescope at altitude of 5 km. The disadvantage is that at high altitude, the probability of ionizing particles hitting the *PMTs* is increased. Secondly, a larger reflector allows to collect more light from the shower. The signal to noise ratio and the sensitivity for weak fluxes improve significantly.
  Third, the fraction of photons lost in the dish's reflection, in the focusing towards the camera and in the conversion in the photosensors, has to be reduced as much as possible. Therefore, the unique strategy is to enhance the available information and subsequently to maintain its integrity.
  In figure 3.6(a), the energy threshold is expressed at different altitudes as a function of the equivalent telescope aperture (S). S represents the equivalent reflective surface area for an ideal light collection efficiency. It can be expressed as:

$$S = \varepsilon \cdot A \tag{3.3}$$

  where A is the real telescope reflective surface and ε is the light collection efficiency (for more details see section 4.4). For the *MAGIC* telescopes, S is in the range $40 \div 50\,\mathrm{m}^2$, namely only the 20% of the real dish's dimension. The corresponding theoretical energy threshold is around 20 GeV, as shown by the blue line. At an altitude of 3500 m a.s.l., where more photons are collected, the limit is lowered to ~ 15 GeV, so 25% better (red line).

- The trigger algorithm, namely the strategy to alert the data acquisition system that there is an event of interest, has to be able to reveal faint gamma images without being dominated by the background, especially the *NSB*. The usual criterion is to demand signals above threshold in some neighbour pixels. Unfortunately,

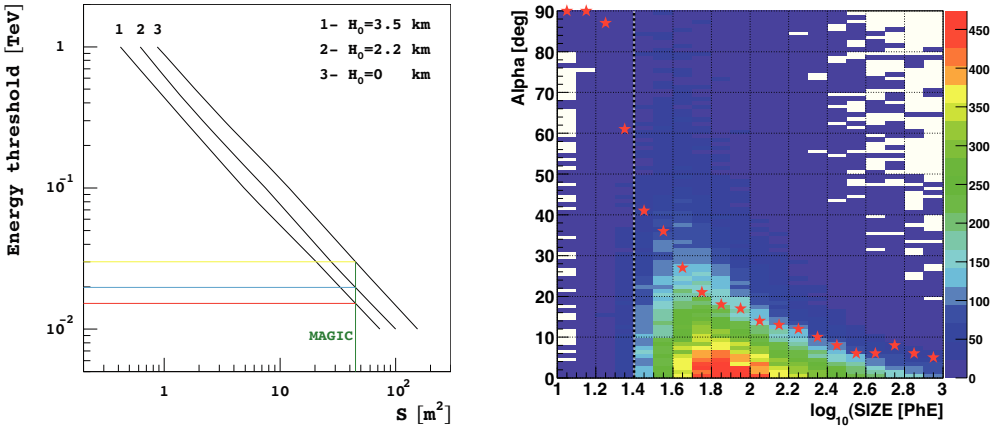

(a) *IACT* energy threshold (b) *Alpha distribution vs* size

Figure 3.6: *Left:* the energy threshold of an imaging Čerenkov telescope as a function of the equivalent telescope aperture and its altitude. The vertical green line represents the *MAGIC* equivalent aperture ($40 \div 50\,\mathrm{m}^2$), while horizontal lines indicate the correspondent energy threshold at different altitudes. The *NSB* effect is not considered in this simulation. (Adapted from [1])
Right: the *alpha* distribution of simulated γ–ray events as a function of *size*. Red stars indicate the cut values, which maximize the quality factor defined in equation 2.16. The black and white vertical line shows the best *alpha* cut for an event containing 25 phe ($\sim$ 25 GeV). The high value, around 50°, demonstrates a significant uncertainty in the estimation of the arrival direction. (Adapted from [39])

the electrical signal produced by an atmospheric shower below 50 GeV is quite small and it requires accepting even pulses with low charge and amplitude. At these low levels, the probability that the *NSB* fluctuations exceed the threshold is so high that the original shower projection can be distorted or it can be lost because the acquisition is saturated by accidental events. It is then important to study how the image topology appears, how the charge is distributed and which is the arrival time evolution at the camera level, to try to improve the trigger efficiency.

✠ The analysis algorithm has to classify properly the events, even if the image contains few photoelectrons. The standard imaging technique seems to be inefficient at low energies, when the shower projections appear less elongated and less regular, introducing significant uncertainties in the calculation of the arrival direction, as well as the gamma/hadron separation (Fig. 3.6(b)). For instance, in the interval between $10 \div 50$ GeV, the image typically consists of $20 \div 70$ phe distributed in a number of pixels which depends on their size. Lowering the pixel size and increasing the QE, the image becomes better defined and it is more easy to apply imaging filters to determinate the shower nature. In addition, it is possible to enlarge the number of pixels in coincidence at the trigger level, getting rid of spurious signals and facilitating the analysis cleaning. However, increasing the number of channels introduces new technical and financial problems.
Another useful information comes from the shower maximum, whereof an accurate determination can correct the energy fluctuations, which dominate over the uncertainty of measuring the impact distance. To this aim the stereoscopy is helpful, but it is not sufficient and it is mandatory to introduce innovative analysis,

which combine spatial and temporal algorithms at the same time.

3.4.1 Performance of trigger algorithms

All current *IACT* telescopes use similar trigger strategies, seemingly leading to similar performance numbers at the TeV regime, but they can differ notably in the detection of low energy events. Nowadays, a digital and an analogue approach exist to plan a trigger system. The first searches for N pixels (multiplicity) with a signal above Q photoelectrons, the second requires a signal formed as the sum of M pixels, above P photoelectrons. The latter solution has been tried with success only by the *MAGIC* collaboration and will be discussed in detail in chapter 5.

Since the aim of this chapter is to study the event morphology at low energies, only the digital solution is considered, because they are based on stringent topological and temporal constraints that can be studied. The analogue technique does not involve any particular topology, therefore it does not allow to understand the event shape. However, this is one of the most important reasons that make it very powerful in the detection of faint events.

As explained in the previous section 3.4, a standard trigger system has to satisfy to two contradicting conditions: the restricted number of available photoelectrons, which translates into low thresholds, and the *NSB* rate, which asks for the contrary. For those algorithms, the afterpulse rate is not so problematic and can be ignored in first approximation.

To find the best compromise, one has to play with the duration of the trigger time gate and the minimum number of pixels involved in trigger (multiplicity). Lowering the time gate or increasing the multiplicity dimension, the accidental triggers induced by the *NSB* are reduced. On the other hand, a large multiplicity is inefficient when the image size is very small and a too stringent temporal constraint could cause the loss of photons of the shower. In figures 3.7(a) and 3.7(b) the simulated trigger rate due to *NSB* for different close compact configurations is shown. Closing the gate at 3 ns, it is possible to lower in average the threshold of 0.3 phe, keeping the same accidentals rate. Checking the probability to trigger γ–rays, it seems that down to a gate of 3 ns, there

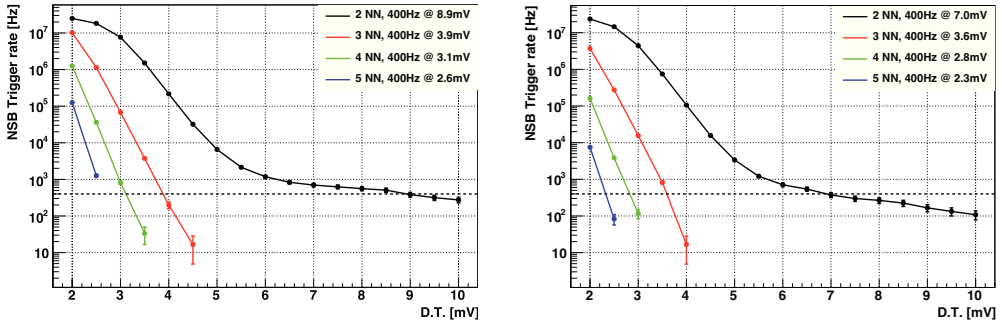

(a) trigger gate 6 ns (b) Trigger gate 3 ns

Figure 3.7: *Left:* the trigger rate due to the *NSB* for different close compact multiplicities and a temporal gate of 6 ns. The threshold is calculated at 400 Hz, which is the limit (The limit of the data acquisition system is $\sim$ 1 kHz, but in addition to the *NSB* the contribution from hadrons must be included.) for an experiment as *MAGIC*. One mV corresponds to 1 phe. *Right:* in this case the temporal gate is imposed at 3 ns. (Images credit: M. Lopez & F. Dazzi)

are no lost events, confirming again the fast evolution of the core pixels (Fig. 3.8(a)

& Fig. 3.8(b)). It seems that the multiplicity of 3 pixels leads to a slightly better result, because it has a good rejection power and its size is similar to the core bunches described in section 3.3. However, except for the multiplicity 2, the others are very close.

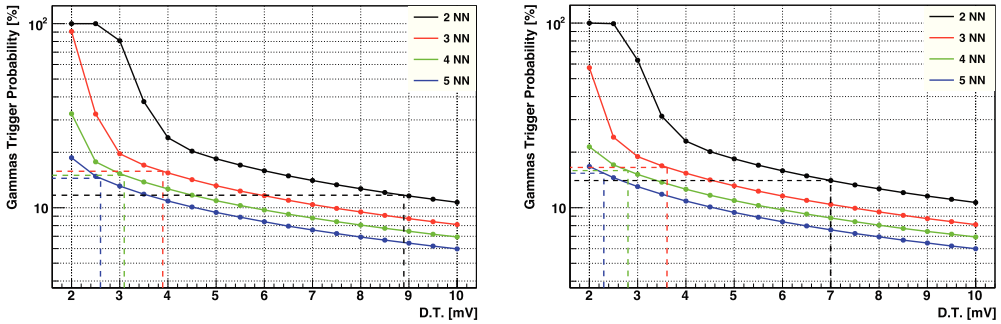

(a) trigger gate 6 ns (b) Trigger gate 3 ns

Figure 3.8: *Left:* the trigger probability to detect a γ–ray in function of the single pixel threshold, using different multiplicities and a trigger gate of 6 ns. The dotted lines indicate the probability at thresholds extrapolated in figure 3.7(a). *Right:* as before but with thresholds calculated from figure 3.8(b) and gate of 3 ns. (Images credit: M. Lopez & F. Dazzi)

It is important to evaluate the topology of the multiplicity. Usually it is distinguished in three categories:

- **Next Neighbour:** N neighbour pixels above the discriminator threshold, so that any N-1 of them are still neighbours. This is the multiplicity used in the previous analysis and its topological constraint is really strong as well as the *NSB* rejection.

- **Majority:** N pixels in a pre-defined region of the camera (e.g. hexagon of 19 pixels) above the discriminator threshold. The topological constraint is absent and more background is accepted.

- **Central pixel**: one pixel (central) and N-1 of their neighbours are above the discriminator threshold. This strategy is based on a soft topological constraint.

Assuming to apply the multiplicity 3 at the few images in figure 3.4, it is evident that between 10÷20 GeV only the *majority* trigger could work, because the photon packets are strongly dissociated. Then, up to 30 GeV even the *central pixel* trigger could become efficient and only beyond the *next neighbour* can be used.
Monte Carlo studies, comparing the performance of the *central pixel* trigger versus the *next neighbouring* one, reveal that effectively several faint events can be detected only relaxing the topological constraint. In figure 3.9(a) the three possible shapes of the *central pixel* trigger are illustrated. The *next neighbour* trigger, which is also the standard trigger used in *MAGIC*, contains only the red configuration. Only 40÷45% of the total fraction of triggered events has been selected by the close compact arrangement. Another 40÷45% comes form the cyan disposition and the rest from the yellow stick shape.

Concluding, for energies higher than $\sim$40GeV the strategy to impose at the same time stringent topological and temporal constraints is successful, but going further

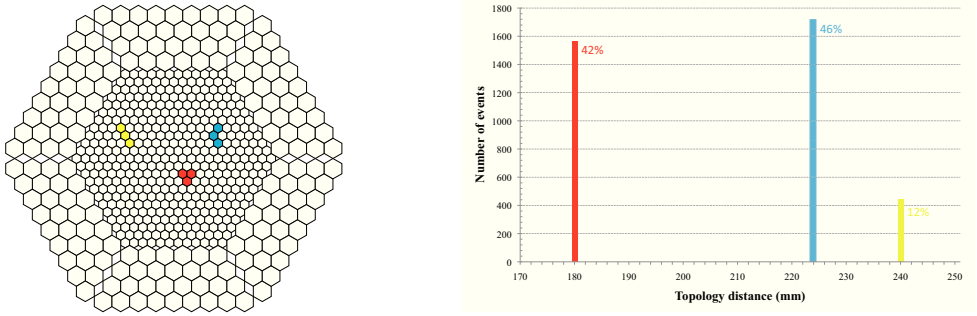

(a) *Central pixel* trigger topologies (b) Detection frequency of the topologies

Figure 3.9: *Left:* the three possible topologies in a *central pixel* trigger with a multiplicity of 3. The red shape is the only one used in the *next neighbour* trigger. *Right:* Frequency of the low energy gamma events in function of the topology. The topology distance has been defined as $\sum_i^{pixel} \sum_j^{pixel} d_{ij}$, considering a pixel with a diameter of 25.4 cm. (Adapted from [59])

down, the Čerenkov projections loose their coherent aspect forming small blobs, sometimes distinct. In this scenario it is mandatory to relax as much as possible the topological constraint and try to reduce the background contribution applying a more selective timing.

4
The MAGIC Telescopes

The two *MAGIC* telescopes are located at Roque de Los Muchachos on the Canary Island of La Palma (~ 2200 m a.s.l). These are *IACT* instruments made for the study of the astrophysical events in the *VHE* range. They can only operate during the night and observe a restricted portion of the sky at a time. The *MAGIC* telescopes are the largest IACTs in operation in the world. Thanks to its low energy threshold, *MAGIC* is the only instrument which can fill the energy gap between satellite and ground-based detectors.
The *MAGIC* design concept differs from the other *IACT* telescopes. First, an innovative carbon fibre structure allows very fast movements. Secondly, the readout electronics is not integrated into the camera frame, but is placed in a remote control house. The dislocation of most electronics from the camera body has many advantages. In first place the weight and the cooling power of the camera are reduced significantly. Another advantage is that one is not limited in space and can access the electronics more easily; maintenance and improvements can be done in a simply way. In fact, the renewal of both *DAQs* is in progress.
In this chapter, the technical description and working principles of the main subsystems of *MAGIC* are presented.

4.1 Telescope design

The idea of a big, single telescope (*MAGIC–I*) was born at the end of the '90s, following the same concept as the parabolic solar concentrator, built near Stuttgart, Germany. The construction of the first *MAGIC–I* telescope ended in fall 2003 and it operated in single mode up to summer 2009. In 2009, the second telescope (*MAGIC–II*) was built, opening the possibility to operate in full stereo mode (Fig. 4.1). Basically, *MAGIC–II* is an improved clone of the former telescope, with some novel technical solutions[1], which became only recently available.

During the design phase it is important to define the goals of the project. *MAGIC* has been conceived to reach the lowest energy threshold in the *VHE* domain, where many unanswered physics questions loom and an overlap with satellite experiments is feasible. The energy threshold (E_{th}) is defined as the peak of the γ–ray energy distribution. It can be expressed as

$$E_{th} \propto \sqrt{\frac{\phi_{NSB} \cdot \Omega \cdot \Delta t}{\varepsilon \cdot A}} \tag{4.1}$$

[1]When not specified, the description of the subsystems deals with both telescopes.

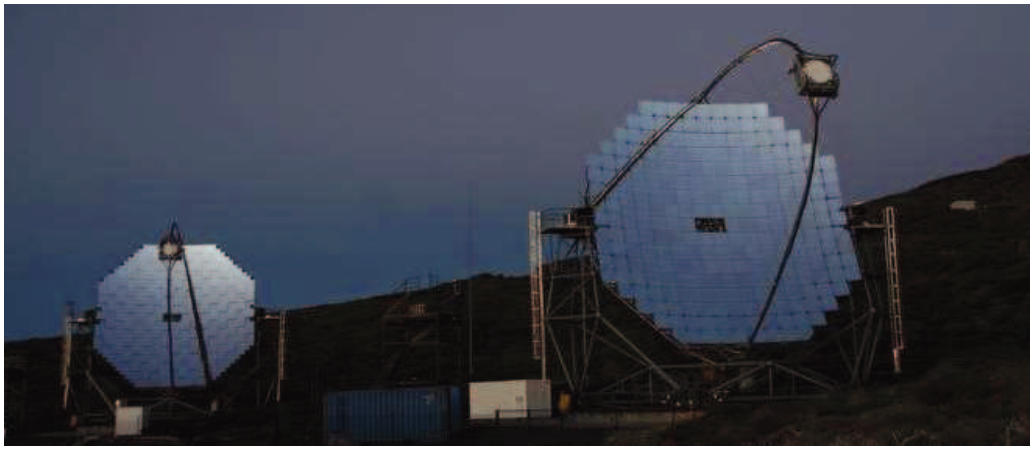

Figure 4.1: A photo of both *MAGIC* telescopes. On the left *MAGIC–I* and on the right *MAGIC–II*. (Adapted from a photo made by R. Wagner)

where ϕ_{NSB} is the *NSB* flux, Ω is the solid angle subtended by a *PMT*, Δt is the signal integration time, A is the reflective surface area and ε is the light collection efficiency [133].
From relation 4.1, it is evident which are the technological strategies to be able to detect faint events. Considering the numerator, either the *NSB* effect is minimized reducing the *PMTs* diameter, or the integration time is shortened with dedicated high-speed electronics. In the denominator, it is clear that the number of recorded photoelectrons has to be increased, focusing more photons with larger reflective surfaces and higher conversion efficiency on the camera. For this reason, *MAGIC* took advantage of the engineering progress in light detection and in the building of large and light structures. As of now *MAGIC* has reached an energy threshold of 50 GeV for the stereo data-taking with the standard trigger, whereas it is lowered to 25 GeV using the *Sum-Trigger* in mono tracking.

Based on the previous assumptions, one can summarize the key elements of *MAGIC* as:

- A light-weight rotating structure, which allows to precisely track the astrophysical sources and to activate the fast repositioning movement, when alerted by the *GRB* monitoring network.

- A large reflective surface to capture and focus the faint Čerenkov flashes initiated by γ–rays in the Earth's atmosphere.

- A camera equipped with adequate light concentrators and high quantum efficiency photosensors to efficiently convert the photons into electrical signals.

- A low latency trigger system which has to identify very small shower projections and, at the same time, has to reject most of the events due to the *NSB* noise.

- A high sampling *DAQ* (*Data AcQuisition system*), which digitalizes and stores the triggered signals, preserving both charge and timing information.

- Powerful analysis tools which can classify and reconstruct the recorded events, as described in section 2.3.

The performance of these elements also characterizes the telescope sensitivity in a specific energy domain.

Some of the above listed elements cannot be upgraded and remain frozen as in the original plan. Others can be replaced with innovative systems based on new ideas and new technologies. For instance, it is impractical to enlarge the mirror dish diameter, but it is feasible to improve the light conversion efficiency, as the *MAGIC* collaboration is doing in the current upgrade of the first telescope.

4.2 The telescope structure

The telescope structure, shown in figure 4.2(a), is a space frame based on carbon fiber-epoxy tubes, joined by aluminium knots (Fig. 4.2(b)). Three tubular layers are laid upon each other and surrounded by as many stiffening rings. The resulting construction is fixed at two sides onto the vertexes of two pyramidal towers. This structure has advantageous features: it is rigid, light weight ($\sim$5.5 tonnes without mirrors), has negligible thermal expansion and an excellent oscillation damping.
The lateral geometry approximates an octagon of 7 m side length, supported by an

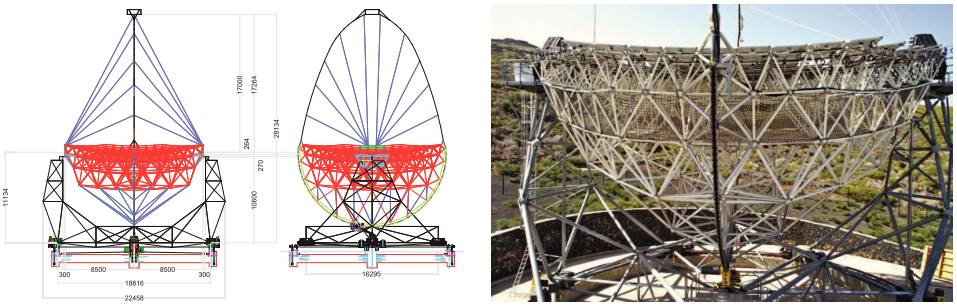

(a) *MAGIC* structure layout (b) Carbon fiber-epoxy tubes

Figure 4.2: *Left:* the *MAGIC* structure layout and the correspondent dimensions from the front and side views. *Right:* an image of the carbon fiber-epoxy tubes, which sustain the reflective surface. (Image credit: MPI für Physik München)

alt-azimuth mount. The camera, located 17 m away from the reflector, is sustained by a metallic Gothic arch, which is stabilized by 10 pairs of 8 mm steel cables tied to the main frame. In this way, the resulting camera bending is kept within an acceptable limit.
Following a circular shape, the arch continues also over the back of the dish for two reasons: first it acts as a rail for the altitude drive, secondly the counterweight is placed on its upper apex.

Simulations performed with a finite elements program return a structure deformation less than 3 mm with respect to the ideal zero weight geometry. Furthermore, the atmospheric conditions at the telescope site could be very adverse and the building has been designed to be resistant to strong storms and ice loads. The idea of a protective dome has been abandoned due to costs.

4.3 Drive system

The structure can be oriented to point and track the sources in the sky [21]. Two types of servo-motors (*Bosch Rexroth MHD112C-058*) move the telescope in the azimuth

(Fig. 4.3(a)) and in the altitude directions (Fig. 4.3(b)). The allowed movement covers the interval from 100° to -70° in declination and from -90° to 318° (0° corresponds to the North) in azimuth. For the azimuth motion around the fixed central joint (Fig. 4.3(c)), two 11 kW motors are mounted in opposite positions on two out of the six bogeys connected on the space frame base, resting on the metal circular rail. Fixed chains form a mechanical drive link for the motors, which are engaged by toothed wheels. The third motor, for the elevation motion, is installed on the arch base, a couple of metres out of its lower apex to increase the declination on the side towards the camera access tower[2]. The elevation drive is also equipped with a holding brake, activated in the case the motor power is switched OFF.
The mechanical position is measured every millisecond by two absolute shaft-encoders

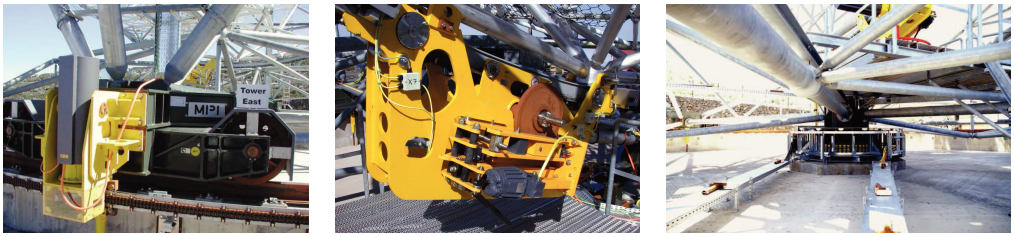

(a) Azimuth motor (b) Elevation motor (c) Central axis joint

Figure 4.3: *Left:* a photo of the azimuth motor that pushes the telescope to rotate on a circular rail. *Centre:* a photo of the elevation motor used to move the structure to different zenith angles. *Right:* a photo of the rotative central axis joint, planted into the ground. (Image credit: MPI für Physik München)

(*Heidenhain ROQ425*) of 13-bit precision/360°. The shaft-encoders give a sinus function between two steps so that a relative resolution of a 15-bit encoder can be reached. One shaft-encoder is placed on the azimuth axis, while the other one is installed on the elevation axis. Then, the real pointing coordinates are verified by a star-guider camera, mounted at the centre of the mirror dish structure. It compares the tracking position of the telescope camera, obtained with a ring of LEDs placed at the edges of the camera, with the pointing direction in the sky, calculated using reference stars. Safety end-switches, connected to the motor controller units, prevent movements beyond the allowed ranges.

During normal operation, the ≈65 tonne telescope can track a source with an accurate precision of the order of 0.02°, including systematics. When a *GRB* alarm arrives, the drive system can reposition the telescope, completing a rotation of 180° in less than 20 s.

4.4 Optics

In the relation 4.1, a significant factor for the threshold energy of an *IACT* telescope is the light collection efficiency (ε). For a camera equipped with PMTs, the ε is a combination of several components, as shown is the following equation:

$$\varepsilon = \int_{300\,nm}^{700\,nm} [R_{dish} \cdot (1 - L_{foc.}) \cdot (A_{pmt} + A_{lc} \cdot R_{lc}) \cdot QE \cdot C_{dy\_1} \cdot (1 - L_{dy\_1})] d\lambda \quad (4.2)$$

[2]In front of the telescope, there is a tower in the North direction to avoid focusing the sun light. When the telescope is in parking position, it is possible to access the camera.

where $R_{dish}(\lambda)$ is the dish reflectivity, $L_{foc.}(\lambda)$ is the fraction of light not reaching photosensors due to bad focusing or photon scattering, A_{pmt} is the *PMT* fraction of active area, A_{lc} is the fraction of active area of the light concentrators, $R_{lc}(\lambda)$ is the reflectivity of the light concentrators, $QE(\lambda)$ is the *PMT* quantum efficiency, C_{dy_1} is the photoelectron collection efficiency onto the first dynode and L_{dy_1} is the loss at the first dynode stage. The chosen integration interval is very conservative, because the main Čerenkov contribution is below 450 nm. The two functions $R_{dish}(\lambda)$ and $L_{foc.}(\lambda)$ are strongly related to the performance of the telescope's optics.

The profile of the *MAGIC* reflector approximates a parabola with a diameter of 17 m. This choice is forced to keep the information of the photon arrival time, since the distance between the mirror facets and the camera is always isochronous. Parallel light rays are focused on the same *PMT*, hence every pixel represents a small range in the incident angles. Photons travelling along the telescope axis are concentrated on the central pixel, as shown in the left sketch of figure 4.4. When the incident light is tilted a little bit, as in the right sketch, the hit pixel is off-centre by an amount ρ that in first approximation is given by:

$$\rho \sim \sin(\beta f) \sim \beta f \tag{4.3}$$

where f is the parabolic mirror surface focal length.

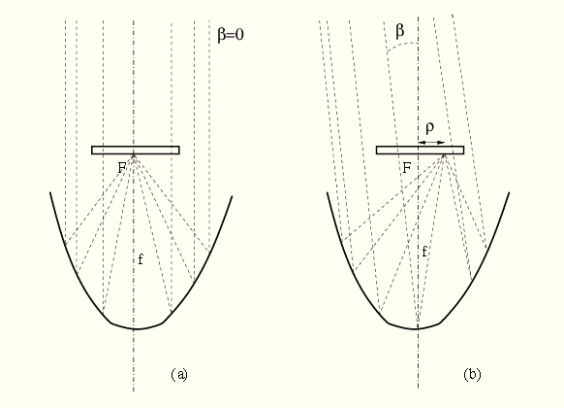

Figure 4.4: Focusing of parallel photons coming from different angles. The photosensors lie in the focal plane F of the mirror reflective surface.

The reflector focal length is 17 m as the dish diameter (D). The ratio (f/D) is 1, which assures a low astigmatism over the FoV of 3.5°.

4.4.1 MAGIC-I mirrors

The *MAGIC–I* octagonal reflector of 236.2 m^2 area is segmented with 964 square all-aluminium mirrors of 49.5 cm by side (Fig. 4.5(a)), attached on 247 support panels (Fig. 4.5(b)). Some of them (223) house 4 mirrors, others, placed mainly on the surface edge, only 3 mirrors.

Not all mirrors are equal, but in general they follow the same sandwich concept used in the aeronautical environments. Each element is an assembly of an open box filled with hexcell honeycomb[3] (*Al 3003-5.2-¼-003P*), and a top plate (Fig. 4.5(c)). The parts are glued using structural adhesive films from 3M™ (*Scotch-Weld AF-163-2K*). The result is a robust and light-weight (∼3 kg) aluminium box, dubbed raw blank. Originally

[3]The honeycomb is a light yet structurally rigid product, which has a geometry that follows the hexagonal cells.

two slightly different designs have been mounted on the reflector. One produced by the *MPI* group (224 units), which does not present the lateral wall, another realized in Padova (740 units), in which the honeycomb is surrounded by walls of the Al box. When studying the behaviour of the mirror over time (ageing), it was discovered that water could condense inside the honeycomb cells, deforming the raw blank original shape during the formation of ice at low temperatures during winters. A third design has been realized to improve sealing. The heating circuit has been moved outside the raw blank to increase the compactness. The contact point between the plate and the box has been changed to favour a sealing with a specific bi-component epoxy-glue (3M™ DP190).

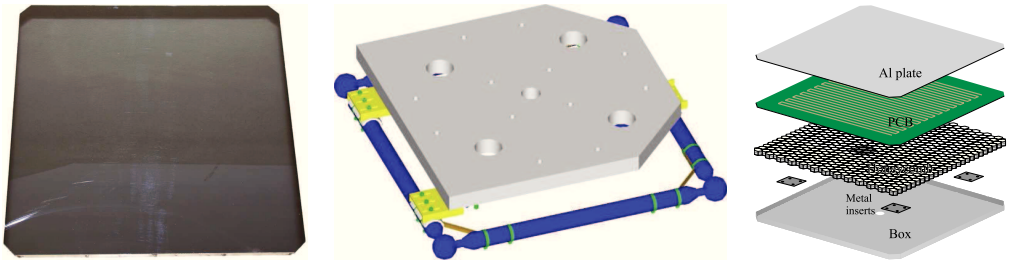

(a) Mirror image (b) Standard support panel (c) Al mirror design

Figure 4.5: On the left, a photo of one of the last produced small aluminium mirror made by the Padova group. In the centre, a sketch of the support panel for four mirrors. (Image credit: MPI für Physik München)
On the right, the general exploded view of the *MAGIC–I* raw blank. In the last version, the heating circuit is connected externally on the back of the aluminium box. (From [9])

The transformation from raw blank to mirror is completed when the upper Al-plate is diamond turned to obtain a local reflectivity of 80÷90% in the optical range (Fig. 4.6(a)). To avoid corrosion, the reflecting surface is finally coated with a protective thin transparent layer of quartz [13].
At the end of the whole process, the roughness *RMS* is well below 10 nm (Fig. 4.6(b)).

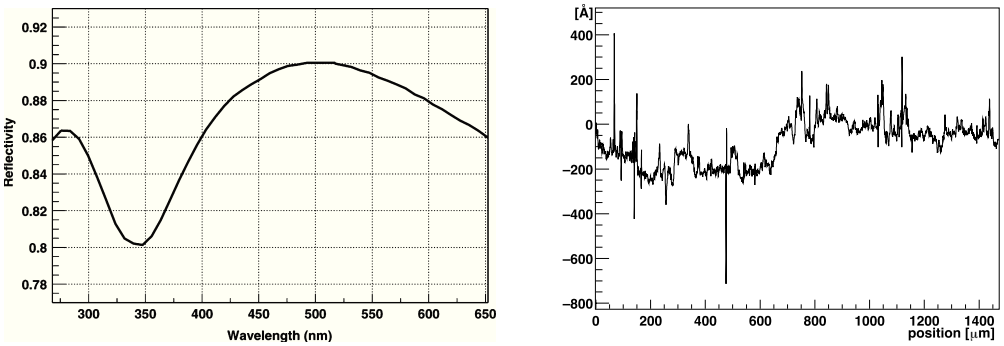

(a) Mirror reflectivity (b) Mirror roughness

Figure 4.6: *Left:* mirror reflectivity measured at different wavelengths with a double-beam spectrophotometer. *Right:* roughness of a mirror sample after milling and coating. The central spike is caused by the milling machine. (From [9])

However there are some regular spikes, which are produced during the passage of the milling machine. Sometimes a reticle is formed and the incident light can be diffracted.

Due to the intrinsic roughness of the mirror surface, in this technique a significant part (up to 15%) of the reflected light is diffuse scattered and not focussed at the focal point. One has to find a compromise between the mirror reflectivity and the costs of the production. The longer the surface is polished with the diamond the lower the surface, however, the higher the costs for the machining.

The mirror profile of each segment is spherical with a curvature radius that spans between 34.018 m and 36.715 m. The radius is dependent on the position of the mirror on the parabolic dish. The typical point spread function is less than 1 cm, so most of the reflected light is contained inside a single *PMT* (more details is subsection 4.5.1).

4.4.2 MAGIC-II mirrors

In *MAGIC–II* two different technologies have been applied. There are 143 1 m^2 all-aluminium mirrors, mounted in the central area of the dish, and 104 cold slumped glass mirrors in the outer rings (Fig. 4.7(a)). The total reflective surface is a little bit larger than *MAGIC–I*, about 236.8 m^2, because the outer ring of the reflector is assembled with 1 m^2 mirrors and not with 3 small mirror facets. The support panels have been eliminated, and the facets are connected directly to the frame structure through the actuators of the *Active Mirror Control* (*AMC*) system, described in the next subsection (4.4.3). The total weight reduction is around 30%, namely from $\sim 25\,kg/m^2$ to $\sim 18\,kg/m^2$.

The aluminium raw blank is an expanded version of the *MAGIC–I* production. The assembled block is composed of an upper plate ($985 \times 985 \times 3$ mm), a honeycomb panel ($971 \times 971 \times 60$ mm), an aluminium back box ($973 \times 973 \times 61.9$ mm) 2 mm thick and 3 fixing pads ($100 \times 100 \times 12$ mm) inserted for the mounting (Fig. 4.7(b)). There is a central hole to house the *AMC* laser to control the mirror position [50]. The increased

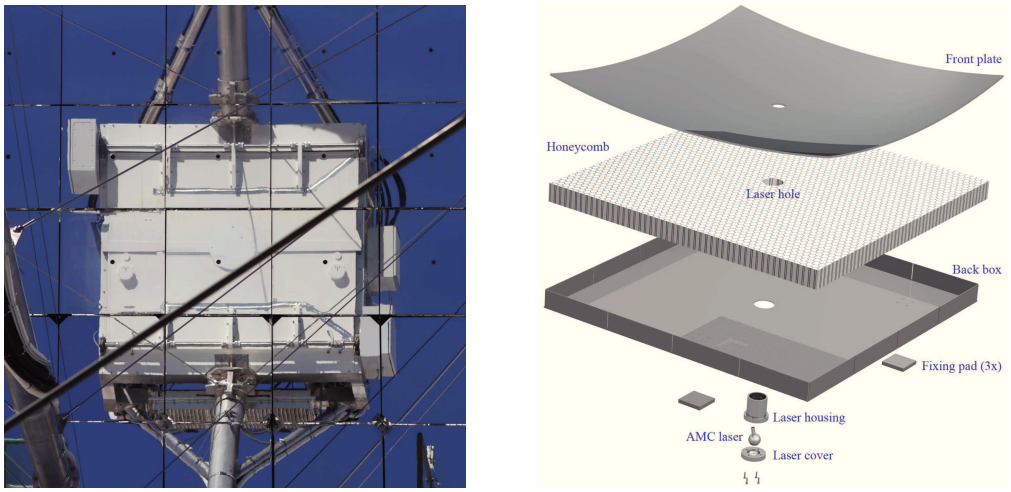

(a) *MAGIC–II* mirrors (b) *MAGIC–I* Al mirror design

Figure 4.7: On the left, a photo of a small portion of the *MAGIC–II* reflector, which is reflecting the camera lid image. The ones with the central hole are 1 m^2 aluminium mirrors, the others are glass mirrors. (Courtesy of M. Garczarczyk)
On the right, the general exploded view of the *MAGIC–II* aluminium raw blank. (Image credit: M. Zago)

thickness of the honeycomb enhances the raw blank rigidity. The consequent diamond

milling is less affected by local deformations and the curvature radius nicely matches the nominal value. The focusing power reaches a resolution of 0.5 mrad for a point-like source. On the other hand, it is more hard to fit the parabolic profile of the ideal dish. The best solution should be astigmatic mirrors with two radii of curvature. Unfortunately, this kind of mirror is still very difficult to produce.

The alternative technological process, developed in collaboration with the *INAF* group and *Media Lario Technologies* company, deforms elastically a glass plate ($985 \times$-985×1.7 mm), forcing it to take the shape of a convex mould. Using a vacuum suction, the glass adheres perfectly to the mould surface and a honeycomb foil (20 mm thick) is glued above it to provide the structural rigidity. The sandwich is completed sticking a second glass plate on the top, applying a structural epoxy resin adhesive. The final steps of the production consist in the vapour deposition on the concave side of a reflective coating layer of aluminium and another protective quartz (SiO_2) layer. The sandwich borders are assured by a silicon based sealant, reinforcing the lateral protection [110]. This technique takes advantage of the large required curvature radius and the thin thickness of the glass sheet. Using the same master mould, it is possible to obtain various curvature radii controlling the spring-back effect during the gluing phase.
Compared with the aluminium facets, the glass mirror presents a higher reflectivity ($85 \div 90\%$), a lower roughness (~ 2 nm), but a worse focusing ($0.5 \div 2$ mrad). The weight of a single facet is 12 kg, $\sim 35\%$ less than the aluminium unit. The last difference is the laser position for the *AMC* system. It has been fixed to one of the four corners of the mirror, as it is to difficult to drill a hole in the centre of the glass mirror.

4.4.3 Active mirror control

The light-weight tubular frame of the *MAGIC* mirror dish deforms slightly, when changing the telescope orientation. The orientation of the mirrors follows directly the dish deformations and is subjected to small misalignments that needs to be corrected. An active mirror control (*AMC*) automatically corrects such changes [14].
The support panel in *MAGIC–I* and directly the $1\,m^2$ mirror in *MAGIC–II* are joined to the space frame at 3 points. One of them is fixed, the others are connected through two longitudinally movable actuators having one and two dimensional lateral degrees of freedom respectively. Each actuator contains a two phase stepping motor and a ball-bearing spindle, which assure a minimum step of 10 μm. Hence, the focused light spot position on the camera plane can be moved with a precision of 1.7 mm.
Each panel/mirror is equipped with a guidance laser ($645 \div 665$ nm) pointing to the camera centre. For *MAGIC–II*, a new laser, not problematic for the *PMTs*, has been installed. It works in the infrared spectrum (1300 nm), where the *PMTs* are completely insensitive.
The laser spot was used initially to estimate the misalignment of the mirror with respect to four reference *LEDs* mounted on the camera lids. The *AMC* system uses a *CCD* camera, which is mounted in the centre of the mirror dish structure. This camera monitors the position of the laser spots on the telescope camera lids. Using this position, respect to the reference *LEDs*, the correction of the inclination of the panels can be calculated and applied with the two actuators.
Nowadays, a high sensitivity *SBIG STL-1001E* camera is utilized. It allows one to see the reflected spot of a star from each mirror segment and to focus the mirrors using stars.
The system is completed by 62 water tight (*IP67*) boxes, which contain the control electronics for the actuators and the lasers. The boxes are connected to the computer

using eight independent *RS-485*[4] lines for parallel operations (Fig. 4.8).

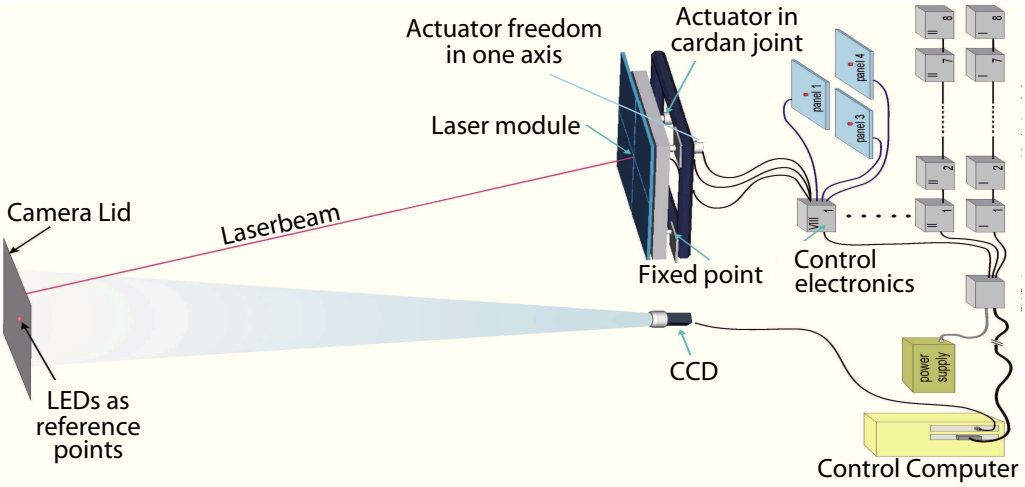

Figure 4.8: General overview of the *AMC* system. On the left, the stuff mounted on the camera structure, in the centre an adaptive optics module and on the right the control electronics. (From [14])

In the first design of the *AMC*, the use of laser pointers was thought to be the standard focussing method. The advantage of the laser pointers is that the mirror position is adjusted, independently from the deformation of the telescope dish. A change of loads on the dish is therefore automatically corrected. The main disadvantage of this procedure is the time needed to focus all 247 panels of each telescope. The fastest way is to adjust in parallel about 30 panels/mirrors at a time, according to a pre-calculated grid arrangement. The operation is completed in a few minutes, since only eight cycles are necessary. However, it is not possible to apply it during data-taking or after a *GRB* alert. The reduction of the observation time (the telescope camera needs to be closed during the usage of the lasers as the *PMTs* are sensitive to the red light, which is also reflected on the closed lids) and the time needed to start *GRB* observations are too long.
Studies of the dish deformations versus zenith angles have showed that the misalignments can be reproduced on large time scales. Using look-up tables containing the position of each actuator at different zenith angles, the overall focussing is replicated very well. An adjustment of the complete reflector takes at maximum 10 s and can be performed while moving the telescope to the next coordinates. In addition this procedure does not require closing the lids and switching on the lasers.

4.5 Camera

The remaining parameters of equation 4.2 are related to the telescope camera, where the light concentrators and the *PMTs* constitute the central elements. With present technology, many of them are, unfortunately, inversely related. The *PMTs* used in the *IACT* experiments present an extended active area, but a poor quantum efficiency (25÷35%). On the other side, there are silicon photosensors with high $QE(\lambda)$ available

[4]The *RS-485* is transmission used mainly in digital communications networks. It is a standard defining the electrical characteristics of drivers and receivers for use in balanced digital multi-point systems.

on the market, but they are small in size and in A_{pmt}. The solution usually adopted is to connect, just in front of the sensor, a light concentrator in order to focus photons in the active area. Even if this technique returns good results, part of the light is lost during the internal reflections of the focusing phase ($R_{lc}(\lambda)$). Moreover, a small fraction of dead area still survives ($1 - A_{lc}$).
In this field, technological progress may bring significant improvements to new generation *IACTs*.

4.5.1 MAGIC-I camera

The *MAGIC–I* camera is an hexagon of 114×104 cm, which covers a field of view of 3.5° in the vertical direction and 3.85° in the horizontal one. It is composed of *PMTs* of two different sizes. The central hexagonal region, 69×61 cm, is covered by 397 small pixels 1" ∅ (0.1° FoV) and the external ring by 180 large pixels 1.5" ∅ (0.2° FoV).
The central pixel has been modified for optical observations. It is mainly used for *Pulsars* studies, where there are periodical and simultaneous emissions in the optical and gamma regime [8]. The typical *Pulsar* frequencies are in the range 1 Hz ÷1 kHz. The *Pulsar* emission changes the output current of the central pixel which is digitized and stored in a dedicated chain for off-line analysis.

The *PMTs*, *Electron Tubes 9116A* and *9117A*[5] (Fig. 4.9(a)), have been modified to enhance the probability to produce photoelectrons in the Čerenkov spectrum peak. A special lacquer[6], doped with a wavelength shifter P-Terphenyl, has been applied on the glass cover, in order to shift the UV component towards the more sensitive yellow band [108]. The quantum efficiency improvement is shown in figure 4.9(b). In addition, the light concentrator geometry has been studied in such a way that the reflected photons can cross twice the hemispherical photocathode, favouring the photoelectrons conversion by a factor of 20÷30% [105].
The *PMT* cathode is powered at the negative voltage of $(0.7 \div 1.45) \cdot 10^3$ V. The internal

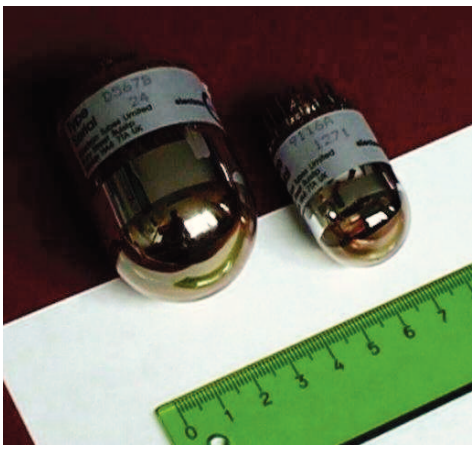

(a) *MAGIC–I PMTs*

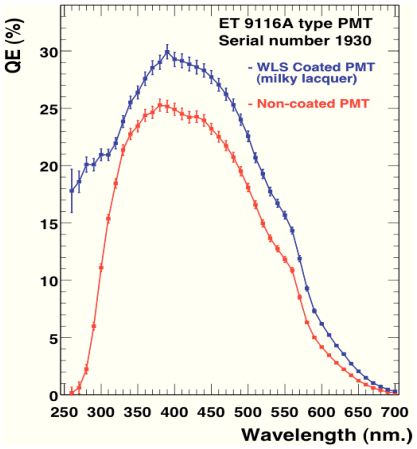

(b) Quantum efficiency

Figure 4.9: *Left:* a photo of both *PMTs* from *Electron Tubes*, installed in the *MAGIC–I* camera. (Photo by R. Wagner)
Right: the final quantum efficiency obtained with the special lacquer coating. (Adapted from [107])

[5] They are hemispherical borosilicate window and rubidiumbialkali photocathode *PMTs*.
[6] It is dichloromethane (CH_2Cl_2) mixed with *Paraloid B72* and *1.4 P-Terphenyl*.

amplification stage is made of 6 dynodes, limited to a gain of around $3{\cdot}10^4$, so that observations with moderate moon light are possible. Its typical DC current, in dark conditions, is $\approx 1\,\mu$A.

Close to the *PMT*, there is a low noise transimpedance pre-amplifier, which further amplifies the signal. Then, the pulse is converted back into light, and transmitted by a *VCSELs* (*Vertical Cavity Surface Emitting Lasers*) into long (162 m) multi-mode optical fibres to the counting house, where the electronics is located (Fig. 4.10(b)). The *VCSEL*, provided by *Honeywell* (*HFE4080-321*), is a product intended for high-speed data communications even in the GHz domain. It generates an output of 850 nm with a typical rise time of 100 ps.
For long transmissions, the optical fibres have practical advantages over standard cables.

(a) *MAGIC–I* camera frontal view (b) *MAGIC–I* camera back view

Figure 4.10: *Left:* frontal view of *MAGIC–I* camera with opened lids. *Right:* the back view of *MAGIC–I* camera without the cover. The green optical fibres and the blue *VCSEL* light transmitters are clearly visible. (Photo by R. Wagner)

They are not affected by cross-talk, no electromagnetic interference and no grounding bounces. Moreover, their cross-section is very small and hence many fibres are packaged in a single narrow retaining cable. The resulting low-weight does not put strain on the telescope mount.

In the camera, the temperature is stabilized around 35÷40 °C by a water cooling system regulated by feedback sensors. The most sensitive devices are the *VCSELs*, whose gain depends strongly on the temperature. Even the air is constantly exchanged to prevent the dew point.
The signal processing and HV control electronics inside the camera dissipate about 1 kW power.
The camera structure can be moved back-and-forth by about 30 cm to adjust the focal point. Usually it is not focused to infinity, but is shifted backwards by 3 cm to focus to ∼10 km above the telescope, where the maximum shower development takes place.
The camera is completed by two lids to protect photosensors from the daylight and strong light sources (Fig. 4.10(a)). The total weight is around 500 kg.

4.5.2 MAGIC-II camera

The *MAGIC–II* camera is quite different from the one of the first telescope [127]. The outside dimensions and the shape still remain similar (Fig. 4.11(a)), but the internal design and the components have been renewed, maintaining the same FoV (Fig. 4.11(b)). The number of *PMTs* (*Hamamatsu R10408*) is doubled (1039) in respect to *MAGIC–I* and all have the same size of 1" ⌀ (0.1° FoV). However, they belong to the same class of

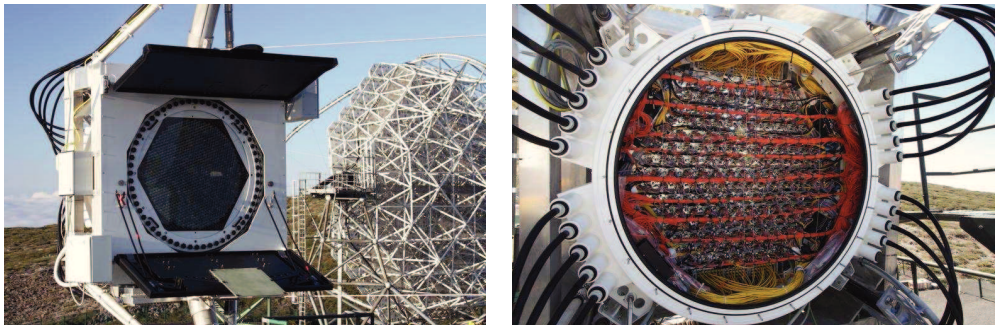

(a) *MAGIC–II* camera frontal view (b) *MAGIC–II* camera back view

Figure 4.11: *Left:* frontal view of *MAGIC–II* camera with opened lids. *Right:* the back view of *MAGIC–II* camera without the cover. The orange optical fibres and the yellow cables for the clusters control are clearly visible. The 19 black cables, that exit from the structure, contain the *PMT* optical fibres. (Photo by R. Wagner)

sensors, namely 6 stages with hemispherical photocathodes and a *Cockcroft-Walton* HV generator[7] included. The quantum efficiency, without any special coating, is around 32% in the blue band (Fig. 4.12(b)) and the afterpulse rate is 0.3% at 4 phe. On the front side, the *PMTs* are equipped with *Winston* cone type light guides to minimize their dead area, same as in *MAGIC–I*.
At the base of each *PMT*, there are some additional circular circuit boards. They house a high bandwidth (800 MHz) and low noise pre-amplifier (*Sirenza SGA-5586*) with a gain of 25.5 dB, a DC current and a HV monitoring, a charge injection input and a *VCSEL* with its bias current monitoring. As in *MAGIC–I* camera, the signal generated in the *PMT* is amplified and immediately converted into an optical signal for the transmission to the control house, 165 m away. The transmission is driven by the *VCSEL* chip *Avalon Photonics AVAP-850SM*, which emits at the wavelength of 850 nm.
Long aluminium tubes cover both the photosensor and the additional devices, forming a compact cylinder, the so-called pixel-module. Seven of these pixel-modules, sorted in a hexagonal configuration, are grouped in 169 clusters (Fig. 4.12(a)). 127 clusters are fully assembled with *PMTs*, while 42, placed in the circumference of the camera, are only partially equipped with *PMTs* in order to approximate a round configuration. The modular subdivision favours the maintenance and the substitution of broken units. Each cluster body incorporates the charge injector generation board, the slow control board and the distribution board for the distribution of power and control signals. This slow control electronics is controlled by a computer, connected via *RS-485* and *VME* optical links.

An innovative feature of *MAGIC–II* camera is given by the pulse injector system. In each cluster, a test pulse, that simulates the *PMT* response, can be injected in the electronic chain, enabling technical measurements even during the day, when the HV cannot be switched on.

A 8 kW water cooling system assures good temperature stability within 2 °C. The clusters are housed in vertical heat exchanging separator plates. The cooling liquid, from small pipes, flows inside these plates. The base of heat exchanging system is thermally connected to the clusters via aluminium rods.

[7] A *Cockcroft-Walton* generator is an electric circuit which generates a high DC voltage from a low voltage AC or pulsing DC input.

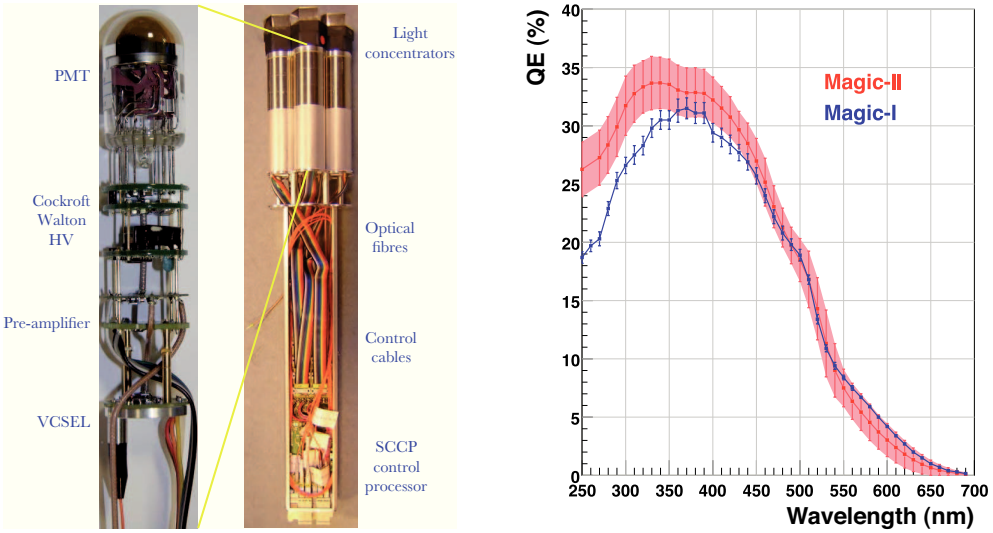

(a) *MAGIC–II PMT* cluster (b) Quantum efficiency

Figure 4.12: *Left:* a photo of a camera cluster of 7 *PMTs*. The zoom (yellow lines) of the upper part of the cluster shows the layout of a single pixel-module. *Right:* the *MAGIC–II PMTs* quantum efficiency (red curve) compared with that one of *MAGIC–I* photosensors (blue). The red band shows the spread over the measured *PMTs*. (Adapted from [128])

In the external ring there are 6 free clusters, which are used to test Hybrid avalanche Photon Detector (*HPD*) from *Hamamatsu* (*R9792U-40*). Currently, they are installed and are being commissioned. The entire camera will be upgraded with them if they prove to be significantly better than the *PMTs*.
The total camera's weight is around 600 kg for a diameter of 1.462 m and a thickness of 0.81 m.

4.6 Electronic chain

Differently from other *IACT* experiments, *MAGIC* has preferred the alternative solution to move the electronics in a dedicated data acquisition building, limiting the problems related to a heavy camera, the temperature control, the miniaturization of components and to difficult access for maintenance.
The *PMT* pulse, transmitted over an optical link, is first converted back into an electrical signal and amplified, then it is split into two parallel branches: the trigger and the data acquisition system. The trigger selects the interesting events and sends the enabling command to the data acquisition to start their sampling.

The trigger system is subdivided into three consecutive levels, with the main purpose to reject light flashes due to the fluctuations of the *NSB*.

- **Level 0 (*LT0*):** it is a simple discriminator with a programmable threshold. Only signals that exceed the set threshold pass to the next level. It fixes the minimum light quantity that should be present in each photosensor and the accepted *NSB* rate. The *NSB* photon flux (ϕ_{NSB}) has been measured at the *MAGIC* site and estimated:

$$\phi_{NSB} = (1.75 \pm 0.4) \cdot 10^{12} \frac{ph}{m^2 \cdot sr \cdot s} \tag{4.4}$$

where *ph* indicates photon [97]. Assuming a reflective surface of 236 m^2, a dish reflectivity of around 80% and a pixel radius of 0.05°, we can calculate the photon rate per pixel:

$$N_{ph} = \frac{\phi_{NSB} \cdot A_{dish} \cdot R_{dish} \cdot \Omega_{pmt}}{s} \simeq 0.8\, ph/ns \tag{4.5}$$

where A_{dish} is the dish area and the Ω_{pmt} the solid angle of a single pixel. In the previous equation 4.5, the diffraction of the mirror is not taken into account, because for small deviations from the nominal angle, it marginally affects the pixel rate due to the isotropic *NSB*. At the utmost, some photons fall in the neighbour photosensors.
The mean number of photoelectrons ($\bar{n}_{phe}$) is:

$$\bar{n}_{phe} = N_{ph} \cdot QE \cdot \Delta t \simeq 1\, phe \tag{4.6}$$

where Δt is the integration time. Considering that the *NSB* follows a Poissonian distribution, the probability that fluctuations exceed a threshold n_{th}, expressed in photoelectrons, is:

$$P(x > n_{th}) = 1 - \sum_{x=0}^{n_{th}} P(x) \tag{4.7}$$

where $P(x)$ is the probability (Eq. 4.8) to have x photoelectrons in the pre-defined integration window time.

$$P(x) = \bar{n}_{phe}^{x} \cdot \frac{e^{-\bar{n}_{phe}}}{x!} \tag{4.8}$$

The single pixel rate is then:

$$f_{pixel} = \frac{P(x > n_{th})}{\Delta t} \tag{4.9}$$

where $P(x > n_{th})$ is obtained from equation 4.7. In table 4.1 some pixel frequencies are reported as a function of the threshold.

Individual pixel rate							
$\mathbf{n}_{th}$ **(phe)**	0	1	2	3	4	5	6
$\mathbf{f}_{pixel}$ **(MHz)**	160	68	21	5.1	1	0.17	0.03

Table 4.1: Some examples of the individual pixel rate as a function of the *LT0* threshold.

✠ **Level 1 (*LT1*):** It is a digital filter, which rejects most of the accidental events due to *NSB*, combining temporal and spatial information at the same time. It takes advantage of the fast evolution of compact projections, caused by the Čerenkov flashes associated to gamma showers, with respect to unrelated *NSB* fluctuations. The algorithm verifies whether N next-neighbour pixels (N=2,3,4,5 dubbed 2NN, 3NN, 4NN and 5NN fold) show a synchronous signal in a time gate of some nanoseconds. The topological constraint imposes that hot pixels must stay in a close compact configuration, so every pixel of that group should be in contact with other two[8] [55]. The generating trigger rate ($T_{NN-fold}$), only due to *NSB* (accidental triggers), is a function of the selected *NN-fold*, the individual

[8] For N=2, as for the 2NN, only two pixels are adjacent.

pixel frequency (R), the time gate duration (G) and the total number of independent close compact combinations in the trigger area ($\rho N_{Comb.}$). It can be expressed as:

$$T_{NN-fold} = R^{NN} \cdot G^{NN-1} \cdot C_{NN} \cdot \rho N_{Comb.} \tag{4.10}$$

where C_{NN} is a geometrical coefficient, which arises from the intersection of the signal arrival time functions in the NN-dimensional space [49]. $N_{Comb.}$ is the number of close compact combinations in the whole trigger area. Due to the trigger modular design (see next subsections 4.6.1 and 4.6.2 for details), some combinations are repeated and others are not independent. ρ represents the corrective factor to scale down to the effective number.
In a normal mono data-taking with a threshold of ~ 6 phe, only a few Hertz of accidentals pass the trigger selection, resulting in a rejection factor of the order of 10^4.

- **Level 3 (*LT3*):** It is the timing coincidence between the *LT1* (*Level 1 Trigger*) signals coming from different telescopes. Further details are available in section 6.2.

Up to one year ago, *MAGIC–I* was equipped with the level 2 trigger, designed for a preliminary topological analysis of the shower images. It was never completely commissioned and for a long time it was activated only in transparent or flag mode. At the present time it is not included in the trigger chain.

In both telescopes, the pulses in the second branch are sampled at the same speed of 2 Gsample/s. Nevertheless, the readouts make use of different electronics. A custom multiplexed system with commercial *FADC*, so-called *MUX*, is adopted in *MAGIC–I*, whereas in *MAGIC–II* the digitization is provided by an analogue ring sampler (*DRS2*) and high resolution *ADC*.

4.6.1 MAGIC-I electronic chain

The *MAGIC–I* electronic chain is illustrated in figure 4.13. The two main systems, the trigger and the data acquisition are shown in the right side of the sketch, after the optical splitting.

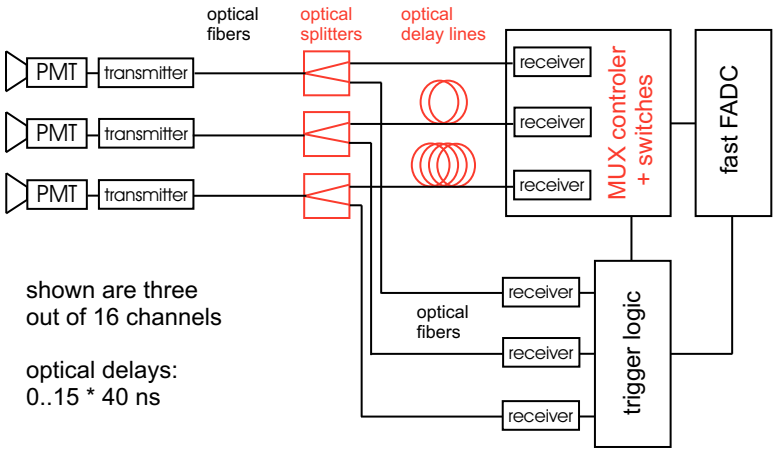

Figure 4.13: The diagram blocks of the *MAGIC–I* electronic chain. (From [64])

The *MAGIC–I* trigger area has a FoV of 2.1°, restricted to 325 pixels. The optical

signals, converted again into electrical ones in the receiver board[9], are digitalized by a programmable threshold (*LT0*) and then elaborated for the next stage, the *LT1*. In this phase, the signal is adjusted in time with *ECL*[10] delay lines, then its width is fixed varying the *RC*[11] value at the output of a flip-flop.
The transfer to the *LT1* electronics is done with 41 semi-custom *MDR* differential cables, each one containing 8 channels. The distribution of these cables over the whole trigger area is shown in figure 4.14(a).

The *LT1* modular design is shared out by 19 partially overlapped trigger cells, dubbed macrocells (Fig. 4.14(b)). Each macrocell, analysed by a single unit (*LT1-board*), is a hexagon composed of 37 pixels, whereof one is specifically blind as 36 is the maximum number of signals that the *LT1-board* can handle with a good timing resolution (300 ps). The macrocell overlap guarantees an efficient coverage of the logic combinations, avoiding macrocell edge effects[12]. The repetition of the channels and their routing to the proper macrocell, or better to the *LT1-board,* is performed by a large motherboard, called *LT1-backplane*.
The *LT1* selection strategy, explained in the previous section 4.6, is implemented in *PLDs*[13] *EPLD128ATC100-7* from *Altera*. In the end, the triggered events from the 19 *LT1-boards* are merged in a global *OR*, processed by a dedicated board so-called *Trigger Processing Unit*. The resulting signal is sent either to the *LT3*, when the telescopes are in stereo data-taking, or directly to the data acquisition system for the event sampling.

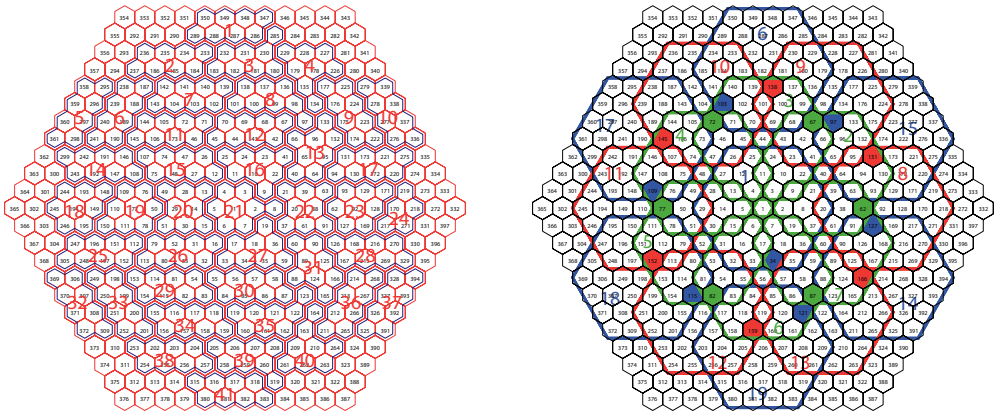

(a) *MAGIC–I* trigger connectors map (b) *MAGIC–I* trigger macrocells

Figure 4.14: *Left:* the subdivision of the trigger area into 41 groups of pixels. Each group symbolizes a connector/cable at the input of the trigger system. *Right:* the representation of the 19 trigger macrocells, partially overlapped within the inner part of the *MAGIC–I* camera. The coloured pixels are blind for the corresponding macrocell with the same colour. (Image credit: D. Corti)

In 2007, a novel trigger was installed in parallel to the standard one. This prototype

[9]The receiver board of *MAGIC–I* has been designed by the *MPI* group.
[10]The *ECL* (*Emitter-Coupled Logic*) is a logic family that achieves high speed by using an overdriven *BJT* differential amplifier with single-ended input.
[11]The capacitor is variable and its capacitance can be changed using a screw driver.
[12]Falling on the boundary of two non-overlapping macrocells, a compact group of activated pixels might not pass the trigger.
[13]*PLD* (Programmable Logic Device) is an electronic device useful to prepare reconfigurable digital circuits.

system, called *Sum-Trigger*, is largely discussed in section 5.1.

The data acquisition system is based on fibre optic multiplexers (*MUX*), which allow to digitize consecutively 16 channels in a single commercial *FADC* [64]. The signals are opportunely delayed before the multiplexer, so they enter in the *FADC* occupying different time slots, spaced 40 ns far from the previous one. No delay is applied to the first channel, while the 16th one is sampled 600 ns later. This approach is possible because the Čerenkov flash duration is very short respect to the trigger frequency (of the order of 1 kHz).
The multiplexers are based on high bandwidth *MOSFET*[14] switches with a low cross-talk of 0.1%. They are controlled by a digital circuit clocked at 800 MHz, corresponding to a switch jitter of only 1.25 ns. The only disadvantage is the introduction of switching noise that affects the last 10 ns of each time slot. However, the peak noise is removed at the software level.
The *FADC* modules (*Acqiris DC282*) have a bandwidth of 700 MHz, a sampling speed of 2 Gsample/s and 10-bit resolution for an input voltage range of 1 V. Each module has 4 *FADCs*, hence it can handle up to 64 channels for a typical consumption of 60 W. The digitized data are temporally stored in four 512 kByte *RAM* and read out at 64 MHz via a cPCI bus. Then, thanks to the fibre channel technology, the data throughput is 100 MByte/s for a trigger frequency beyond 1 kHz. The data acquisition dead time is about 25 μs and saturation appears at around 800 phe.
The main advantage of this solution is to maintain a high sampling resolution at a lower cost compared to using one ultra-fast *ADC* per channel.

4.6.2 MAGIC-II electronic chain

The electronic concept utilized in *MAGIC–I* is replicated in *MAGIC–II*, but most of the devices have been renewed. In this section only the differences between the two telescopes are presented.

The *MAGIC–II* trigger area has been enlarged to 2.5° FoV, covering 559[15] pixels. The number of macrocells and their shape remain the same, whereas the overlap is reduced to only one pixel (Fig. 4.15(b)). The advantage is motivated by the possibility to trigger showers at higher impact parameters, improving the wobble mode data-taking. It can happen that some events, that fall between two macrocells, are lost, but from Monte Carlo studies this is not sufficient to object to the new strategy.

The receiver board has been completely redesigned by the *IFAE* group, but it is still fully compatible with *MAGIC–I* electronics (Fig. 4.16(b)). Compared to the *MAGIC–I* version, it is completely programmable and houses more functions as the *IPR*[16] for measuring the single pixel rate, the DC voltage injector to calibrate the analogue branch and the pattern injector for testing the digital trigger (Fig. 4.16(a)). It is characterized by a very high bandwidth limited at 750 MHz despite the gain of 18.5 dB and a negligible cross-talk (0.1%). The working range spans from 0.25 to 1150 mV with an *RMS* noise smaller than 200 μV. The programming precision of the pulse width and its delay has been lowered to 10 ps, keeping a huge range respectively of 2.7÷12.7 ns and 0÷20 ns. A single board manages 24 channels with a maximum power consumption of 75 W.

[14] The *MOSFET* (*Metal Oxide Semiconductor Field Effect Transistor*) is a transistor used for amplifying or switching electronic signals.
[15] In the outer ring there are 12 blind pixels, so the effective number is 447.
[16] The *Individual Pixel Rate* is a system of scalers that count the frequency in each pixel after the threshold of the *LT0*.

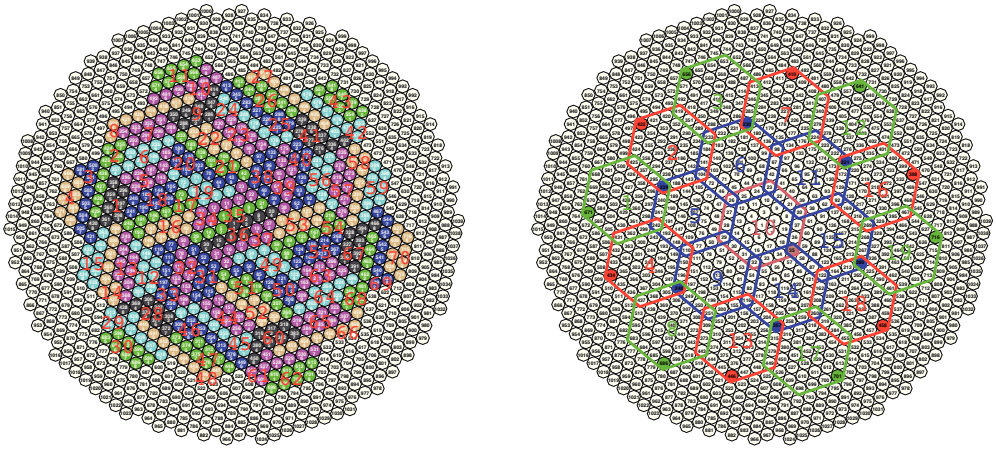

(a) *MAGIC–II* trigger connectors map (b) *MAGIC–II* trigger macrocells

Figure 4.15: *Left:* the subdivision of the trigger area into 70 groups of pixels. Each group symbolizes a connector/cable at the input of the trigger system. *Right:* the representation of the 19 trigger macrocells, partially overlapped within the inner part of the *MAGIC–II* camera. The coloured pixels are blind for the corresponding macrocell with the same colour. (© F. Dazzi)

The receiver boards are accommodated in four *VME* crates and, as the entire *DAQ* system, they are controlled by a multi-thread C++ software called *MIR* (*Magic Integrated Readout*).

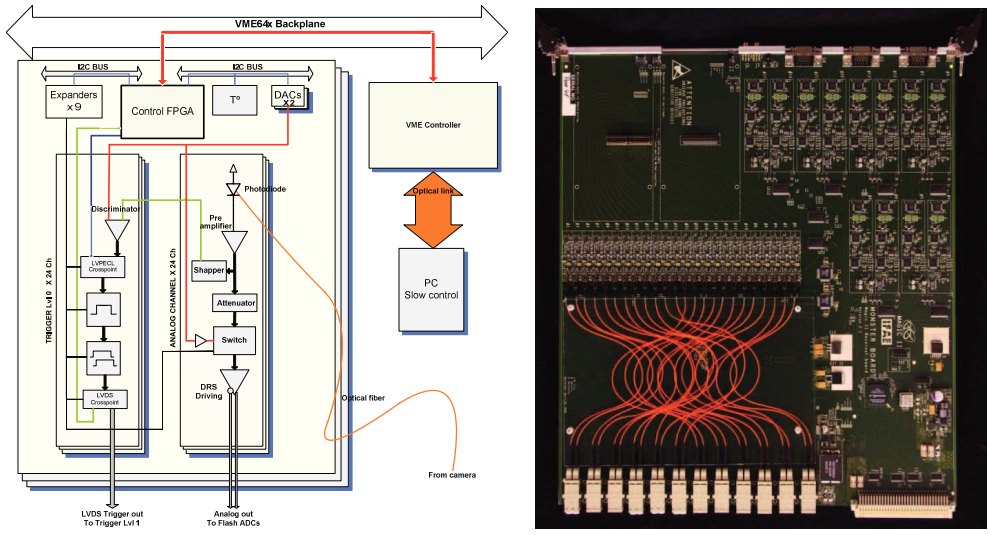

(a) The receiver board diagram (b) Receiver board *PCB*

Figure 4.16: *Left:* the block diagram of the receiver board. (Courtesy of M. Barcelo & J. M. Illa)
Right: a photo of the receiver board *PCB*. (From [124])

The number of cables that connects the receiver boards with the *LT1* is increased to 70 units (Fig. 4.15(a)) to include the new channels. The new trigger area has forced the design of a new *LT1-backplane*, which takes into account the new distribution of the pixels over the macrocells. The board is a fully differential 20 layers *PCB*, where

the lengths of the traces have been notably reduced to around 25 cm respect to the backplane mounted in the first telescope. The performance follows the requirements of the system: it can handle more than 1 Gbps with a low multi cross-talk of $\sim 3\%$ at the most.
Compact adapters have been introduced between the *LT1-backplane* and the *LT1-boards* in order to convert the differential *LVDS* format into the single-ended *LVTTL*. The *LT1-boards* have been replicated, exchanging only the obsolete *PLDs* with the new version *EPLD128AETC100-5*. The *TPU*, which processes the trigger commands for the *DAQ*, is still the same.

The *MAGIC–II* data acquisition system is based on an ultra-fast analogue sampler, the so-called *DRS2* (*Domino Ring Sampler version 2*), with a bandwidth of 200 MHz. Its working principle is summarized in figure 4.17(a). The signal charge is stored in 1024 small capacitors (200 fF) arranged in a ring buffer layout. The sampled speed is determined by the clock of a shift register that sequentially enables the capacitors. Currently the clock is fixed at 2 GHz, locked by a *PLL* synchronization circuitry. When the trigger command arrives, the sampling is stopped and the stored charge is read out at a frequency of 40 MHz. Finally, the voltage is digitized by a 12-bit resolution *ADC* from *Analog Devices* (*AD9235BRU-65*).
A single *DRS2* chip can handle up to 10 channels and two of them are integrated in

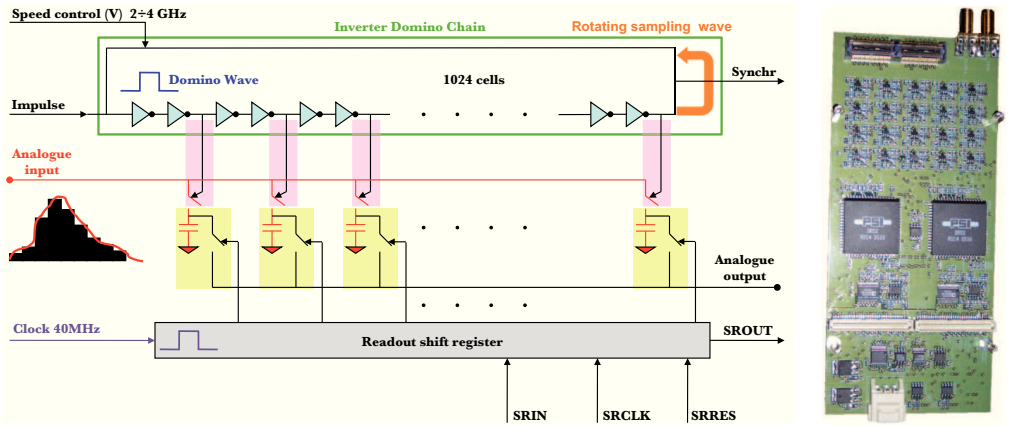

(a) The *DRS2* principle (b) *DRS2* card

Figure 4.17: *Left:* a sketch of the *DRS2* principle. The green line holds the ring of inverters that sequentially enable the array of capacitors by means of fast switches (pink area), when a pulse (*Domino wave*) is injected. The analogue signal (red line) is sampled by the capacitors (yellow rectangles) until a trigger occurs and stops the *Domino wave*. The stored charge is successively read out at 40 MHz using a shift register. *Right:* a photo of the mezzanine card that accommodates 2 *DRS2* chips (black squares in the centre). (Adapted from [15])

standard card mezzanines (Fig. 4.17(b)). Four mezzanines (80 channels) are plugged into a 9U *VME* general purpose board, called *PULSAR*[17]. The *PULSAR* board processes the readout sequence and builds a formatted data packet for the recording phase. Through an optical link, the data are transferred to a single computer for the recording on a storage system. The entire system is composed of a set of 14 *PULSARs*, connected in two *VME* crates [15].
Two additional *PULSARs* are utilized for special control tasks. One, named *DIGITAL*,

[17] More details about this board will be presented in chapter 6.

is programmed to measure the arrival time of the trigger command with the aim to synchronize the acquisition on the same event. The second, named *BUSY*, returns the control to stop the acceptance of further triggers, when the acquisition is still on going. As reported previously, *MIR* is also the slow control program of the readout system. Differently, the event building by merging data from different *PMTs*, the data integrity check, the calibration of the Domino chips response and the conversion to the raw data format are performed by another multi-thread C++ program, dubbed *DominoReadout* [124].

The advantage of this data acquisition system is the compactness, the low cost per channel and the low power consumption, keeping a sampling rate in the GHz domain. The main intrinsic disadvantages are the huge dead time of 512 μs due to the fact that all the 1024 cells must be read out every time, and both the residual charge effect and the leakage charge in the capacitors.

4.7 Calibration system

The calibration of the photosensors and the electronic chain is performed firing the camera with artificial light. A matrix of multi-colours LEDs is the core of the *MAGIC–I* calibration box, while in *MAGIC–II* there is a frequency tripled *Neodym YAG* microchip laser, which can be attenuated by a set of attenuation filters. The calibration light emission can be activated in special long runs, mainly used for technical reasons, or interleaved during data-taking for applying a precise scaling coefficient to the real events. Besides that, the calibration system can generate pulses to produce pedestal triggers, namely fictitious triggers to force the acquisition of empty events. This is an estimation of the baseline noise. During data-taking, the calibration system generates typically 25 Hz (calibration) plus 25 Hz (pedestal) of external triggers, so it is possible to keep under control most of the short-term time changes due to temperature, humidity and electronic fluctuations.

The *MAGIC–I* calibration box contains 64 powerful ($10^8 \div 10^{10}$ photons/sr) single quantum well[18] *LEDs*[19] programmable at three different wavelengths: 370 nm (UV), 460 nm (blue) and 520 nm (green) (Fig. 4.18(a)). The circuit, that activates at the most five *LEDs* in parallel, consists of two avalanche transistors discharging a small capacitance (33 pF) charged at 600 V. A very high current of around 10 A flows through the *LEDs*, discharging the capacitor in a short time. The emitted flash has a duration of about 3÷4 ns *FWHM*.
The *LEDs* are arranged in 16 slots, four containing the green ones, other four the UV ones and the rest blue *LEDs*. The slots are independently enabled via *GaAs* analogue switches controlled by a *CAN*[20] bus controller. Each module generates between roughly 10÷500 phe per pixel, depending on the colour and the number of *LEDs*. The standard flash, used in the interleaved runs, provides 35÷40 phe.

An interesting feature of the calibration system is provided by the capability to produce continuous light, which simulates the response of the *PMTs* to the light of the night sky, even with the presence of the moon.

The *MAGIC–II* calibration system is based on a frequency tripled passively *Q-Switched Nd-YAG* laser, installed at the centre of the dish. The emitted light flash

[18] It is a laser that uses the quantum well technology, so the efficiency is greater than that of standard laser, because the electrons that contribute to laser action are quantized.

[19] The *LED* models are *NISHIA NSPB300* and *NSHU590*.

[20] *CAN* is a message-based protocol widely used in automotive applications and in industrial automation.

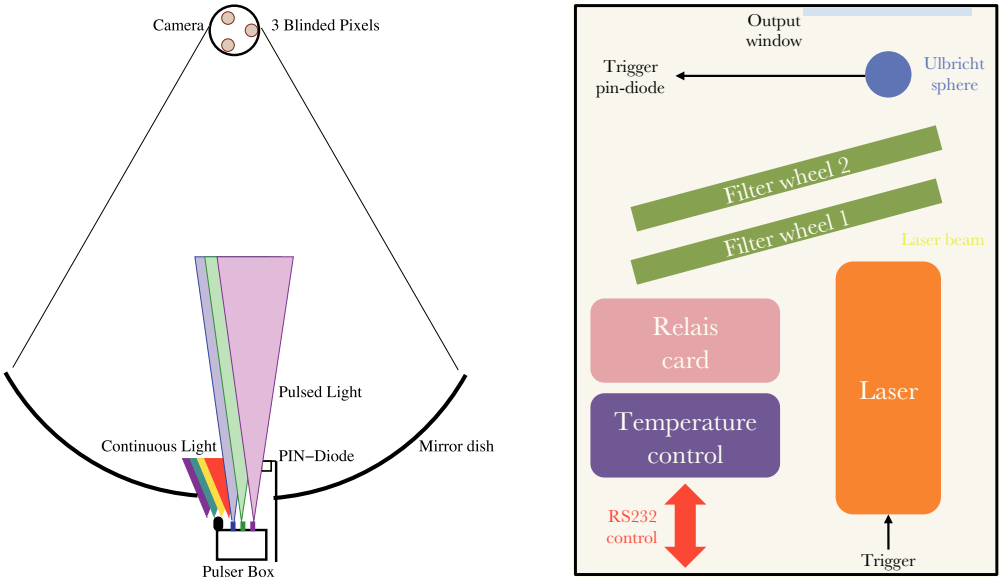

(a) *MAGIC–I* calibration system (b) *MAGIC–II* calibration box

Figure 4.18: *Left:* a sketch of the *MAGIC–I* calibration system. (From [63])
Right: a simplified scheme of the *MAGIC–II* calibration box mounted in the centre of the telescope dish.

has a wavelength of 355 nm and an intensity of 2 μJ, around 50.000 phe per pixel. Its duration is very short, around 700 ps *FWHM*. In front of the laser, there are two filter wheels with 10 attenuator glasses each, which allow up to a linearity calibration of 100 steps, from single to 1000 phe. The light emission homogeneity is then assured by taking advantage of an *Ulbricht* sphere with Si-diode (Fig. 4.18(b)).
The triggers for the calibration box are produced by a VME pulser board called *TCU* (*Trigger Calibration Unit*) located in the counting house. The transmission to the calibration box is split into four *RS232* links, managed by an optical multiplexer.

4.8 Central control and other subsystems

As previously described, the *MAGIC* telescopes are composed of different subsystems controlled by independent programs, which do not communicate with each other. A Central Control (*CC*) software has been developed to coordinate all of them, with a single convenient *GUI* interface, giving the full control over the telescopes to the operators. Hence, it is at the same time easy and quick to access the detector resources and monitor their status. Moreover, it forces the people on shift to operate the telescopes in an orderly manner and it contains automatic routines, which can be activated to check the correct configuration of the subsystems inside safety limits. For instance, when the humidity is too high or the light too strong, the camera automatically closes. The *CC* is written in *LabView 8.5*[21] and runs in a single computer under *Linux* operating system. A continuous polling at the frequency of 1 Hz keeps the *CC* updated on the status of the subsystems. The reports are written in *ASCII* format and are transmitted over Ethernet using the *TCP/IP* protocol.
Most of the subsystems are replicated in the telescopes, sometimes completely, other

[21] *LabVIEW* is a graphical programming environment.

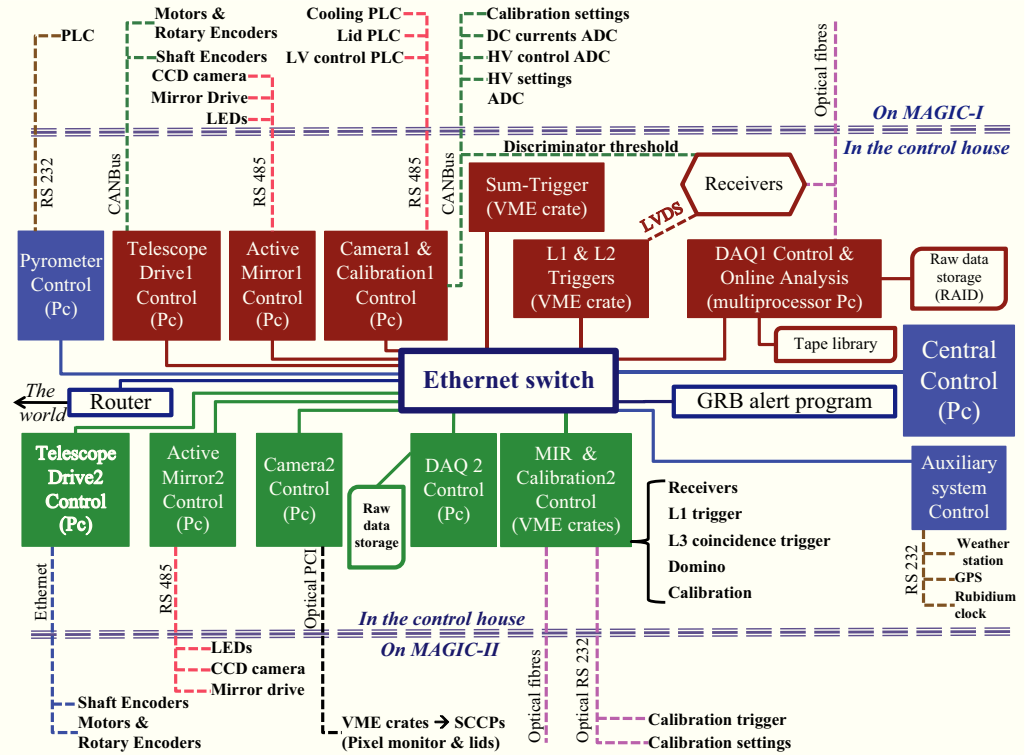

Figure 4.19: Flow diagram of the *MAGIC* telescopes Central Control program. (Adapted from [137])

times only in functionality (in which case the specific software is adapted). For the drive systems the programs are called *Cosy-1* and *Cosy-2*, for the active mirror control they are called *AMC-1* and *AMC-2*, for the camera they are *Guagua* and *Caco2* and for the readouts they are *MuxDaq* and *DominoReadout*. The calibration is included in *Guagua* in *MAGIC–I* or in *MIR* in *MAGIC–II*.
There are still few single subsystems that are common for both telescopes.

- **Pyrometer**: a system that measures the radiation, the temperature of the sky and the humidity, extrapolating the atmosphere conditions. This device is installed on the left side of the *MAGIC–I* dish and it is controlled via *RS-232* protocol.

- **Lidar**: a device that estimates the differential atmospheric absorption and scattering losses along the light path. It is composed of a pulsed (1 kHz) fast laser (source), a small optical telescope (photons concentrator) and a high quantum efficiency *HPD* (detector). The *Lidar* requests the telescope coordinates to the *CC*, then it moves in that direction, takes data and reports the atmospheric parameters back to the *CC*.

- **GRB alert**: this program monitors the *GCN* (*Gamma-ray burst Coordinates Network*) messages and reacts to any interesting *GRB* alert. The *CC* is immediately noticed and the telescopes could be repositioned using the fast drive movement.

- **Time stamp**: the time stamp for the readout is provided by two autonomous

clocks, which are continuously compared through a *NIM* module. One comes from a *GPS* receiver, the other from a rubidium atomic clock. The data transmission is sustained by a serial *RS232* connection.

- **Weather station**: it is a high quality steel *Reinhardt MWS 5MV* microprocessor with data logger. The data are sent via a serial connection and recorded onto a file shared with the *CC*.

4.9 The MAGIC upgrade

An upgrade is in progress[22] with the main aim to have both telescopes identical, with some renewed subsystems, simplifying the controls, the analysis chain and the maintenance. The plan contains four main topics:

- The upgrade, with the new chip *DRS4*, of the data acquisition systems in both telescopes.
- A new *LT1* system for *MAGIC–I* equal to *MAGIC–II*.
- Rearrangement and renovation of the electronic and computer rooms.
- A new camera for *MAGIC–I* equal to *MAGIC–II*.

The most important part of the upgrade involves the data sampler. The limitations of the *DRS2* chip will be eliminated by the new version *DRS4*. First, the dead time has been reduced of a factor 10, because it is possible to record only the region of interest (*ROI*) where the analogue pulse lies. Secondly, the new chip is quite linear and not strongly temperature dependent. Furthermore, the introduction of the differential technology makes it immune to common noise. The resulting chip is more stable, especially in terms of noise. Finally the bandwidth of the new mezzanine, which hosts 3 *DRS4*[23], has been increased to around $600 \div 700$ MHz.

A *LT1* system, with an enlarged area as in *MAGIC–II*, has been prepared. A single improvement has been done: the *LT1-backplane* routing has been redone paying attention to the signal integrity and has a lower skew. The result is a maximum skew of 360 ps with an *RMS* of only 67 ps.

The motivation to renew the electronic room is driven by the necessity to place the new electronics, based on the *DRS4*, in a temperature controlled and clean environment. The racks are kept closed and the internal temperature is stabilized by a powerful cooling system. The computers have been moved in a adjacent room, with another independent cooling system. The floor of the room has been covered by an antistatic paint to prevent the deposit of dust.
Moreover, the arrangement of the racks has been studied to both minimize the propagation time of the local triggers (see subsection 6.3.1 for more details) and to facilitate the access and maintenance to the electronics (Fig. 4.20).

The main design of the new camera is basically equal to that one mounted on *MAGIC–II*. Some mechanical changes are mandatory because the structures of the two telescopes are slightly different. In addition, even the entrance window has been refined, supporting the plexiglas in four isostatic floating pins. The electronics of the pulse injector system has been modified, improving the signal stability, fundamental to

[22] At the time of writing.
[23] Each *DRS4* handles up to 8 channels.

Figure 4.20: A temporal sequence of the renovation of the electronic room. (Images credit: J. L. Lemus)

perform reliable test during the day. The only parts completely redesigned are the low power boxes, metal containers that host the low power supply and its control for the whole camera. They will be changed in both telescopes.

5 The Sum-Trigger-II

ONE OF THE main goals of the new generation *IACT* telescopes, is to lower the energy threshold in the unknown, but promising, domain under 50 GeV. In 2007, *MAGIC* already succeeded in this sense, developing an innovative analogue trigger able to operate down to 25 GeV. For the first time, the *Pulsar Crab* nebula was detected in the gamma field, opening a new window to amazing physics. That system was designed as a prototype to demonstrate the feasibility of the technique, and no effort was applied in terms of reliability, stability and resilience. In this chapter, a professional new analogue trigger, which is an evolution of the old system, is presented. Obviously, a quick introduction is dedicated to the prototype *Sum-Trigger* as the starting point of the new project, called *Sum-Trigger-II*.

5.1 The original Sum-Trigger

Gamma-ray induced showers are strongly concealed by hadrons and *NSB* light. The current *IACT* telescopes take advantage of special trigger techniques to get rid of the dominant background processes. However, these techniques considerably reduced the rejection power and the efficiency of observation, lowering the event size. This has greatly limited the energy threshold, preventing new prospects in the observation of *Pulsars*, distant *AGNs* and *GRBs*.
As explained in chapter 3, the Čerenkov photon distribution of low energy events, in the camera plane, is complex and not easy to parametrize. The total amount of light is very poor and often not well concentrated in just a few neighbouring pixels. The technological solution, proposed by the *MAGIC* collaboration, tried to relax the topological constraints and, at the same time, to minimize the acceptable time gate.
In October 2007, a prototype *Sum-Trigger* was installed on *MAGIC–I*. It had a dedicated electronic path, independent of the standard trigger, allowing an easy integration and commissioning.

5.1.1 Sum-Trigger description

The basic principle of the analogue trigger was to add neighbouring pixels belonging to a small area (macrocell) and then apply a threshold to the final signal (Fig. 5.1). This changed the sequence present in the standard digital trigger, where first the individual channel is digitalized and subsequently the selection algorithm enters into play. In the

Sum-Trigger, even very small events, below the standard digital threshold, participated in the final decision.
This reversal approach favoured the contribution of all the pixels hit by the Čerenkov

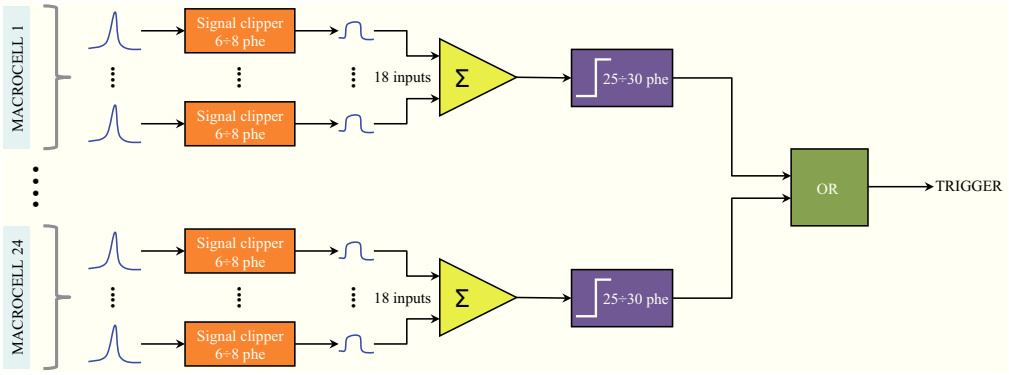

Figure 5.1: The principle of the original *Sum-Trigger* installed in *MAGIC–I* in 2007. 18 clipped channels from a macrocell are added and then digitalized. The camera is subdivided by 24 partially overlapped macrocells. The output trigger is the OR function of these macrocells. (© F. Dazzi)

light, even if they were not necessarily connected. In fact, inside a macrocell every distribution of photons was considered and processed. Furthermore, it increased the signal to noise ratio[1] and relaxed the strong topological constraint of the standard trigger to request, at the same time, a group of close compact pixels above threshold. To keep a low noise rate, even if any particular shape restriction was applied, the *Sum-Trigger* used a narrow effective coincidence time between pixels of around 3 ns, sufficiently small since the spread time of a low energy γ–ray event is below 3 ns. A pulse width of this dimension optimized the trigger efficiency and so the discriminator threshold could be pulled down without being dominated by Poissonian fluctuations of the *NSB*. Monte Carlo studies have revealed that the best summation threshold should stay in the range 25÷30 phe [111].

This idea is simple to apply, but it is affected by the intrinsic *PMT* spikes, called afterpulses. The main cause of afterpulses is an imperfect vacuum sealing of the tube. Residual molecules, staying between the cathode and the first diode, can be ionized by collision with electrons. Then, these ions are accelerated backwards by the electric field and when they strike the photocathode, additional electrons are generated. The result is a huge noise pulse, following the primary signal pulse (Fig. 5.2(a)).
As shown in figure 5.2(b), the afterpulses became relevant above $\sim$7 phe and still maintained a rate of some hundreds hertz above 25 phe. This prevented the use of the *Sum-Trigger* as a simple analogue sum of adjacent *PMTs*, for the detection of faint events that require a low threshold. The adopted solution was to clip every signal at the amplitude of 6÷8 phe, just before the summation stage. The signal cuts did not affect the gamma events, but rejected the afterpulses (Fig. 5.3).

Several trigger configurations and different overlapping regions were simulated to obtain the largest collection area and the lowest trigger threshold. The final layout covered a ring between 0.26°÷0.86° in the camera, for a total of 216 pixels (Fig. 5.4(a)). This was a compromise between a simplified electronic design and the maximized distribution of Čerenkov photons between 20 and 30 GeV, which is of the order of 80% in this

[1]This means that the linear sum of correlated signals is always higher than the sum of uncorrelated Gaussian noise sources, if the *RMS* noise value does not exceed the signal amplitude.

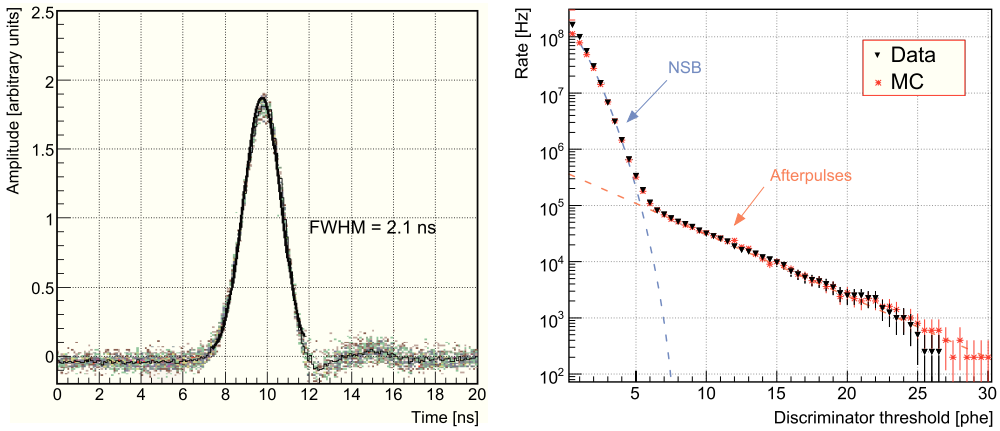

(a) The *PMT* afterpulse signal (b) The *PMT NSB* and afterpulse count rate

Figure 5.2: *Left:* a record of the *PMT* afterpulse signal shape at the input of the *Sum-Trigger*. It is a narrow signal of ~ 2 ns. (Courtesy of M. Shayduk)
Right: the count rate above a discriminator threshold for a single *PMT* exposed to *NSB* (black points). The red crosses denoted the simulation with a *NSB* level of 0.18 phe/ns. The afterpulse trend matches with an exponential threshold spectrum, which extends beyond the *NSB* curve. (Adapted from [112] and [65])

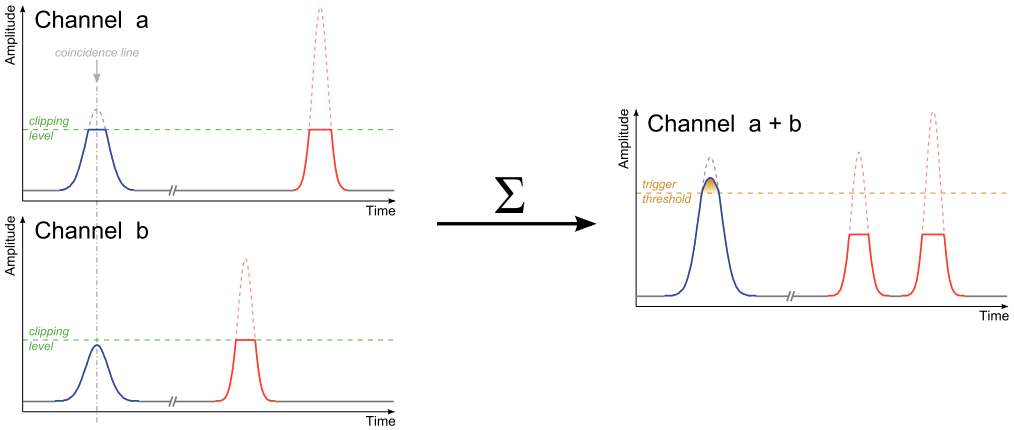

Figure 5.3: A scheme of the clipping principle. The blue signals come from Čerenkov events, while the red ones are *PMT* afterpulses. Dashed curves represent the continuation of the pulse, if the clipping is not applied (green line). The blue pulses are synchronous and their addition exceeds the discrimination threshold (brown line). The red pulses are not correlated in time, and after the clipping they do not activate the trigger. (From [65])

region. The overlap required each *PMT* to lie inside two different macrocells. Hence, every macrocell of 18 pixels was divided in 3 sub-macrocells of 6 elements (Fig. 5.4(b)), which were shared with another macrocell.

The electronic system, as shown in figure 5.1 with different colours, was divided in four main stages.

❶ Clip stage (orange). There were 27 Clip-boards with eight input channels each.

❷ Sum stage (yellow). This stage was divided into two different kind of boards. There were 36 boards to add signals inside every sub-macrocell, providing three

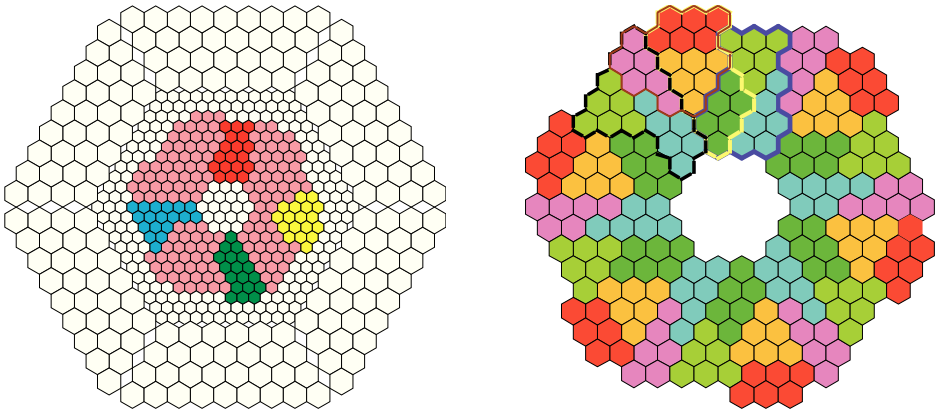

(a) The Sum-Trigger area & macrocells (b) The sub-macrocells

Figure 5.4: *Left:* the *Sum-Trigger* area (salmon) and the macrocell shapes (other colours). *Right:* the sub-macrocells are displayed. Each macrocell consists of 3 sub-macrocells with 6 *PMTs* each. One macrocell is underlined with a thick blue line, another with a thick yellow line and finally other two with thin black and brown lines. (Adapted from [111])

output copies for the macrocells' overlap. Then, in other 24 boards, the results of three sub-macrocells were piled up.

❸ Discriminator stage (violet). The same boards that hosted the second sum stage, managed this function. Once the signals belonging to a macrocell were added, a programmable discriminator threshold was applied.

❹ OR stage (green). There was a single board to generate the final trigger from the OR of 24 discriminator stage outputs.

5.1.2 Sum-Trigger advantages and limitations

The aim of the *Sum-Trigger* was to lower the energy threshold, recording events in the domain under 50 GeV, where the standard digital trigger was not so efficient. The *Sum-Trigger* was built with a meticulous fine tuning, while the standard trigger, to this day, is configured in a conservative way. The most evident discrepancies between the sum and digital trigger were the effective coincidence gates, respectively $\sim$3ns and $\sim$6ns, and the trigger rates, $\sim$250 Hz and $\sim$800 Hz. The trigger rate is inversely proportional to the trigger threshold, which was so low for the *Sum-Trigger* that about 50% of the recorded events were *NSB*.
In figure 5.5(a), it is possible to compare the trigger threshold, as the energy distribution peak of a γ–ray source with a spectral index of -2.6, for both systems. The energy threshold went down by about a factor of two, while the rate was boosted by 50%. The higher sensitivity at low energies is shown in the plot 5.5(b). This is not the case for energies above 200 GeV, where the wider area of the digital trigger dominates.

The *Sum-Trigger* manifested excellent performance, although it was a prototype with many limitations. Following a list of drawbacks is reported.

✠ The trigger area was small and did not allow the telescope to be run in wobble mode[2]. This doubled the data-taking duration, because the time slot was shared

[2]In this data-taking mode, the signal and the background are recorded at the same time, moving the pointing direction at two sky positions 0.4° far from the source, every 20 minutes.

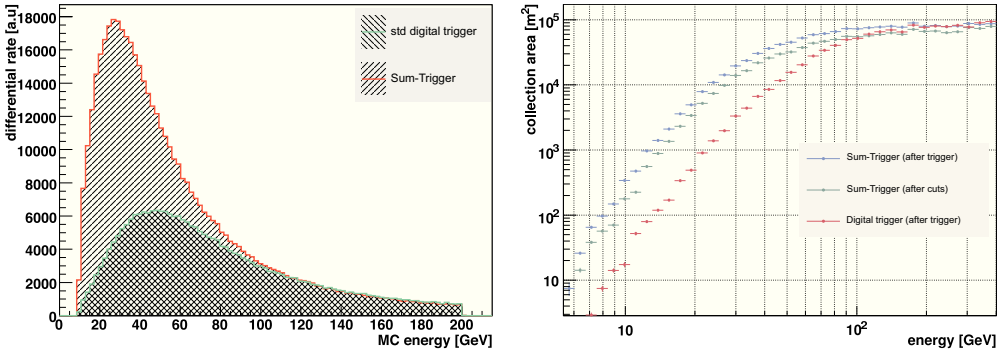

(a) Differential rate comparison (b) Collection area comparison

Figure 5.5: *Left:* the differential rate for simulated γ–rays with a power law spectral index of -2.6, using the standard digital trigger and the *Sum-Trigger*, both in mono configuration. The peaks of the distributions represent the energy thresholds, 55 GeV for the digital trigger and 25 GeV for the analogue one. *Right:* the collection area for the two systems. (From [111])

out between the ON (source) and OFF (background). Moreover, a wider trigger region increases the collection area.

- The channel delays adjustment was made by hand, adding cables with different lengths. This method was very time-consuming and not so precise. The adjustment resolution was determined by the minimum cable step of 0.5 ns. The process was done once at the beginning of the system set-up and never repeated due to the cable-routing complexity. This caused a continuous and unavoidable decline of the signals' synchronization.

- The signals' amplitude equalization was performed manually using the oscilloscope. It was a time-consuming and inaccurate measurement, renewed very rarely, about once per year.

- The lack of an automatic and fast amplitude equalization, made it impossible to perform independently both the pixels charge flat-fielding and the *PMTs* replacement. The operation was authorized only just before the *Sum-Trigger* annual maintenance.

- The system layout is very far from being compact and the accessibility to the boards is problematic.

The system operated very well for a couple of years, showing the feasibility of this innovative idea for a single telescope configuration. The defects described above have compromised a long and extensive deployment of the instrument, but have opened a lot of room for further improvements.

5.1.3 Physics discoveries

The *Sum-Trigger* was employed to detect *Pulsars* and to monitor distant *AGNs*, such as for instance the BL Lac object *PG 1553+113*. However, the analysis chain was only optimized for *Pulsar* studies, so the main discovery has been related to the *Crab Pulsar* [36]. A good data set was collected between October 2007 and February 2008 for a total

amount of 22.3 hours. The achieved low energy threshold enabled an interesting comparison with data measured by satellite detectors, leading to elaborate and interesting discussions on the best theoretical scenario. As explained in 1.4.2, the spectrum cut-off changes depending on which model of *Pulsar* emission is taken into consideration. The *Polar cap* predicts a super-exponential cut-off around some GeV, while the *Outer gap* foresees an exponential cut-off at higher energies. Therefore, detection of γ–rays above 10 GeV would allow one to discriminate between different *Pulsar* emission mechanisms. The detection of the pulsed signal from *Crab Pulsar* has demonstrated that the spectrum extends into the GeV domain, favouring γ–ray production far away from the neutron star surface, as in the *Outer gap* model [35]. A joint fit is performed on the *MAGIC* and *EGRET* data with the following generalized function:

$$f(E) = AE^{-a} \cdot exp\left[-\left(\frac{E}{E_0}\right)^{\beta}\right] \tag{5.1}$$

where A is a normalized constant, E_0 is the cut-off energy, and β measures the steepness of the cut-off. Figure 5.6(b) shows all three fitted functions for $\beta = 1$ (red line), $\beta = 2$ (blue line), and the best fit, $\beta = 1.3$ (green line). In figure 5.6(a), the associated

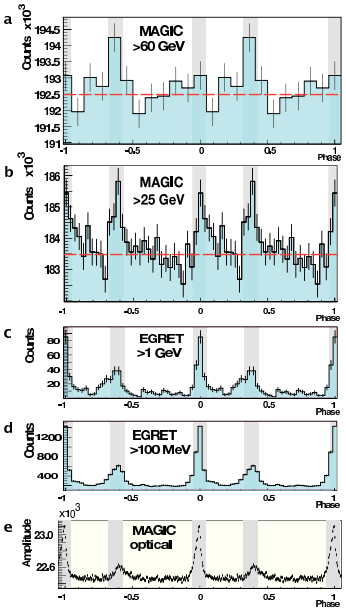

(a) The earliest *Crab* pulsed emission in different energy bands

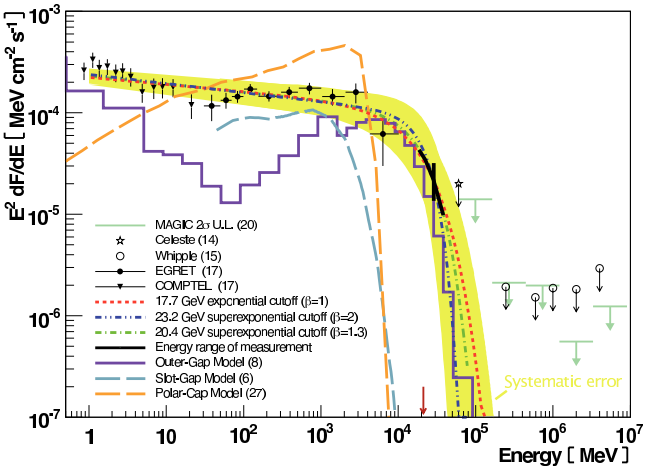

(b) The pristine *Crab Pulsar* spectrum

Figure 5.6: *Left:* the shaded areas show the signal regions for *P1* and *P2*. They are in phase for all shown energies and the ratio of *P2*/*P1* increases with energy from (d) to (a). *Right:* the *Crab Pulsar* spectrum. The solid circles and triangles represent flux measurements from *EGRET*, while the arrows on the right denote upper limits from various previous experiments. The black line indicates the energy range, the flux and the statistical error of *MAGIC* measurement. The yellow band illustrates the joint systematic error of all three solutions. (From [35])

pulse phase diagram shows the pulsed signal in 11 bins for γ–ray events above 25 GeV and the counterparts in the *HE* and optical range. The optical emission was measured simultaneously by *MAGIC* in winter 2007–2008, using its central pixel. The overall

obtained significance was $6.4\,\sigma$, with 8500 ± 1330 events. The main pulse (*P1*), at phase zero, had a significance of $4.3\,\sigma$, while the inter-pulse (*P2*), at phase around 0.4, had a significance of $7.4\,\sigma$.

Data taken in the winter 2008–2009, which did not manifest a significant yearly variability, were combined with data from the previous year and compared with the energy spectra measured by the *Fermi-LAT* instrument [29]. The results revealed that the spectrum is not compatible with an exponential cut-off, but its trend followed a power law [39]. Considering the event excesses in both *P1* and *P2* (Fig. 5.7(a)), the function which best describes data is a power law:

$$f(E) = F_{30} \left(\frac{E}{30\,GeV} \right)^{-\Gamma} \tag{5.2}$$

where the best parameters are $\mathrm{F}_{30} = (14.9 \pm 2.9\,\mathrm{stat} \pm 9.6\,\mathrm{syst}) \times 10^{-9}\,\mathrm{cm}^{-2}\,\mathrm{s}^{-1}\,\mathrm{TeV}^{-1}$ and $\Gamma = 3.4 \pm 0.5\,\mathrm{stat} \pm 0.3\,\mathrm{syst}$. This fit was inconsistent with any standard pulsar model.

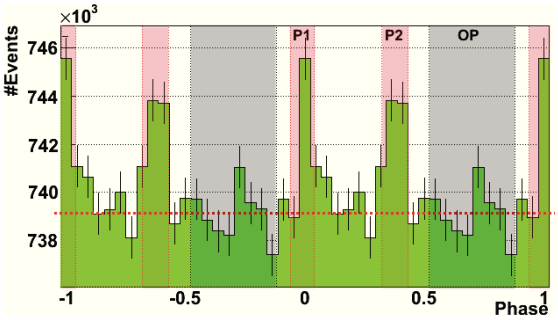

(a) The *Crab* pulsed emission adding data of winter 2008–2009

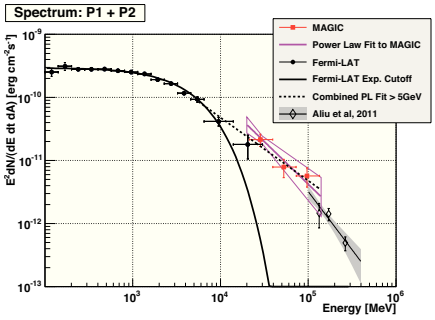

(b) The new computed *Crab Pulsar* spectrum

Figure 5.7: *Left:* the pulse profile of the *Crab Pulsar* adding the new data set of winter 2008–2009. The red shaded area indicates the signal phases *P1* and *P2*, while the black shaded area indicates the background control phases. *Right:* the energy spectra *P1* + *P2*. The black solid line and dots are obtained from the public *Fermi-LAT* data, while red points denote the *MAGIC* measurements. The pink line and a butterfly shape indicate the power law fit to the *MAGIC* data and its statistical uncertainty. The gray shade with a black line and open diamonds show the *VERITAS* measurements. The dotted line is the combined fit above 5 GeV. (From [39])

The recent announcement of signal from the *Crab Pulsar* above 100 GeV [43], by the *VERITAS* collaboration, has consolidated the *MAGIC* position in favour of a spectrum described by a broken power law with γ–ray production more than ten stellar radii away from the neutron star. The extended fit in figure 5.7(b), seems to be in agreement with the new *VERITAS* data. Nevertheless, it is important to verify this assumption by an in-depth study in the overall *VHE* domain or eventually foresee the presence of another component above 100 GeV, as announced by *MAGIC* in a recent publication [38]. For this reason, a higher sensitivity is essential, as well as a wide dynamic range and a low energy threshold, all of which could be provided by a stereoscopic analogue trigger system.

Thank to these promising outcomes, which stimulate new investigations, it has been decided to upgrade the original *Sum-Trigger*, including a new one for the *MAGIC–II* telescope.

5.2 The Sum-Trigger-II system

Several reasons urged the *MAGIC* collaboration to develop a revised stereoscopic *Sum-Trigger*. The first was the poor reliability and difficulty to adjust the original *Sum-Trigger* which necessitated both a complex manual tuning and constant maintenance. An improved automatic computer control[3] is essential to calibrate the system and precisely adjust its settings. Another reason was the desire to improve the telescopes' performance at very low energies, where *Pulsars*, distant *AGNs* and *GRBs* can provide fundamental information relating to extreme acceleration mechanisms and exotic physics. A more precise signal synchronization and a higher bandwidth favour a better topological and temporal selection of faint events. Last, but no less important, a larger trigger area similar to the standard trigger was considered to be essential.
The project of the new *Sum-Trigger-II*, at the same time, tries to sort out the weak points of the old system and to improve its functioning, in order to ensure new useful results.

5.2.1 Sum-Trigger-II simulation

At the beginning, different designs were taken into account in order to find the best compromise between performance, costs, complexity and easy integration into the pre-existing electronic chain. The decision is based on the comparison of the energy distribution for different numbers and layout of the macrocells in the camera. The choice of the most reasonable arrangements is forced by the request to cover, as much as possible, the same area as the standard digital trigger, which imposes the cabling that can be put in place.
The preference for the single macrocell dimension is dictated by Monte Carlo studies, which demonstrate that about 20 pixels are optimal in the energy range of $10 \div 30$ GeV [111]. In fact, involving few pixels increases the probability of losing part of the faint Čerenkov flash, while conversely a larger macrocell might be dominated by accidental triggers. The hexagonal shape is the preferred one, because it guarantees both a symmetrical overlap and a central symmetry. In most of the simulated configurations, the macrocell is defined as a hexagon of 19 pixels.

Five possible macrocell mappings have been analysed with the *MAGIC* standard simulation program (*CameraSim*) (Table 5.1). The first mapping (Fig. 5.8(a)) is the

Name	Nr. macrocells	Nr. pixels in macrocell	Macrocell shape
Sum_mapping_V1	37	19	Hexagon
Sum_mapping_V2	47	19 (18;17)	Hexagon
Sum_mapping_V3	46	19	Hexagon + (*)
Sum_mapping_V4	55	19 (15)	Hexagon
Sum_mapping_V5	51	19 (18;17;15)	Hexagon

Table 5.1: The main properties of the studied trigger configurations for the *Sum-Trigger-II*. The first column indicates the configuration's name, the second the total number of macrocells that compose the mapping and the third one shows the number of pixels inside a macrocell. Sometimes the number could be lower (in brackets), if the macrocell exceeds the standard trigger layout.
(*): it is an irregular polygon, designed to obtain a complete overlap.

[3] In the *Sum-Trigger* software control, dubbed *Sumo*, the signal calibration was missing.

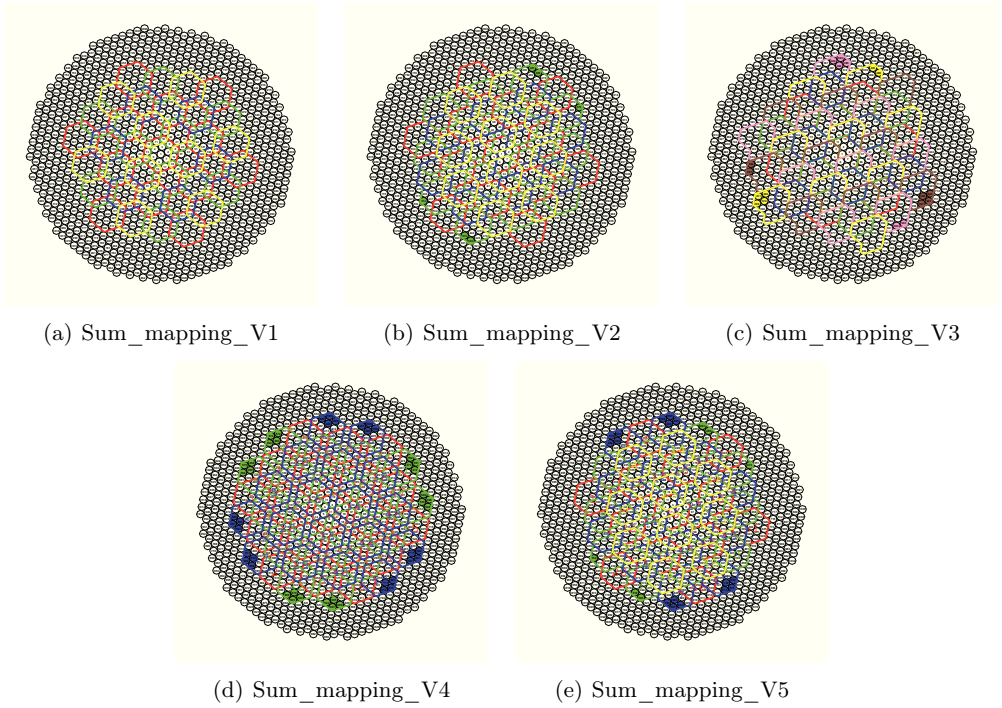

(a) Sum_mapping_V1 (b) Sum_mapping_V2 (c) Sum_mapping_V3

(d) Sum_mapping_V4 (e) Sum_mapping_V5

Figure 5.8: The five simulated mapping configurations. The full coloured pixels are outside the standard digital trigger area and cannot be routed in the *Sum-Trigger-II*. (© F. Dazzi)

simplest layout, with only 37 macrocells. It shows a nice circular symmetry, but the overlap is very poor (Fig. 5.9(a)), limited to one pixel. The second mapping (Fig. 5.8(b)) increases the number of macrocells to 47, in order to improve the common regions (Fig. 5.9(b)). The macrocells' arrangement follows the digital trigger numbering path, resulting in a global shape, which is a little bit asymmetric. The fifth version (Fig. 5.8(e)) is simply an upgrade of the previous one, where four macrocells are added on the top and bottom side with the aim to obtain a more circular shape and a homogeneous overlap of the trigger area (Fig. 5.9(e)). The main source of inspiration for the third layout (Fig. 5.8(c)) is to have a complete and equally distributed overlap (Fig. 5.9(c)). The unavoidable drawback is the resulting odd shape, consequent to the irregular polygon used in addition to the hexagon. Finally, the fourth mapping (Fig. 5.8(d)) tries to cover the digital trigger area with a precise circular symmetry. The final shape provides a good and regular overlap (Fig. 5.9(d)), but it needs the highest number of macrocells: 55.

The first simulated parameter is the number of triggered gamma events as a function of the energy (Fig. 5.10(a)). All layouts offer very similar detection capabilities within $\sim 1\%$, and a very close distribution peak (trigger threshold), in the interval $20 \div 25$ GeV. However, the Sum_mapping_V2 (consequently Sum_mapping_V5 too) and the Sum_mapping_V4 are slightly better, especially in terms of energy threshold, which is lowered to 20 GeV.

The second study verifies the trigger efficiency with a fixed standard clipping of 6 phe and a variable final sum threshold between 25 and 29 phe (Fig. 5.10(b)). Even in this case, the difference is minimal, but again always a little bit in favour of the second and fourth version.

The last investigation treats the spatial trigger response homogeneity. The centre of

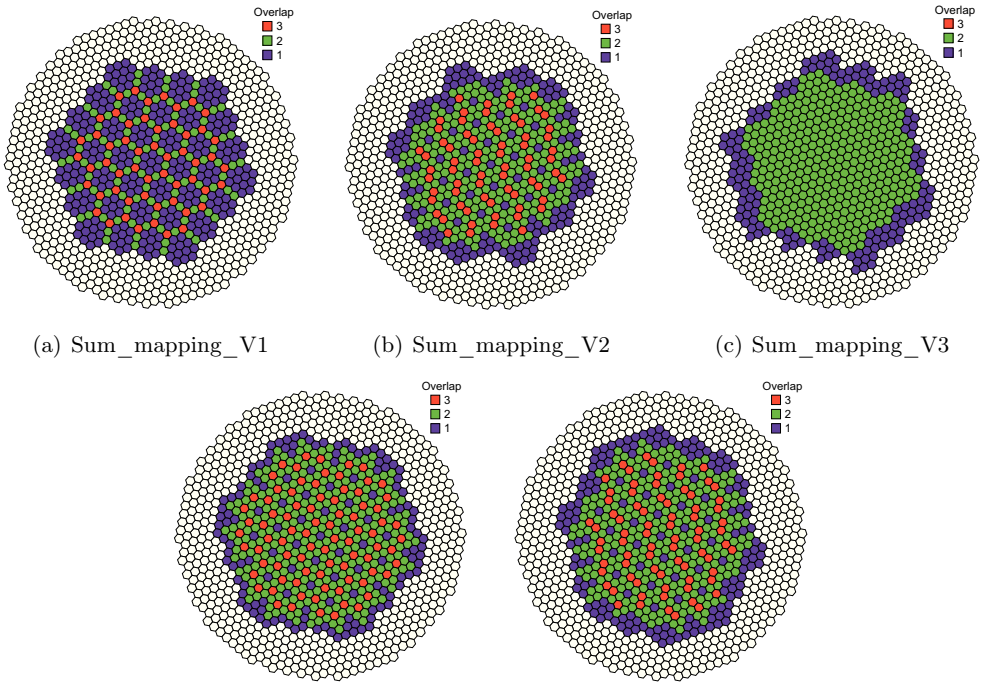

(a) Sum_mapping_V1 (b) Sum_mapping_V2 (c) Sum_mapping_V3

(d) Sum_mapping_V4 (e) Sum_mapping_V5

Figure 5.9: The overlap of the five simulated mapping configurations. The colours show the overlap size between macrocells. (Images credit: M. Lopez & J. L. Lemus)

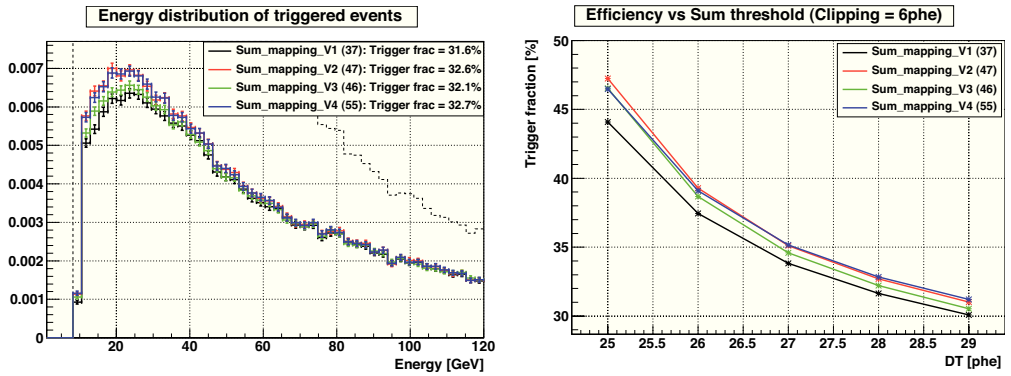

(a) Energy distribution vs mappings (b) Trigger efficiency vs threshold

Figure 5.10: *Left:* the energy distribution for gamma events using different macrocell layouts. The peak of the curve corresponds to the energy threshold. The electronic parameters are 6 phe for the clipping level and 27 phe for the final threshold. *Right:* the trigger efficiency as a function of the final applied sum threshold in the range 25÷29 phe. The clipping level is fixed at the standard value of 6 phe. (Images credit: M. Lopez).

gravity (CoG) distributions of the triggered events are outlined in figure 5.11. Obviously, a circular mapping assures a rotational symmetry, which is the best geometry for the wobble data-taking and from the analysis point of view.

The best solution seems to be the *Sum_ mapping_ V4*, having the highest number of macrocells. However, the mechanical layout and the electronic scheme do not change

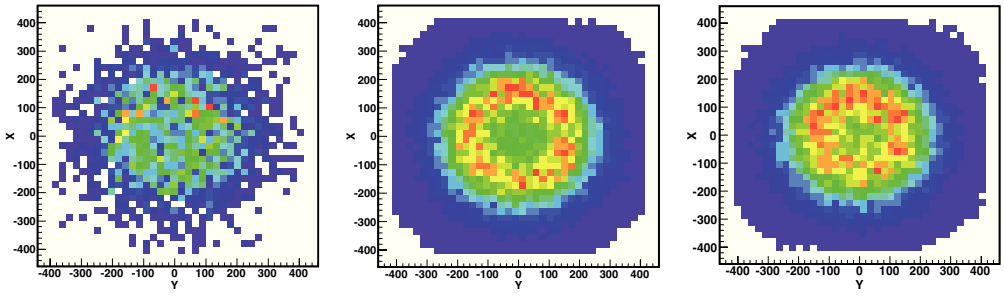

(a) *CoG* mono, size < 40 (b) *CoG* mono, size < 200 (c) *CoG* stereo, size < 200

Figure 5.11: *Left:* the simulation of the mono *CoG* using the *Sum_ mapping_ V4* and applying a size cut at 40 phe. *Centre:* the same plot as before, but with a cut in size of 200 phe. *Right:* the stereo *CoG* with again a cut at 200 phe. (Images credit: T. Schweizer & E. Prandini).

significantly up to 57 macrocells, thanks to the introduced modular design. It could be argued that the *Sum_ mapping_ V1* is composed of 33% less macrocells (37 vs 55) and offers similar performance, thus reducing the production time, the routing complexity and the cost of the components. However, the limited overlap makes it too sensitive to the dead pixels. For these reasons, *Sum_ mapping_ V4* was selected for the final design.

In the *Sum_ mapping_ V4*, each macrocell is surrounded by six other macrocells, equally disposed every 60°. It can be divided in three layers, two out of three with the same shape, but a different rotation (Fig. 5.12). It is comprised of 529 channels, which become 997 after the splitting due to the macrocells' partial overlap. Some parameters of the selected mapping are reported in table 5.2.

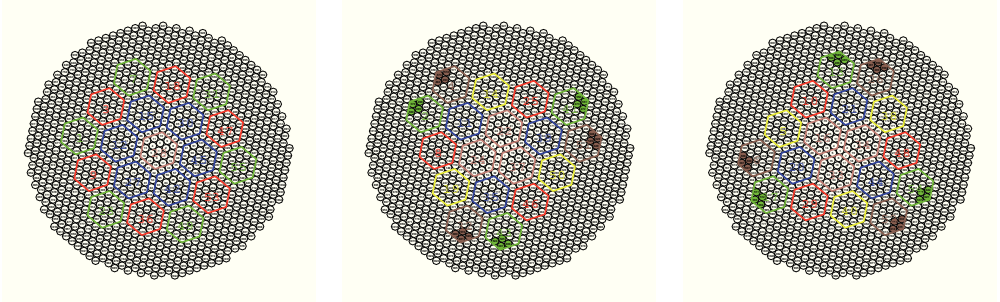

(a) Layer 1 (b) Layer 2 (c) Layer 3

Figure 5.12: The three layers of the *Sum_ mapping_ V4*. The layers number 2 and 3 present the same arrangement, but a different orientation. The full coloured pixels are outside the standard digital trigger area and cannot be connected. (© F. Dazzi)

It is fundamental to compare the performance of the new Sum-Trigger-II versus the old one. In order to find the best configuration for the selected mapping, the *NSB* influence has been analysed by scanning a high number of setting combinations. The program used is called *CameraSim*[4], which simulates the reflector, the photosensors and the electronic chain of the telescopes.
The accepted accidental rate was fixed at 400 Hz, because the global mono trigger rate,

[4]The software has been mainly developed by M. Lopez.

***Sum_mapping_V4* parameters**	
Total pixels	529
Blind pixels	48
Total pixels after the split stage	997
LT1 pixels not covered	30

Table 5.2: Some important parameters of the selected configuration *Sum_ mapping_ V4*.

including the cosmic ray contribution, will be around 800÷900 Hz, a little bit less than the *DAQ* saturation limit. As for the old system, the best clipping level and the sum threshold still remain confined around respectively 6 phe and 27 phe.
Subsequently, a gamma source with spectral index -2.6 has been simulated at low energies and the events have been processed by *CameraSim*, configured with the new extrapolated threshold. For the time being, the clipping level is left as a tunable parameter. Finally, the energy distribution of triggered events (Fig. 5.13(a) & Fig. 5.13(c)) and the collection area (Fig. 5.13(b) & Fig. 5.13(d)) are computed for the old and the new *Sum-Trigger-II*.
Considering, for instance, the green curves (clipping at 6 phe), the energy threshold

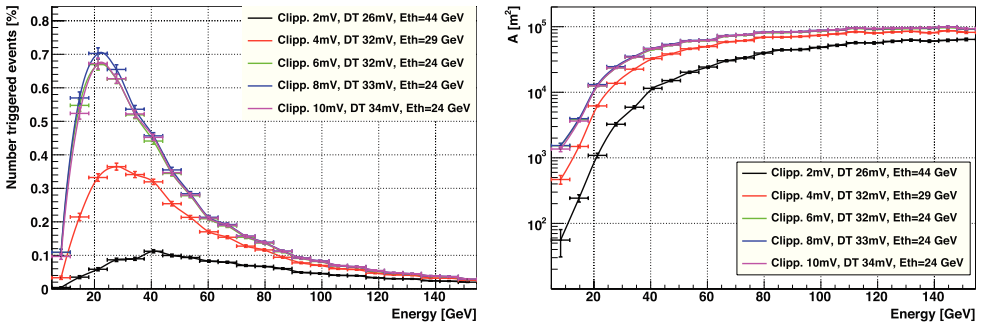

(a) Energy distribution *Sum-Trigger*

(b) Collection area *Sum-Trigger*

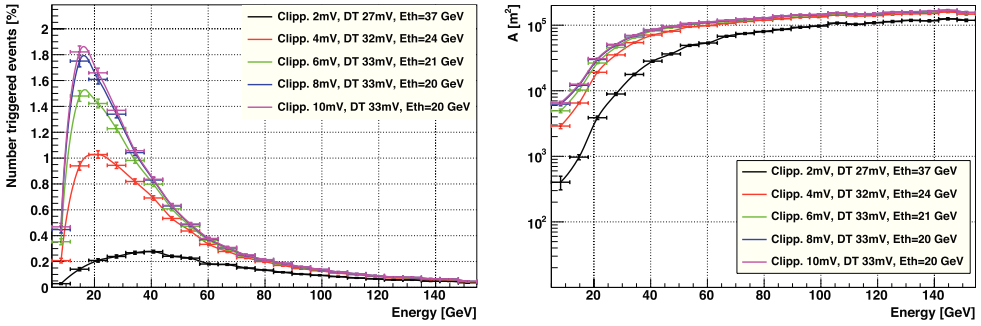

(c) Energy distribution *Sum-Trigger-II*

(d) Collection area *Sum-Trigger-II*

Figure 5.13: *Top left:* the simulated differential rate of the old *Sum-Trigger* for a γ–ray source with a power law spectral index of -2.6. The peak of the distribution represents the energy thresholds: $\sim$25 GeV. This plot is a repetition of figure 5.5(a), but obtained with the new program *CameraSim*. *Top right:* the collection area with the same conditions of the adjacent figure. *Bottom left:* the differential rate of the new *Sum-Trigger-II*. The energy threshold is around 20 GeV. *Bottom right:* the collection area of the new analogue trigger. (Images credit: M. Lopez).

is lowered by 20%, that is from 25 GeV to 20 GeV. The fraction of triggered events is

more than doubled, especially in the range 10÷40 GeV. Moreover, the collection area shows promising results too. At 20 GeV it is doubled from $\sim 12000\,\mathrm{m}^2$ to $\sim 25000\,\mathrm{m}^2$. It is very interesting to see that the collection area still continues to be more efficient at standard energies, above 100 GeV.
In stereoscopic data-taking mode, the performance of the new *Sum-Trigger-II* seems even better. In figures 5.14(a) and 5.14(b), the energy distribution and the collection area for the stereo mode are shown. Assuming an analogue pulse width of 3 ns, a

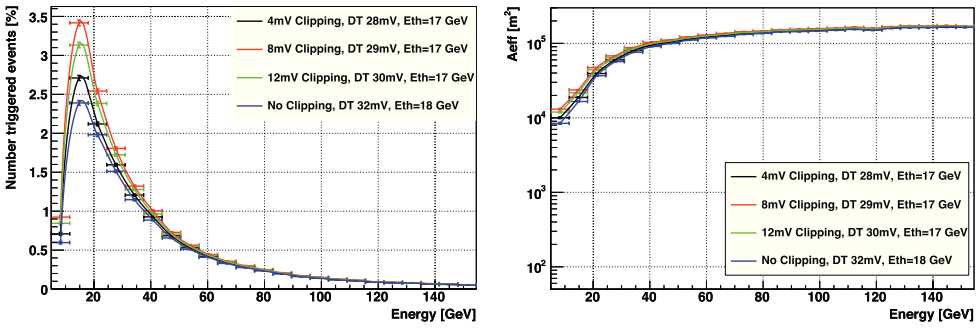

(a) Energy distribution *Sum-Trigger-II* stereo (b) Collection area *Sum-Trigger-II* stereo

Figure 5.14: *Left:* the simulated differential rate of the stereo *Sum-Trigger-II* for a γ–ray source with a power law spectral index of -2.6. The peak of the distribution represents the energy thresholds: ~ 17 GeV. *Right:* the collection area with the same conditions as in the adjacent figure. (Images credit: M. Lopez).

stereoscopic trigger gate of 70 ns and an accidental rate of 50 Hz, the results are quite impressive. The energy threshold is lowered to ~ 17 GeV and the number of trigger events is increased by 25% in respect of the mono data-taking. Finally, the collection area becomes more than three times larger than the prototype system, namely $\sim 40000\,\mathrm{m}^2$ at 20 GeV.

The conclusion is that the extended *Sum-mapping_ V4* layout, composed of overlapping hexagonal macrocells, ensures a slightly lower energy threshold and in addition a much higher number of triggered events. This means that the time required to detect a source will be considerably reduced.

5.2.2 System overview and subsystem description

The main concept of the *Sum-Trigger-II* project is identical to the previous version. The flow chart is reported in figure 5.15. The signals (green pulses) are originated in the camera, which is divided into 55 partially overlapping macrocells of 19 *PMTs*. The analogue pulses are first synchronized and equalized in amplitude, then are clipped to reject the *PMT* afterpulse noise. This is done in the boards dubbed *Clip-boards* (pale-orange). Later on, the pulses belonging to a macrocell are added and compared with a programmable threshold, as in the original system. These functions are performed in the boards called *Sum-boards* (orange). The part relevant for the control, processing and interface has been completely redesigned and exhibited in blue. The main board is called *Astro-board*, which receives the discriminator's output and splits it in three paths. One goes to the global OR trigger, another to the single macrocell counting unit and the last one to a D flip-flop to verify the pulse arrival times with respect to the reference signal. Finally, the data are downloaded and analysed by a dedicated computer, which then uploads the proper parameters.

The implementation of the programmable analogue delay lines and attenuators in the

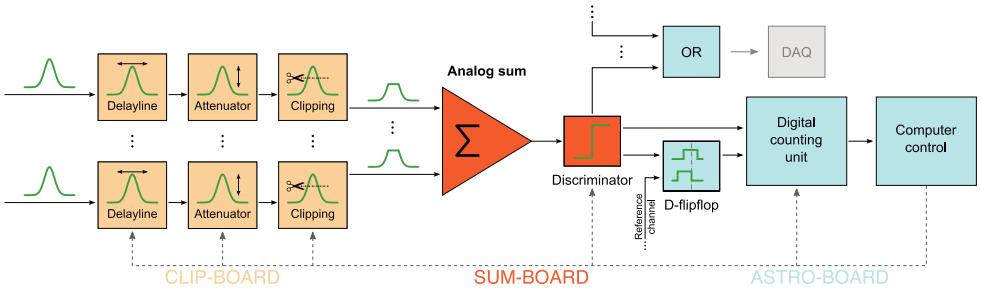

Figure 5.15: The principle of the new *Sum-Trigger-II*. (© D. Häfner & F. Dazzi)

Clip-board is completely innovative. Another important upgrade is made in the control and processing stage, which is more powerful and automated.

The system is very compact and based on modular boards, which can be easily exchanged and swapped. It fits in an 18-crate unit, where the top side is assigned to the 18 *Clip-boards* and the *Astro-board*. The bottom is designated to the 19 *Sum-boards* (Fig. 5.16(a)).

The fast analogue pulses come from the receiver boards, where dedicated mezzanines (*Sum-mezzanine*) are plugged to interface with the *Sum-trigger-II* system. The signals travel for 5 m, before reaching the *Clip-boards*. Here, they are synchronized using programmable analogue delay lines, equalized in amplitude using programmable attenuators and clipped using amplifiers with programmable clamp thresholds. Finally, each signal is split three times to ensure the required overlap between different macrocells (top left in figure 5.16(b)).

Afterwards, each signal must be connected to the assigned macrocells, through a com-

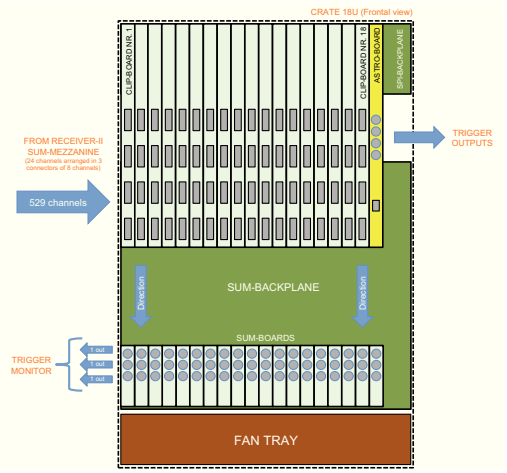

(a) Crate frontal view

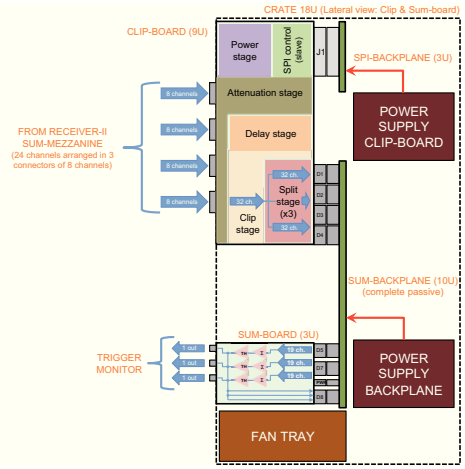

(b) Crate lateral view

Figure 5.16: *Left:* the frontal view of the *Sum-Trigger-II* crate. In the upper part, the 18 *Clip-boards* and the *Astro-board* (yellow) are shown. In the lower side, there are the 19 *Sum-boards*. *Right:* the lateral view of the crate. In this sketch, the connection between the *Clip-boards* and the *Sum-boards* through the *Sum-backplane* is emphasized. (© F. Dazzi)

plete passive backplane, so-called *Sum-backplane*, which works as an interface between the *Clip-boards* and the *Sum-boards*. Here, the analogue summation of 19 pixels is gen-

erated (on the bottom of figure 5.16(b)) and compared to a programmable threshold. When exceeded, a trigger is sent to the *Astro-board* for the global *OR* (Fig. 5.17(b)). Each *Sum-board* manages three macrocells.

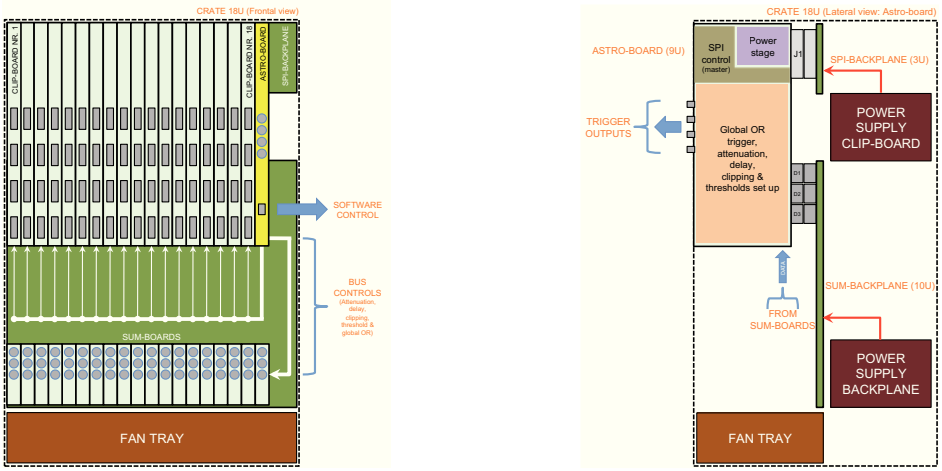

(a) Crate frontal view: the *SPI* & parallel buses

(b) Crate lateral view: *Astro-board*

Figure 5.17: *Left:* the frontal view of the bus for the control of the *Clip-boards* and *Sum-boards* parameters. *Right:* the lateral section of the *Astro-board*, located in the top right side of the crate. This board, with the assistance of the software control, prepares and sends the configuration data through the *SPI-backplane* and the *Sum-backplane*. (© F. Dazzi)

All the programmable parameters, such as delays, attenuations, thresholds, macrocell trigger counters and global trigger *OR* are in the charge of the *Astro-board* and a dedicated computer.
Commercially available *ADCs*[5] and *TDCs*[6] are the optimal solution for measuring the signals' amplitude and their arrival time, but the global cost for the implementation is prohibitive. The alternative simple solution, adopted in the *Astro-board*, is based on the coincidence rate of the signal under test and a reference one[7]. This approach requires a quite long iterative procedure, but it can be done with a basic circuitry, disposed in a compact area.

The *Astro-board* and the *Sum-boards* communicate by means of a parallel bus in the *Sum-backplane*, while the data transmission with the *Clip-boards* passes through the *SPI-backplane*[8] (Fig. 5.17(a)).

5.2.2.1 Mechanics layout

The electronic system is accommodated in a *Schroff* composite crate of the *EuropacPRO* series. Every metal piece and all the additional attachments are designed for a complete shielding against electromagnetic noise and to avoid electrostatic discharges. Furthermore, even the shielding to the front of the crate is achieved by electromagnetic-

[5] *ADC* (*Analogue to Digital Converter*) is a device that converts a continuous voltage to a discrete time digital representation.

[6] *TDC* (*Time to Digital Converter*) is a device which calculates the arrival time of an incoming pulse, returning its value in a digital form.

[7] The reference signal is simply a channel in the trigger area.

[8] The *SPI* (*Serial Peripheral Interface*) bus is a synchronous serial data link standard named by Motorola that operates in full duplex mode.

compatible textile gaskets, glued on the left side of the panel profiles with temperature-resistant adhesive. Their semi-spherical shape allows a good metal continuity and their *CuNi* coating guarantees high shielding for a long time, typically 40 dB at 2 GHz.
The structural layout and some important dimensions are documented in figure 5.18. The power supplies are laid on the back, very close to the *Sum-Trigger-II* boards, but in distinct cases. Their position can be regulated on site to obtain the best connection to the electronic devices and an easy accessibility during maintenance.

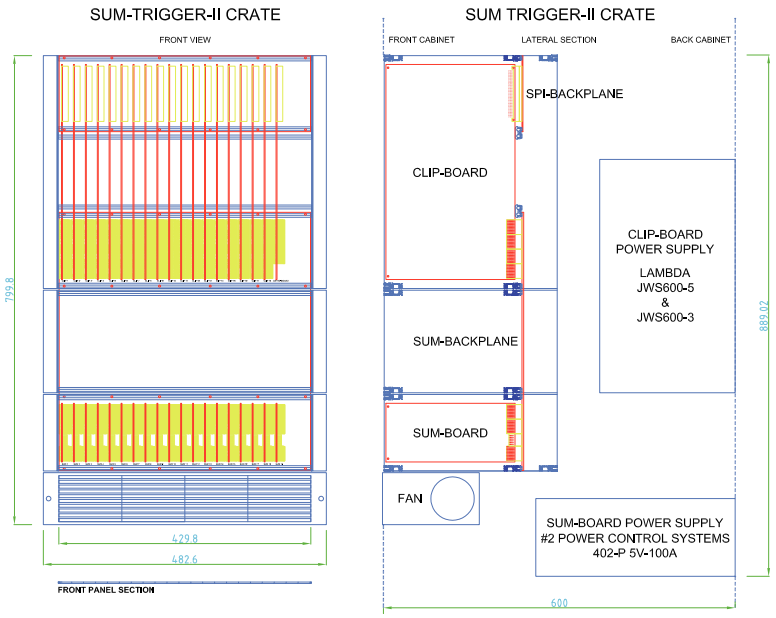

Figure 5.18: The mechanical overview of the *Sum-Trigger-II* crate and the power supply modules. All the blocks in red are electronic boards, while the connectors are indicated in yellow. The metal components are coloured in blue. The power supply position can be modified to optimize the arrangement on site. (Image credit: D. Corti & A. Bortoluzzi)

Below the crate, a 2U fan system (*Schroff LE2 60713-002*) is installed. This is a high-air capacity tangential blower, which produces a flux of 330 m^3/h (Fig. 5.19(a)). This facilitates the air flow to regulate the correct stable temperature.

(a) The blower

(b) The *Power Control System* module

Figure 5.19: On the left photo, the blower located on the bottom of the *Sum-Trigger-II* crate. On the right, one power module used to supply the *Sum-boards* (± 5 V).

The power system is divided in two parts. The first feeds the *Clip-boards*, recycling the old power switching modules (*Lambda JWS600-5 & JWS600-3*) of the former

MAGIC–I racks. The nominal output voltage is respectively 5 V and 3.3 V, for a maximum current of 120 A. The dominant noise is the voltage output ripple, which is always below 70 mV in *AC* mode. Considering also the common mode, the noise tolerance should be extended to 150 mV.
The second feeds the *Sum-boards* and it consists of two low-noise switching power supplies (Fig. 5.19(b)). They are provided by *Power Control Systems* company, model *S402-P*. Each module delivers 5 V for a maximum of 100 A with a maximum noise and ripple level of less than 50 mV. The ground of the first power pack is connected to the positive of the second, to deliver ± 5 V.

5.2.2.2 Sum-mezzanines and FCI cables

The *Sum-mezzanine* is the interface between the *Samtec QMSS* output connector of the receiver board and the *FCI* cables[9], which are connected to the *Clip-board* on the other end. Each receiver board can accept up to 24 optical fibres from the *PMTs*, so the *Sum-mezzanine* output stage is divided into three *FCI* connectors[10] with 8 differential channels each (schematics in appendix A).
The mezzanine is an eight-layer *PCB* with the traces routed internally to reduce the noise effect. The differential wires have an impedance of 100 Ω and their length is equalized inside 1.5 mm, namely ∼ 10 ps.

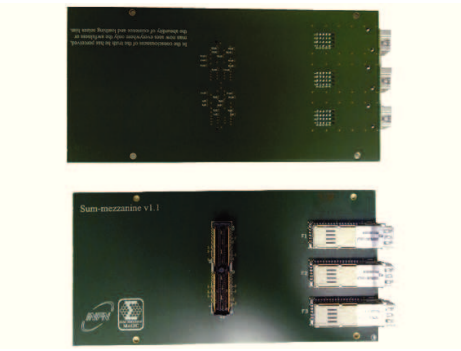

(a) The *Sum-mezzanine* (version 1.1)

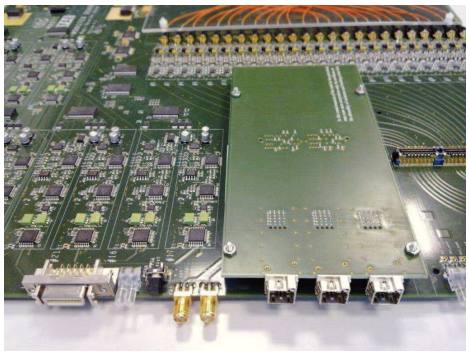

(b) The *Sum-mezzanine* plugged in the receiver board

Figure 5.20: *Left:* the top and bottom side of the *Sum-mezzanine* board. *Right:* the mezzanine connected to a receiver board (Medusa version).

The main design constraint is to preserve the features of the fast analogue signal, ∼ 2.6 ns *FWHM*, which determines the right pile-up. This implies high bandwidth electronics, high signal integrity, low cross-talk and very low skew between channels. To measure these parameters, a simple set up has been prepared with the following devices.

- A pulse generator *HP 8082A*.
- A *VCSEL* laser transmitter with a DC current of 3 mA.
- An optical fibre 1 m long with *LX5* connectors.
- One receiver board (Medusa version).

[9] The model is *10054999-N0500AULF*.
[10] The model is *10076181-101LF*.

- One *Sum-mezzanine* (Version 1.1).
- A *FCI* cable 5 m long (Fig. 5.21(a)).
- An adapter board from *FCI* to *SMA* (Fig. 5.21(b)).
- An oscilloscope *Tektronix DPO 7354* with a bandwidth of 3.5 GHz and a sample rate of 40 GS/s.

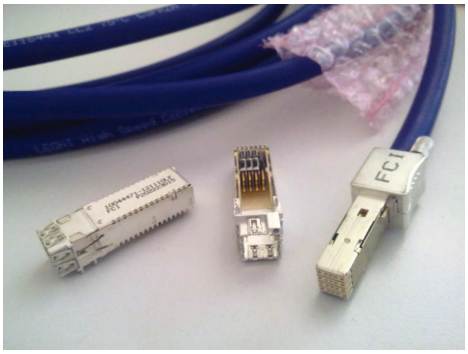

(a) The *FCI* cable & connectors

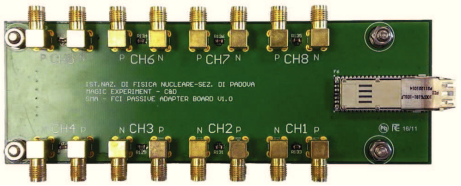

(b) The adapter board *FCI* to *SMA*

Figure 5.21: On the left photo, the *FCI 10054999-N0500A ULF* cable and connectors. On the right, a photo of the adapter board used to read the signals from the *FCI* cable with an oscilloscope.

The output signal is shown in figure 5.22(a). Its quality is very high, neither oscillations nor noise are visible and the positive and the negative components are perfectly synchronized. The rise time of the pulse (~ 1.3 ns) is a little bit larger than the typical value obtained from the camera *PMTs*, because it is limited by the generator slew rate and the receiver output bandwidth of ~ 300 MHz. In fact, it is very similar to the rise time of the input signal.
It is not possible to quantify precisely the cross-talk, because it is so small that it is

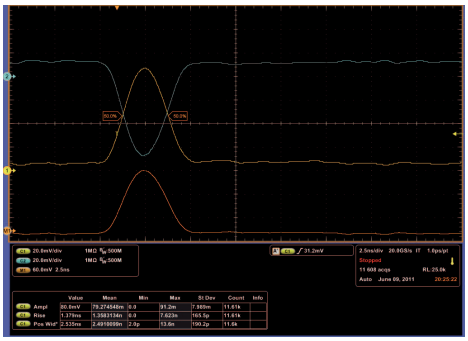

(a) Signal *Sum-mezzanine* & *FCI cable*

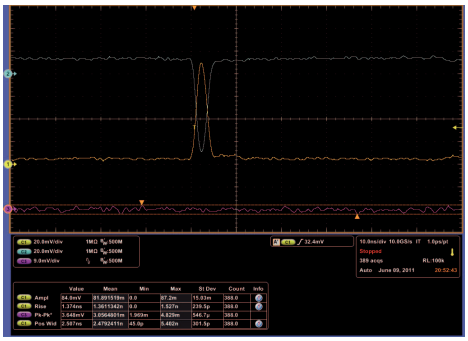

(b) *Sum-mezzanine* & *FCI cable* cross-talk

Figure 5.22: *Left:* the analogue differential signal at the end of a test chain composed of a pulse generator, a laser injector, an optical fibre, a receiver board, a *Sum-mezzanine*, a *FCI* cable and an adapter *FCI* to *SMA*. The yellow pulse is the positive, the blue one the negative, while the orange is their subtraction. *Right:* the maximum cross-talk between two close channels.

dominated by the electronic noise. In figure 5.22(b), the aggressor signal amplitude is

84 mV and the victim's response seems to have no cross-talk. The electronic noise level is around $\sim 3 \div 3.5$ mV peak-to-peak, even in other channels with higher amplitude, up to 100 mV. We conclude that the cross-talk is lower than 3%.

The *FCI* cable is designed for high-speed transmission over long distances. Its low profile allows a compact cable routing, even in a very dense system, such as *Sum-Trigger-II*. It can work perfectly up to 2.5 Gb/s, keeping an excellent signal integrity performance and an independent pair shielding. Other important characteristics are listed in table 5.3.

***FCI* CABLE SPECIFICATIONS**	
Electrical performance	
Differential impedance	$100 \pm 10\,\Omega$ at 100 ps (20-80%)
Insertion loss connector	< 1.0 dB at $0 \div 3$ GHz
Insertion loss cable	< 5.0 dB at $0 \div 1$ GHz
Near-end multi-line crosstalk	$< 1.5\%$ at 50 ps (20-80%)
Within pair skew	10 ps per metre
Pair-to-pair skew	50 ps per metre
Current rating	0.5 A per contact
Shielding	> 45 dB at $0 \div 1.2$ GHz
Mechanical performance	
Durability	200 mating cycles
Mating force	50 N max
Cable strain relief	50 N min
Side load resistance	75 N min

Table 5.3: The electrical and mechanical specifications of the *FCI* cable.

5.2.2.3 Clip-board

The *Clip-board*, designed by the *MPI* group, shapes the signal and prepares it for the selection logic. The embedded processes involved an amplification[11], a delay and a clipping stage. In the chosen design architecture, these three stages are laid out in long and low modules (Fig. 5.23(b)), which are vertically plugged and equally spaced in the 9U *Clip-board PCB* (Fig. 5.23(a)).

In the upper side of the module, the signal is converted from differential to single-ended, then it is attenuated with a high bandwidth (2.4 GHz) radio frequency chip, the *DAT-31R5-SP+* from *Mini Circuits*. It offers an attenuation range up to 31.5 dB with a resolution of 0.5 dB step, controlled by a six-bit serial interface. The gain flat-fielding is important to balance any contributions in the final summation and to make easier the conversion from voltage to photoelectrons.
Then, the signal passes a disable switch enclosed in the amplifier, which can be used to black out some channels during tests or calibration runs.

On the *Clip-board* the different signal arrival times, due to the transition time in *PMTs* and delays in both long optical fibres and electronic devices, are compensated by adjustable analogue delay lines (Fig. 5.24). This operation is fundamental to allow a perfect pile-up of very narrow signals of a few nanoseconds, getting rid of the uncorrelated spurious *NSB* events [65].

[11] The signal is first amplified by a factor A and then adjusted in amplitude with an attenuator, in the range $[(1/A) - k] \div [(1/A) + k]$, where 2k is the maximum attenuation.

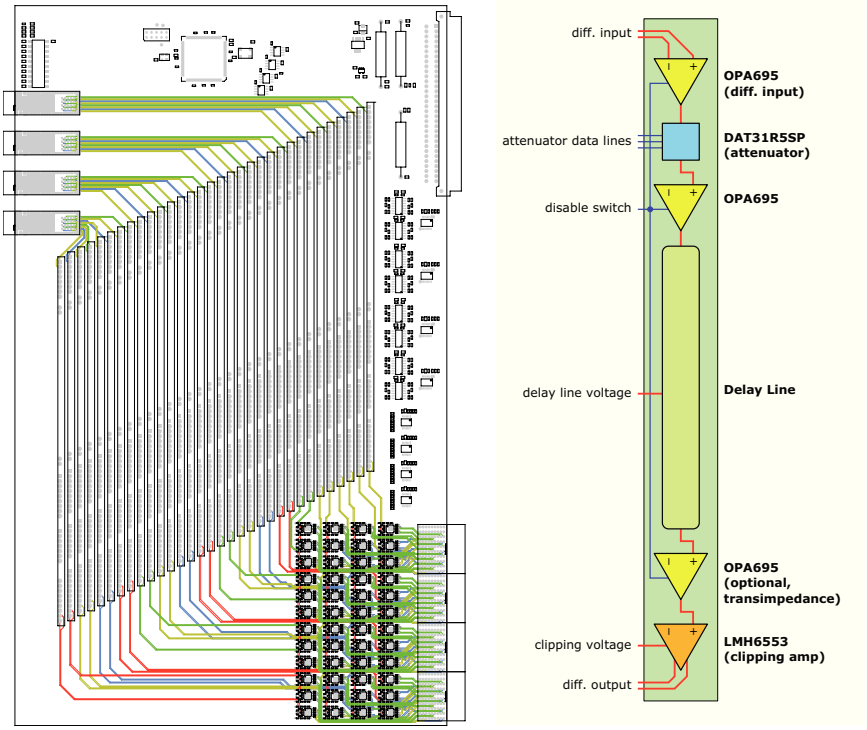

(a) The *Clip-board* layout (b) The vertical module sketch

Figure 5.23: On the left, the partially routed *Clip-board PCB* layout. On the top left side of the image, there are four *FCI* connectors which receive 32 signals from the receiver boards. On the top centre, there is the communication controller and, a little bit to the right, the power stage. In the centre, the long vertical module arranged to cover the available space and to minimize the traces' skew. On the bottom right, each channel is replicated three times and transmitted to the proper *Sum-board*. (Courtesy of *MPI* electronic workshop)
On the right, a simple sketch of the *Clip-board* main functions placed in a single long vertical module. The upper part contains an input differential amplifier, an attenuator and a disable switch. In the centre, there is the analogue delay line, while the end hosts the clipping amplifier. (Courtesy of D. Häfner)

Each prototype delay module is a ladder-unbalanced network composed of a series of 25 variable small LC filters[12]. This design is more efficient, in terms of bandwidth and signal quality, than using a single inductor plus a capacitor. The inductance is fixed, while the capacitance can be changed applying the right voltage to the varactor diodes[13]. This modifies the transmission line impedance, and consequently the signal propagation speed, which is $1/\sqrt{LC}$. The total delay range spans continuously up to 6 ns (Fig. 5.25), and the acquired precision is correlated to the resolution of the voltage, set to the diodes.
The drawback is the production of small reflections, caused by the impedance mismatch. The termination is inserted at the end of the delay line, but it cannot always match the variable impedance of the network, function of the varactor capacitance. Figure 5.25

[12]The selected number of sections are determined by the compromise between the space limitation and performance, which are not so different for higher values.

[13]A varactor diode is a type of diode, which has a variable capacitance that is a function of the voltage impressed on its terminals. It operates in reverse-biased mode, so the capacitance is modulated, changing the thickness of the depletion zone, in function of the applied bias voltage ($0 \div 30$ V).

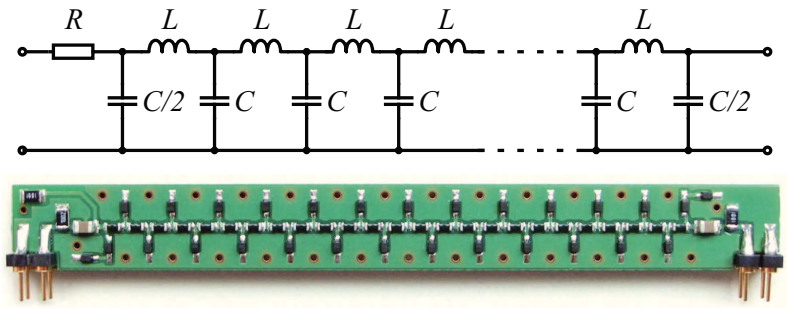

Figure 5.24: On the top, the circuit of the prototype analogue delay line. On the bottom, the image of the small module. In the final design, this function will be completely integrated in the main vertical module. (Adapted from [65])

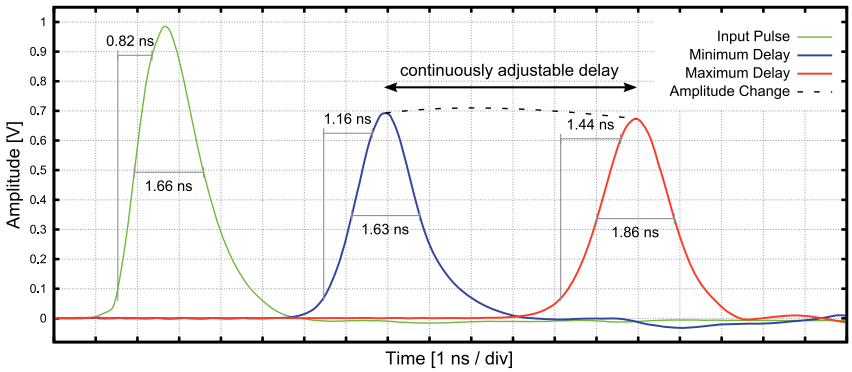

Figure 5.25: The analogue signal delayed in a delay line prototype module. The green pulse is measured at the input of the analogue delay line. The blue one is recorded at the line output, imposing the minimum delay. The propagation time is ~ 5.4 ns. For the red pulse, the maximum delay is uploaded, which is 6 ns after the previous one. (Adapted from [65])

shows an example of undershoot, 7 ns after the peak (blue pulse), whose amplitude is ~ 40 mV, that corresponds to 6% of the delayed signal. However, the reflection is far from the pulse peak, so it does not affect the *Sum-Trigger-II* concept. Even the pulse amplitude variation, when the minimum and maximum delays are applied, is limited to less than 3%, so it can be easily corrected during the flat-fielding process.
The comparison of signal specifications, before and after the delay line, is pointed out in table 5.4. When the minimum delay is loaded, the *FWHM* does not change and the rise time increases a little bit (340 ps). This aspect is worst at the maximum delay. The signal widens by 0.2 ns and its edge is 620 ps slower. A small distortion is present, but it does not drastically affect the signal shape. On the contrary, the resulting pulse is more symmetrical, which could be better in the summation stage.
The average delay line bandwidth is higher than any commercial product on the market that can delay a signal up to 6 ns. To obtain this product, a varactor diode with a very low serial resistance (0.35 Ω) is chosen: *SMV1413* from *Skyworks Solutions*.
The bandwidth is a function of the transmission line parameters, so it is correlated to the required delay. The frequency response has been measured with a network analyzer (Fig. 5.26). The high cut-off frequency appears around 200 MHz for both curves. This is the worst case, which considers even very low frequency components. Typically, the *PMT* pulse is very fast and its frequency spectrum stays above ≈ 50 MHz. Calculating

Signal	FWHM (ns)	Rise time (ns)	Amplitude (mV)
Input - green curve	1.66	0.82	985
Minimum delay - blue curve	1.63	1.16	690
Maximum delay - red curve	1.86	1.44	675

Table 5.4: The summary of the signal timing and amplitude features as a function of the applied delay. The bandwidth is lower for higher delay, smoothing a little bit the signal shape.

the -3 dB limit[14], starting from this new point, the cut-off enhances to ≈ 240 MHz for the maximum delay and ≈ 270 MHz for the minimum [65].

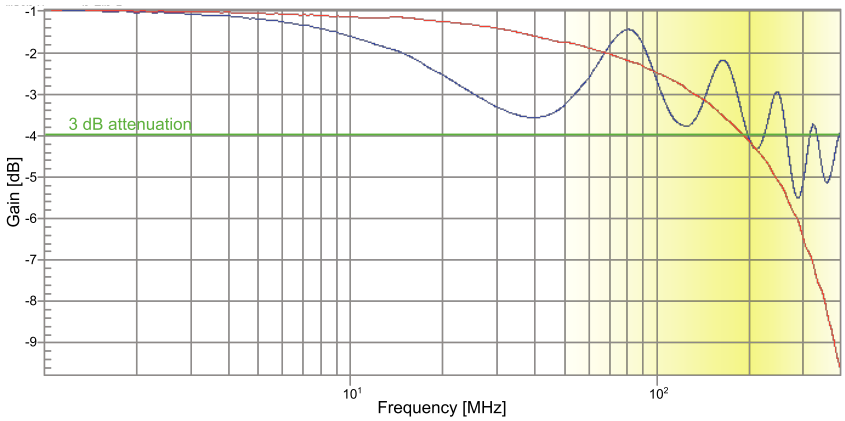

Figure 5.26: The bandwidth of the analogue delay line. The blue line represents the minimum delay, while the red one the maximum. The high cut-off frequency is indicated by the cross point between the green line and the curves (~ 200 MHz). Considering that the analogue pulse is made of frequencies above ≈ 50 MHz (yellow zone), the -3 dB green line can be shifted 1 dB down. (From [65])

At the end of the main module, the signal is clipped at a programmable level[15]. This operation is carried out with the current feedback amplifier *LMH6553*, from *National Semiconductor*. It is a 900 MHz full differential amplifier with an integrated adjustable output limiting clamp. However, it can even be configured as single-ended input to differential output gain block. The bandwidth has been simulated in this configuration (the same used for the clipping circuit), achieving 635 MHz.
A simple test board has been built to test the clipping circuit (Fig. 5.27). The measurements, obtained with the *LLP8* package, have been presented in figure 5.28. The signal quality after the clipping is quite poor, regardless of the input amplitude or the clipping level, but it gets worse for very huge input signals and clipping levels below 500 mV.
The circuit has been simulated to understand if the output deformations are intrinsic to the design or are due to some problems related to the *PCB*. In figure 5.29, the results are presented. The differential pulses are measured at the output pins of the *LMH6553* amplifier. For clarity, the negative signal is artificially inverted.

[14] The -3 dB limit is the value which defines the cut-off frequency. Beyond this point, the transferred power is less than half.

[15] From the Monte Carlo simulation, the best value is around $6 \div 7$ phe. To translate it in terms of volts, an absolute calibration is essential to extrapolate the conversion factor.

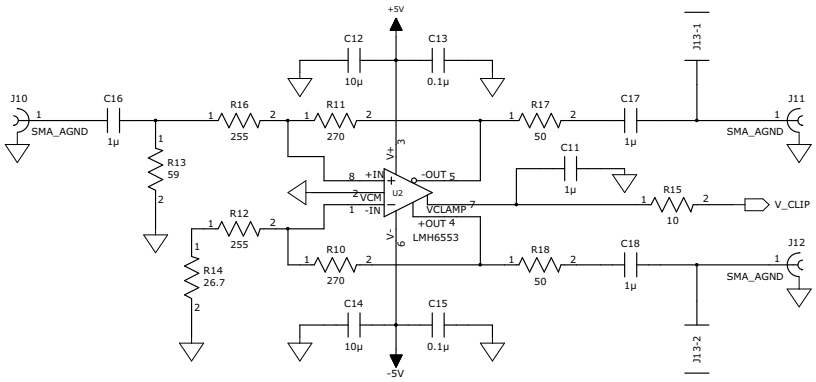

Figure 5.27: The clipping circuit under test, based on the amplifier *LMH6553*. (Courtesy of D. Häfner)

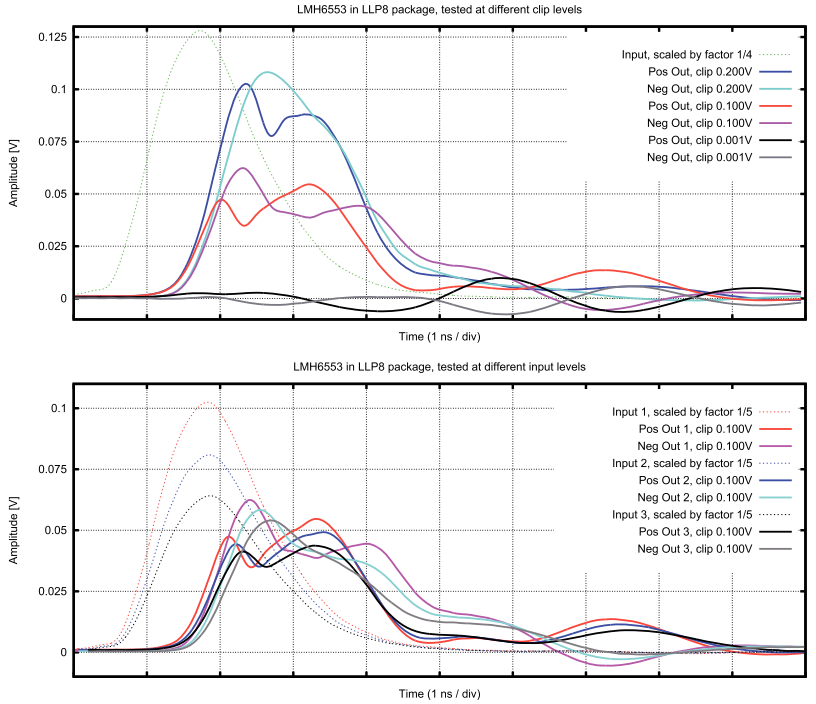

Figure 5.28: On the top, the positive and negative outputs of the clipping circuit at different levels. On the bottom, the same measurement, but changing the input amplitude with a fixed clamp voltage of 100 mV. (Courtesy of *MPI* electronic workshop)

The signal's quality is very much better than that shown in figure 5.28. There is a small overshoot and an undershoot, respectively on the positive and negative pulse edges, of the order of $\sim 4\%$. This effect appears only for clamp levels higher than 300 mV, so it should not affect the sum stage, because this is more or less the voltage that corresponded to $\sim 6 \div 7$ phe in the prototype *Sum-Trigger*. The positive and the negative pulses are very similar, but displayed a constant relative offset of ~ 20 mV. This is also not a problem, because an eventual *DC* component is completely eliminated by the following bypass capacitors.
In contrast to the signal integrity, the clipping function shows a couple of defects. The working clamp level is not equal to the set voltage. For low clipping voltages, the offset

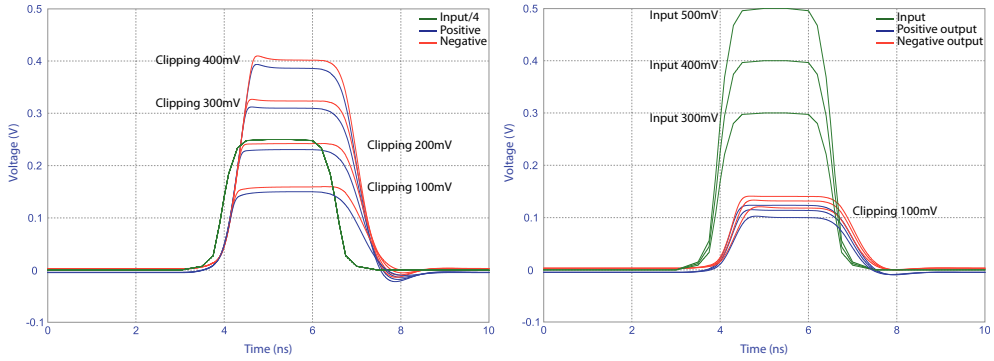

Figure 5.29: *Left:* the simulation of the differential output (blue & red pulses) clipping circuit at different clamp levels and an input of 1 V (green). *Right:* the same simulation with a fixed clamp at 100 mV and different input amplitudes. The input signal, which matches the *PMT* pulse, is described by this function: $f(t) = \sum_{i=1}^{5} a_i e^{-\frac{(t-b_i)^2}{2c_i^2}}$, where a_i, b_i and c_i are constants. (© F. Dazzi & G. Galeazzi)

error can reach even 50% (e.g. clipping set at 100 mV and clipping measured = 150 mV). This offset is not constant, but it is a function of the input signal amplitude and the clipping level, namely it gets worse with huge pulses and low clamps. It seems that the discrepancy becomes more noticeable as the differences between the clamp voltage and the input signal amplitude increase. Only for ratios below 2.5, it is negligible. Considering a clipping level of 6 phe, the offset is problematic for very high energetic events, containing more than 15 phe per pixel. This changes a little bit the trigger efficiency in the very high energy domain, which is not essential. Nevertheless, a slightly higher clipping level could allow a higher afterpulse accidental rate. This must be evaluated in the future on-site measurements.
The simulation demonstrates the suitability of the circuit design. The low signal integrity of the prototype clipping board is likely due to the *PCB* layout. The signals in figure 5.28 seem to be affected by reflections and oscillations, typical of high frequency amplifiers.

Finally, the signals are repeated three times and transmitted to the *Sum-backplane*, using a differential amplifier *ADA4927-2* from *Analog Devices*.
The performance of the drivers is obtained with a dedicated test board, dubbed *CTB-FCI* (Fig. 5.30), and designed by the Padova/Udine group. It groups eight equal blocks, each one formed by an input *SMA* connector, a differential transmitter *ADA4927*[16], a channel pair in a *FCI* cable[17], a differential receiver equal to the original one mounted in the *Sum-board* and an output *SMA* connector for the connection to the oscilloscope (schematics in appendix B). The *CTB-FCI* test board allows to test, at the same time, the *Clip-board* transmitter stage, the *FCI* cable and the *Sum-board* receiving stage.
The measured bandwidth of the transmitter stage is around 1.3 GHz (Fig. 5.31(a)), although the *PCB* presents a grounding problem and the contact point of the network analyzer's probe is not perfect. The thermal pads are not connected in the internal ground planes, which result in a floating voltage. Some blind holes have been made up to the copper surface of each internal ground plane. Then, the planes are short-circuited to the ground line. This prevents a complete impedance mismatching of the

[16] Every chip *ADA4927-2* contains two transmitter amplifiers *ADA4927*.
[17] In the final project, the Sum-backplane is inserted at this level, in place of the cable. The capacitive load will certainly be different, however, it would be even more problematic to drive a 5 m cable.

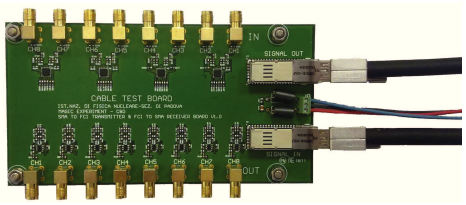

Figure 5.30: Picture of the *CTB-FCI* board, designed to verify the performance of the transmitter stage of the *Clip-board*, the receiver stage of the *Sum-board* and the *FCI* cable. On the top, there are 8 single-ended inputs and just below the dual transmitters *ADA4927-2*. On the right, the output and the return of the *FCI cable*, while on the bottom the 8 current-feedback amplifiers *OPA695* with the corresponding *SMA* output connectors.

internal traces and assures the ground shielding. However, it is mechanically impossible to drill a blind via every time there is a trace's passage between distinct layers, which can force the current return to be very close to the signal. For the same reason, the probe's terminals are a little bit spaced out.
The same measurement has been repeated, but adding a *FCI* cable of 5 m. The band-

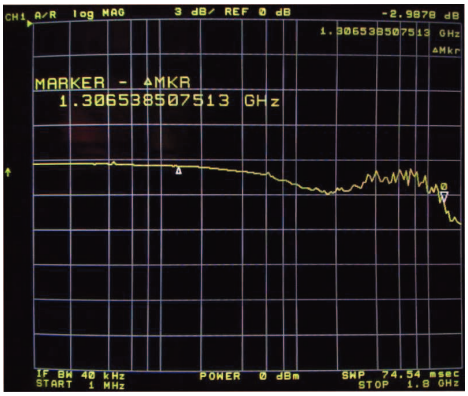

(a) Bandwidth transmitter *ADA4927-2*

(b) Bandwidth transmitter plus 5 m *FCI* cable

Figure 5.31: *Left:* The bandwidth of the transmitter output stage of the *Clip-board*. *Right:* The bandwidth adding the capacitive load due to the 5 m *FCI* cable.

width obtained is around 820 MHz (Fig. 5.31(b)). In first approximation, the cable upper frequency cut-off can be extrapolated by the following formula:

$$\frac{1}{f_{out}} = \sqrt{\frac{1}{f_{trans.}^2} + \frac{1}{f_{cable}^2}} \tag{5.3}$$

where $f_{trans.}$ and f_{cable} are respectively the transmitter and the cable frequency cut-off. Substituting the previous bandwidth values, we obtain:

$$\begin{aligned} f_{cable} &= \left(\sqrt{\frac{1}{f_{out}^2} - \frac{1}{f_{trans.}^2}}\right)^{-1} \\ &= \left(\sqrt{\frac{1}{(0.82 \cdot 10^9)^2} - \frac{1}{(1.3 \cdot 10^9)^2}}\right)^{-1} \\ &= 1.06\,GHz \end{aligned} \tag{5.4}$$

indicating a cable bandwidth of about 1 GHz.

Finally, even the receiving stage has been considered. Unfortunately, the bandwidth drops down drastically, dominated by the limited bandwidth (~ 450 MHz) of this last stage. In subsection 5.2.2.5, this portion of the circuit has been thoroughly analysed and improved, resulting in a higher bandwidth of around 800 MHz.

5.2.2.4 Sum-backplane

The *Sum-backplane* is a passive 10U printed circuit motherboard (Fig. 5.32(a)), which connects the *Clip-boards* to the *Sum-boards*, following the mapping *Sum_ mapping_ V4*. To make future maintenance easier, the 19 bottom slots have a hardware coding, so the *Sum-board* address is bound by the board position in the crate and it is not necessary to change it every time. It makes the system swappable and board position independent.

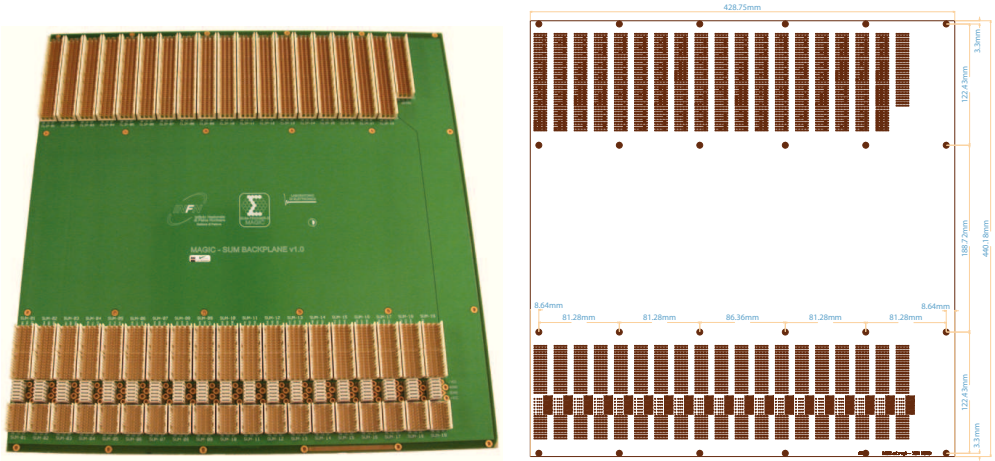

(a) The *Sum-backplane* motherboard (b) The *Sum-backplane* dimensions

Figure 5.32: On the left photo, the *Sum-backplane* 10U motherboard. On the right, the board's dimensions. They are quite considerable, around 43×44 cm.

For the electronic point of view, this is the most critical part of *Sum-Trigger-II*. The *PCB* layout has been projected considering that 997 fast differential analogue signals have to be routed to 55 macrocells, preserving the isochronism inside 50 ps, a bandwidth higher than 1 GHz and a low cross-talk ($< 1\%$). These constraints demanded to an accurate design strategy, where the macrocell numbering, the *PCB* stack-up, the trace impedance and the components' placement and routing have been studied and optimized in a very huge board (Fig. 5.32(b)).
All the traces must be adjusted to the longest one, applying meandering[18] routing. It is fundamental to keep the maximum length difference as short as possible, to avoid extended and space-consuming paths, which affect the signal quality and make impossible the complete routing.
Considering the board's dimensions and the relative position of all connectors, different arrangements have been simulated to find the solution, which minimizes the length adjustment. The calculated skew, after the routing phase, is shown in figure 5.33. It is clear that the requirements are theoretically fulfilled, even if the average wire length

[18]The net is not routed in a straightforward manner searching the minimal path, but a zigzagging method is used to match the longest net.

has been increased to 68.5 cm by some routing limits, far from the simulated value obtained in the place and route phase (30 cm).

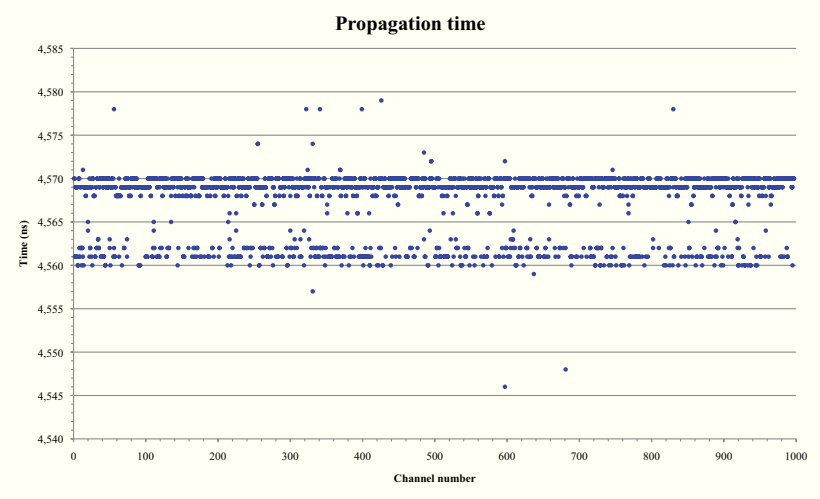

Figure 5.33: The propagation time of the 997 traces routed in the *Sum-backplane*, calculated by the *CAD* software. The trace's length and the line impedance are considered in the simulation. The propagation time is ~ 4.5 ns, the maximum skew between channels is 33 ps and the maximum skew inside a differential net is 26 ps.

Other parameters, such as for instance the trace's width, the differential line separation and the dielectric constant are mapping-independent, but they are relevant for the signal properties. The *PCB* stack-up counts twenty layers, nine of which are reserved for signal routing. This is the cheapest layout that allows an efficient escape

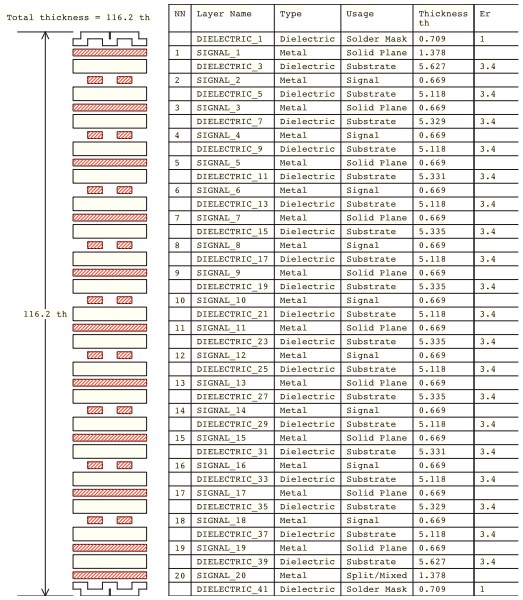

NN	Layer Name	Type	Usage	Thickness th	Er
	DIELECTRIC_1	Dielectric	Solder Mask	0.709	1
1	SIGNAL_1	Metal	Solid Plane	1.378	
	DIELECTRIC_3	Dielectric	Substrate	5.627	3.4
2	SIGNAL_2	Metal	Signal	0.669	
	DIELECTRIC_5	Dielectric	Substrate	5.118	3.4
3	SIGNAL_3	Metal	Solid Plane	0.669	
	DIELECTRIC_7	Dielectric	Substrate	5.329	3.4
4	SIGNAL_4	Metal	Signal	0.669	
	DIELECTRIC_9	Dielectric	Substrate	5.118	3.4
5	SIGNAL_5	Metal	Solid Plane	0.669	
	DIELECTRIC_11	Dielectric	Substrate	5.331	3.4
6	SIGNAL_6	Metal	Signal	0.669	
	DIELECTRIC_13	Dielectric	Substrate	5.118	3.4
7	SIGNAL_7	Metal	Solid Plane	0.669	
	DIELECTRIC_15	Dielectric	Substrate	5.335	3.4
8	SIGNAL_8	Metal	Signal	0.669	
	DIELECTRIC_17	Dielectric	Substrate	5.118	3.4
9	SIGNAL_9	Metal	Solid Plane	0.669	
	DIELECTRIC_19	Dielectric	Substrate	5.335	3.4
10	SIGNAL_10	Metal	Signal	0.669	
	DIELECTRIC_21	Dielectric	Substrate	5.118	3.4
11	SIGNAL_11	Metal	Solid Plane	0.669	
	DIELECTRIC_23	Dielectric	Substrate	5.335	3.4
12	SIGNAL_12	Metal	Signal	0.669	
	DIELECTRIC_25	Dielectric	Substrate	5.118	3.4
13	SIGNAL_13	Metal	Solid Plane	0.669	
	DIELECTRIC_27	Dielectric	Substrate	5.335	3.4
14	SIGNAL_14	Metal	Signal	0.669	
	DIELECTRIC_29	Dielectric	Substrate	5.118	3.4
15	SIGNAL_15	Metal	Solid Plane	0.669	
	DIELECTRIC_31	Dielectric	Substrate	5.331	3.4
16	SIGNAL_16	Metal	Signal	0.669	
	DIELECTRIC_33	Dielectric	Substrate	5.118	3.4
17	SIGNAL_17	Metal	Solid Plane	0.669	
	DIELECTRIC_35	Dielectric	Substrate	5.329	3.4
18	SIGNAL_18	Metal	Signal	0.669	
	DIELECTRIC_37	Dielectric	Substrate	5.118	3.4
19	SIGNAL_19	Metal	Solid Plane	0.669	
	DIELECTRIC_39	Dielectric	Substrate	5.627	3.4
20	SIGNAL_20	Metal	Split/Mixed	1.378	
	DIELECTRIC_41	Dielectric	Solder Mask	0.709	1

Figure 5.34: This is the *Sum-backplane* stack-up. It is composed of twenty copper layers, nine dedicated to the signals routing. This means that the board thickness will be out of standard (~ 2.8 mm), even if the chosen support (*Nelco N4000-13*) has a low dielectric constant of 3.4. This material is an enhanced epoxy resin system engineered to provide both outstanding thermal and low signal loss properties for high-speed applications. For the purposes of the *Sum-backplane*, it is perfect, because it assures an optimum signal integrity and a precise impedance control.

routing from the backplane connectors. These pressfit connectors (*ERmet ZD 223396*) are provided by the *ERNI* company and are designed for high-speed and low-voltage differential transmissions, up to 10 Gb/s. They provide 30 contact pairs[19], each one

[19]There are 60 signal pins and other 30 for ground.

with a differential impedance of 100 Ω and a ground shielding.
The trace characteristics are summarized in table 5.5 and the features of the meandering delay lines have been selected to have, at the same time, a precise skew control and a low signal deterioration. The ratio between the meander height, typically around 2 mm, and its width is never more than 2.5. Up to 200 meandering curves are sometimes applied to match the required delay adjustments.

TRACE SPECIFICATIONS				
Trace type	**Min. width (um)**	**Typ width (um)**	**Max. width (um)**	**Diff. pair spacing (um)**
Analogue pairs	90	100	100	100
Digital pairs	90	100	100	100
Others	200	200	200	200

Table 5.5: The main properties of the *Sum-backplane* traces. For the analogue and digital pairs, they are calculated to obtain a differential impedance close to 100 Ω.

Another crucial point is the evaluation of the cross-talk, which could increase the signals' amplitude during the sum stage, resulting in fake triggers. The minimal trace separation, from edge to edge, is fixed to three times the line width to keep negligible the mutual electromagnetic interaction.
The cross-talk has been simulated with the *Hyperlinx* software. A step function with a rise time of ∼ 750 ps and a voltage drop of ∼ 1200 mV is injected in an aggressor line, while the output is calculated at the end of a victim adjacent wire[20] (Fig. 5.35). The choice of a step function is determined by the desire to be very conservative in the estimation of the cross-talk. Its frequency components are extremely high, more than the *PMT* analogue response, and the amplitude is fixed to four times the amplitude of a clipped signal (≈ 350 mV).
As displayed in figure 5.35, the cross-talk seems to have an inductive nature, because

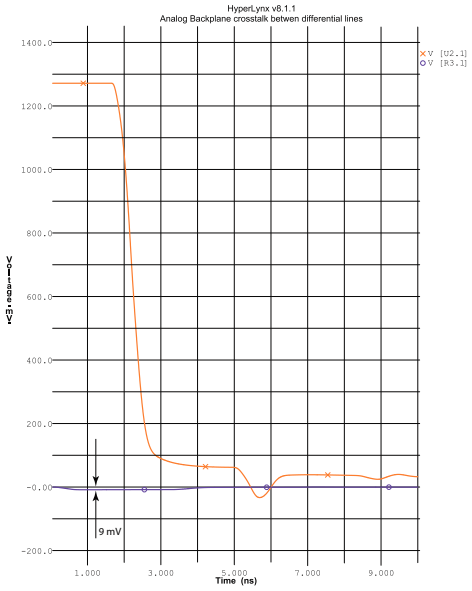

Figure 5.35: The simulation of the *Sum-backplane* cross-talk between two close lines. A huge step function (orange curve) is injected in one line, while the amplitude in an adjacent one is calculated (blue curve). This could be considered the worst case, taking into account the characteristics of the aggressor signal. The maximum cross-talk is around 0.75%. (Courtesy of *INFN-Padova* electronic workshop)

it appears in the correspondence of the signal edge and it is negative. The maximum

[20] In electronics, this is defined as the far-end cross-talk.

value is ∼9 mV, namely 0.75% of the aggressor amplitude. It should be underlined that the differential signalling offers superior immunity to common mode noise such as crosstalk and simultaneous switching noise.
Cross-talk coupled to a victim differential pair comes only from the differential component of the generated electromagnetic field, because the common mode is cancelled at the receiver. This contribution only exists because the distance between the aggressor and the victim slightly changes, when the inside or the outside trace is taken into account.
In figure 5.36 the real case of the *Sum-backplane* is illustrated. The aggressor is the

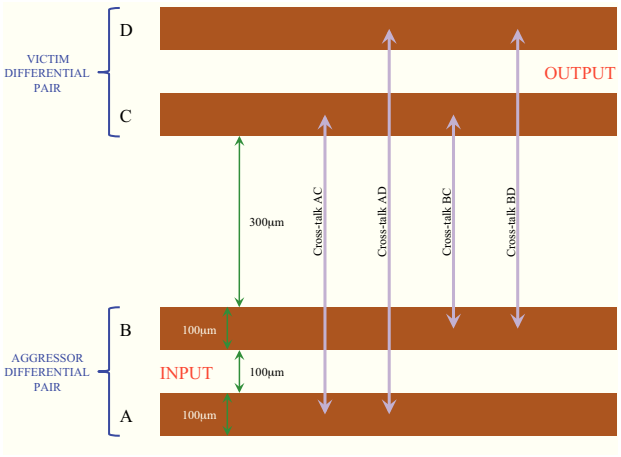

Figure 5.36: A sketch in scale that represents two close differential lines in the *Sum-backplane*. The green arrows show the dimensions and the violet ones the single contributions to the differential cross-talk. (© F. Dazzi)

pair composed of the wire A and B, whereas the victim is the pair C and D. The signal is injected at the input of the aggressor line and the far cross-talk is registered at the output of the victim. Both lines are correctly terminated to prevent wrong estimations due to reflections. Then, the differential cross-talk component has been calculated superimposing the four contributions, marked with the violet arrows, between the two differential lines. The differential cross-talk can be expressed by the following equation:

$$XT_{diff} = XT_C - XT_D \tag{5.5}$$

where XT_C and XT_D are the induced voltage fractions measured respectively at the line C and D. In first approximation they can be obtained from relations 5.6 and 5.7.

$$XT_C = XT_{AC} - XT_{BC} \tag{5.6}$$
$$XT_D = XT_{AD} - XT_{BD} \tag{5.7}$$

It must be underlined that the sources A and B have equal and opposite signals, so the same property is transferred in the generated electromagnetic field. This explains the negative sign before XT_{BC} and XT_{BD}. Substituting the variables in equation 5.5, we get the final formula 5.8.

$$\begin{aligned} XT_{diff} &= (XT_{AC} - XT_{BC}) - (XT_{AD} - XT_{BD}) \\ &= XT_{AC} - XT_{BC} - XT_{AD} + XT_{BD} \end{aligned} \tag{5.8}$$

Every single contribution has been quantified in the whole spectrum from 1 MHz to 1 GHz with a sinusoidal signal of 0 dBm (Fig. 5.37). The curves trends do not follow the same profile, so it is not trivial to combine them. A quantitative analysis tells us that one of the worst cases occurs, for instance, at ∼600MHz. In table 5.6 the results

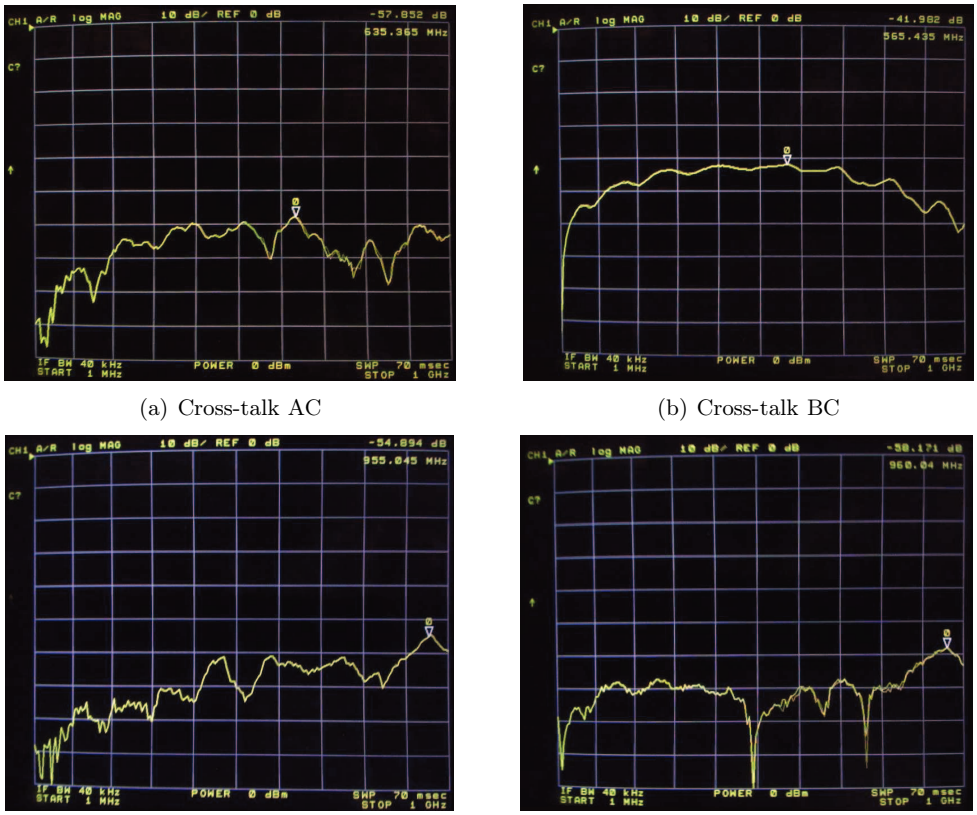

(a) Cross-talk AC

(b) Cross-talk BC

(c) Cross-talk AD

(d) Cross-talk BD

Figure 5.37: The far end cross-talk of a single differential line coupling to another differential line in the spectrum from 1 MHz to 1 GHz. The four contributions between traces are measured independently. *Top left:* the cross-talk spectrum in trace C, when A is the aggressor. *Top right:* the cross-talk spectrum in trace C, when B is the aggressor. *Bottom left:* the cross-talk spectrum in trace D, when A is the aggressor. *Bottom right:* the cross-talk spectrum in trace D, when B is the aggressor.

extrapolated at different frequencies, including 600 MHz, are reported. It is evident that the cross-talk is dominated by the component XT_{BC} (0.6%), namely between only the closest traces. The rest is a factor ten lower, so practically negligible. In fact, increasing the separation between traces, their coupling is reduced following a power law. Moreover, in differential stripline there is an inherent shielding. The inside trace of the pair partially shields the coupling to the outside trace.

DIFFERENTIAL CROSS-TALK						
BW (um)	$\mathbf{XT}_{AC}$ **(dB)**	$\mathbf{XT}_{BC}$ **(dB)**	$\mathbf{XT}_{AD}$ **(dB)**	$\mathbf{XT}_{BD}$ **(dB)**	$\mathbf{XT}_{diff}$ **(dB)**	$\mathbf{XT}_{diff}$ **(%)**
300	-68	-44	-78	-70	-44.9	0.57
600	-62	-44	-63	-70	-44.6	0.59
900	-65	-57	-60	-62	-60	0.10

Table 5.6: The differential far end cross-talk fraction measured at different frequencies.

At this point, it is important to estimate the effect of the multi cross-talk. The

worst case comes when the victim is surrounded by two aggressors, assuming that the others, not adjacent to the victim, have no influence. Therefore, the maximum multi cross-talk is around 1.2%.
These measurements only ensue from the *PCB*, because the contribution from the connectors[21] is not considered. However, only rarely there are traces that travel in parallel inside the *PCB* and end up on neighbouring pins of the same connector.

The bandwidth, measured with a network analyzer *HP* model *HP 4396A*, is around 600 MHz (Fig. 5.38(a)). This value is not perfectly in agreement with the simulation that returns $\sim$700 MHz. A weak point is the two hand-made connectors, necessary to match the network analyzer I/O format with the *Sum-backplane ERNI* contacts. Even part of the oscillations in the bandwidth curve can be pinpointed to these adapters. In fact, simply by improving the shielding in the conjunction point, the oscillations have been reduced by $\sim$50%, recovering 2 dB. Another contribution to the mismatch can come from the huge tolerance (15$\div$20%) in the dielectric thickness, resulting in the *PCB* build-up process.
An additional simulation, cutting into halves the trace length (30 cm as foreseen in

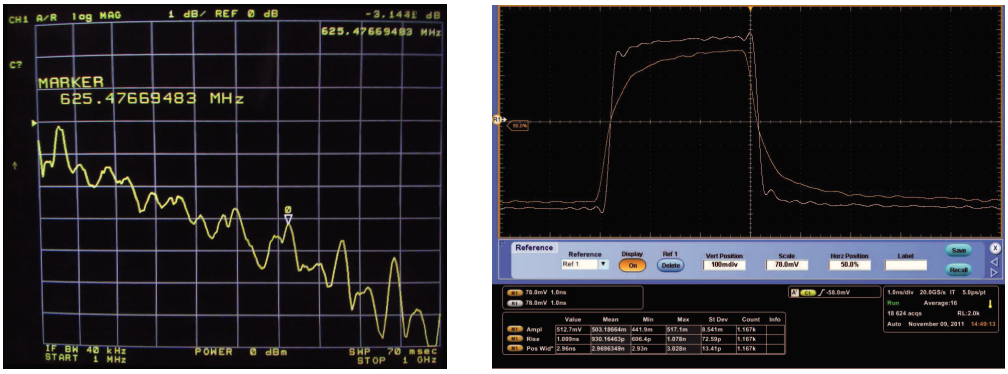

(a) The *Sum-backplane* bandwidth (b) The differential signal

Figure 5.38: *Left:* the *Sum-backplane* bandwidth measured with a network analyzer. *Right:* the differential signal at the input of the *Sum-backplane* (white line) and at the output (orange line).

the design phases), was carried out to check the bandwidth cut-off. The result was at the same time clashing and interesting: 2.7 GHz, indicating that the GHz domain is possible with the appropriate length. The next step will be to examine the feasibility to increase the number of layers, hence the routing space, while reducing the trace dimensions as much as possible. Obviously, this will considerably affect the *PCB* cost, which does not increase linearly with the number of layers. For instance, the price for 28 layers is double that of twenty.
A very fast pulse generator has been used to test the signal integrity. In figure 5.38(b) the differential signals before and after the *Sum-backplane* are shown. The signal is quite good, and either reflections or ground bounce are visible. The limitation is again the bandwidth. The behaviour is typical of an RC low-pass filter, which modifies the input signal rise time ($<$ 200 ps) to around 1 ns. In fact, the *Hyperlinx* simulation of the produced *PCB* estimates a capacitive load of 75 pF.

[21] The multiline cross-talk is less than 3% at 100 ps and the insertion loss is less than 1 dB up to 3 GHz

5.2.2.5 Sum-board

The *Sum-board* is the main board for the final event selection (Fig. 5.39). It can handle up to three macrocells covering the whole mapping with only 19 units, still keeping the compactness of a small 3U card. It is a high-speed mixed analogue and digital system, which can be controlled either automatically by the *Astro-board* and the software or manually providing the commands directly to the front panel input connectors.
The function diagram is shown in figure 5.40. The differential analogue signals are

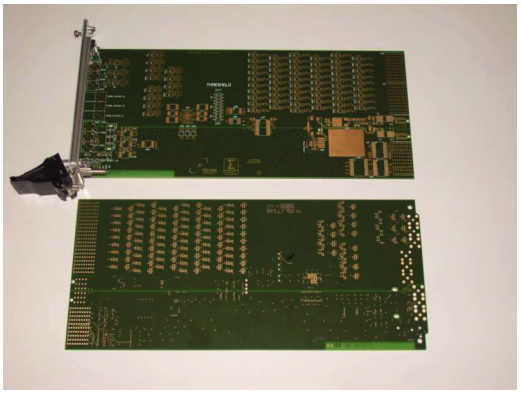

Figure 5.39: A photo of the *Sum-board*. In the upper area there is the analogue electronics, while below the pale-green horizontal line (ground separation) there is the digital one. *DAC* is the device between the two areas.

converted to single-ended format in preparation for the sum stage. The summation is executed in two successive steps to avoid the amplifier's saturation (4.2 V), in case 19 signals clipped at 300÷400 mV are piled up. In the first block, four groups of five[22] channels are added up, attenuated and only in a second amplifier the four outputs are added. The consequent signal is compared with a programmable threshold and a trigger is generated when it is exceeded. The electrical schematics are given in appendix C.
The rest of the electronics is used for the threshold control, data transmission and monitoring. The main three devices are a single package multi-*DAC*, a voltage reference and a magnitude comparator for the board address verification. The *DAC* (*AD5582*) is a 12-bit quad voltage output digital-to-analogue converter. A doubled-buffered parallel interface offers a fast settling time and a read-back mode of the internal input registers. Assuming that the electronic chain amplification returns ∼50 mV every photoelectron, as in the prototype *Sum-Trigger*, and the *Sum-board* gain is fixed around 0.25, the pulse will be ∼12.5 mV/phe at the comparator level. The working voltage of *DAC* is enabled between 0 ÷ 2 V, so that the resolution obtained is 0.5 mV. This corresponds to 0.04 phe, well below the electronic noise level.

Standard signal integrity techniques have been used in the *Sum-board*, too. The stack-up counts 14 layers, divided into six for signals and eight for the ground and the power voltages. The *PCB* structure has been plotted to get a differential pair impedance of 100 Ω and the single-ended of 50 Ω. All of them are striplines[23] disposed among ground layers, while the ± 5 V are isolated at the centre of the board.
The traces' length has been carefully calculated during the design phase. The channels' skew in the portion from the input connector and to the first sum stage is less than 11 ps (Fig. 5.42(a)), while between the two sum amplifiers is null. The total propagation time up to the trigger output is 3.4 ns, always with the same extremely low skew (Fig. 5.42(b)). Even comparing channels belonging to different macrocells, the timing

[22] This number is necessary because of the worsening of the bandwidth for signals greater than 2 V.
[23] A stripline is a trace of metal sandwiched between two parallel ground planes. The surrounding insulating material of the substrate forms a dielectric.

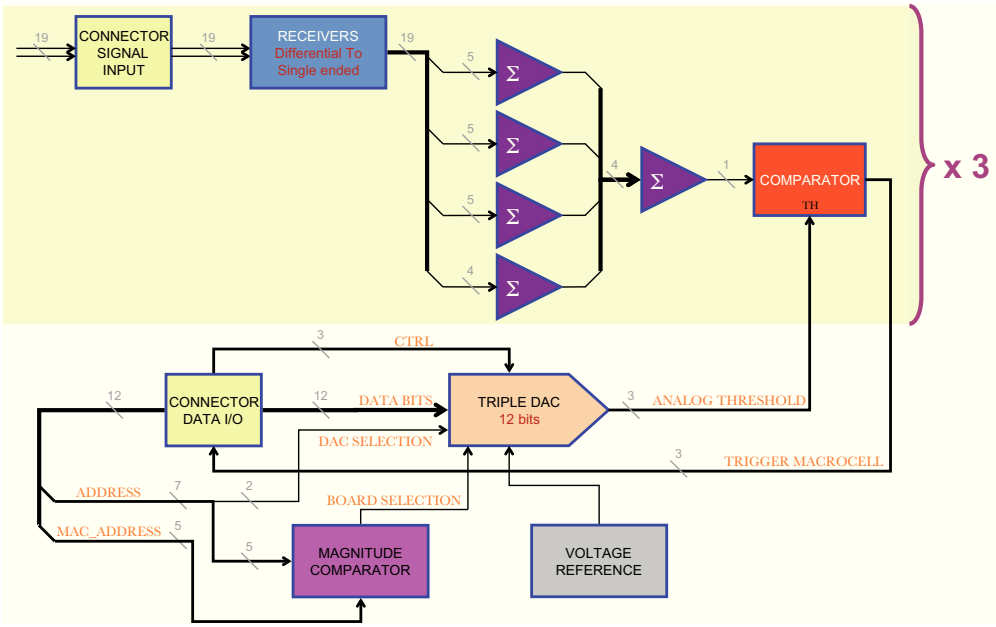

Figure 5.40: At the beginning, the differential analogue signals are converted in single-ended (blue rectangle) lines, then they are added in two steps (violet triangles). At the end, the output is compared with a programmable threshold (red rectangle). On the bottom side, there are the digital commands for the threshold control and the data transmission. (© F. Dazzi)

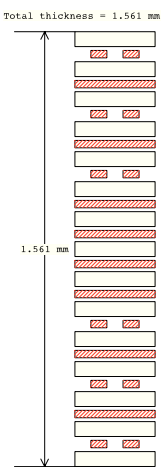

NN	Layer Name	Type	Usage	Thickness mm	Er
	DIELECTRIC_1	Dielectric	Substrate	0.01	1
1	SIGNAL_1	Metal	Signal	0.014	
	S1	Dielectric	Substrate	0.07	4.1
2	GND1	Metal	Solid Plane	0.014	
	S2	Dielectric	Substrate	0.1	4.1
3	Sig_50_ohm_1	Metal	Signal	0.014	
	S3	Dielectric	Substrate	0.121	4.2
4	GND2	Metal	Solid Plane	0.014	
	S4	Dielectric	Substrate	0.1	4.1
5	Sig_diff_100_1	Metal	Signal	0.014	
	S5	Dielectric	Substrate	0.121	4.2
6	GND3	Metal	Solid Plane	0.014	
	S6	Dielectric	Substrate	0.1	4.1
7	PS_P	Metal	Solid Plane	0.014	
	S7	Dielectric	Substrate	0.121	4.1
8	PS_N	Metal	Solid Plane	0.014	
	S8	Dielectric	Substrate	0.1	4.1
9	GND4	Metal	Solid Plane	0.014	
	S9	Dielectric	Substrate	0.121	4.1
10	Sig_diff_100_2	Metal	Signal	0.014	
	S10	Dielectric	Substrate	0.1	4.2
11	GND5	Metal	Solid Plane	0.014	
	S11	Dielectric	Substrate	0.121	4.1
12	Sig_50_ohm_2	Metal	Signal	0.014	
	S12	Dielectric	Substrate	0.1	4.2
13	GND6	Metal	Solid Plane	0.014	
	S13	Dielectric	Substrate	0.07	4.1
14	SIGNAL_8	Metal	Signal	0.014	
	DIELECTRIC_17	Dielectric	Substrate	0.01	1

Figure 5.41: This is the *Sum-board* stack-up. It is composed of fourteen copper layers, six dedicated to the signals' routing. The support material is the standard *FR4* with a dielectric constant around 4.2. The high-speed signals travel only in striplines enclosed between two ground planes to avoid electromagnetic noise.

precision is not affected ($< 13\,\mathrm{ps}$).

Another important topic is the bandwidth and the preservation of the signal properties. In fact, a long study has been carried out, and is still in progress, to find the best configurations for the receiving and the summing stages. As in the prototype *Sum-Trigger*, the current-feedback amplifier *OPA695*, from *Analog Devices* has been the initially preferred device. It is a wideband chip that combines exceptional $4300\,\mathrm{V}/\mu\mathrm{s}$ slew rate and low input voltage noise.

The receiving stage is a difference amplifier with some passive components to match the characteristic transmission line impedance (schematics sheet nr. 4 in appendix C). Preliminary tests demonstrate that this circuit introduces some asymmetries, slightly

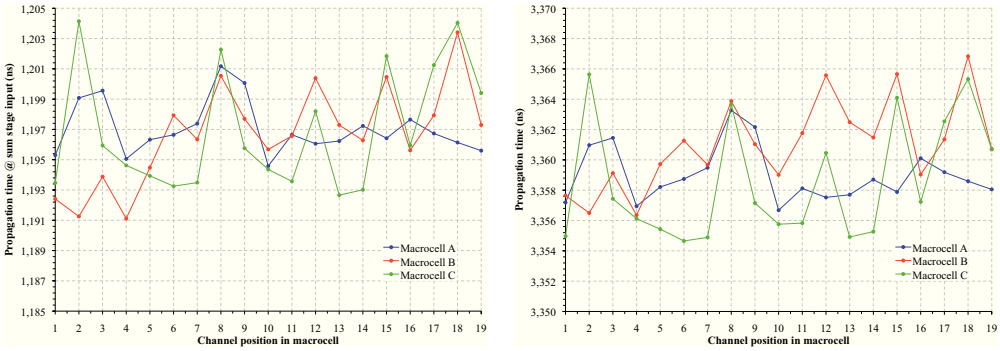

(a) Delay measured at the sum stage (b) *Sum-board* propagation time

Figure 5.42: On the top, the estimated propagation time up to the sum stage input for each channel. Channels in different macrocells are coloured differently. The maximum skew is less than 11 ps. On the bottom, the same evaluation, but considering the overall board. As before, the skew continues to be negligible, less than 13 ps.

deforming the signal shape. The positive and negative input bandwidths have been measured separately with a network analyzer (Fig. 5.43). The result reveals two dissimilar

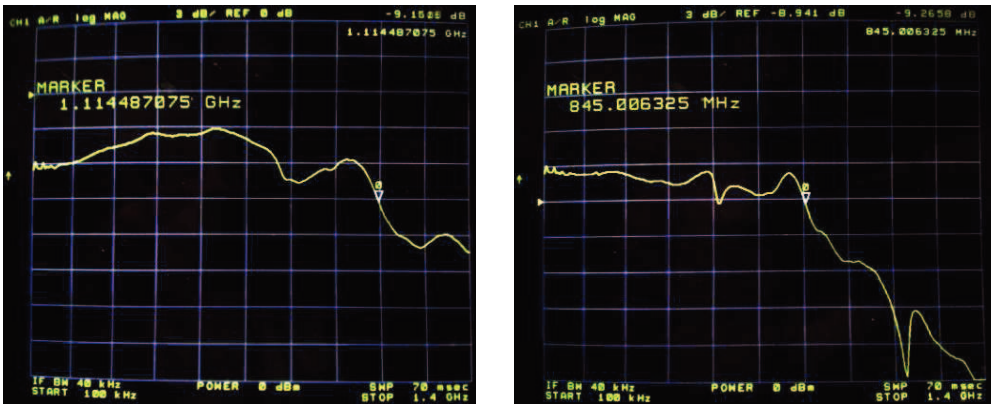

Figure 5.43: *Left:* the positive input bandwidth of the difference amplifier. The cut-off point is above 1.1 GHz. *Right:* the same bandwidth of the negative input. Here, the -3 dB limit occurs around 845 MHz.

curves with distinct cut-off[24]. An additional test, duplicating the pulse generator signal with a power splitter (Microlab/FXR DA-3FN) and stimulating simultaneously both inputs with the same positive pulse, confirms the asymmetric behaviour (Fig. 5.44(a)). The output voltage should be constantly zero, but two bumps, corresponding to the signal edges, are visible. Probably the rise time of the inputs are differently affected by the two bandwidths, therefore the voltages do not increase with the same speed, resulting in a no zero function. In fact, the positive path returns a steeper edge (t_{rise}(positive) - t_{rise}(negative) $\approx$ -200 ps) compared to the negative.
This effect seems to be irrelevant, when only one signal is injected and the receiving stage is observed (Fig. 5.45). However, we have to remember that the system can pile up to 19 pulses, involving other two amplifiers in series. An asymmetric shape is not

[24]For both inputs of the *Sum-board*, there is a resistive termination of 50 Ω, which lowers the signal by -6 dB. The relative -3 dB cut-off occurs at -9 dB.

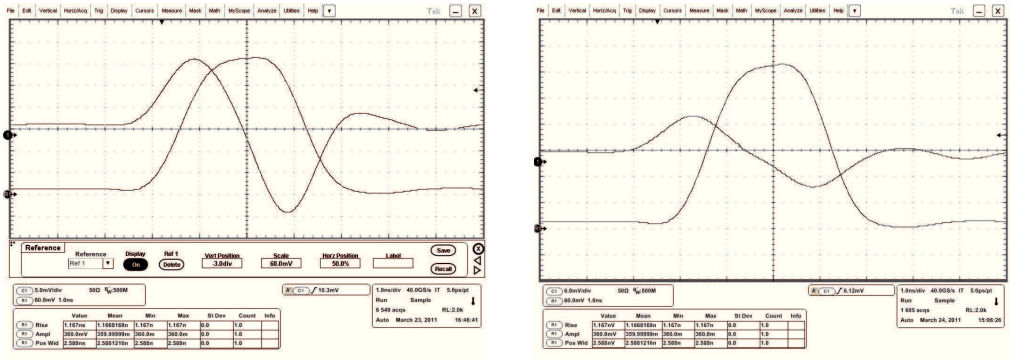

(a) Output asymmetry (b) Output asymmetry with filter

Figure 5.44: *Left:* the difference amplifier output (curve 1), when stimulated with the same signal (A = 360 mV; $FWHM = 2.6$ ns; $t_{rise} = 1.16$ ns) in both inputs (curve R1). The peak-to-peak output amplitude returns 35 mV (9.7% input amplitude). *Right:* the same verification, but introducing a low-pass filter before the positive input in order to equalize the bandwidth responses. There is an improvement, but it is not sufficient (16 mV, namely 4.4%).

democratic in the summation phase, because its contribution depends on which signal portion is overlapped with the others.
Further studies have been elaborated to reduce this discrepancy. A low-pass filter[25]

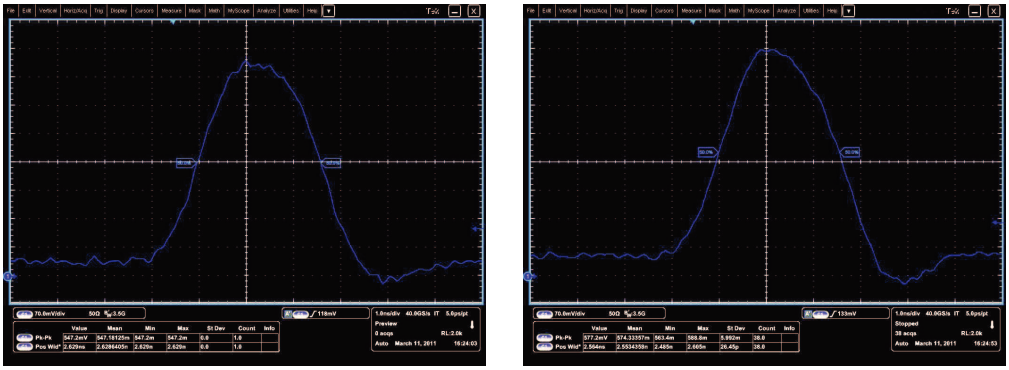

Figure 5.45: *Left:* the pulse at the input of the difference amplifier. *Right:* the same pulse at the output level. The asymmetry is visible mainly on the peak. There is a bump corresponding to the positive edge end, which increases the amplitude of 30 mV with respect to the original pulse.

has been introduced just before the positive input in order to approach the negative input bandwidth. As shown in figure 5.44(b), an improvement is achieved, but it does not completely solve the problem, suggesting that either there are some contributions of the second order that are not well understood or the filter adds new undesired complications.
The input impedance behaviour has been simulated in both amplifiers' inputs. The circuit has been designed to obtain a differential input impedance of 100 Ω, equally divided between the positive and the negative branch. Figure 5.46(a) proves the accuracy up to 2 GHz. Introducing the filter, both impedances are stable around 50 Ω up to

[25] A capacitor of 10 pF has been connected between the positive amplifier input and ground.

300 MHz, but the one that refers to the positive input starts to drop down (Fig. 5.46(b)). Around 800 MHz, the original value is lowered by 20%, dominated by the impedance of the low-filter capacitor, as expected. The component of the positive pulse that enters in the amplifier is lowered in consequence, unbalancing yet again the response. On the one hand, the bandwidth has been equalized, on the other hand part of the positive signal is lost.

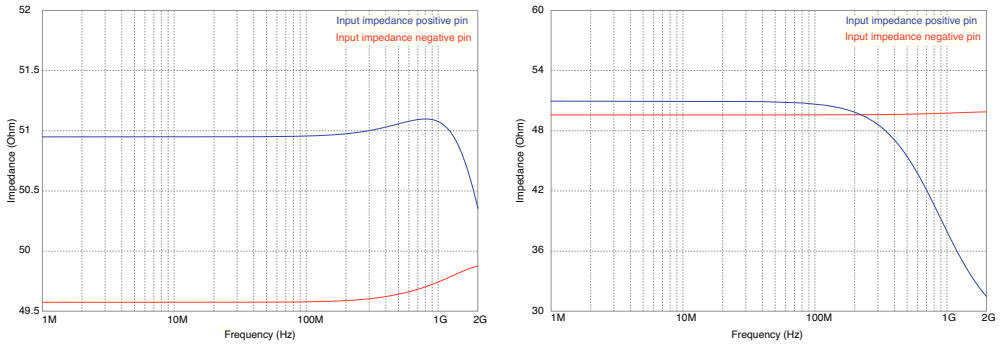

(a) The input impedance (b) The input impedance with filter

Figure 5.46: *Left:* the input impedance of the receiving stage calculated from both inputs of the difference amplifier without the low-pass filter. *Right:* the same simulation with the filter inserted. (© F. Dazzi & G. Galeazzi)

Finally, the different propagation time of both positive and negative components that compose the differential signal are simulated with the filter (Fig. 5.47(a)) and without (Fig. 5.47(b)). The original skew is ∼40 ps (positive output - negative output), which increases to around -100 ps. This delay, due to the low-pass filter, is another contribution that affects the output signal symmetry. In fact, inside the amplifier, the subtraction is performed by slightly shifted pulses. The earlier pulse dominates on the output rising edge, while the later one on the falling edge.
According to the results of the previous analysis, some modifications have been made

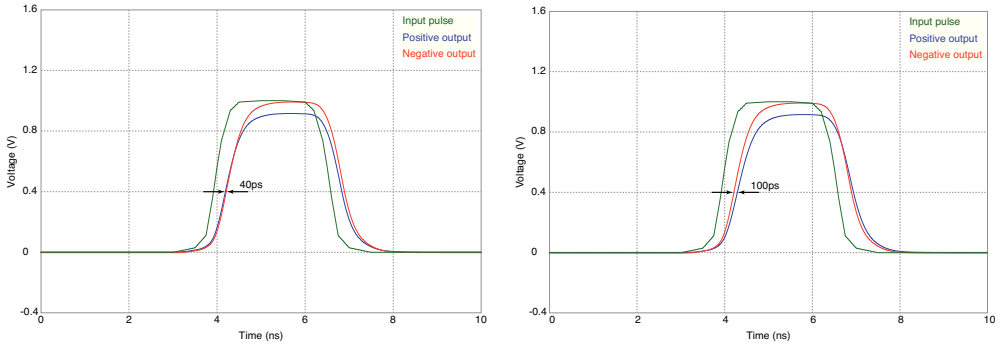

(a) The input propagation time (b) The input propagation time with filter

Figure 5.47: *Left:* the simulated propagation time of both branches (positive & negative) of the same circuit without the low-pass filter. *Right:* the same simulation with the filter inserted. (© F. Dazzi & G. Galeazzi)

to the circuit. The capacitance of the low-pass filter has been lowered to 7.5 pF to reduce both the delay with respect to the negative input and the impedance drop at high frequencies. The resistive divider at the positive input has been changed to increase a

little bit the amplitude of the positive signal. The new resistance values are respectively 22 Ω and 27 Ω. The bandwidth has been further enhanced, bringing down the feedback resistance to 301 Ω. Even the corresponding resistance at the negative input has been modified to 301 Ω to match the expected gain. The resultant performance is quite good and the causes of the original problems seem to be well understood. Currently the bandwidths have been perfectly equalized at the frequency around 950 MHz (Fig. 5.48). To

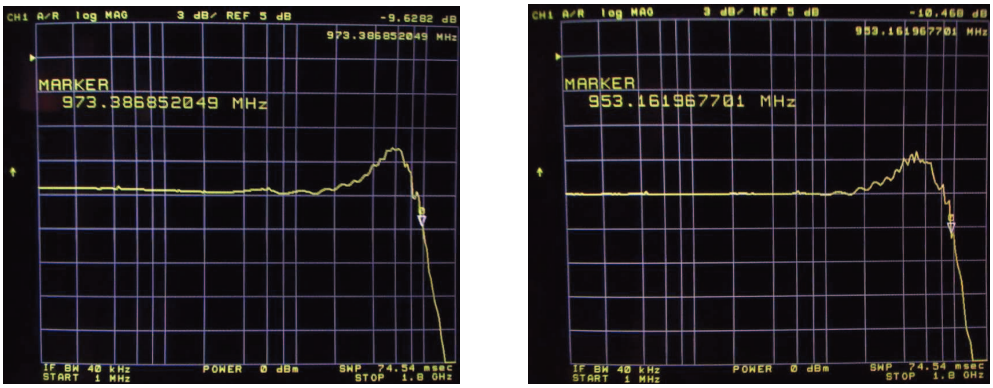

Figure 5.48: *Left:* the positive input bandwidth of the difference amplifier at the receiving stage of the *Sum-board*. The cut-off point is around 970 MHz. *Right:* the same bandwidth (950 MHz) of the negative input.

test the circuit behaviour in the whole bandwidth range, a Digital Signal Generator *Tektronix DTG 5274* coupled with one differential output module *DTGM30* has been borrowed from experimental nuclear physics group. Thanks to the internal clock of 2.7 GHz, it can generate very fast and symmetric pulses with a rise time of ∼200 ps (Fig. 5.49(a)). Repeating the output signal measurement by injecting the same pulse into both inputs shows that even this problem has been shrunk to well under 10 mV (Fig. 5.49(b)).
Using the same equipment, even the two sum stages have been examined showing the

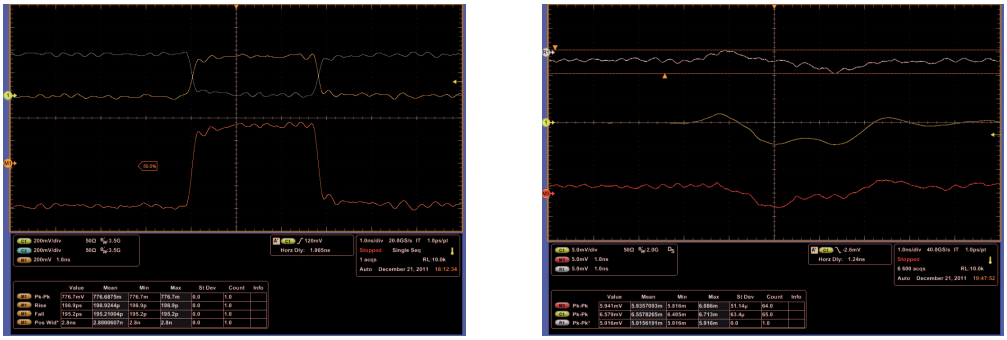

(a) Pulse from Digital Signal Generator (b) Output asymmetry

Figure 5.49: *Left:* the pulse generated by the high-speed Digital Signal Generator *Tektronix DTG 5274*. *Right:* the voltage output asymmetry injecting the same pulse in both inputs. The yellow signal is the amplifier output, while the red one is the math function subtracting the contribution from the pulse generator (white signal).

analogue signal evolution from the board input (Fig. 5.50(a)) to just before the digitalization (Fig. 5.50(b)). The signal becomes little by little smaller, because the entire

board's gain (x 0.25) has been fixed to reach the voltage limit of around 2 V, when all the 19 channels inside the same macrocell are firing. Considering that the pulses will be clipped at around 300÷400 mV, the output would exceed 6.5 V, without the gain normalization.
Further tests are foreseen in the immediate future in order to evaluate the behaviour

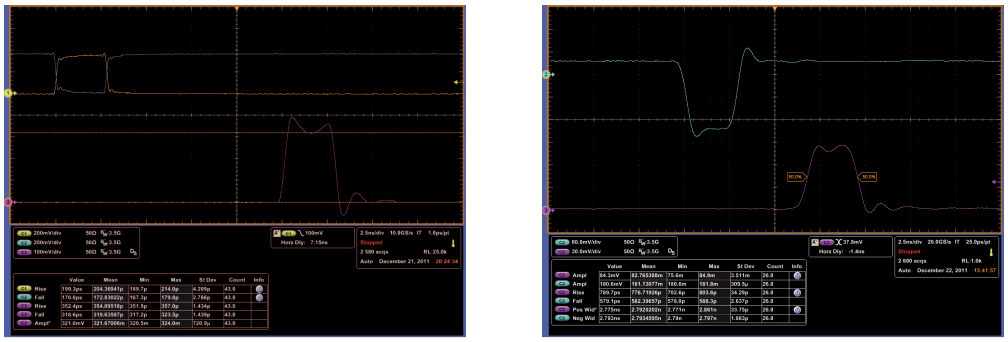

(a) Signal input & receiver stage (b) First & second sum stage

Figure 5.50: *Left:* the differential pulse from the generator (yellow & blue) and the output of the receiver stage (violet). *Right:* the output of the first (blue) and the second (violet) sum stage.

of the board with several injected pulses, randomly delayed.
The bandwidth of the whole board, including the receiver, the first sum and the second sum stage, is shown in figure 5.51(a). The frequency spectrum is extremely flat up to 300 MHz, and the bump underlined in the receiver stage has been removed. The -3 dB limit is measured at ∼650MHz.
The cross-talk has been measured in the long (11÷12 cm) stretch of trace between

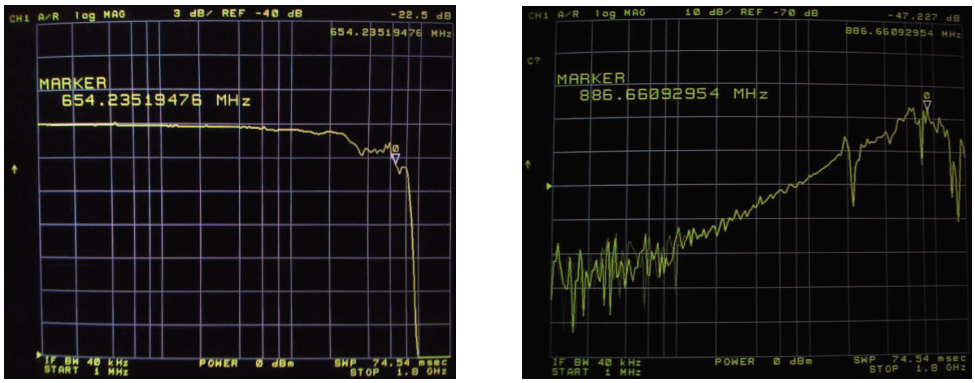

(a) *Sum-board* bandwidth (b) Single far-end cross-talk

Figure 5.51: *Left:* the bandwidth of the whole *Sum-board*. *Right:* The frequency spectrum from 1 MHz to 1.8 GHz of the single far-end cross-talk.

the receiver and the first sum stage. The peak, limited at a very small band around ∼900 MHz, returns -47 dB (0.44%). The cross-talk curve decreases drastically at different frequencies. At 200 MHz, it is around -60 dB (0.1%) and, at 100 MHz, -70 dB. The contribution in the short differential lines at the receiver input, as well as in the spaced traces after the first sum stage, is negligible.

Currently, another amplifier fully compatible with the previous one, *LMH6702* from

National Semiconductor, is under test. This is a wideband operational amplifier designed specifically for systems requiring exceptional signal fidelity. Benefiting from the current-feedback architecture, it offers a good stability at high frequencies. The signal shape with this new amplifier has been simulated with the complete circuit. The result is presented in figure 5.52. The receiving stage of the circuit shown in figure 5.52 has

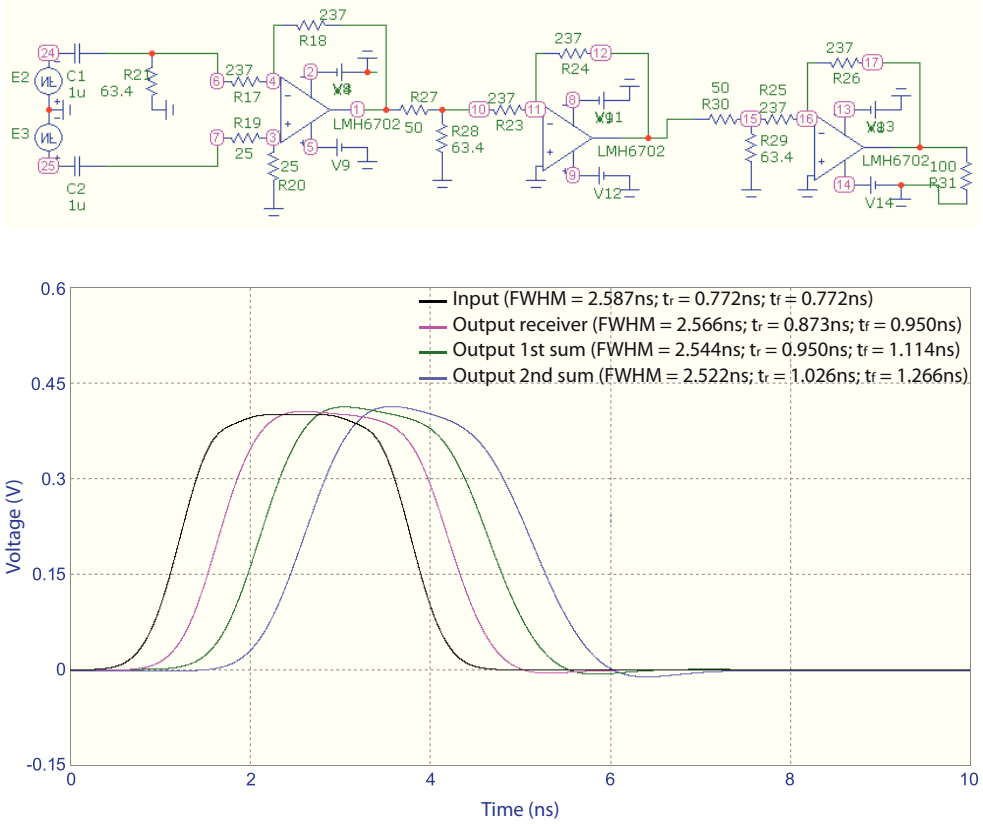

Figure 5.52: On the top, the circuit used for the simulation. The summing stages are simplified with only one input. On the bottom, the performance of the circuit. Shown are the input pulse (black curve), the differential stage output (pink curve), the first sum output (green curve) and the second sum output (blue curve).

been mounted on the *Sum-board* and tested. This is the configuration suggested in the chip data sheet to obtain the best performance. Actually, the signal integrity is really impressive, but the bandwidth is limited at $\sim 500\,\mathrm{MHz}$, which is too low for our purpose. As for the *OPA695*, the bandwidth response increases, lowering the resistor in the feedback. Finally, an acceptable bandwidth is obtained with a $100\,\Omega$ resistor in feedback, another equal to the negative input and a small capacitive filter before the positive input to match the different behaviour of the inputs (3.3 pF). The effect is completely analogous to the one discovered, testing the *OPA695* amplifier (Fig. 5.53(a)). The comparison with the *OPA695* amplifier reveals that the new chip behaves similarly, but with some limitations (Fig. 5.53(b)).
The bandwidth is lower than before, because the rise time of the chip passes from $\sim 307\,\mathrm{ps}$ to $\sim 388\,\mathrm{ps}$, injecting a very steep signal from the generator ($\sim 200\,\mathrm{ps}$). Nevertheless, the oscillations are more evident and the asymmetry is stronger. For these reasons, the *OPA695* is preferred.

The last point deals with the quality control of the digital functions of the board. A

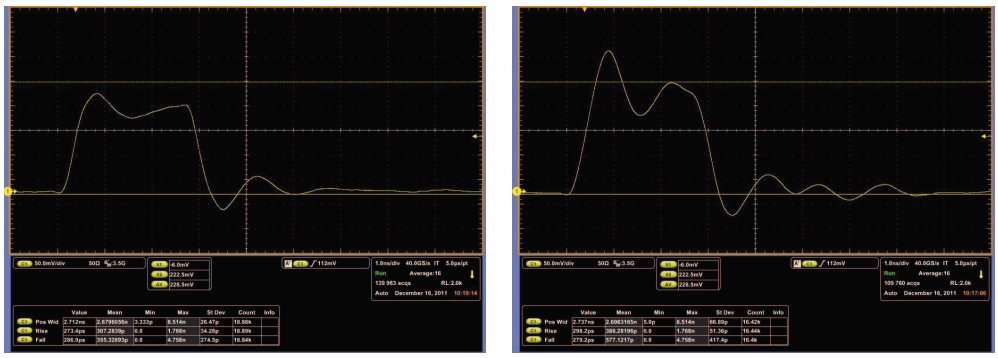

(a) Receiving stage with *OPA695* (b) Receiving stage with *LMH6702*

Figure 5.53: *Left:* the output signal of the final receiving stage, using the current-feedback amplifier *OPA695*. *Right:* the output signal of the receiving stage, this time with the voltage amplifier *LMH6702*.

specific board has been designed (schematics in appendix D) to plug a single *Sum-board* and connect it to the logic analyzer (Fig. 5.54(a)). We have used the logic analyzer *Hewlett Packard 16500B*, which can generate very fast and low differential signals that can be quite similar to the *PMT* pulse. The set-up is shown in figure 5.54(b).

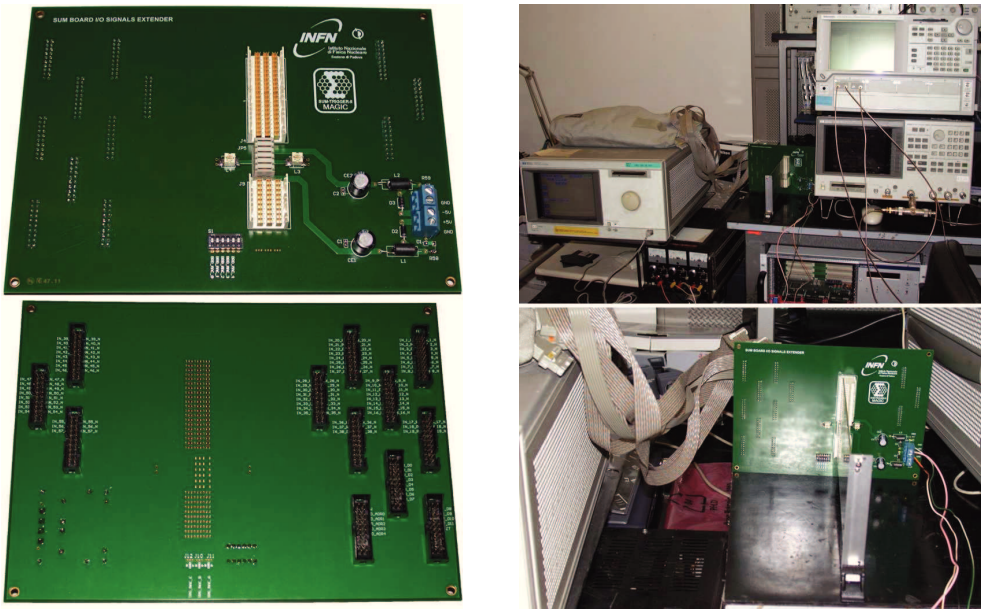

(a) The *Sum-test-board* (b) The quality control with the logic analyzer

Figure 5.54: On the left, the *Sum-test-board* designed to perform a quality control of all the functionalities of the *Sum-board*. On the right, a photo taken during a test.

5.2.2.6 Astro-board and software interface

The *Astro-board*[26] is the final stage of the *Sum-Trigger-II* electronic chain. It interfaces with the control software, processes the macrocell trigger rates and manages the trans-

[26] It means *Analog Sum-Trigger-II prOcessing board*.

mission of the parameters for the automatic adjustment of both the signal amplitude and delay.

Each macrocell can generate its own local trigger, so the *Astro-board* may potentially receive up to 55 triggers at the same time. It merges these local triggers through a global OR[27], sending a single command to the prescaler, which activates the *DAQ* for the recording phase.
The local information is also helpful to avoid high trigger rate alterations due to bright stars in the FoV, artificial light sources, moonlight or variation of the weather conditions. The *Astro-board* reads the trigger frequency of each macrocell, compares it with a predefined allowed range and automatically adjusts the discriminator thresholds of that *Sum-board*, until the rate does not stabilize inside the limits. The feedback approach makes the system very stable.

During the amplitude equalization, the *Astro-board* plays the role of an interface between the *Sum-board* and the *Clip-board*. The desired threshold is loaded to the *Sum-board* fast comparator, the channel under test is enabled (the rest, in the same macrocell, is disabled) and the first attenuation value is set in the *Clip-board*. The trigger rate is recorded and saved via software control. Then, the *Astro-board* changes the attenuation value and registers another rate. The process continues until there are enough points that well fit a cumulative function and the transition region from 100% to 0% of trigger counts is well covered. Finally, the software calculates the optimal value, which is at a count rate of 50%, and orders the *Astro-board* to set the channel at this precise amplitude (Fig. 5.55(a)).

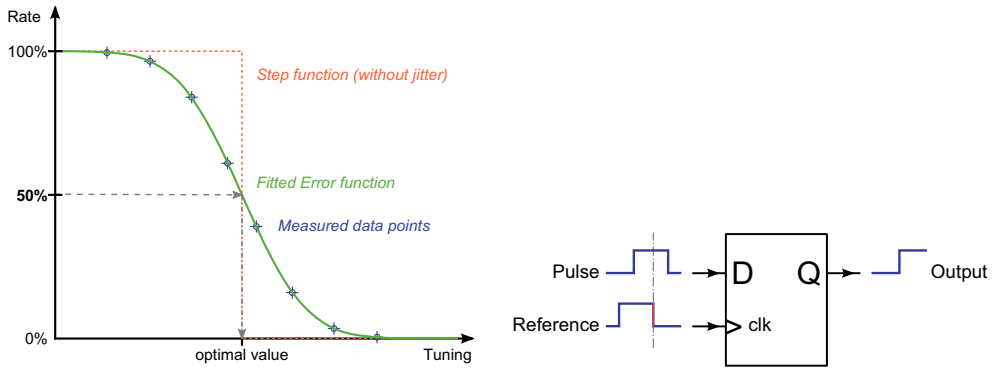

(a) The cumulative distribution function

(b) The flip-flop for the delay adjustment

Figure 5.55: *Left:* the cumulative distribution function. Since the count rate distribution is Gaussian, the cumulative function can be described with an error function ($f(t) = \frac{2}{\sqrt{\pi}} \int_0^t e^{-x^2} dx$). The 50% value coincides with the point where the second derivative is nullified, namely it is the peak of the Gaussian distribution. *Right:* the utilization of a fast flip-flop to synchronize a signal with the reference one. When the edge of the reference signal activates the clock, the input state is loaded in the output pin. Delaying the pulse, it is possible to assess the relative timing difference.

A very similar procedure is adopted for the delay synchronization, but it uses different devices of the *Astro-board*. The signal timing is determined counting the output rate either of an *FPGA* input register or of a fast flip-flop *NB7V52M*[28], when the ref-

[27]The OR operator performs logical disjunction on two boolean expressions. If either expression evaluates to the logic state "HIGH", OR returns "HIGH". If neither expression evaluates to "HIGH", OR returns "LOW".

[28]The NB7V52M is a 10 GHz differential D flip-flop. The differential input and the clock incorporate

erence pulse[29] is connected to the clock port (Fig. 5.55(b)). Then the signal is delayed relatively to the reference one, changing the bias voltage of the corresponding delay line in the *Clip-board*. Even in this case, the optimal point is selected as 50% of the cumulative distribution function.
The *ON Semiconductor* flip-flop offers an exceptional short set-up time (typically 15 ps) and a maximum random jitter of 0.8 ps *RMS*. These features eliminate the possibility of having the flip-flop in a metastable state.

Both previous procedures will not be enabled for a pixel one step at a time, but the calibration is performed in parallel, activating many channels in distinct macrocells. In this way, the whole trigger area can be covered in 27 rate scans. The time required by a single run is tied to the required resolution, but in the worst case two minutes should be sufficient. In less than one hour, the complete equalization should be done.

The board, which is under the responsibility of the *MPI* team, is still in the design phase and there are no prototype *PCBs* to test. It will be a full digital 9U board, located in the last position of the upper crate row. The core will be an *FPGA Altera Cyclone IV*, which will manage the 55 blocks for the amplitude and delay adjustment. The global OR trigger will be generated either in a dedicated *PLD* or in a wired OR in order to increase the timing precision. The board will be equipped with many transceivers for the data transmission between the *Sum-boards* and the *Clip-boards*, by means of the *Sum-backplane* and the *SPI-backplane* respectively. The general block diagram is described in figure 5.56.

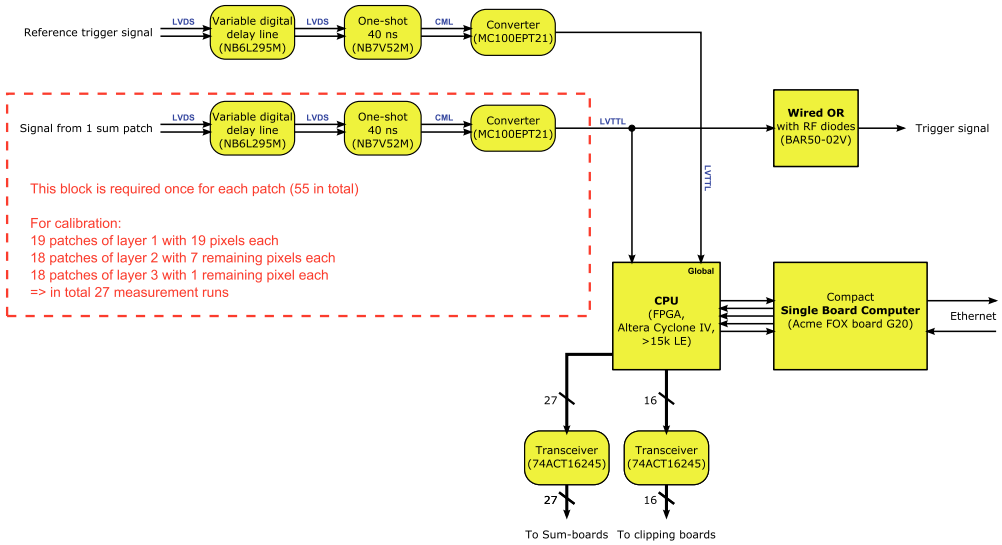

Figure 5.56: The main block diagram of the *Astro-board*. (Courtesy of D. Häfner)

5.2.2.7 SPI-backplane

The *SPI-backplane* is a 3U passive board with 18 *DIN41612* 96 contact connectors for the connection of the *Clip-boards* and another one for the *Astro-board*. The main functions are the power distribution and the availability of a serial bus for the data transmission to the *Clip-boards* (Fig. 5.57).

dual internal 50 Ω termination resistors, accepting *LVDS* logic levels. The chip is offered in a low profile 3×3 mm, 16 pins *QFN* package.

[29] It is the generic signal transmitted in a channel belonging to the *Sum-Trigger-II*.

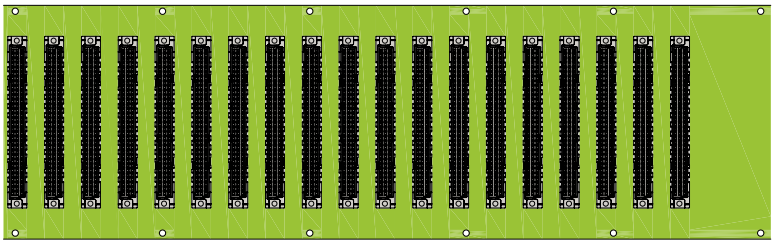

Figure 5.57: The 3U *SPI-backplane* with 19 connectors.

The *SPI* serial bus is based on the master/slave mode, where the master device provides the clock and starts the data communication. This bus works with a single master and with one or more slave devices. In the *Sum-Trigger-II* case, the master is placed in the *Astro-board*, while each slave, the *Clip-board*, is not connected by a daisy chain[30] configuration. From each slave, an independent bus is routed to the master, in order to minimize the jitter even in the data transmission.
This serial protocol consists of 4 lines:

SCLK: serial clock from the master. This is a control line.

MOSI - SIMO: master output and slave input. This is a data line (Tx).

MISO - SOMI: master input and slave output. This is a data line (Rx).

SS: slave select (active low). This is a control line, one for each slave.

They are administered by the central *FPGA* of the *Astro-board* and dedicated *PLDs* installed in each slave.
The transmission is activated when the *SS* is "LOW". One bit per clock cycle is sent from *MOSI* to *SIMO* and from *SOMI* to *MISO*, and it is recorded in a shift register. To stop the communication, the *SS* bit is set to "HIGH" again.

5.2.3 Prototype boards test

A small prototype of the new *Sum-Trigger-II* system, able to manage eight channels, has been designed and tested at the *MAGIC* site by the *MPI* team. The aim was to demonstrate the functionality and the reliability of the new design, especially the signal adjustment procedure.
This prototype was composed of four small boards (Fig. 5.58):

Clipping board prototype: It is a simplified version of the *Clip-board*. The input signals are amplified in two steps by a factor of 20. Then, they are equalized in amplitude and time using a 12-bit resolution serial *DAC*[31]. Finally, the clipping is applied with the amplifier *LMH6553*.

Old summing board: This is the *Sum-board* of the old system. Here, only the summation stage is performed.

[30] A daisy chain is a wiring scheme, in which multiple devices are wired together in sequence or in a ring.
[31] The *DAC7568-A*, from *Texas Instruments*, for the attenuation, while the version *-C*, with a wider range, for the delay lines.

Discriminator board prototype: This board provides the discrimination stage and the counting rate electronics, currently included respectively in the *Sum-board* and in the *Astro-board*. Very fast *ECL* comparators (*MAX9600*) are followed by one-shot chips to stretch the signals for the signal processing.

Computer control board: It manages all the functions for the data transmission control and the software interface. It houses an *USB* interface module (*IO-Warrior56*[32] from *Code Mercenaries*), the *SPI* master *CPLD* and the *RS-485* transceivers. A basic *C* software, with the *IO-Warrior56* dynamic library installed, communicates to the computer control board.

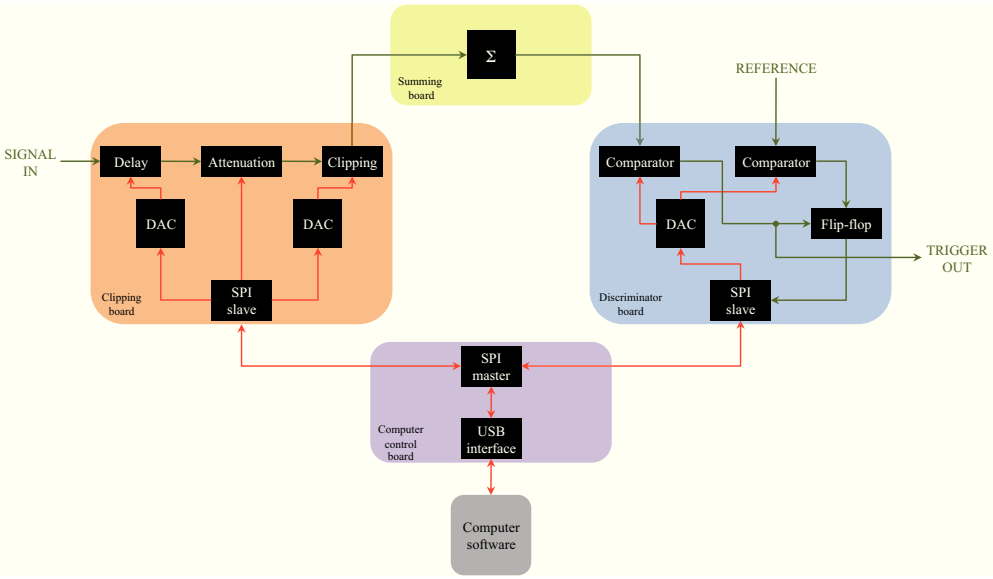

Figure 5.58: The functional blocks of the prototype system. The green lines show the signal and the reference path, while the red ones indicate the controls.

For the test, nine unused channels were drawn from the analogue output of the receiver boards. One of them was used as a reference signal for the timing adjustment. The timing and the delay flat-fielding was performed analysing interleaved calibration pulses (25 Hz), triggered applying an artificial gate centred on them. This prevented any corruption of the equalization, which might have introduced pulses from background or showers.
The recorded counting rates during the delay equalization are inserted in the plot presented in figure 5.59(a). They optimally fit with an error function, proving the Gaussian nature of the jitter distribution. The crossing points between the horizontal and the vertical arrows indicate when the reference and the signal under test are synchronous. The resultant resolution is very good, around 100 ps as demonstrated in figure 5.59(b). Moreover, long-term measurements revealed a high stability and the numbers were confirmed even after some days had passed.
The amplitude calibration was not as good as the timing one, but the cause can be pinpointed to the large fluctuations of the pulse. Its amplitude changes up to 10% in a time-scale of 20 minutes, sometimes manifesting large deviations, far from a Gaussian

[32] It is an universal *USB* controller with 50 I/O pins, which contains a high-speed *USB* to *SPI* converter.

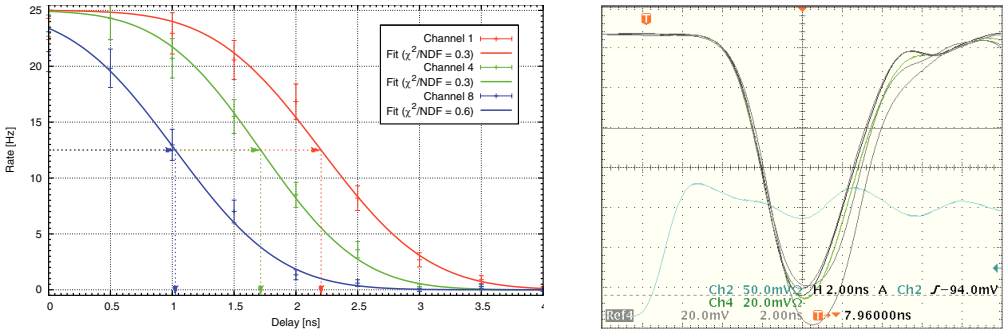

(a) The delay error function (b) Pulses delay adjustment

Figure 5.59: *Left:* the delay error function of three channels. The 50% rate value is marked with an horizontal arrow. *Right:* an image of the analogue pulses at the output of the summation stage (inverted polarity), after the delay adjustment. The blue signal is the gate for the selection of calibration pulses. (From [65])

distribution. However, looking again the pulses in figure 5.59(b), one can see that the tolerance is less than 20%.

This experience reinforces the original assumption that an accurate and recurrent calibration of both signal amplitudes and delays is fundamental. In fact, the measured amplitude variation in the whole trigger area is on average of the order of 30%, while the time jitter distribution is spread over 1 ns [65]. These fluctuations are caused by intrinsic properties of the electronic chain, but also by external conditions such as temperature and humidity. They might be affected by strong changes, even in the short term, so it is mandatory to keep them well under control.

Finally, some rate scans were performed using a clipping level of 6 phe, during the normal *MAGIC* data-taking (Fig. 5.60). The cosmic rate is around 23 Hz, which is roughly in agreement with the classical single macrocell rate of the old system ($\sim$ 50 Hz). These measurements confirm the reliability of the new concept for a small group of

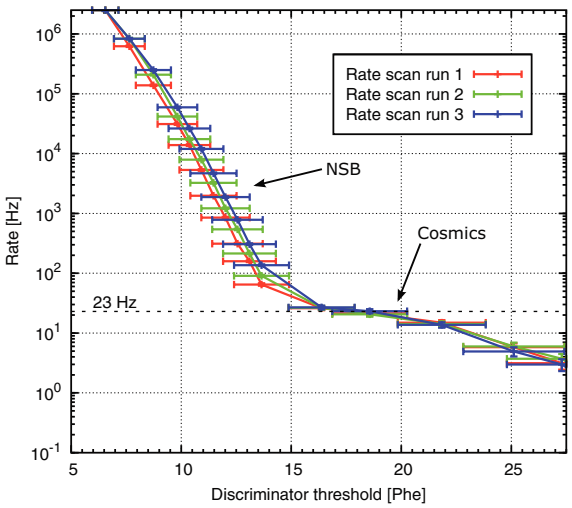

Figure 5.60: Three rate scans recorded during normal data-taking with the prototype of the new system. Below 15 phe the trigger rate is dominated by the *NSB* while, above 15 phe, $\sim$ 23 Hz of cosmic events are registered. (From [65])

pixels. The following step will be to check the same specifications for the whole trigger area.

6

The new stereoscopic trigger: MiniPulsar

LOOKING with two eyes is better than with one. This may be a strange statement to summarize the essence of this chapter. By enabling the stereoscopic observation with more than one telescope, several improvements are achievable: lower energy threshold, better angular resolution, more precise impact parameter determination, improved energy reconstruction and higher sensitivity.
In this chapter, the main features and some technological aspects of the stereoscopy are presented. Later, an upgrade of the *MAGIC* trigger system, based on the custom and multi-purpose *MiniPulsar* board, will be described in detail.

6.1 Stereoscopy

In the standard definition, stereoscopy refers to the optical technique to create a three-dimensional (*3-D*) illusion, exhibiting two offset images independently to the left and right eye. More generally, it is the enhancement of the depth perception from a simple two-dimensional (*2-D*) plane.
The stereoscopy basis resides in the geometrical stereopsis principle. The human eyes, located in two distinct lateral positions some centimetres away, record slightly different images. This disparity of the eyes is exploited by the brain, which merges the images and derives supplementary information regarding the depth and the spatial position of the object in view. The images must be presented simultaneously and well aligned to the eyes.
The sensory human experience of Nature relies on a 3-D space, where width, height and depth are considered unitary elements of an orthonormal base. In contrast, most of the communication tools are based on *2-D* supports, like photographs, book images, paintings and technical projection designs. It is spreading the demand to easily pass from one dimension to another. Stereoscopy reconstructs *3-D* objects completely by matching some (≥ 2) portable independent 2-D supports.
The same approach is used in many other environments such as television, cinema, aerial topography, civil and mechanical engineering and science. For instance, in biology and chemistry, complex molecular structures are often rendered in stereo-pairs. In most cases, it can be applied to any mathematical parameter, which is a function of two variables.
Another feature of stereoscopy, similar to the method used in astronomy, is expressed by

the calculation of the distance from the camera and an object in the picture [125, 101]. The differences between the images, the cameras' separation, the focal length and some geometrical derivations are the main elements used to estimate it. The precision of the reconstructed position is subordinated by single image quality and the cameras' disposition in relation to the selected target. In this context, high resolution is not sufficient to obtain an elevated quality image. The background must be distinguished from the object, which is not possible if, for example, they have the same uniform colour. On the contrary, a variegated background in contrast with the area of interest, emphasizes the stereoscopic effect.
It will be made clear, in the next subsection, that the stereo *IACT* technique has many affinities with the optical stereoscopy described above. The final goal is different, but the way in which the single images are combined to get further discernments, is the same.

6.1.1 The stereoscopic technique in IACT telescopes

It has been demonstrated in chapter 2, that the *IACT* technique is strongly based on the analysis of imaging parameters. One of the productive ways to improve the *VHE* γ–rays detection quality is to make use of stereoscopy.

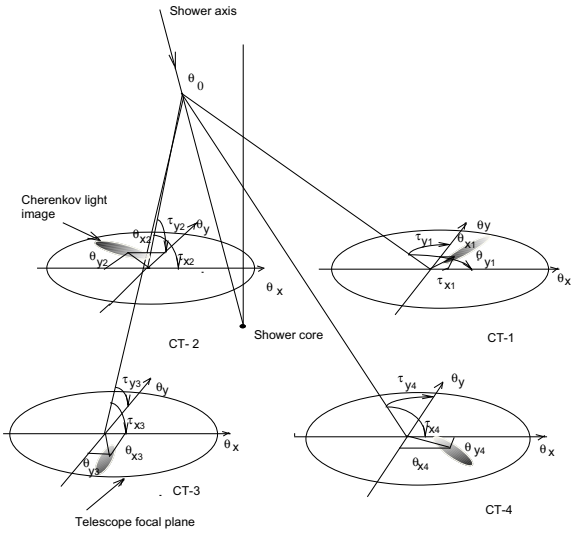

Figure 6.1: An example of an atmospheric shower image reconstruction with a stereo array of four telescopes. (From [1])

In *VHE* gamma astrophysics, stereoscopy records the image of an extended atmospheric shower, initiated by a γ–ray, with at least two neighbouring telescopes at the same time (Fig. 6.1). The achievable advantage is stringently related to a better image morphology reconstruction and an additional time constraint at the trigger level. Compared to the mono observation, stereoscopic data recording allows a precise three-dimensional determination of the shower core position, an effective *Hillas* parameter extrapolation, a good energy resolution and a more stringent rejection of muons, hadrons and *NSB* flashes, which rarely hit two or more telescopes contemporaneously. This should open a new research window toward sources with weak flux or a still not well-defined spatial distribution of the γ–ray emission region. Moreover, the stereo approach should accurately resolve extended sources inside 1° and, concerning the temporal profile, the strong variable *VHE* emitters.

Specific requirements drive the design of the *IACT* array. It is important to calculate which is the best distance between the telescopes (D_{tel}). Considering that the Čerenkov light pool, from an *EAS*, evolves in first approximation in a circle with a radius (R_{eas}) of more or less 120 m (Fig. 6.2), the maximum acceptable D_{tel} is fixed by R_{eas}.

Then, the stereo effective area should be determined estimating the common geomet-

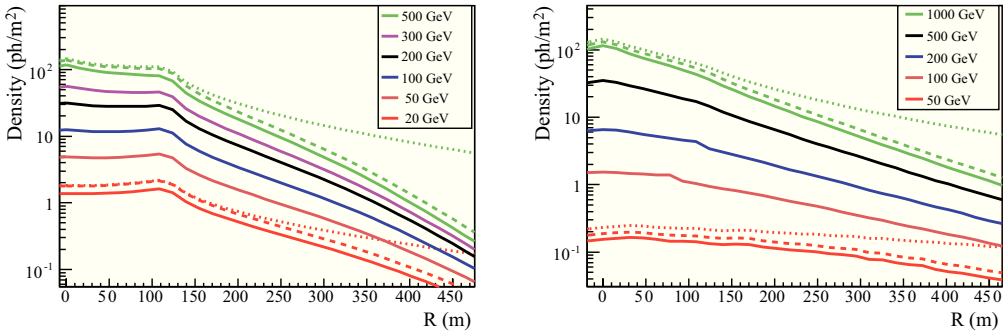

(a) Lateral density distribution: γ–rays (b) Lateral density distribution: protons

Figure 6.2: The average lateral density distribution for different primary energies and impact parameter 0. On the left, due to primary γ–rays at 2.2 km a.s.l.. On the right, due to primary protons at 2.2 km a.s.l.. Dotted, dashed and solid lines present distinct Monte Carlo sets. Dotted lines do not consider atmospheric absorption, dashed lines take into account the light in the camera FOV (5°), while solid lines add the constraint of atmospheric absorption. (From [122])

rical light pool portion seen by the telescopes in trigger coincidence[1] (Fig. 6.3(a)). We can say that the stereo collective area is proportional to the intersection between the collective areas of individual telescopes in stereo trigger (Fig. 6.3(b)). The single col-

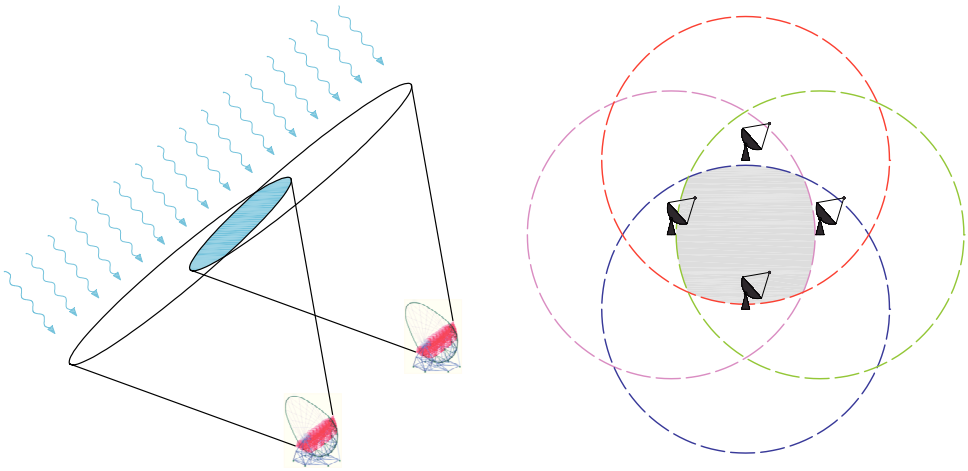

(a) Stereo light pool portion (b) Effective area intersection

Figure 6.3: On the left, a sketch of the common geometrical light pool portion in a *stereo-cell* of two telescopes (not to scale). The dimension of each cone is determined by the size of its camera trigger region. On the right, the effective area intersection at the ground level, for an *IACT* array. (Images credit: A. Bortoluzzi & F. Dazzi)

lective area for a primary γ–ray from a point source, can be mathematically expressed as

$$A^{\gamma}_{eff} = 2\pi \int_0^{\infty} P^{\gamma}(E, r)\, r dr \tag{6.1}$$

[1]Hereafter, the sub-array, in which the telescopes are configured to be in trigger coincidence, is called *stereo-cell*.

where $P^{\gamma}(E,r)$ is the detection probability for a gamma with energy E and impact parameter r. In case of n telescopes in coincidence, the global detection probability becomes

$$P^{\gamma}_{array} = \begin{cases} P^{\gamma}_{telescope-1}(E,r) \\ \cdot \\ \cdot \\ \cdot \\ P^{\gamma}_{telescope-n}(E,r) \end{cases} \tag{6.2}$$

Finally, the stereo effective area results

$$A^{\gamma}_{eff}(n) = 2\pi \int_0^{\infty} P^{\gamma}_{array}(E,r)\; r dr \tag{6.3}$$

Reducing the D_{tel} and the number of telescopes in coincidence, the common effective area increases and consequently the energy threshold is brought down.
Unfortunately, a third aspect prevents reducing the distance between telescopes too much. In fact, for very small D_{tel}, the correlation between the image projections is tangible and every benefit from the stereoscopy is nullified. In addition, when the shower's core is close to the telescopes ($\lessapprox 50\,\mathrm{m}$), the image starts to become circular rather than elliptical and the indetermination of the Čerenkov light intensity starts to be considerable (Fig. 6.4(a)). It is reasonable to find a likely compromise in the range $R_{eas} \div R_{eas}/2$.
The previous assumption is always valid for a source at zenith angle zero. For different

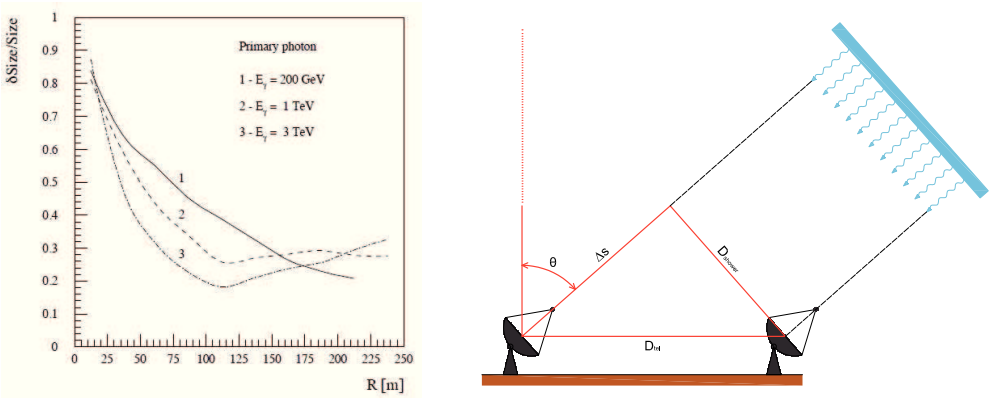

(a) Čerenkov light fluctuation

(b) Definition of D_{shower}

Figure 6.4: *Left:* the fluctuations of the total number of photoelectrons produced in the telescope camera by γ–rays at different energies. (From [2])
Right: the telescopes' separation, met by the Čerenkov light from an *EAS* (D_{shower}). (Image credit: A. Bortoluzzi & F. Dazzi)

sky positions, the crucial parameter is not the distance between the telescopes on the ground, but on the plane perpendicular to the shower axis (D_{shower}). This is the telescopes' distance, viewed by the Čerenkov photons (Fig. 6.4(b)). It is a function of both the zenith and azimuth angle, where the maximum discrepancy with D_{tel} comes out when the shower axis ($\sim$ pointing direction) is on the same plane of the joining telescope line. The effective distance becomes

$$D_{shower} = D_{tel} \cdot \cos(\theta) \tag{6.4}$$

where θ is the zenith angle. Hence, the geometrical array configuration, as seen by photons, changes for different observing directions. Up to a zenith angle of 50° the variation is less than $\sim 25\%$.

The precision used to calculate the shower parameters, conversely to the energy threshold, increases when 3 or 4 telescopes are used in conjunction. The reason is that, with only two views, the events that fall close to the hypothetical line passing through the telescopes have the same projection angle and may not be reconstructed. As shown in figure 6.5, it is more often possible to find some two out of four quite different independent projections, which allow a very distinct gamma/hadron separation. The

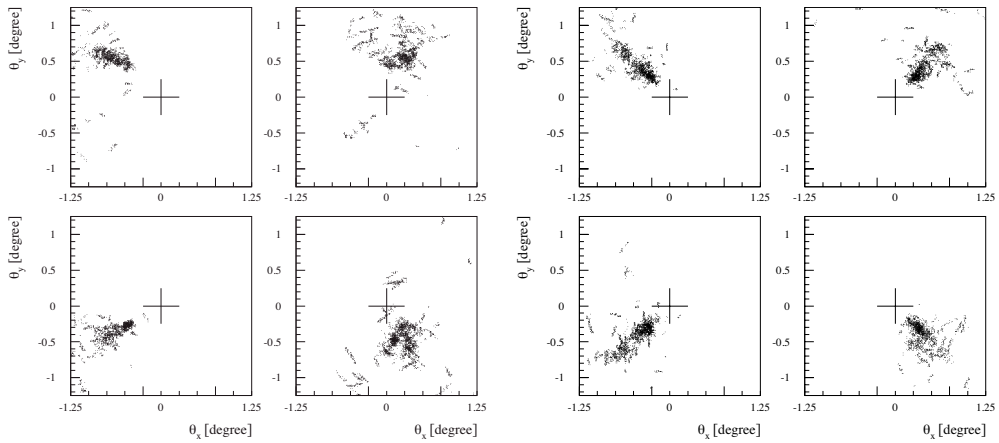

(a) Proton stereo projection (b) Photon stereo projection

Figure 6.5: Čerenkov light images of vertical 100 GeV γ–ray (right) and 300 GeV proton (left) detected by an array of four telescopes spaced 100 m apart from each other. Both showers cross the centre of the *stereo-cell*. While two proton's projections look like γ–ray (narrow and regular), the other two images indicate the hadronic nature. (From [1])

best array's layout is configured to have always a triangular or a quadrangular *stereo-cell* disposition with $\sim 60 \div 120$ m side [1]. This is the right compromise which takes into account the collective area dimension, the background rejection power and the quality of the shower image that is built up. Even the symmetry and the orientation of the *stereo-cell* arrangement is important to optimize the effective area, because it is also a function of the azimuth angle [95, 44]. The placement on the ground of the main current *IACT* telescopes is shown in figure 6.6.

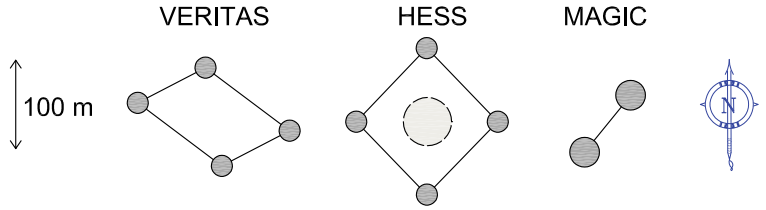

Figure 6.6: The placement layout of the three main *IACT* telescopes. The dashed circle indicates the *HESS-II* telescope under construction. The drawing is scaled-down except for the telescope dishes, which are double the scale size. (Image credit: A. Bortoluzzi & F. Dazzi)

The stereoscopic technique should be very powerful, even in the not sufficiently

explored energy domain between 10÷100 GeV [1]. A Monte Carlo simulation of an *IACT* array, composed by a square of four medium size telescopes (⌀ 10 m), shows a gamma detection rate peak around 100 GeV (Fig. 6.7(a)). The telescope performance is quite conservative for a typical IACT: a) *PMT* quantum efficiency of 15%; b) mirror reflectivity 85%; c) reflective surface $\sim 80\,m^2$. It is evident that the rejection power for a point source is very high, keeping alive only the noise contribution from electrons, which appear to be very similar to γ–rays (Fig. 6.7(b)).

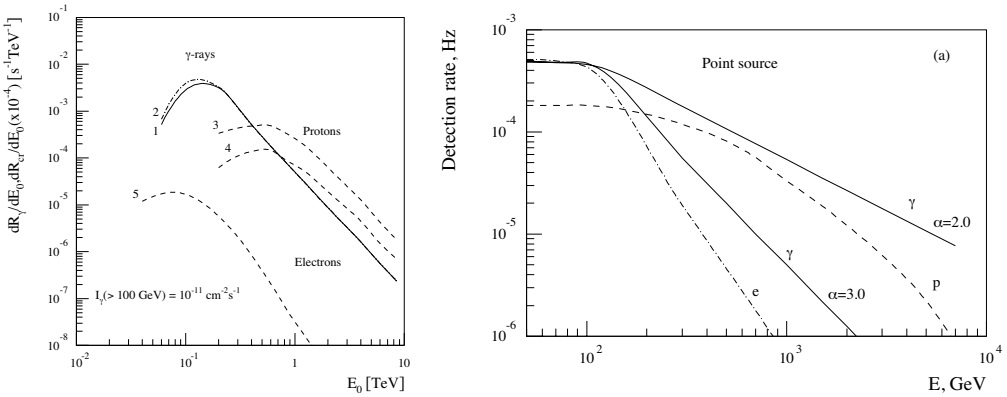

(a) Differential detection rates

(b) Rates after analysis cuts

Figure 6.7: *Left:* the differential detection rates of protons, electrons and a γ–ray point source (index -2.5) with an *IACT* array of four telescopes. Curves 2 and 4 are calculated with pixel size 0.15°, all others with size 0.25°. *Right:* the detection rates of γ–rays (solid lines), protons (dashed) and electrons (dot-dashed) after relaxed software imaging cuts have been applied. (From [1])

After the best single *stereo-cell* configuration is selected to achieve the requirements for a stringent background suppression, further progress is made by expanding the collective area, thus increasing the number of *stereo cells* mutually connected and partially overlapped.

6.1.2 The MAGIC stereoscopic system

The *MAGIC* stereoscopic system is composed of two *IACT* telescopes placed at a distance of 85 m and an angle of $\sim 38°$ North-West. As explained in the previous subsection, this configuration, with only two telescopes, is not optimized for the cosmic ray background suppression and the image parameter reconstruction, but it is perfect to guarantee a wide stereo effective area and a low energy threshold. Figure 6.8 shows

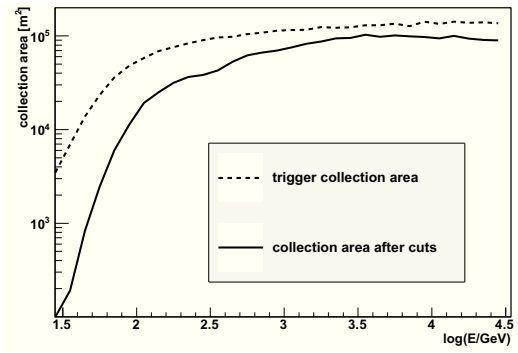

Figure 6.8: The Monte Carlo simulation of the *MAGIC* stereo γ–rays collection area at the trigger level (dashed line) and after the standard analysis cuts. (From [40])

a flat collection area of $10^5\,\mathrm{m}^2$ for energies higher than 1 TeV, while it is reduced to a factor 10 around 100 GeV.
The stereoscopic observation mode records only events that trigger both telescopes inside a temporal gate of 100 ns. The single telescope trigger imposes the condition that three close compact pixels are simultaneously (< 6 ns) above threshold. The *NSB* and muon rejection is severe, reducing the final rate to about 200 Hz, mainly due to protons. To compensate for the low number of telescopes in the array, a complex and advanced off-line stereo analysis has been developed. Innovative algorithms succeed in extracting accurately stereo parameters such as the impact point of the shower in the plane perpendicular to its axis (impact parameter) and the height of the shower maximum. The obtained geometrical parameters are then used to extract the energy of the primary particle, with a resolution as good as 15÷20% (Fig. 6.9(a)). The energy threshold, namely the peak of the energy distribution of γ–ray events after trigger, is approximately 50 GeV for a point source with a differential spectral index of -2.6.
A relevant advancement in the stereo analysis is made by calculating the primary par-

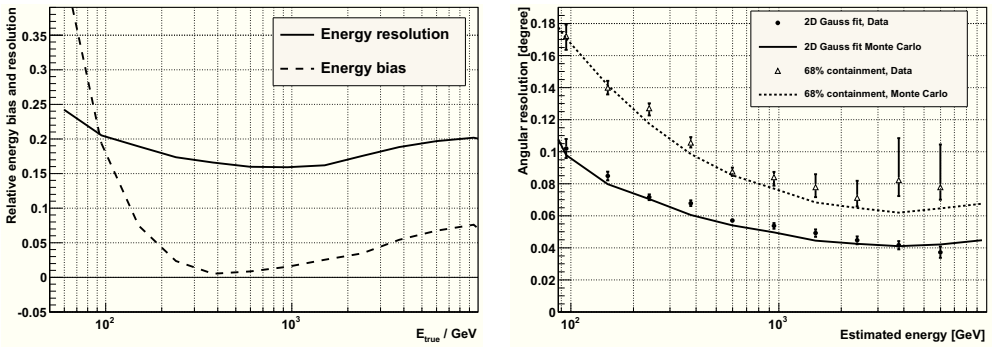

(a) Stereo energy resolution (b) Stereo angular resolution

Figure 6.9: *Left:* the stereo energy resolution (solid line) and the bias (dashed) obtained with the Monte Carlo simulations of γ–rays. The resolution corresponds to the σ of the Gaussian distribution $(E_{rec} - E_{true})/E_{rec}$, while its mean value is the bias. Mild cuts are applied: hadronness < 0.6, $\theta^2 < 0.03$. *Right:* the stereo angular resolution as a function of the estimated energy obtained with the *Crab* nebula data sample (points) and compared with the Monte Carlo simulations (lines) for the 2-D Gaussian fit (solid line, full circles) and the 68% containment radius (dashed line, empty triangles). The resolution is defined as the standard deviation of the 2-D Gaussian distribution of the reconstructed events direction. For a point-like source, it coincides to a radius containing 39% of the γ–rays. (From [40])

ticle direction. The simple crossing point between the main axis of the event ellipses is not always satisfactory and an upgraded method, the so-called *Stereo DISP-RF*, has been introduced. For each telescope image, the *DISP* parameter (the angular distance between the centre of gravity of the image and the estimated source position) is estimated using multidimensional decision trees (*Random Forest*). Then, the crossing point of the main axes and the two *DISP* parameters are combined. The resulting angular resolution is considerably improved, as underlined by the plot 6.9(b). The *Stereo DISP-RF* method allows us to obtain a precision of $\sim 0.07°$ at 300 GeV.

In the domain of few hundred GeV, the current *MAGIC* sensitivity[2] is less than 0.8% of the *Crab* nebula flux, in agreement with the Monte Carlo predictions (Fig. 6.10(a)). In comparison with the single telescope performance, the improvement in significance

[2]The minimum flux that assures a $5\,\sigma$ detection ($N_{excess}/\sqrt{N_{bgd}}$) in 50 h of observation.

is compatible by a factor 2÷3. An incontrovertible proof of the obtained progress is given by the stereo *Crab* nebula spectrum in the range 70 GeV to 11 TeV, which agrees with the results of the other *IACT* telescopes Fig. 6.10(b).

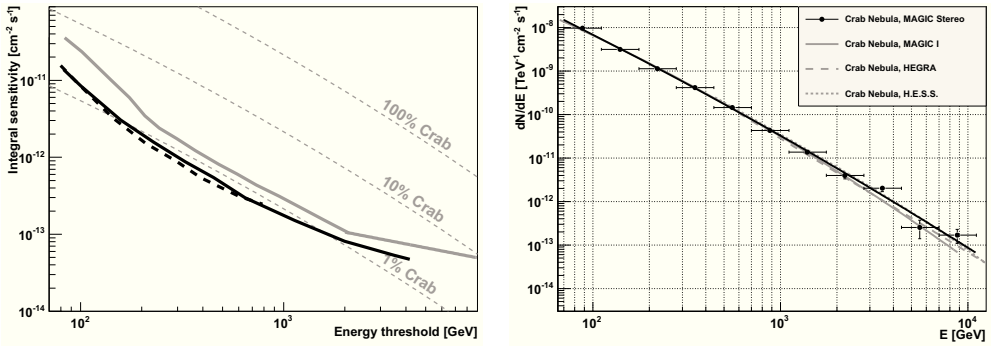

(a) Stereo integral sensitivity

(b) Stereo *Crab* nebula spectrum

Figure 6.10: *Left:* the integral sensitivity of the *MAGIC* stereo system for data (black solid line) and Monte Carlo (black dashed line), compared with the *MAGIC–I* telescope (solid gray line) one. *Right:* the spectrum of the *Crab* nebula obtained with the *MAGIC* stereo system (black curve) compared with other experiments (gray curves). (From [40])

6.2 The MAGIC stereoscopic trigger

In 2009, the second telescope (*MAGIC–II*) started to operate with *MAGIC–I*. During the commissioning phase, they worked independently, tracking simultaneously the same sources. The off-line analysis compared the arrival time in both telescopes, flagging as originated by the same shower if inside a small temporal gate of some tens ns. This was a preliminary and simple way to detect stereo images, in order to extract the stereoscopic parameters. At the analysis level, the procedure worked very well and immediately the effectiveness was clear in the event reconstruction. Nevertheless, no hardware stereo trigger was applied to reduce the accidental and muon rate that could also improve the dead time and lower the pixel threshold without saturating the *DAQ*. In order to work in a muon-free background environment, a narrow time coincidence trigger between the two telescopes was implemented in a second stage. Obviously, this stereo trigger decision comes only after the local triggers have been selected. As shown in figure 6.11, the single telescope trigger pattern is formed by eight different local signals [55]. Some of them, such as the *LT1* (standard digital trigger), *SUMT* (analogue Sum-Trigger) and the *LT3* (stereo trigger), are source triggers, while others, such as *CAL* (calibration trigger), *PED* (pedestal trigger) and *INJ* (pulse injector trigger), are used for calibration and technical runs. The readout can be activated by one of these local triggers or by the stereoscopic trigger *LT3*.
The interface between the local triggers and the readout is made by the *prescaler*. This board, located in the *LT2* system, uploads the trigger pattern and controls the rate to prevent the saturation of the acquisition system. All information is provided via a *LVDS* bus in order to exclude faint triggers due to the noise.
Some examples could optimally clarify the concept of the system. Supposing that the *SUMT* is enabled in *MAGIC–I*, and *LT1* in *MAGIC–II*, the saved events have respectively passed the *Sum-Trigger* and *Level 1 trigger* barrier. On the other hand, when the *LT3* bit is enabled, showers that exceed in both detectors the standard local

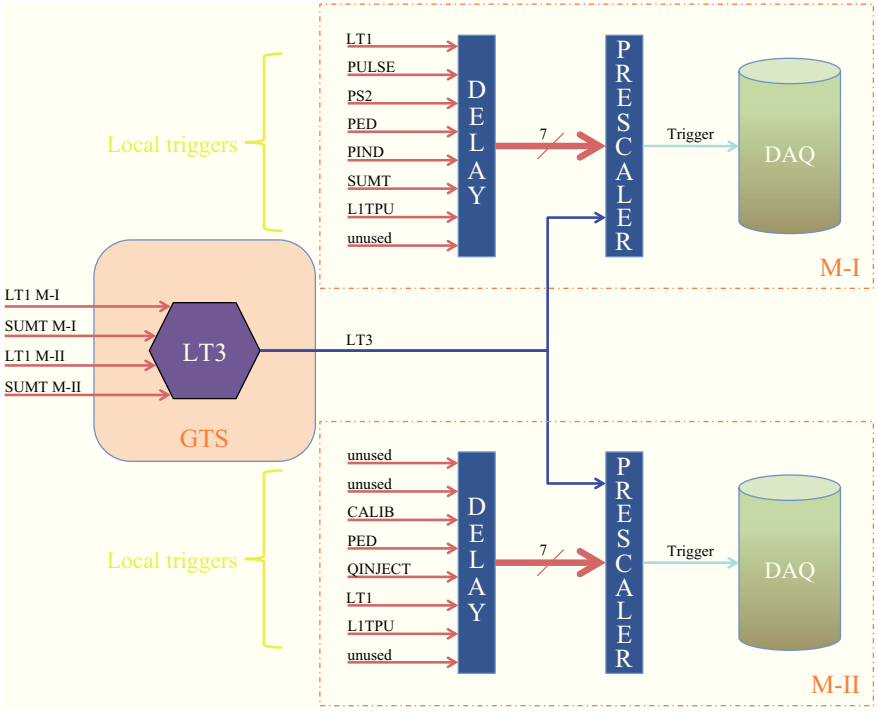

Figure 6.11: A simplified diagram of the trigger electronic chain. The 8 local triggers enter in the *prescaler* board to activate the final enable signal for the readout. The stereo trigger flag is defined inside the *GTS* logic. (© F. Dazzi)

trigger constraints inside a common timing window of 100 ns, are recorded (Fig. 6.12).

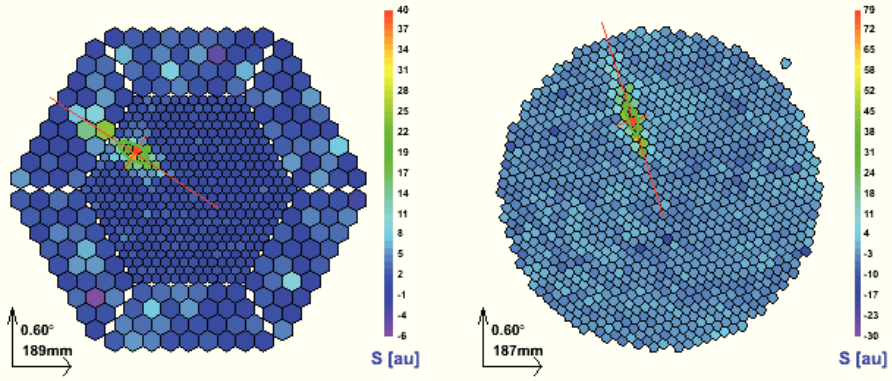

Figure 6.12: The camera image projections of a γ–ray event triggered by the stereoscopic system and recorded by telescopes.

There are a lot of possible trigger combinations, which are handled by a dedicated system, the so-called *GTS* (*Global Trigger System*) [109]. The *GTS* manages both mono and stereo trigger associations. The main functions of the *GTS* can be understood looking at the simplified diagram of the trigger array system (Fig. 6.13(a)), while all the connections with the other subsystems are shown in figure 6.13(b). Its configuration sets the readout operational mode in order to sample events triggered by the local imposed trigger and/or by the stereo blend. In the last case, the number of telescopes

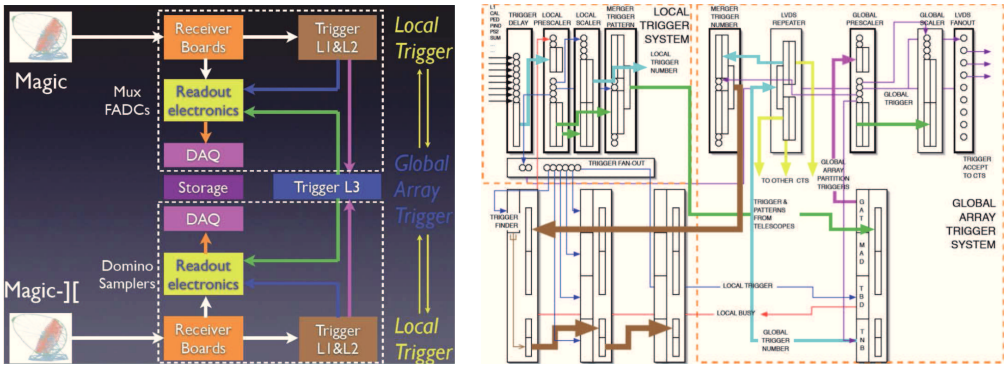

(a) *GTS* concept (b) *GTS* connections

Figure 6.13: *Left:* an overview of the trigger system for the MAGIC telescopes array. Two telescopes are controlled by the *GTS*. *Right:* the detailed connections between the *GTS* and other subsystems such as the local triggers and the readout. (From [109])

involved in the final decision can be fixed up to four units[3]. This flexibility provides the possibility to change the dimension and the *stereo-cell* layout. The assignment of the telescopes in a specific *stereo-cell* is called "trigger partition" (Fig. 6.14). The current system can control up to four *trigger partitions*, namely four independent *stereo-cells*. The *DAQ* is armed in any case by the local trigger, while the final decision to accept the event is taken only if one of the enabled *trigger partitions* returns a positive flag.

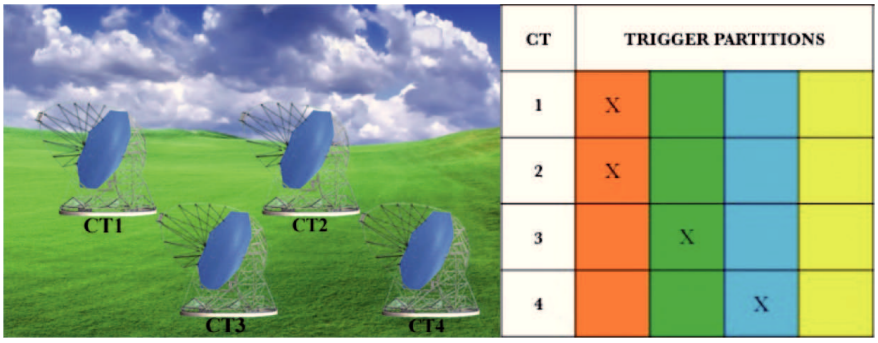

Figure 6.14: A sketch of the *trigger partitions*. The orange partition is a *stereo-cell* composed of the telescopes *CT1* and *CT2*. The green one works in single mode with the *CT3*, as well as the blue one with the *CT4*. The last yellow partition is not in use. (© F. Dazzi)

6.2.1 Signal path length and timing

The *MAGIC* stereo trigger (*LT3*), a sub-function of the *GTS*, makes a tight time coincidence between both telescopes, taking into account possible sources of relative delay in the event arrival times. Basically there are two main sources, one fixed, due to the different electronic chain paths, and another variable coming from the telescopes' pointing direction.

[3]Up to now, the stereoscopic system was composed of two telescopes, and the two additional units had never been considered.

The first component arises when the signal path length from the reflective surface to the *LT3* is considered. There are several known contributions, some intrinsic to the array's geometry and subsystems' arrangement, and others from the different electronics used in the two telescopes. A simple list is presented, where Δt is defined as (t_{M1} - t_{M2}):

- The mirrors' shape and their supports are different. An uncertainty of some centimetres is present between the reflective dish and camera. (-0.5 ns $\lesssim \Delta t \lesssim$ 0.5 ns)
- The devices used in the camera electronics are completely dissimilar, such as *PMTs*, charge transimpedance preamplifiers and *VCSEL*, but the layout is very comparable. (-8 ns $\lesssim \Delta t \lesssim$ 8 ns)
- The optical fibres' length is not exactly the same. In *MAGIC–I* the propagation time is 802 ns, while in *MAGIC–II* it is 810 ns. (Δt = -8 ns)
- The logic of receiver boards is equal but the components are different. (-5 ns $\lesssim \Delta t \lesssim$ 5 ns)
- Different cabling between the receiver boards and the *LT1* crate. ($\Delta t \sim 15$ ns)
- The *LT1* systems have installed different backplanes, covering different trigger areas in the camera. ($\Delta t \sim 4$ ns)
- Different cabling between the *LT1* crate and the *GTS*. ($\Delta t \sim 15$ ns)

After the measurement of the relative delay performed in La Palma, no delay has been applied at the input of the *LT3*, because the various contributions annul each other.
The second component, correlated to the different arrival times of the Čerenkov light front on the detectors, is corrected every 10 s introducing an additional delay, calculated from the telescopes' pointing coordinates. As shown in figure 6.4(b), the same shower arrives to the telescopes covering two different paths, hence resulting in distinct timing. The spatial difference corresponds to the variable Δs, function of the azimuth and zenith angles. $\Delta s(\theta, \varphi)$ can be expressed as the scalar product between the vector joining the two telescopes ($\overline{OP}$) and the pointing direction versor $\bar{u}$, when it has the same direction of the shower core axis. The vector $\overline{OP}$ has an azimuth angle of 38°, as reported in subsection 6.1.2. In figure 6.15, a simple sketch shows how they appear in a Cartesian base. The $\overline{OP}$ coordinates, expressed in metres, are

$$\begin{aligned}\overline{OP} &= \big(D_{tel} \cdot \sin(38^\circ), \quad D_{tel} \cdot \cos(38^\circ), \quad H_{tel}\big) \\ &= \big(85 \cdot \sin(38^\circ), \quad 85 \cdot \cos(38^\circ), \quad 0.14\big) \\ &= \big(52.33, \quad 66.98, \quad 0.14\big)\end{aligned}$$

where H_{tel} is the elevation difference of 14 cm[4]. The versor $\bar{u}$ coordinates are

$$\bar{u} = \big(\sin\theta \cdot \sin\varphi, \quad \sin\theta \cdot \cos\varphi, \quad \cos\theta\big);$$

the relative path obtained by the scalar product, ignoring H_{tel}, is

$$\Delta s = \overline{OP} \cdot \bar{u} = sin\theta \cdot \big(52.33 \cdot \sin\varphi + 66.98 \cdot \cos\varphi\big); \tag{6.5}$$

the corresponding plot is shown in figure 6.16.
Every time the central control updates the telescopes' position, the delay contribution

[4]The position of *MAGIC–I* is 2186.98 m a.s.l., while for *MAGIC–II* is 2187.14 m a.s.l.

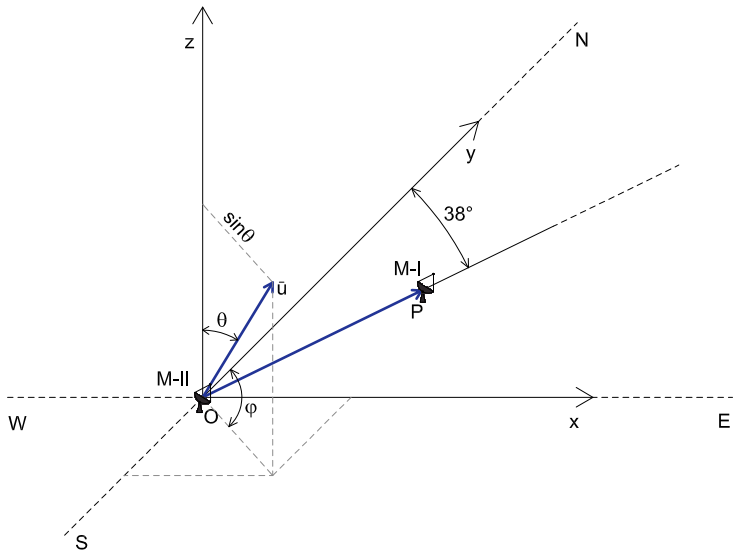

Figure 6.15: Geometrical representation of the the Čerenkov light paths towards the two dishes as a function of the azimuth and zenith angles (θ, φ). The vector $\overline{OP}$ defines the position of *MAGIC–I* with respect to *MAGIC–II*, while the versor $\bar{u}$ indicates the telescopes' pointing direction. The scalar product between these two vectors determines the paths' spatial difference. For simplicity, the elevation between the two telescopes is not depicted. (Image credit: A. Bortoluzzi & F. Dazzi)

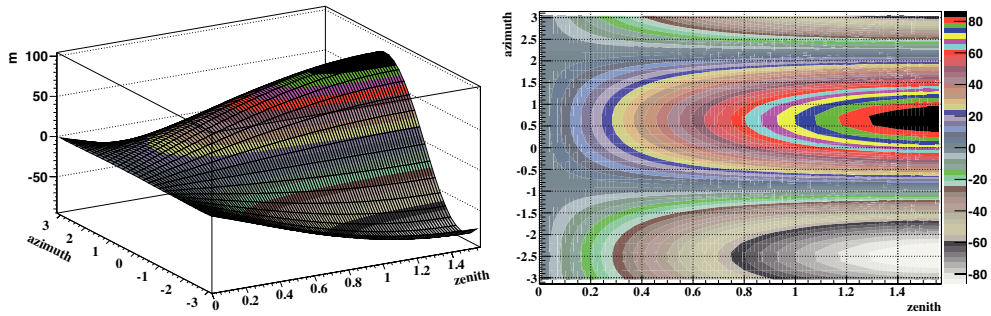

Figure 6.16: The graphic representation of the function $\Delta s(\theta, \varphi)$ in the interval $0 \div \pi/2$ for the zenith and $-\pi \div \pi$ for the azimuth. One maximum of the plot is visible at the coordinates: $\theta = 90°$ and $\varphi = 38°$. (© F. Dazzi)

is calculated again and the signals' synchronization is applied at a level of the local telescope triggers. This operation is done with a very fast algorithm, because the available time range is limited by synchronization with the readout system. Even if the memory depth of *DRS2* is restricted to only 512 ns, the main constraint is given by the acquisition trigger to *MUX-FADC*. It occurs 320 ns after the local trigger is generated. The different arrival time on the telescopes, which is the largest source of delay, can be calculated from equation 6.5. The maximum is around 250 ns[5], which should be added to the cabling contribution of ~ 15 ns and the *LT3* propagation time of ~ 48 ns.

[5]The maximum of the equation 6.5 is 85 m, when $\theta = 90°$ and $\varphi = 38°$. It corresponds to a delay of 283 ns. The deemed maximum is fixed to 250 ns, because there are no observations for zenith angles higher than 60° so far.

Equation 6.5 is true for particles that have a trajectory along the telescope pointing direction. An uncertainty is introduced if we consider a generic shower falling inside the telescope's FoV. The new spatial variable is called $\Delta s^{\dagger}$ and is given by the scalar product between the vector $\overline{OP}$ and the shower axis ($\bar{n}$), which can be far from $\bar{u}$ up to 3.5°. $\Delta\theta$ and $\Delta\varphi$ are the angular variations respect to the pointing direction.

$$\begin{aligned}\Delta s^{\dagger} &= \overline{OP}\cdot\bar{n} \\ &= \sin(\theta\pm\Delta\theta)\cdot\big(52.33\cdot\sin(\varphi\pm\Delta\varphi)+66.98\cdot\cos(\varphi\pm\Delta\varphi)\big)\end{aligned} \tag{6.6}$$

The maximum difference between Δs and $\Delta s^{\dagger}$ tells which is the foreseen jitter of the arrival time of Čerenkov flashes. Considering that $\Delta\theta$ and $\Delta\varphi$ are close to zero, we may assume the following relation.

$$\begin{aligned}\Delta s-\Delta s^{\dagger} = d\Delta s &= \frac{\partial\Delta s}{\partial\theta}d\theta+\frac{\partial\Delta s}{\partial\varphi}d\varphi \\ &= \cos\theta(P\sin\varphi+Q\cos\varphi)d\theta+\sin\theta(P\cos\varphi-Q\sin\varphi)d\varphi\end{aligned} \tag{6.7}$$

where P= 52.33 m and Q = 66.98 m. Then the maximum is found imposing:

$$\begin{aligned}\nabla(d\Delta s) &= \left(\frac{\partial(d\Delta s)}{\partial x};\quad \frac{\partial(d\Delta s)}{\partial y}\right)=0 \\ &= \begin{cases}-\sin\theta\big(P\sin\varphi+Q\cos\varphi\big)d\theta+\cos\theta\big(P\cos\varphi-Q\sin\varphi\big)d\varphi=0\\ \cos\theta\big(P\cos\varphi-Q\sin\varphi\big)d\theta-\sin\theta\big(P\sin\varphi+Q\cos\varphi\big)d\varphi=0\end{cases} \\ &= \begin{cases}\big(P\sin\varphi+Q\cos\varphi\big)=\frac{d\varphi\cos\theta}{d\theta\sin\theta}\cdot\big(P\cos\varphi-Q\sin\varphi\big)\\ \cos\theta\big(P\cos\varphi-Q\sin\varphi\big)d\theta-\sin\theta\big(P\sin\varphi+Q\cos\varphi\big)d\varphi=0\end{cases} \\ &= \begin{cases}\big(P\sin\varphi+Q\cos\varphi\big)=\frac{d\varphi\cos\theta}{d\theta\sin\theta}\cdot\big(P\cos\varphi-Q\sin\varphi\big)\\ \cos\theta\big(P\cos\varphi-Q\sin\varphi\big)\cdot\big(d\theta^2-d\varphi^2\big)=0\end{cases} \\ &= \begin{cases}\theta=90^{o}\\ \varphi=128^{o}\end{cases}\end{aligned} \tag{6.8}$$

For symmetry, it is sufficient to consider this maximum, which returns a $d\Delta s$ of 5.19 m, that is 17.3 ns. The intrinsic fluctuation of Δs† generates a time jitter at the *LT3* input level, confirmed experimentally with the picture 6.17. The recorded jitter is a little bit higher than the prediction of equations 6.8, but the contribution from the electronic chain has to be included.
The spread of the relative arrival time distribution can be used to discriminate particles that are not coming from the tracked source. For a point-like source, the minimum time gate is delimited by the angular resolution acceptance at very low energies and by the variation of the Čerenkov angle for huge events. Conversely, for extended sources that do not exceed the FoV, the limit is fixed by their extension. Obviously, these are ideal limits for electronic systems without jitter. In the first case, the maximum of equation 6.7, with dθ and dφ equal to 0.1°, is 14 cm ($\sim$0.5 ns). Lowering the *LT3* gate in the range 0.5$\div$17.3 ns would improve significantly the background exclusion capacity.
Even if the current rejection power of the trigger system is of the order of $\sim 10^4$, most of the recorded events are hadrons, while γ–rays of interest are still completely negligible. Assuming that the hadrons are isotropically distributed, the telescope trigger acceptance is determined by the solid angle of the FoV (Ω_{FoV}). Applying the stereo relative arrival time as discriminator, the trigger acceptance for a point-like source is

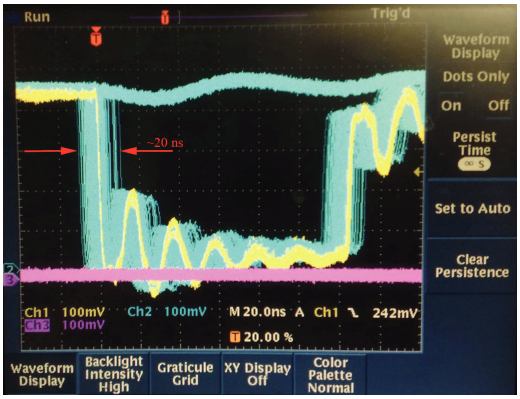

Figure 6.17: The picture of the *LT3* jitter measured at La Palma during normal data-taking. The yellow signal is the local trigger from *MAGIC–I* at the *LT3* input, the blue one the signal of *MAGIC–II*.

reduced proportionally to the solid angle seen by the angular resolution Ω_ξ. Defining R_{FoV} as the current stereo trigger rate and R_ξ the new rate applying a more stringent gate, the ratio should be:

$$\begin{aligned} \frac{R_\xi}{R_{FoV}} &\propto \frac{\Omega_\xi}{\Omega_{FoV}} \\ &\propto \frac{2\pi(1-\cos(\Delta\xi/2))}{2\pi(1-\cos(FoV/2))} \\ &\propto \left(\frac{1-\cos(\Delta\xi/2)}{1-\cos(FoV/2)}\right) \end{aligned} \tag{6.9}$$

where the solid angle formula of cones with aperture $\alpha = \mathrm{FoV}$ and $\Delta\xi$ is used. For the *MAGIC* telescopes, we obtain:

$$R_\xi \propto R_{FoV} \cdot \left(\frac{1-\cos(\Delta\xi/2)}{1-\cos(FoV/2)}\right) = R_{FoV} \cdot 8.16 \cdot 10^{-4} \tag{6.10}$$

where $\Delta\xi = 0.1°$ and $FoV = 3.5°$.
An additional rejection factor of three orders of magnitude can be introduced in the electronic chain. Actually, the local trigger arrival time is stored in on-line histograms with 25 ns resolution. Amending this information, even if it remains far from the ideal resolution of some ns, could be applied at the hardware level to reject some of the showers abundantly out of the pointing direction.

6.2.2 The Pulsar trigger board

The core of the *GTS* is a *Pulsar* (*PULSer And Recorder*) board (Fig. 6.18), a 9U *VME* motherboard developed by the University of Chicago for High Energy Physics applications [94]. In *MAGIC–II*, it is also used for the readout system and the management of the *DAQ* control [15].
The *Pulsar* board houses three powerful *FPGAs Altera APEX20K400* that make it very versatile for any purpose. This choice is largely driven by data transfer requirements, as this chip has a 652 pins *BGA* package with about 500 I/O connections. Furthermore, it is supplied by an internal 26 KiB memory and two of them are connected to two fast *SRAM* memories, *Cypress CY7C1350-F*. This memory is a synchronous-pipelined burst *SRAM* designed specifically to eliminate wait states during write/read transitions, dramatically improving the throughput. The storage capacity of 4 Mb is distributed to a common architecture 128 Kib × 36. These two *FPGAs* exercise an interface with

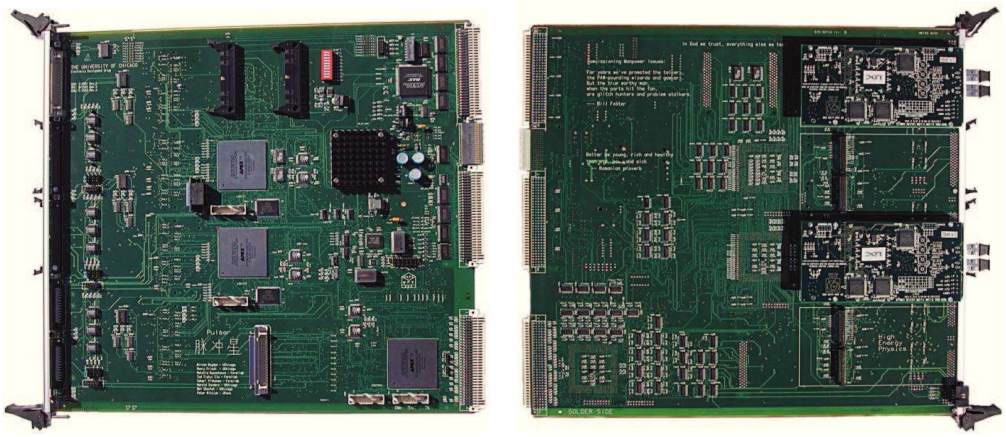

(a) *Pulsar* board top view (b) *Pulsar* board bottom view

Figure 6.18: On the left, the top view of the *Pulsar* board. The three big gray squares are the *Altera FPGAs*. On the right, the bottom view of the board, with connected two mezzanines. (From [94])

the I/O modules, while the third one merges data from the previous two devices and prepares them for a potential transmission through the *VME* bus.
The board is predisposed to accommodate up to four mezzanines, which can be used to implement some additional functions or to extend the compatibility with other signal formats and any industrial standard link. Every mezzanine has 83 bidirectional connections visible to the motherboard *FPGAs*, fully compatible with the transmission system *S-Link*[6] [60]. The *PCB* dimensions meet the *CMC* standard (Common Mezzanine Card), so it is possible to implement different communication standards based on mezzanine cards and the same interface with the *Pulsar* board. The data flow power is enhanced by other four *LVDS* connectors at the front of the board with more than 200 connections. In the case of the *Pulsar* trigger board, the I/O on the front side of the board handle the following signals:

- A 64–bit bus for trigger input pattern.
- A 64–bit bus for trigger output pattern.

The mezzanines manage these other signals:

- The four local triggers from the telescopes. The *LT1* signals are available on coaxial differential cables with 100 Ω impedance, while the *Sum-Trigger* ones on a coaxial single-ended cable with 50 Ω.
- The four output trigger partitions.
- A 32–bit bus for the global trigger number.
- The global veto signal and some auxiliary calibration triggers.

On the first two mezzanines, the local input and the output triggers are synchronized using the programmable delay chips *Data Delay Devices 3D3428-5* with a maximum delay of 1.2 μs, divided in 255 steps for a resolution of 5 ns/step (Fig. 6.19).

[6] *S-LINK* is a data link, designed at *CERN*.

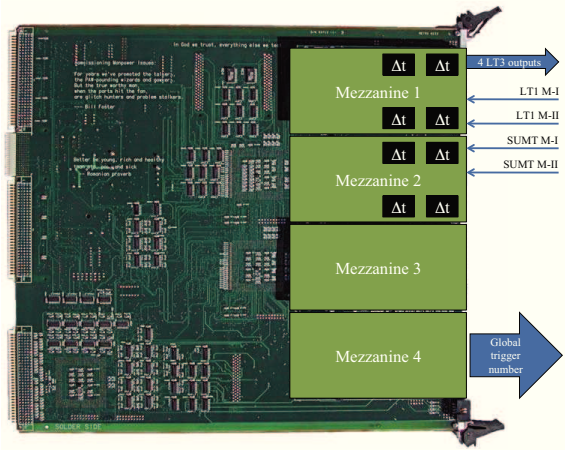

Figure 6.19: The four mezzanines located on the back side of the *Pulsar* trigger board. The first two accept the local triggers from the single telescopes and they send around the global stereo triggers, while the last one distributes the global trigger number.

6.3 The future stereoscopic trigger

As described in section 4.9, an upgrade of the telescopes is under way. An important goal is to improve the stereoscopic trigger, on the one hand reducing the cabling delay contribution and on the other introducing a new powerful and compact board to replace the *Pulsar* trigger board. In fact, this board is no longer in production and the available units will be used for the *MAGIC–I* readout upgrade. The main idea is to exchange all the *Pulsars* with a service aim, saving some of them as spares. The replacement board is called *MiniPulsar*, a 6U *VME* card that can be used in the trigger and *DAQ* environments.

6.3.1 Electronic room upgrade

In subsection 6.2.1, the useful time windows for the stereo trigger has been calculated. The available gate is very tight and observations at very high zenith angles ($\gtrsim 60°$) are prevented by the hugely different arrival times on the two telescopes. This limit could become narrower for a telescope array extension, compromising the stereoscopic trigger efficiency. For the *MAGIC* upgrade, the rearrangement of the electronic room took into account the relative rack position in order to downsize the cable length between different source of physics triggers. In figure 6.20, the layout before and after the upgrade is shown. The potential physics triggers come from the orange racks (*LT1*) and the green ones (*Sum-Trigger*). Currently, the configuration which returns the shortest connections between them has been chosen.

The variation of some important operative conditions affects the circuit performance, causing a degradation in the electrical signal quality. Temperature and humidity could change some parameters of the electronics, resulting in functionality and reliability problems. A huge temperature gradient varies the propagation time, introducing different relative delays. Moreover, a temperature enhancement increases the signals' jitter, lowering the timing resolution. To prevent this, in the new electronic room all racks are closed and the internal temperature and the air flow are monitored by an adequate cooling system.

6.3.2 MiniPulsar general description

The *MiniPulsar* (Fig. 6.21) takes inspiration from the *Pulsar* board. Its main goal is to substitute the *Pulsars* that have a service role in the *MAGIC* electronic chain.

(a) Photo of the new electronic room

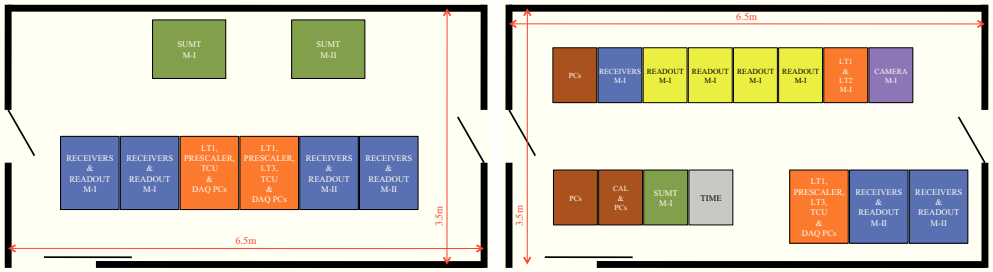

(b) Electronic room arrangements, before and after the upgrade

Figure 6.20: On top, the photo of the new electronic room. (Image credit: J. L. Lemus) On bottom, the arrangement before (left) and after (right) the *MAGIC* upgrade. (© F. Dazzi)

The production of *Pulsar* boards has stopped and some components are obsolete. The necessity to save as many spares as possible for the readout is vital for the experiment. Moreover, the *Pulsar* was created to satisfy several purposes in the data transmission environments, but it was not realized to manage isochronous signals with sub nanosecond precision. The design of new *MiniPulsar* tries to meet the current requirements.

The *MiniPulsar* is a 6U *VME* motherboard, which houses a low-cost and versatile *FPGA Cyclone-II* (*EP2C70F896*) from *Altera*. It is a programmable device containing a 2-D row and column-based architecture to implement custom logic (Fig. 6.22(a)). Column and row wires provide signal interconnections among logic array blocks (*LABs*), embedded memory blocks, and embedded multipliers. Every *LAB* is constituted by 16 logic elements (*LEs*[7]) (Fig. 6.22(b)), for a total amount of 68416 *LEs*. It appears in a very compact *BGA* package with 896 pins, of which 622 are usable I/O. It can provide up to 1.1 Mb of embedded memory, a global clock network of 16 lines distributed to

[7]The logic element is the smaller programmable entity of *FPGA*. In this device, it is composed of 4 look-up table inputs, a programmable register and a carry chain connection.

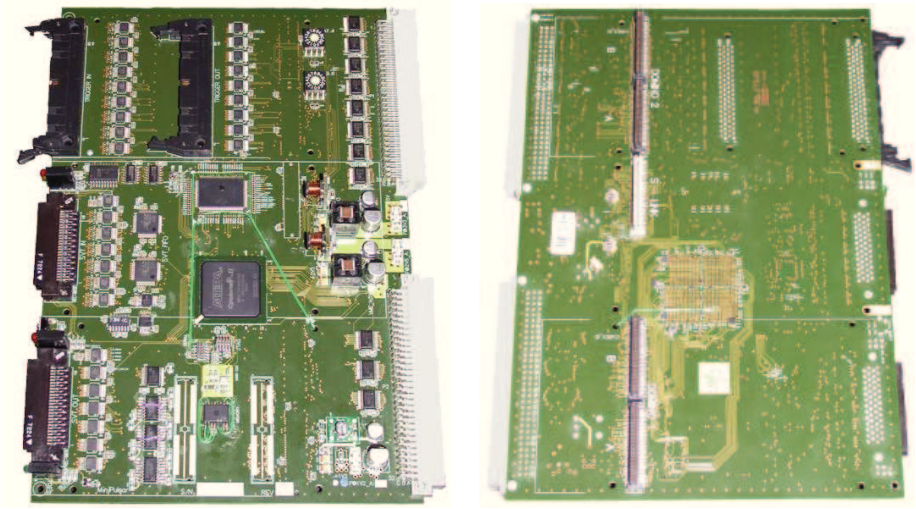

(a) *MiniPulsar* board v.1.8 top view (b) *MiniPulsar* board v.1.8 bottom view

Figure 6.21: *Left:* the top view of the first *MiniPulsar* prototype (version 1.8). *Right:* the bottom view.

all resources, four *PLLs* and 150 embedded multipliers. This chip can be configured to

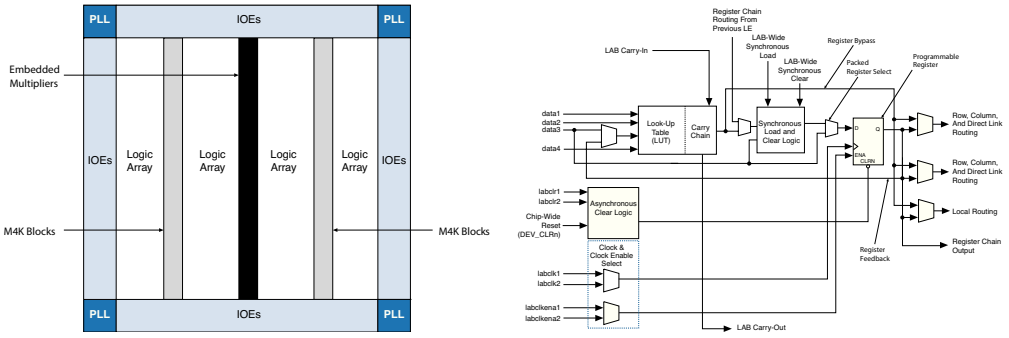

(a) *Cyclone-II* architecture (b) *Cyclone-II* logic element

Figure 6.22: *Left:* the architecture of a generic *Cyclone-II* device. *Right:* the schematics of the logic element. (From *Cyclone-II* handbook)

perform complex combinational functions between digital signals of different formats at a maximum data rate of 805 Mbps for inputs and 640 Mbps for outputs. In the current design, for single-ended lines the *LVTTL* is adopted, while for differential lines the *LVDS*. The I/O pins are grouped together into eight I/O banks, and each bank has a separate power bus. The preferred I/O standard can be selected for a given bank, increasing the interconnection flexibility. The maximum internal clock frequency, reachable for simple data process, is 405 MHz (speed grade -6), but it changes according to the implemented function. In addition, some analogue features, such as the slew rate and drive strength on each output pin, can be programmed.
Cyclone-II devices support a broad range of external memory interfaces. In the *MiniPulsar* project, a *DDR2 SRAM* memory (*CY7C1380D*) from *Cypress* is embedded with a high speed rate bus at 333 Mbps. The memory integrates 524288×36 cells with advanced synchronous peripheral circuitry and a two-bit counter for internal burst

operation. Most of the connections, such as addresses and data, are synchronous, gated by registers controlled by a positive edge-triggered clock input.

The main functions of *MiniPulsar* board are emphasized in figure 6.23. Most of the *Pulsar* features are perfectly reproduced in the new project. The innovation lies in the architecture, which is significantly simplified. One single *FPGA* manages all the stages and both the data-gathering and the data-processing, providing higher performance than before. The board dimension is reduced to 70% (from 9U to 6U) with the single drawback that it can host three mezzanines out of four, but the great advantage that it can be moved to the standard *LT2 VME* crate, closer to the local trigger drivers. It is very portable and easy to adapt in every custom test set-up, ensuring a fast and effective integration.

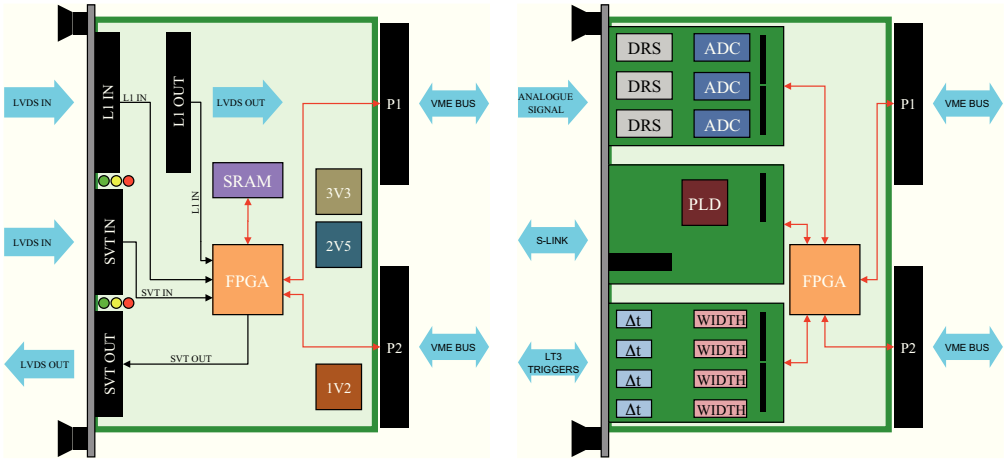

(a) *MiniPulsar* top functions (b) *MiniPulsar* bottom functions

Figure 6.23: The main functions diagram of the *MiniPulsar* top side (left) and bottom side (right). The front I/O connectors, *SVT* and *L1* are exactly the same as the *Pulsar* board. Even the pin-out for the mezzanines is the same. (© F. Dazzi)

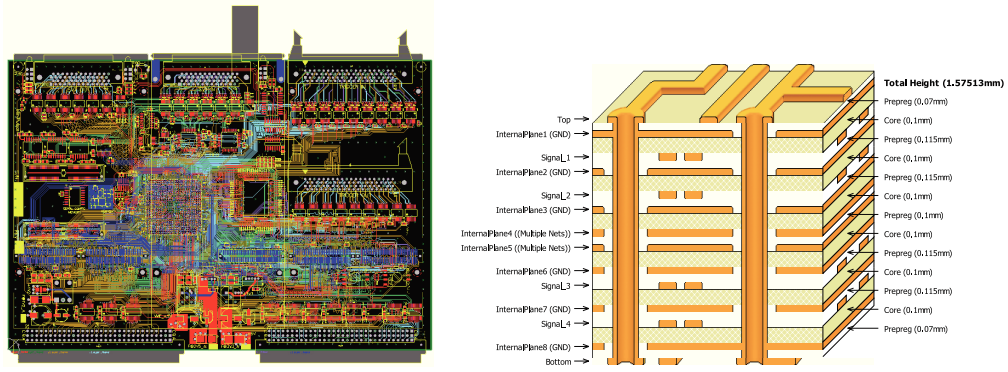

(a) The all layers of *MiniPulsar PCB* (b) The *MiniPulsar* stack-up

Figure 6.24: *Left:* the complete routing on the fourteenth layers of the *MiniPulsar* board. Most of the traces are connected to the central *FPGA*. *Right:* the complex stack-up of the board.

The optimization, for a generic high-speed timing purpose, is likely to be one of the most essential new features of this board (Fig. 6.24(a)). Every single trace has

been accurately studied in terms of skew, impedance and cross-talk. For this reason, a complex *PCB* stack-up has been designed following the standard signal integrity rules (Fig. 6.24(b)). It is composed of fourteen layers, four of which are internal planes for high-speed signals, completely interposed between two internal ground planes in order to isolate them from the electromagnetic background noise. The other two external layers, on the top and bottom, are for slow control signals. The layers' thickness and the material dielectric constants have been carefully calculated to obtain a final transmission line impedance of 50 Ω for single-ended traces and 100 Ω for the differential one.
The I/O wire length is equalized to keep the skew down as much as possible. The lines to the front connectors are designed with a maximum timing difference of 50 ps, while the traces to the mezzanines present a more relaxed constraint at 250 ps. The meandering routing technique has been applied, as displayed in figure 6.25. The maximum wave dimensions and the minimum distance between neighbour lines have been fixed to obtain a cross-talk lower than 10%.

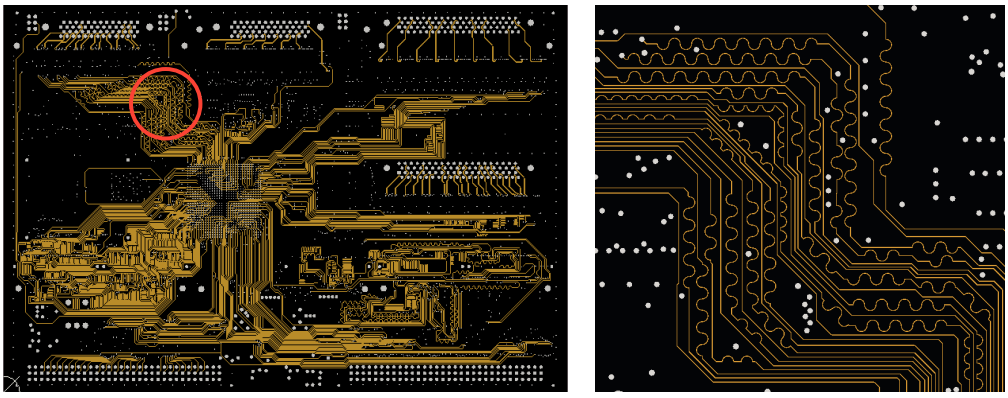

(a) The signal layer nr.1 (b) A zoom of a small layer portion

Figure 6.25: The complete view (left) and a zoom of a restricted zone (right) of the signal layer number one. The meandering traces for the length/timing adjustment are shown.

6.3.3 MiniPulsar prototype

The *MiniPulsar* prototype (version 1.8) can be divided in five important stages, as illustrated in figure 6.23. Every single part has been independently and deeply verified, spotting the design errors and wrong functionalities. A specific test bench firmware[8] has been uploaded to check the board performance. Afterwards, a report of the stage list with the final test result is made. The symbol "✓" indicates a completely successful upshot, while "✗" means there is something wrong.

- ✗ Power distribution
- ✗ *FPGA*
- ✓ External *SRAM*
- ✓ Front I/O connectors

[8]The *VHDL* code is copied in appendix E.

✖ Mezzanines connections

The main power line is taken from the 5 V *VME*, then it is transformed in 3.3 V, 2.5 V and 1.2 V. The first two power lines feed the I/O drivers, the mezzanines and the *FPGA*, while 1.2 V supplies its core.
Switching voltage regulators have been selected, because they provide high current ($\sim$10 A) generating not much heat. This feature is ideal when the board has to feed power-consuming mezzanines in provisional test environments without cooling systems. The disadvantage is the high noise due to the regulators switching frequency that couples with some high speed wires.
In figures 6.26(a) and 6.26(b), the 3.3 V power line is shown respectively in DC and AC oscilloscope mode. The voltage is not stable and the peak-to-peak variation is $\sim$500 mV. Searching the source of noise, using the oscilloscope probe as an antenna[9], two components can be distinguished. The first noise arises when the probe-antenna is located close and parallel to the regulator transformer (Fig. 6.26(c)), while the second when close and parallel to the *PCB* and the chips (Fig. 6.26(e)). By shielding the regulator with a small metal box, connected to ground, the first contribution with a square shape disappears (Fig. 6.26(d)), whereas the regular spikes still survive (Fig. 6.26(f)). The likely two independent sources of noise are the *PWM* control[10] in the voltage regulator ("square noise") and the high frequency switching in the *FPGA* and I/O drivers (spikes). In fact, the spikes present a frequency equal to that applied in the *FPGA*.

Concerning the *FPGA* and the surrounding circuitry, three design mistakes have been spotted during the tests. In the first case, a wrong package for the external flash memory (*EPCS64*) had been selected. This device is important because in the *SRAM*-based devices, such as the Cyclone-II, configuration data must be reloaded each time the chip powers up, the system initializes, or when new configuration data is needed. *EPCS64* is a flash memory with a serial interface that can store configuration data and reload it to the *FPGA* upon power-up or reconfiguration. For this prototype version, the problem has been fixed with a hand-made wiring between the chip and the *PCB* pads (See in figure 6.21 the green wires on the bottom area of the top layer).
The second fault was the missing connection of two important configuration pins: *ASDO* and *nCSO*. They send a control signal from the *FPGA* to the serial configuration device in active serial mode. *ASDO* is used to read out stored data, while *nCSO* to enable the configuration device. As before, the solution has been further hand-made wirings (See in figure 6.21 the green wires on the central area of the top layer).
The third one was caused by the connection to 1.2 V instead to 3.3 V of one of the eight power banks in the *FPGA*. More than half the generating signals for the mezzanine nr.1 have a wrong amplitude of 1.2 V, not compatible with *LVTTL* standard. There are no possible solutions for the prototype version.

The *SRAM* interface and the I/O connections present no problems and work properly. In figure 6.27(a), an example of a *LVDS* signal output is shown. The yellow line is the positive signal, while the blue one the negative. Their difference is mathematically represented with the orange function. In figure 6.27(b), the main controls for the *SRAM* memory are recorded.

A major mistake was made in the connectors of mezzanines number 1 and 3. Unfortunately they are wrongly orientated by 180° around the axis perpendicular to the connectors themselves. A small *PCB* adapter has been set up as a temporary solution.

[9] Connecting the ground peg with the probe terminal, a coil, which acts as an antenna, is created.
[10] A *PWM* (*Pulse Width Modulation)* control is a device commonly used to manage the power in the modern electronic power switches.

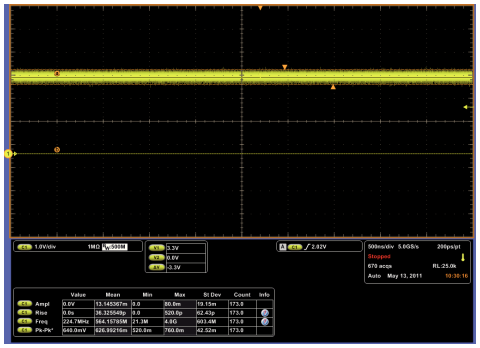

(a) The 3.3 V power line in DC mode

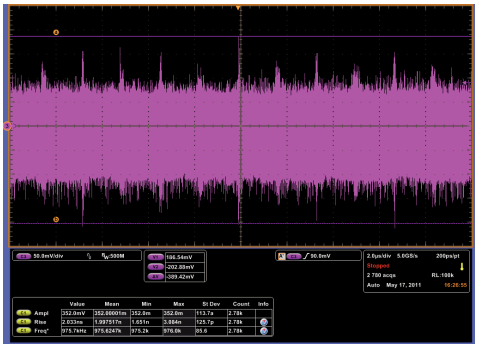

(b) The 3.3 V power line in AC mode

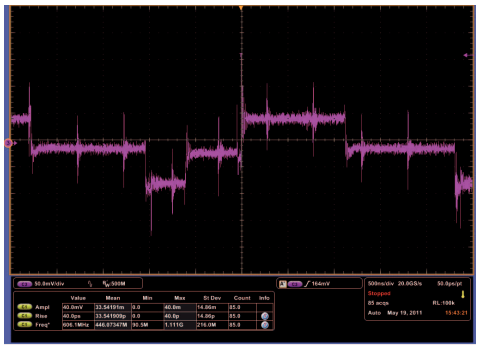

(c) Radiated noise without shield on the vertical plane

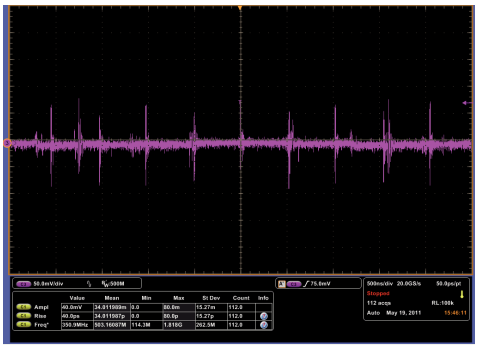

(d) Radiated noise with shield on the vertical plane

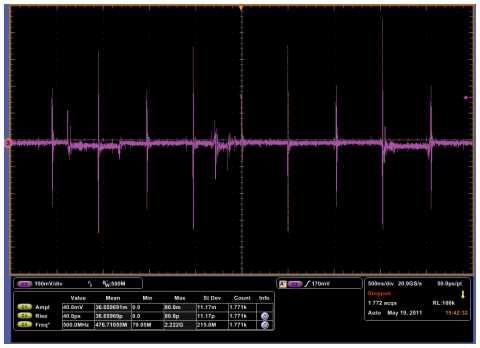

(e) Radiated noise without shield on the horizontal plane

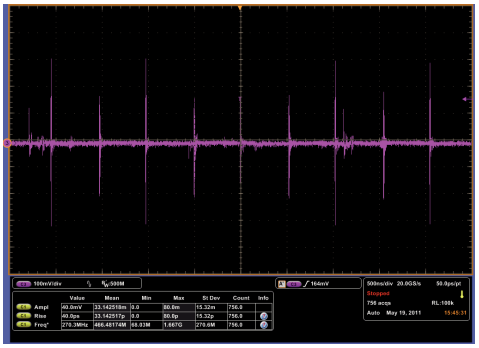

(f) Radiated noise with shield on the horizontal plane

Figure 6.26: Measurements about the power system quality and study of the noise. On the top, the 3.3 V voltage recorded in DC (a) and AC mode (b). In the centre, the electromagnetic noise radiated around the regulator, without (c) and with (d) a metal box shield. On the bottom, the same estimation, without (e) and with (f) shield, parallel to the *PCB* surface.

6.3.4 MiniPulsar final version

A new version[11] of *MiniPulsar* board has been designed in order to fix the bugs of the first prototype. The main modification has been made in the power stage, where a big source of noise has been discovered. A triplet of different capacitor values on the supplies has been used in order to prevent resonances that could create unwanted

[11] This is the version 2.1. The schematics are available in appendix F.

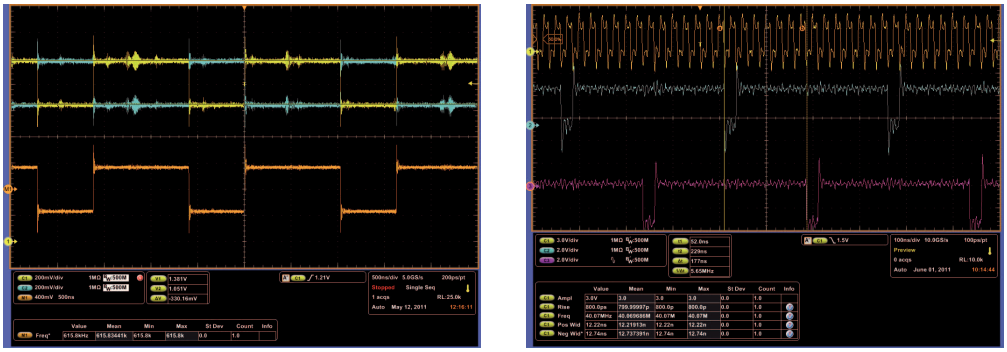

(a) The *LVDS* output signal

(b) Some control signals of *SRAM*

Figure 6.27: *Left:* the *LVDS* output measured on the connector *L1 OUT* pin 31. *Right:* the clock (yellow), the global write (blue) and the output enable (violet) signal controls for the external *SRAM* memory.

spikes. This should minimize the local impedance to the ground plane and increase the immediate available charge during fast transients. Even under the *FPGA* package, the capacitance array has been improved.
The *MiniPulsar* is a multi-purpose board that can be employed in different systems. It should be very adaptable at any environment, serving always the requested efficiency. Hence, there is not an unique power solution which can provide high current and low noise, without dissipating a lot of heat. The implementation of a design, compatible with three distinctive power systems, has been the chosen strategy. The new *PCB* can host three types of voltage regulators, one linear and two switching.
Following the main features of the three architectures:

- The switching regulator, selected for the prototype board, is still available in the new version. *PTR08100W*, from *Texas Instruments*, is a highly integrated, low-cost and variable module that delivers up to 10 A. The package layout is compatible with the standard *TO-220* linear regulators, but it provides output current at a much higher efficiency and with much less power dissipation, thereby eliminating the need for a heat sink. Its characteristics make it attractive for applications that require high current without cooling control. The drawback is the elevated noise, unpleasant for analogue and high speed conditions (green and blue hands in figure 6.28).

- Using the same footprint with a slightly different passive circuitry, three linear regulators can be mounted. *TPS75933* and *TPS75925* supply the 3.3 V and the 2.5 V lines (blue hands in figure 6.28), while *LP38843* the 1.2 V part (green hand in figure 6.28). The first two chips offer 7.5 A current output with a low dropout. The *LP38843* is a 3 A output current regulator, typified by a fast response and an excellent stability. This configuration needs the heat sink and a good air flow control. It is recommended to use this as first choice, when fast and high quality signals are treated.

- Last option is a compromise solution based on a switching micro-module. The *LTM4608*, from *Linear Technology*, is a complex 8 A switch mode power supply (red hands in figure 6.28). It supports an output voltage range of 0.6 V to 5 V, set by a single external resistor. The current mode architecture enables a very

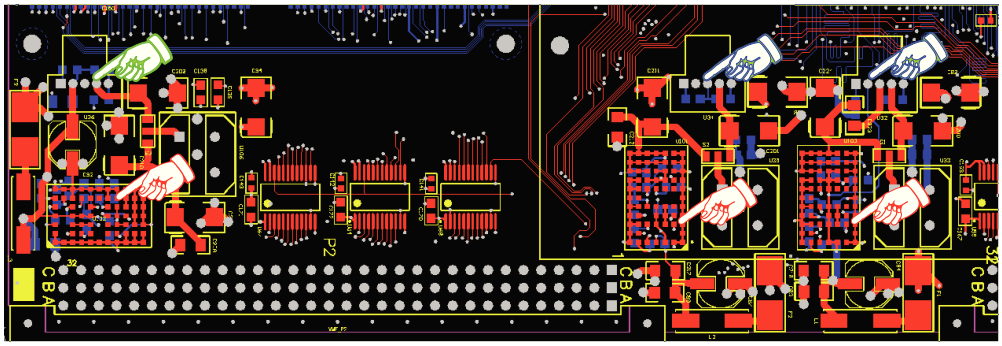

Figure 6.28: The new power stage of the *MiniPulsar v.2.0*. The small coloured hands indicated the new voltage regulators. The green hand is the 1.2 V footprint, while the blue hands are the 3.3 V and the 2.5 V. It possible to mount the switching or the linear regulators. The red hands show the switching module from *Linear Technology*.

fast transient response to line and load changes without sacrificing stability. The typical switching frequency is 1.5 MHz, but for noise sensitive applications, it can be externally synchronized from 0.75 MHz to 2.25 MHz. Even spread spectrum switching can be implemented in the design to reduce noise. Finally, the device supports an output voltage tracking for voltage margining.

7 Conclusions and outlook

THE CURRENT upgrade of the *MAGIC* telescopes moves in two ambitious and crucial directions. The first is the reduction of the energy threshold down to around 15 GeV, where interesting physics has still to be explored. The second is a significant improvement of the cosmic ray background rejection efficiency, both with advanced image analysis techniques and with innovative electronic systems and novel photodetectors. In this sense, the new *Sum-Trigger-II* plays an important role, especially for the first aim. In this last chapter the outcomes of this thesis work and the future perspectives are summarized.

7.1 Summary of the Sum-Trigger-II project

The stereo *Sum-Trigger-II* is an ambitious and complex project, which is realized to improve the detection power of low energy events, born from a collaboration between the *MAGIC-Italia* group, mainly Padova, Udine and Pisa, and the *Max-Planck-Institut für Physik* in Munich. All these teams have well-established knowledge and experience in the design of the trigger architectures for *IACT* experiments. In fact, the Italian groups have built the standard digital trigger and the current *LT3*, while the German group has developed the prototype of the first *Sum-Trigger*.

The compatibility with the already running layout[1] and the mechanical constraints have been the starting points of the planning. Then, the attention has been focused on the challenging electronic properties, demanding selection algorithms adapted to the Čerenkov flash features. Since the *Sum-Trigger-II* principle is established on temporal and topological constraints, a full control of the signal elaboration is decisive. High bandwidth, good signal integrity and excellent timing synchronization are the key factors for a successful system, as demonstrated in the prototyping phase.
Most of the system, especially the selection event stage, is realized with analogue electronics, while the digital devices take care of the control and data processing.

The *Sum-Trigger-II* is currently under construction, and it is not yet operational, but it will be one of the most important elements of the *MAGIC* upgrade. Some subsystems have already demonstrated good behaviour, within design specifications. Others require additional studies and tests.
On the basis of Monte Carlo simulations, we expect that the new system will reach an

[1] The final layout is based on the *DRS4* readout.

energy threshold of $\sim 20\,\mathrm{GeV}$ and a collection area of $20000\,\mathrm{m}^2$ in mono mode data-taking. Compared with the prototype *Sum-Trigger*, the improvement is significant, especially in the number of triggered events. In addition, the performance is even more interesting in stereo mode data-taking, where the analysis will also benefit in the event reconstruction. The energy threshold is lowered in the domain under 20 GeV with an impressive collection area of $\sim 40000\,\mathrm{m}^2$.

7.2 Main goals

This innovative project has three main goals. The first is a larger trigger area which increases the telescope sensitivity and allows wobble mode data-taking.
The second goal is the implementation of a complete automated tuning of the signal properties and the trigger processing parameters, to remove the constant and time-consuming need of manual adjustments. Moreover, this should improve, at the same time, the system's reliability, the quality of the recorded data and the rejection of spurious events. In fact, most of the devices of the telescopes could change their properties or could gradually degrade. For instance, due to ageing, the photoelectron conversion efficiencies of the *PMTs* constantly decrease, each one with a different rate, thereby modifying the electronic chain gain. Periodically they need to be equalized, calculating new standard high voltage settings. A continuous control of the parameters of the telescopes allows one to record optimal data sets, always in very similar conditions, even over long time intervals.
Finally, the new system will be installed on both telescopes, enabling stereo observation in *Sum-Trigger* mode. This will allow the detection of faint events and to take advantage of the stereo image reconstruction. For instance, the fluctuation in the extrapolation of the height of the shower maximum affects heavily the energy resolution. The light yield varies significantly, especially when the shower axis is close to the telescope, as it often happened with the prototype *Sum-Trigger*. Figure 7.1 shows, for three different impact parameters, how the amount of light seen by telescopes varies with the height of shower maximum. The light yield is independent of the hight of shower maximum only for impact parameters greater than $\sim 100\,\mathrm{m}$. A precise calculation of the

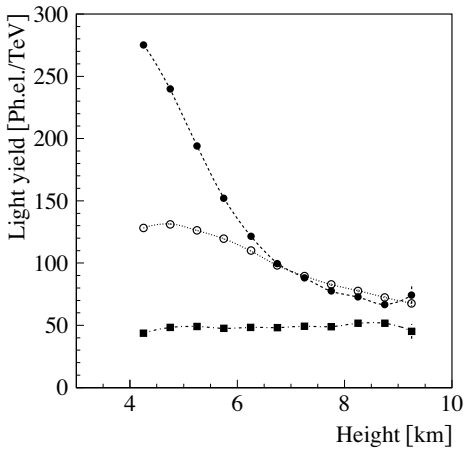

Figure 7.1: Simulation of the light produced in a shower as a function of the height of maximum Čerenkov emission for different shower core distances: the full circles are for a distance of $40 \div 50\,\mathrm{m}$, the open circles for $90 \div 100\,\mathrm{m}$ and the full squares for $140 \div 150\,\mathrm{m}$. (From [73])

height of the shower maximum could become fundamental for the reconstruction and understanding of gammas at low energies, where the classical *Hillas* parameters loose their power.

The achievement of these three goals will significantly improve observations in the domain below 50 GeV, by gaining crucial information for the understanding of *Pulsar*, distant *AGNs* and *GRBs*. The importance of this energy range is beyond dispute, as emerged in some recent hot cases. One has been clearly illustrated in the sub-section 5.1.3. The *Crab Pulsar* has been detected above 25 GeV[2], with a spectrum trend that follows a power low, confuting the *Fermi-LAT* assessments and excluding some models. Another important topic is the *Crab* nebula *Inverse Compton* peak estimation [136]. The cross-correlation between *MAGIC* and *Fermi-LAT* has allowed to perform an unprecedented measurement[3] (Eq. 7.1), illustrated in figure (7.2).

$$IC_{peak} = 59 \pm 6\,\mathrm{GeV} \tag{7.1}$$

Being the uncertainty dominated by systematic errors ($\sim 15\%$), more precise measurements will add information about the properties of a *Supernova Remnant*, such as the shock and the associated magnetic field.

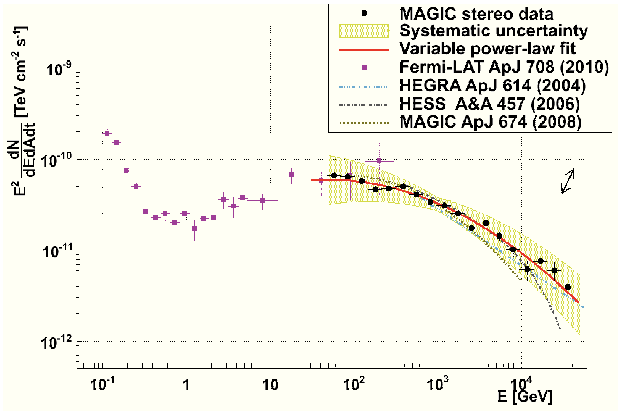

Figure 7.2: The spectral energy distribution (*SED*) of the *Crab Nebula* obtained with the *MAGIC* telescopes, together with the results from previous γ–ray experiments. The black arrow indicates the systematic uncertainty (14%) on the energy scale. (From [136])

Lowering the energy threshold is not only driven by the desire to explore a not well known energy domain, but it will provide better experimental overlapping with the *FERMI/LAT* satellite measurements. It must be stressed that this kind of overlap is presently unique in the world.
A deeper understanding of the properties of known *AGNs* and of the *SSC* model is foreseen. Finally, the low energy threshold will allow the detection of higher redshift sources allowing *MAGIC* to observe a more distant Universe.

7.3 Future perspectives

This new trigger system will not be of benefit only for *MAGIC*, since it is a topic under study also for the future large size telescopes of *CTA*[4] array. Several teams are performing complex simulations to understand which will be the best solution for the future *IACT* systems. These kinds of preparatory studies are not limited to very low energy capabilities, but they have to take into account other important parameters, such as cost, reliability and the possibility to be upgraded. *MAGIC* will be the only telescope in the world, which can directly compares such systems, providing precious

[2] Recently it has been detected up to 400 GeV by *VERITAS* and *MAGIC*.
[3] The peak is estimated by fitting the data set with a power law function.
[4] *CTA* (*Čerenkov Telescopes Array*) is an array of *IACT* telescopes with three different mirror sizes.

knowledge. In this sense, *MAGIC* should be considered as a real test-bench of *CTA*, in particular for the large size telescopes located at the centre of the array.

A

Sum-mezzanine schematics

In this appendix, the schematics of the *Sum-mezzanine* are presented.

A.1 Sum-mezzanine schematics sheets

These schematics refer to the *Sum-mezzanine* version 1.1.

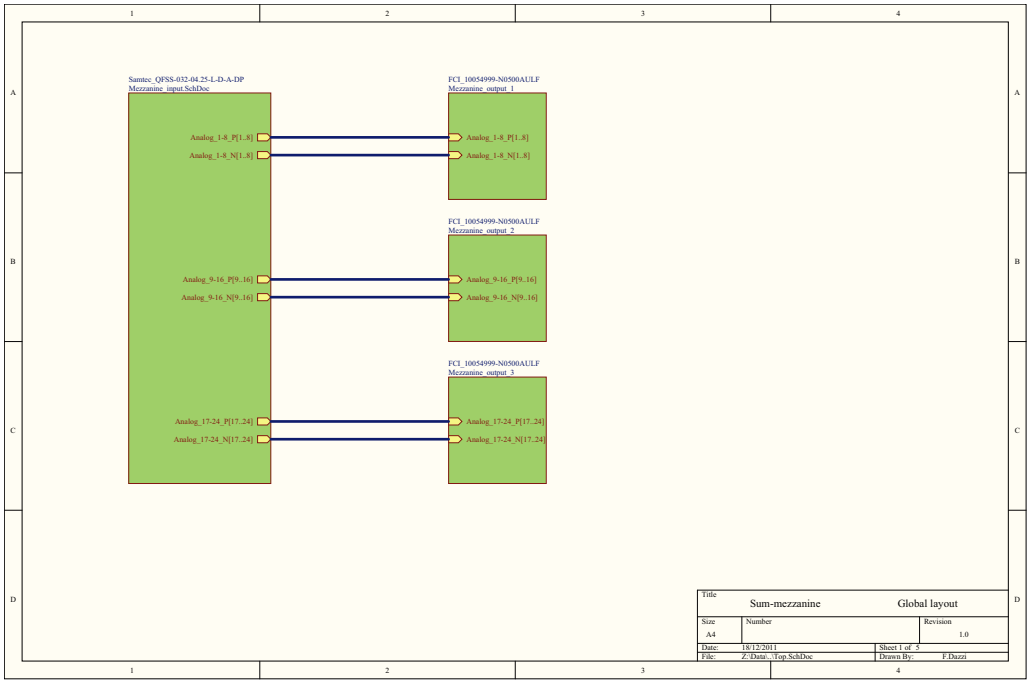

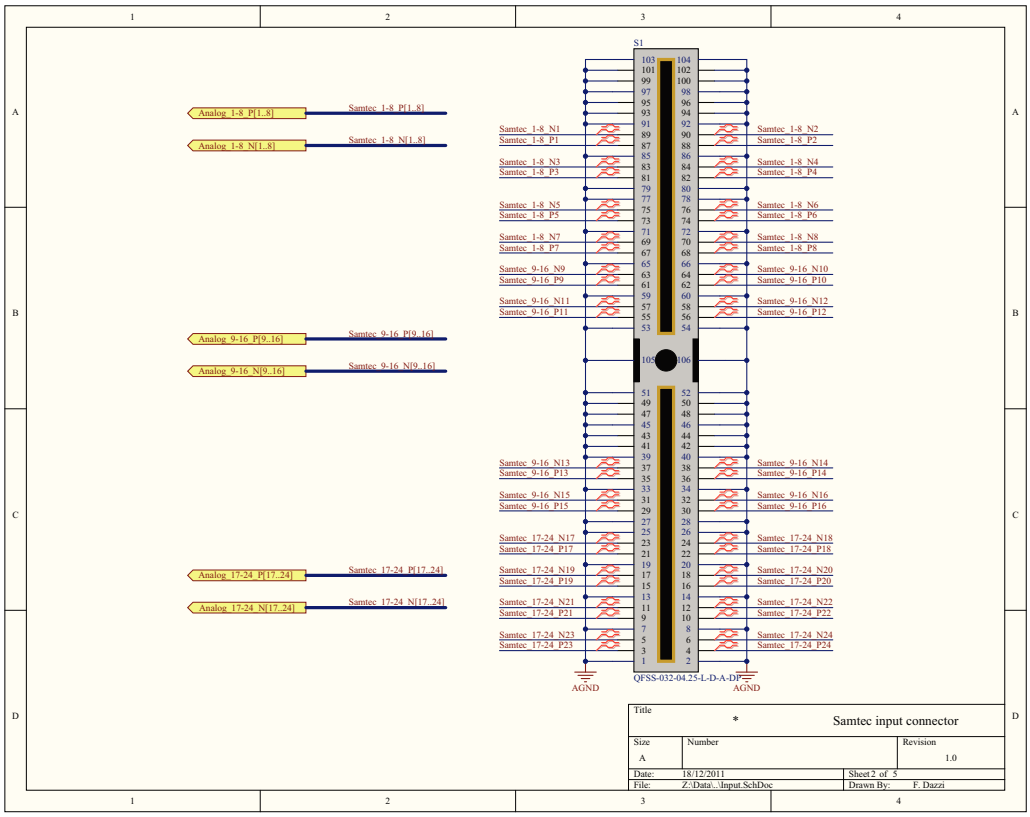
S1
Analog_1-8_P[1..8]
Analog_1-8_N[1..8]
Analog_9-16_P[9..16]
Analog_9-16_N[9..16]
Analog_17-24_P[17..24]
Analog_17-24_N[17..24]
Samtec_1-8_P[1..8]
Samtec_1-8_N[1..8]
Samtec_9-16_P[9..16]
Samtec_9-16_N[9..16]
Samtec_17-24_P[17..24]
Samtec_17-24_N[17..24]
Samtec_1-8_N1
Samtec_1-8_P1
Samtec_1-8_N2
Samtec_1-8_P2
Samtec_1-8_N3
Samtec_1-8_P3
Samtec_1-8_N4
Samtec_1-8_P4
Samtec_1-8_N5
Samtec_1-8_P5
Samtec_1-8_N6
Samtec_1-8_P6
Samtec_1-8_N7
Samtec_1-8_P7
Samtec_1-8_N8
Samtec_1-8_P8
Samtec_9-16_N9
Samtec_9-16_P9
Samtec_9-16_N10
Samtec_9-16_P10
Samtec_9-16_N11
Samtec_9-16_P11
Samtec_9-16_N12
Samtec_9-16_P12
Samtec_9-16_N13
Samtec_9-16_P13
Samtec_9-16_N14
Samtec_9-16_P14
Samtec_9-16_N15
Samtec_9-16_P15
Samtec_9-16_N16
Samtec_9-16_P16
Samtec_17-24_N17
Samtec_17-24_P17
Samtec_17-24_N18
Samtec_17-24_P18
Samtec_17-24_N19
Samtec_17-24_P19
Samtec_17-24_N20
Samtec_17-24_P20
Samtec_17-24_N21
Samtec_17-24_P21
Samtec_17-24_N22
Samtec_17-24_P22
Samtec_17-24_N23
Samtec_17-24_P23
Samtec_17-24_N24
Samtec_17-24_P24
AGND
AGND
QFSS-032-04.25-L-D-A-DP
Title
*
Samtec input connector
Size
A
Number
Revision
1.0
Date:
18/12/2011
Sheet 2 of 5
File:
Z:\Data\..\Input.SchDoc
Drawn By:
F. Dazzi

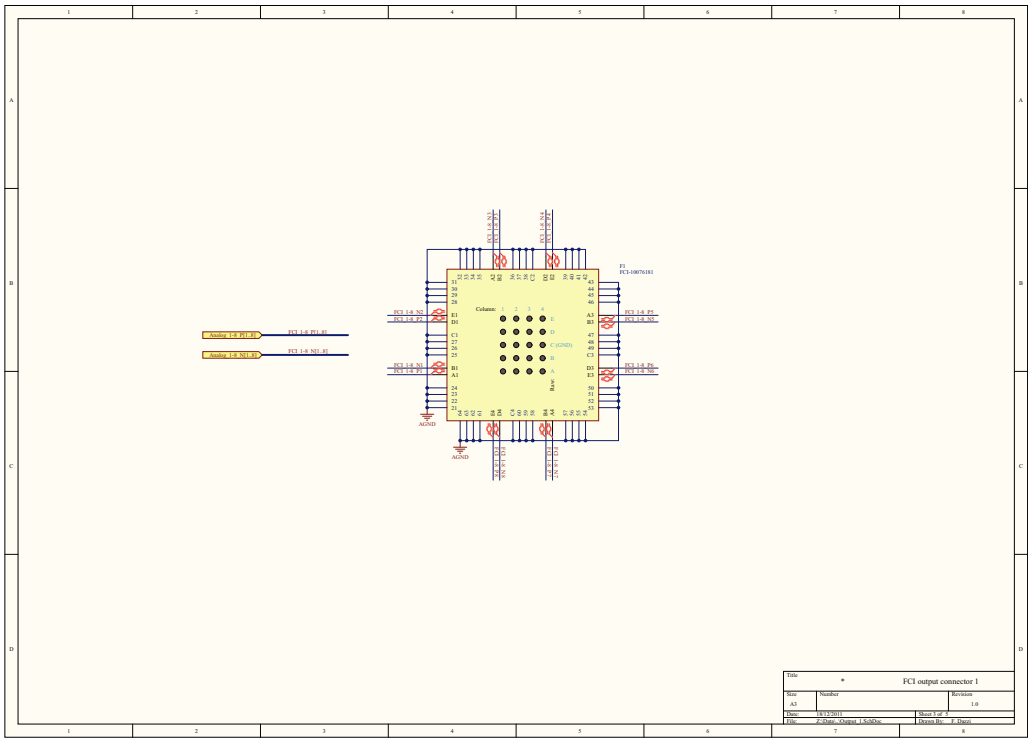
Analog_1-8_P[1..8]
Analog_1-8_N[1..8]
FCI_1-8_P[1..8]
FCI_1-8_N[1..8]
FCI-10076181
AGND
AGND
Title
*
FCI output connector 1
Size
A3
Number
Revision
1.0
Date:
18/12/2011
Sheet 3 of 5
File:
Z:\Data\..\Output_1.SchDoc
Drawn By:
F. Dazzi

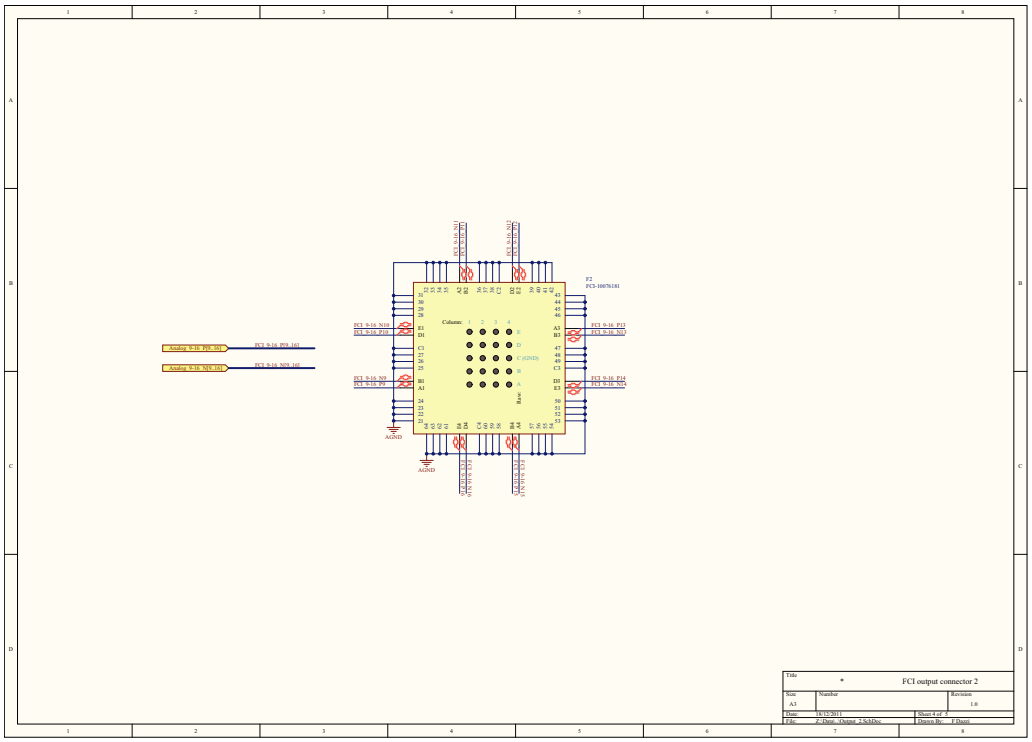
FCI output connector 2
F2
FCS-100761X1
Column:
C (GND)
Row
AGND
Analog_9-16_P[9..16]
Analog_9-16_N[9..16]
FCI_9-16_P[9..16]
FCI_9-16_N[9..16]

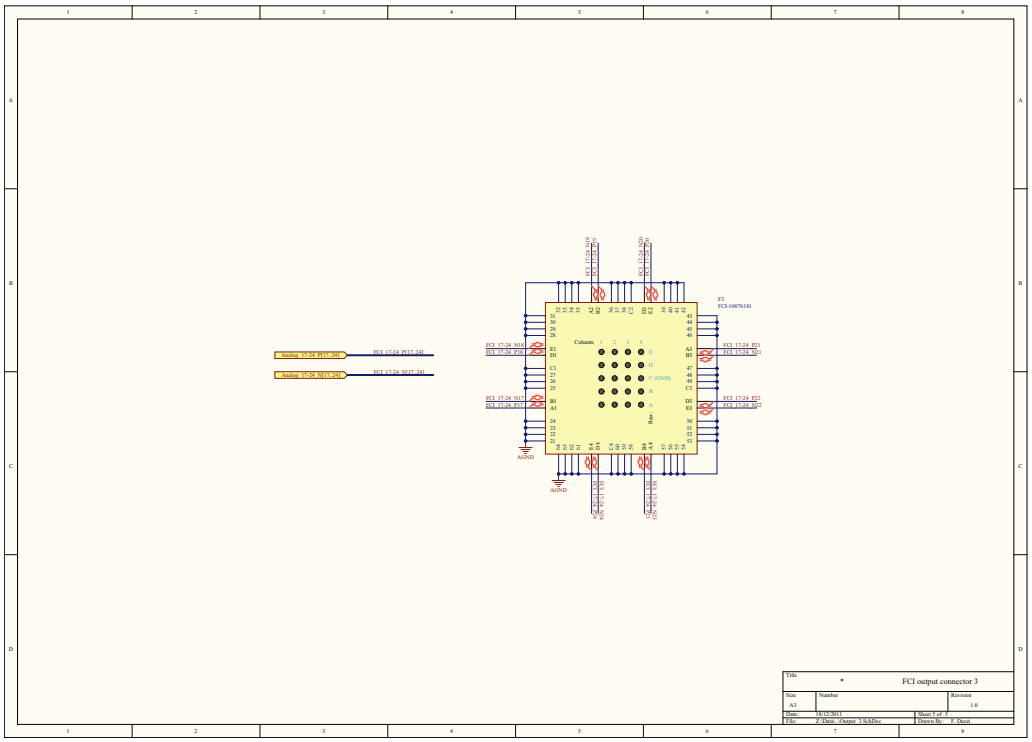
FCI output connector 3
F3
FCS-100761X1
Column:
C (GND)
Row
AGND
Analog_17-24_P[17..24]
Analog_17-24_N[17..24]
FCI_17-24_P[17..24]
FCI_17-24_N[17..24]

B

CTB-FCI schematics

In this appendix, the schematics of the *CTB-FCI* are presented.

B.1 CTB-FCI schematics sheets

These schematics refer to the *CTB-FCI* version 1.7. The transmitter stage has not

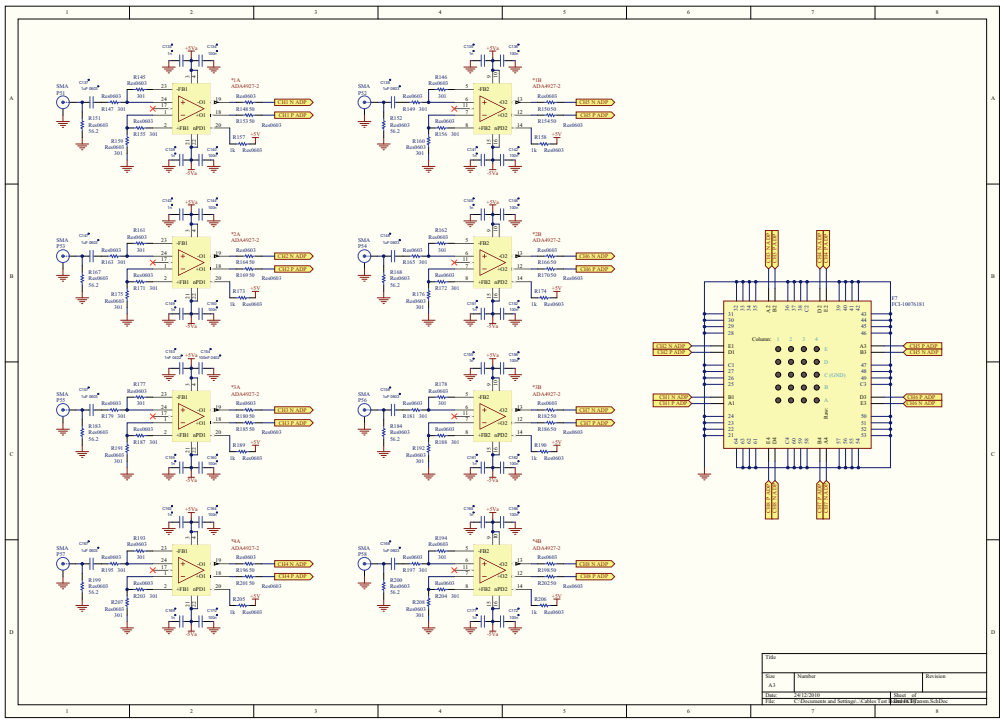

been modified during the test phase, whereas some passive components in the receiver amplifier have been changed. The two series inductances and the RC filter have been

removed and the value of the input resistors have been reduce in order to increase the bandwidth.

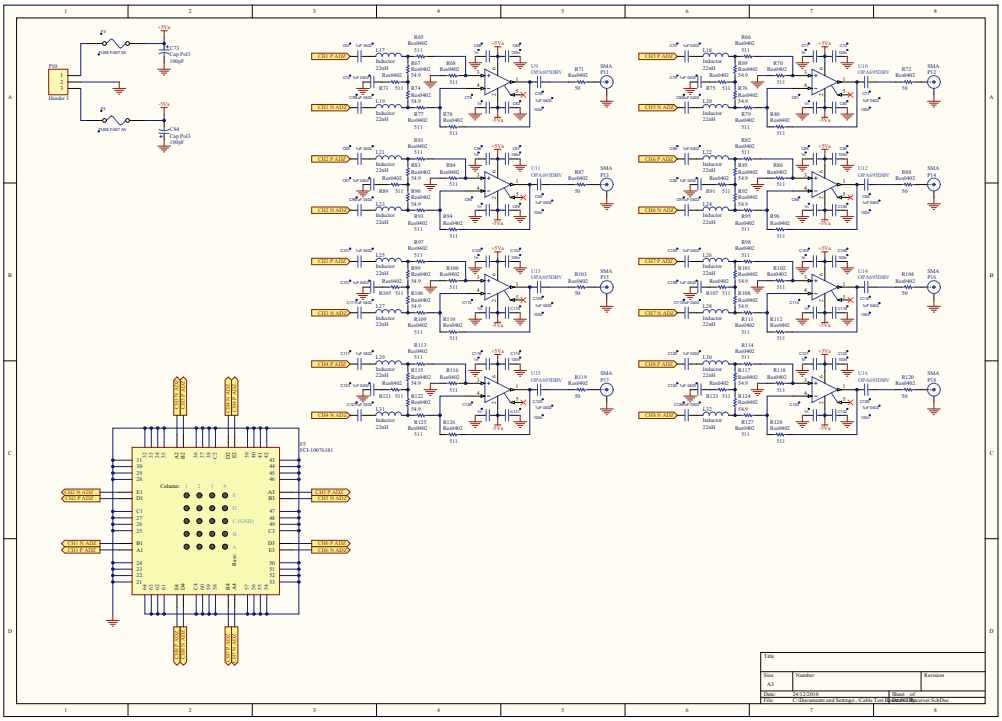

C
Sum-board schematics

In this appendix, the schematics of the *Sum-board* are presented.

C.1 Sum-board schematics sheets

These schematics refer to the *Sum-board* version 1.4.

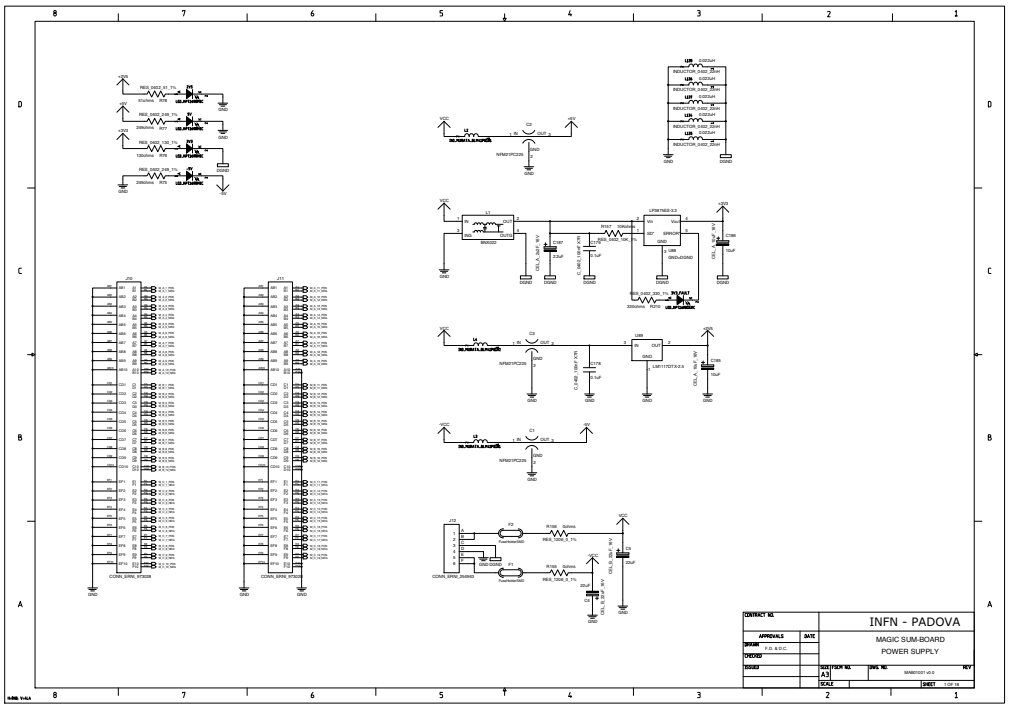

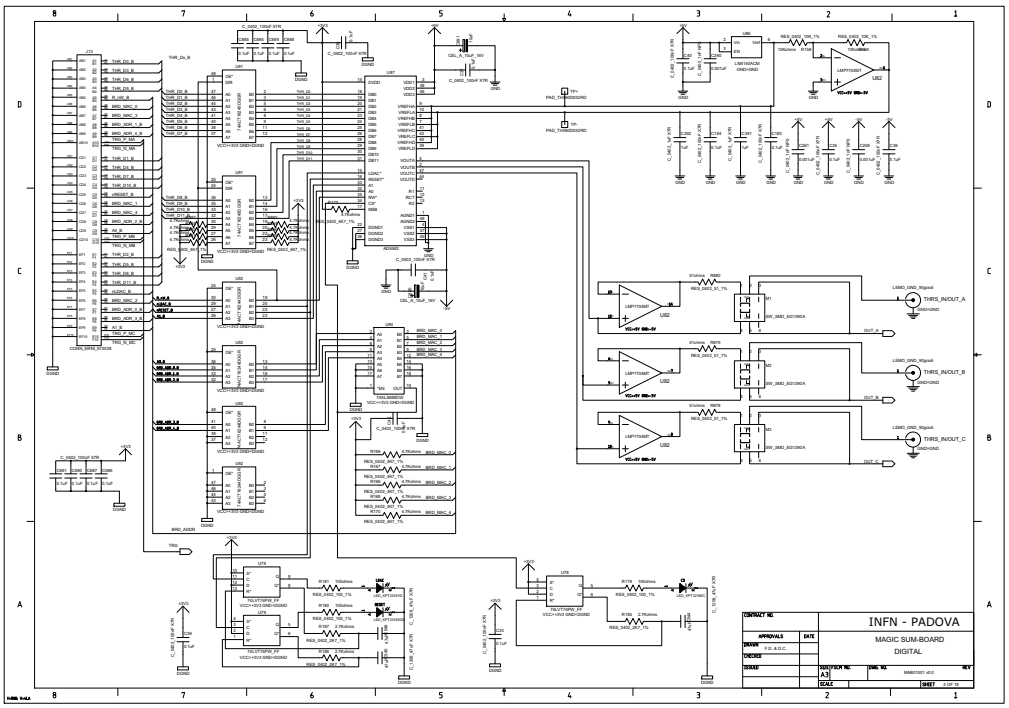
INFN - PADOVA
MAGIC SUM-BOARD
DIGITAL

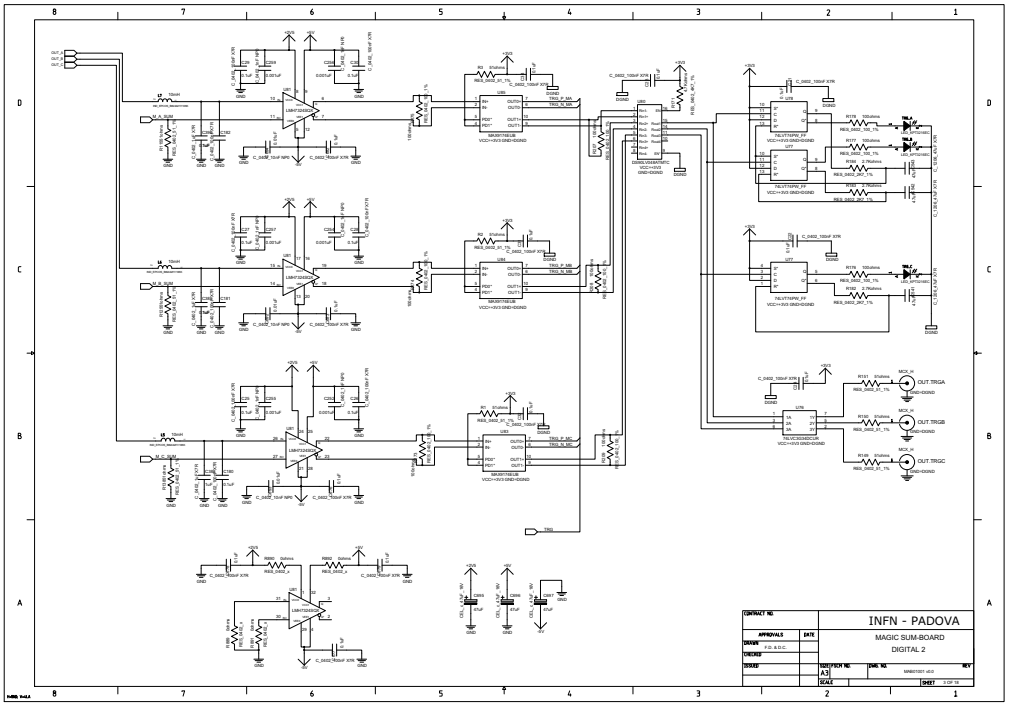
INFN - PADOVA
MAGIC SUM-BOARD
DIGITAL 2

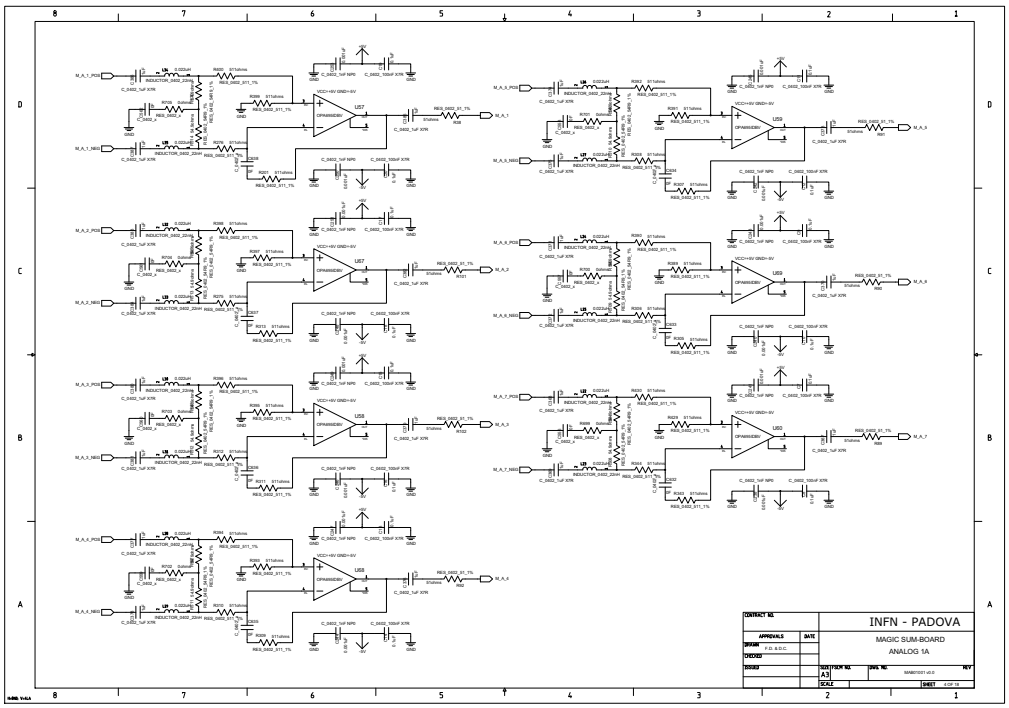
INFN - PADOVA
MAGIC SUM-BOARD
ANALOG 1A

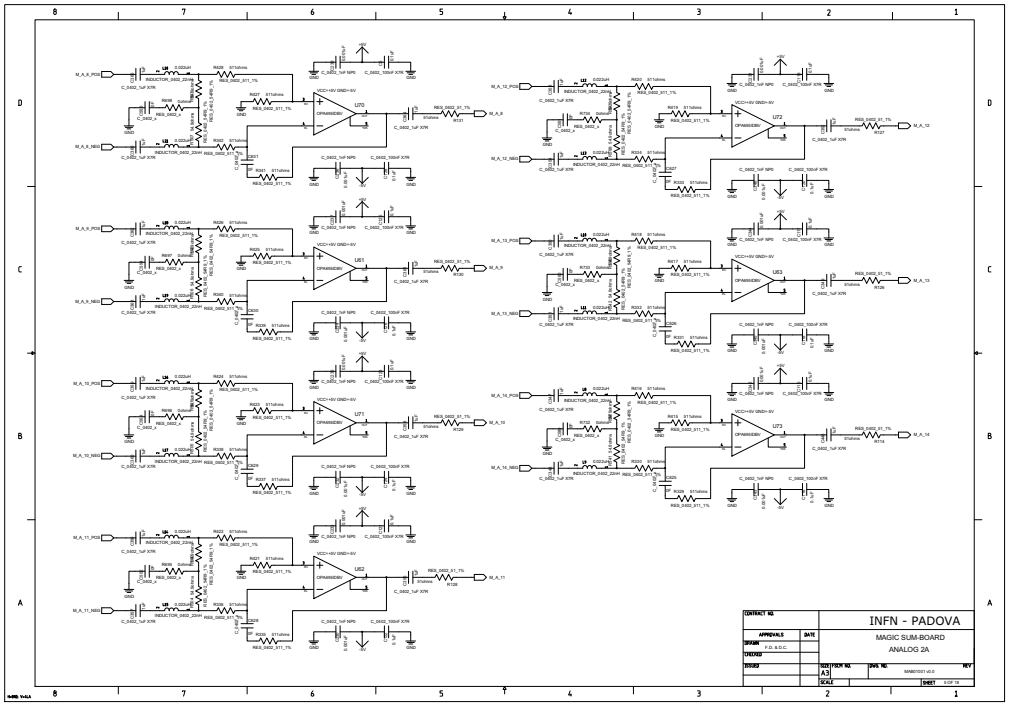
INFN - PADOVA
MAGIC SUM-BOARD
ANALOG 2A

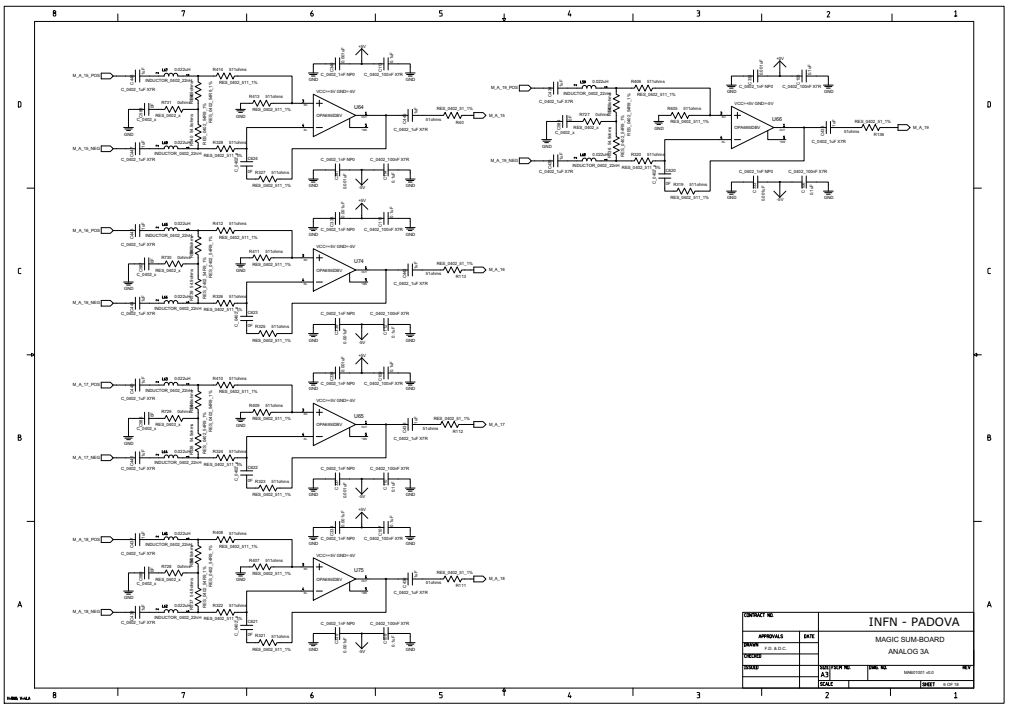
INFN - PADOVA
MAGIC SUM-BOARD
ANALOG 3A

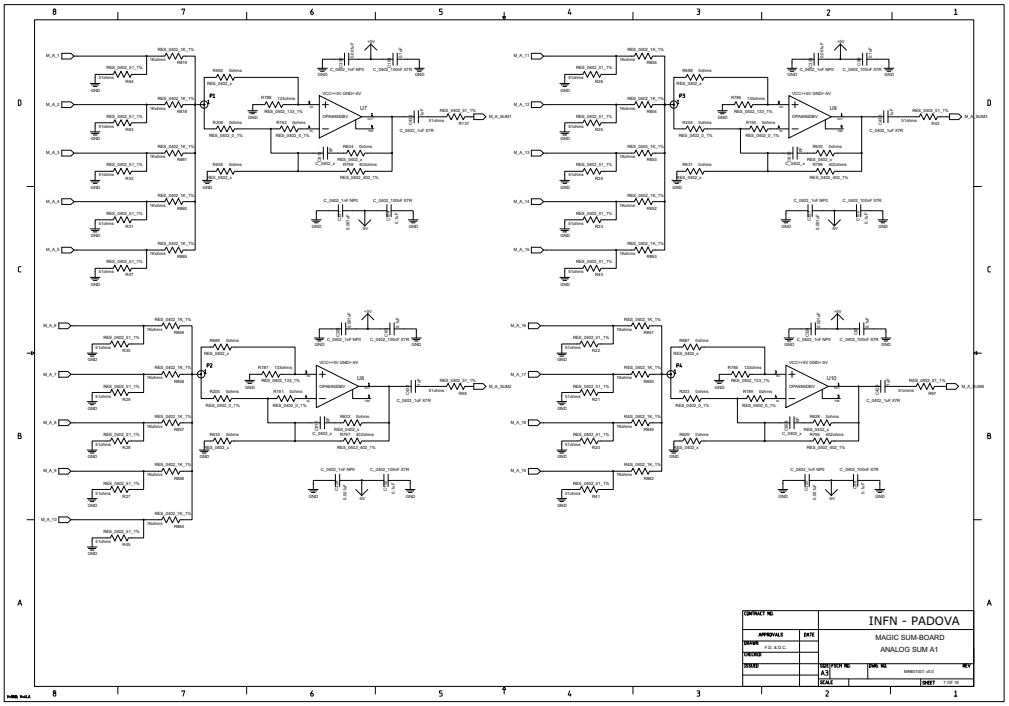
INFN - PADOVA
MAGIC SUM-BOARD
ANALOG SUM A1

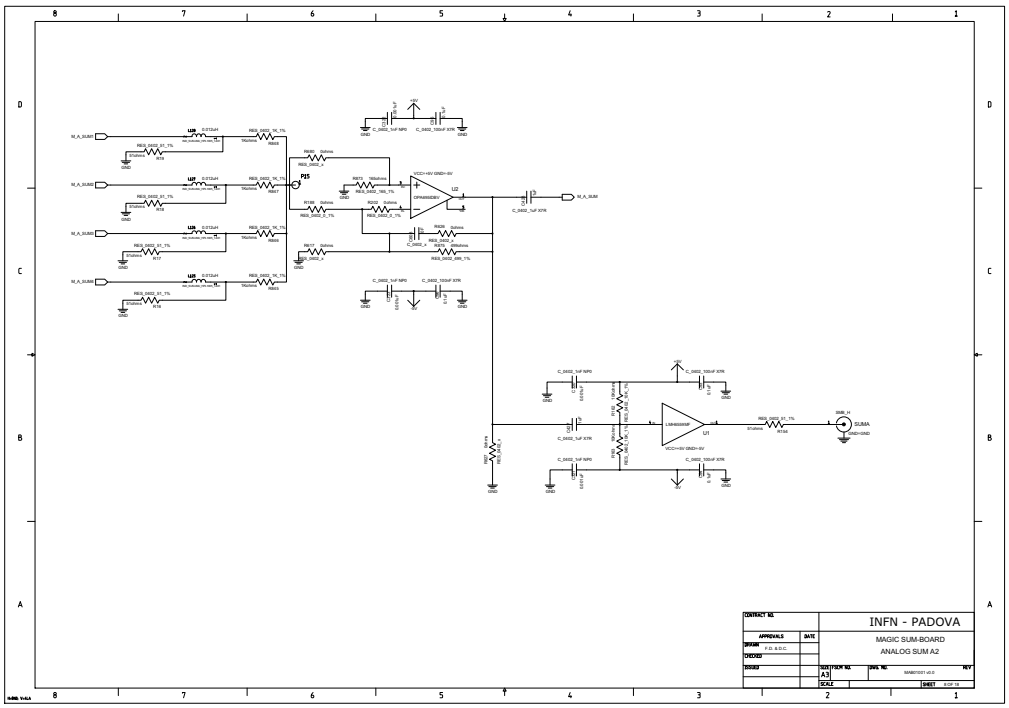
INFN - PADOVA
MAGIC SUM-BOARD
ANALOG SUM A2

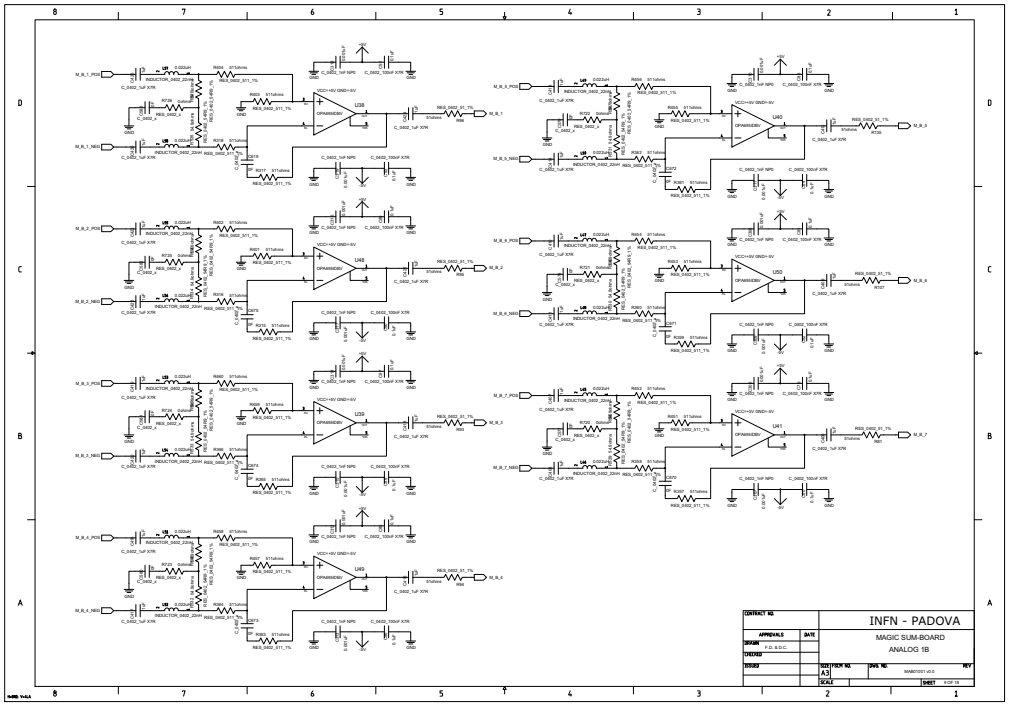
INFN - PADOVA
MAGIC SUM-BOARD
ANALOG 1B

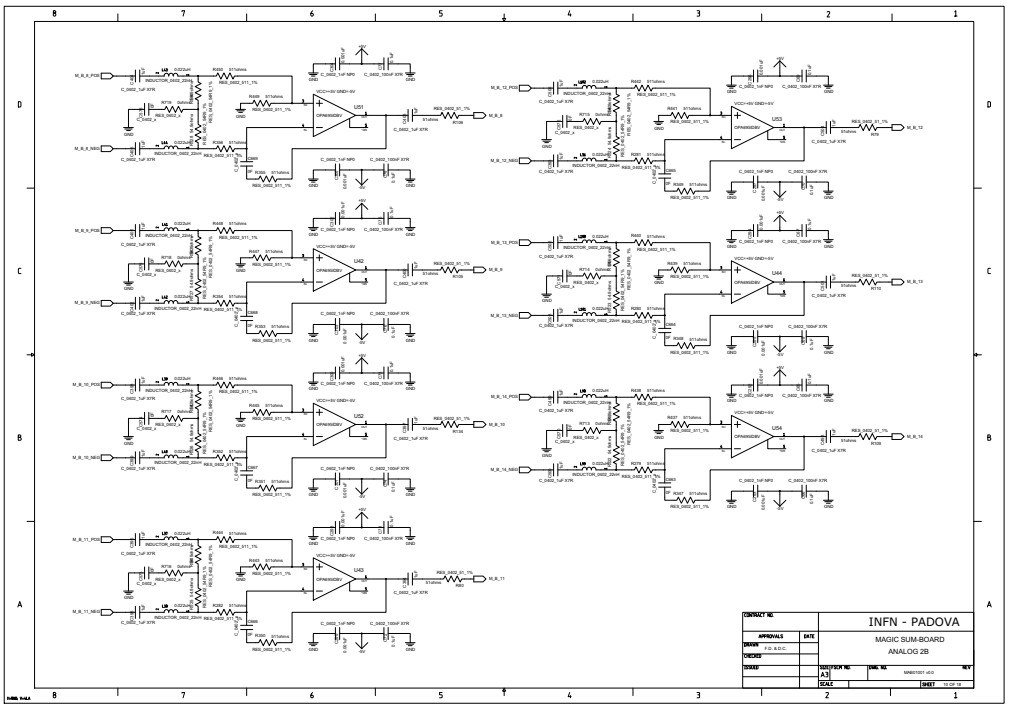
INFN - PADOVA
MAGIC SUM-BOARD
ANALOG 2B

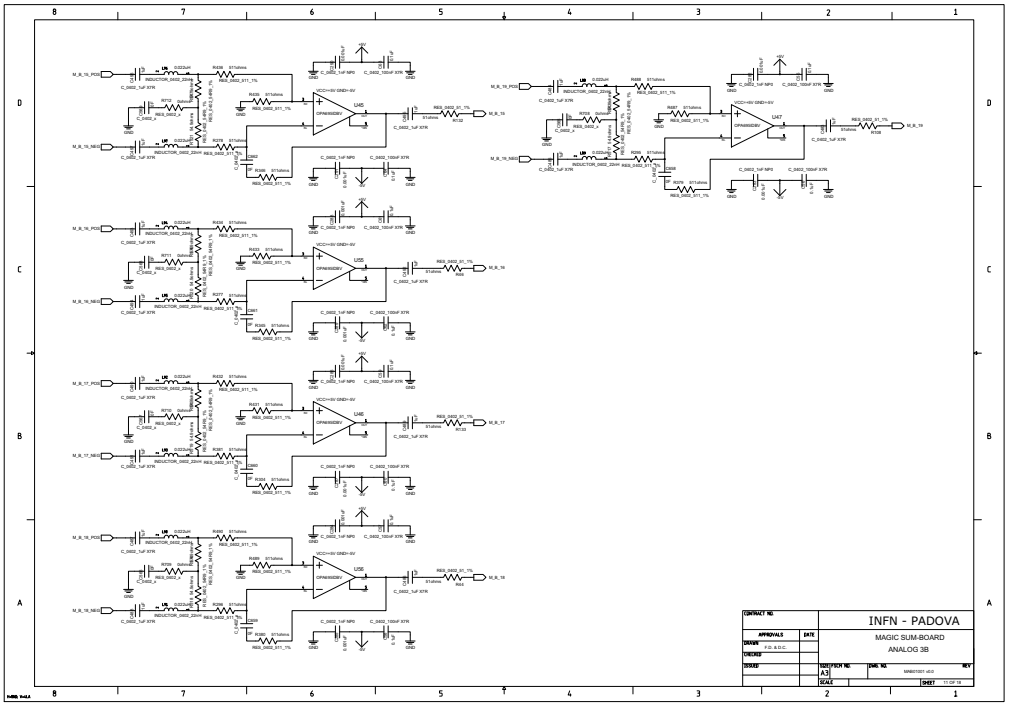
INFN - PADOVA
MAGIC SUM-BOARD
ANALOG 3B

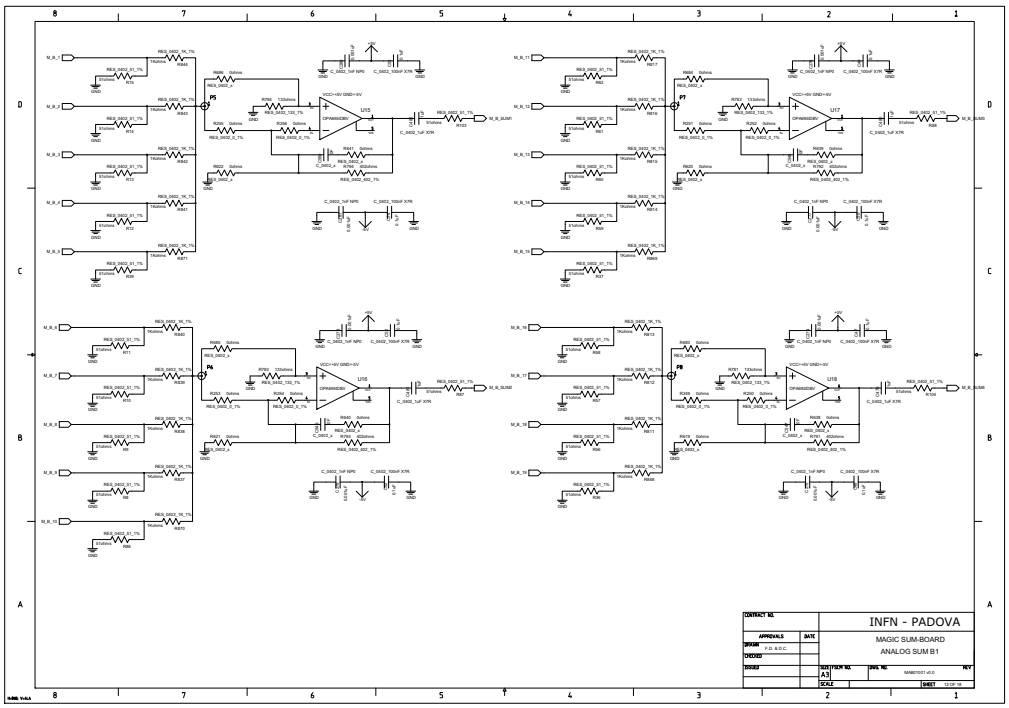
INFN - PADOVA
MAGIC SUM-BOARD
ANALOG SUM B1

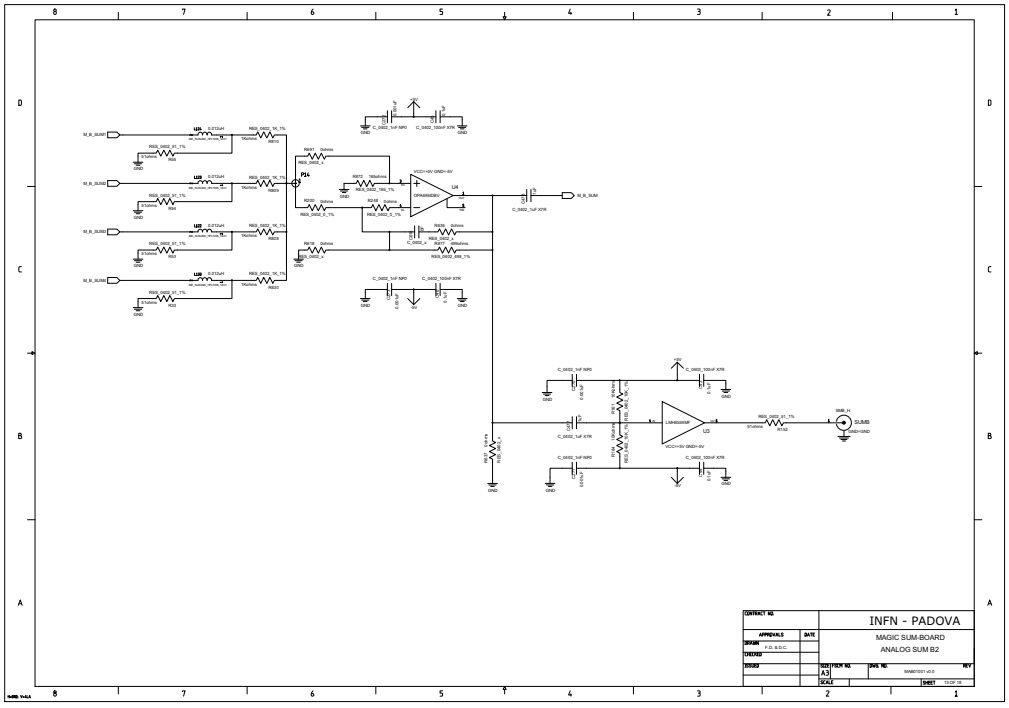
INFN - PADOVA
MAGIC SUM-BOARD
ANALOG SUM B2

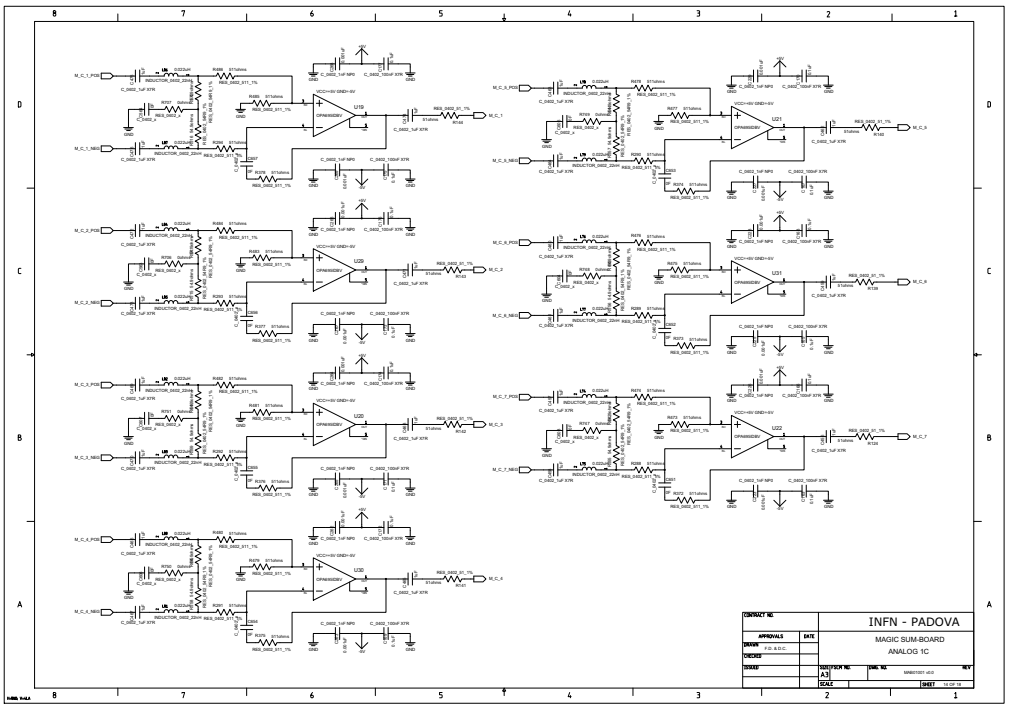
INFN - PADOVA
MAGIC SUM-BOARD
ANALOG 1C

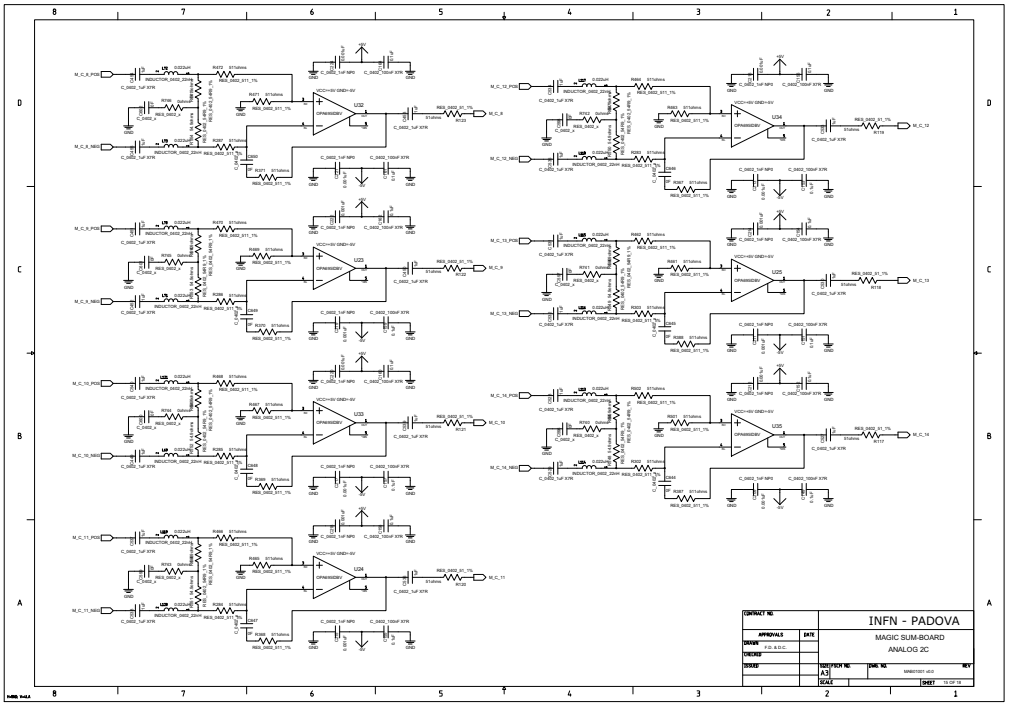
INFN - PADOVA
MAGIC SUM-BOARD
ANALOG 2C

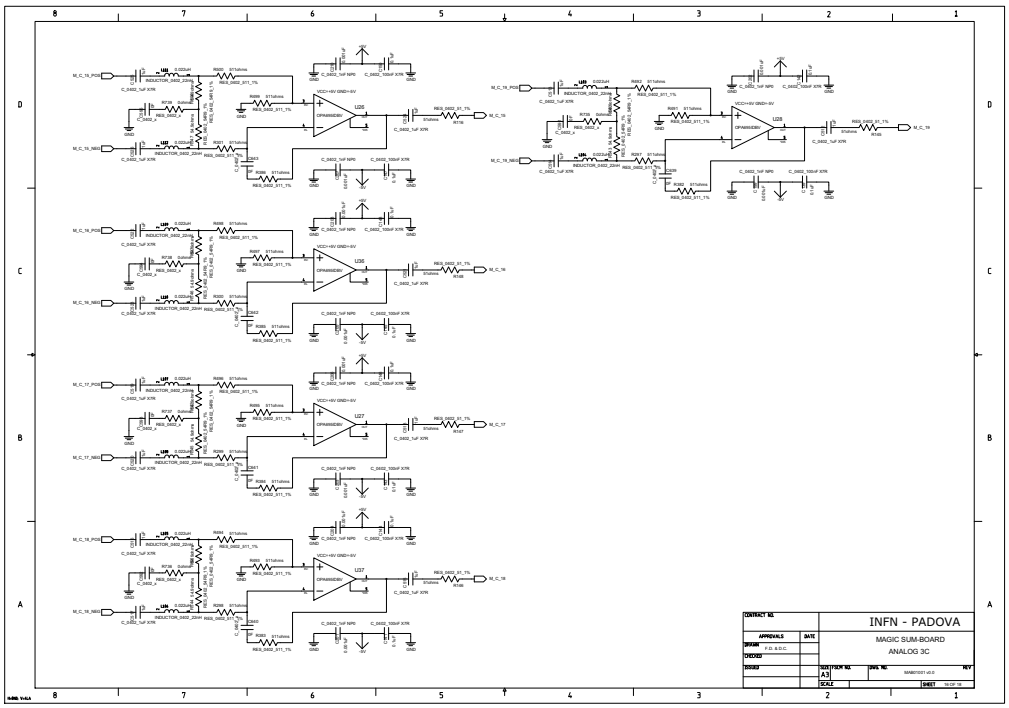
INFN - PADOVA
MAGIC SUM-BOARD
ANALOG 3C

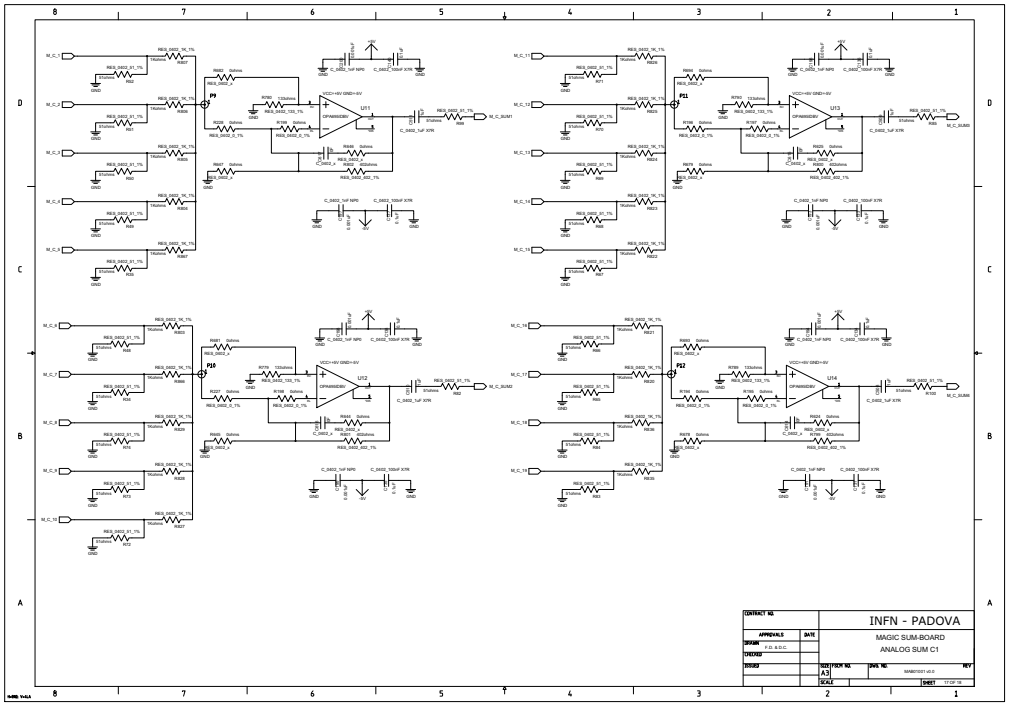
INFN - PADOVA
MAGIC SUM-BOARD
ANALOG SUM C1

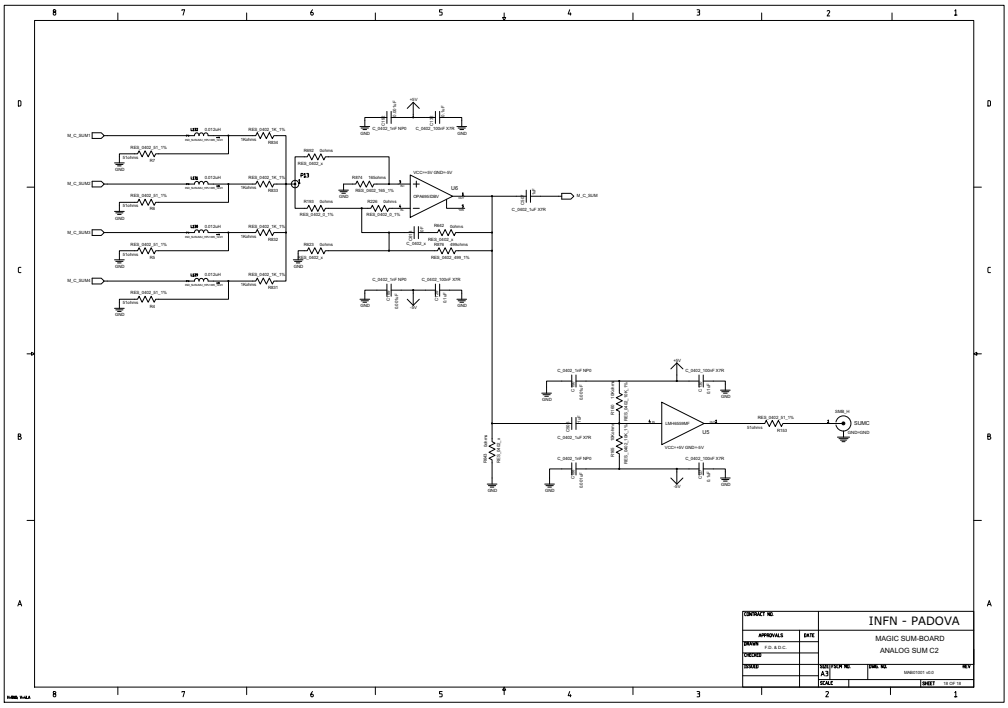
INFN - PADOVA
MAGIC SUM-BOARD
ANALOG SUM C2
A3
SHEET 1 OF 1
M_C_SUM
SUMC

D

Sum-test-board schematics

In this appendix, the schematics of the *Sum-test-board* are presented.

D.1 Sum-test-board schematics sheets

These schematics refer to the *Sum-test-board* version 2.0.

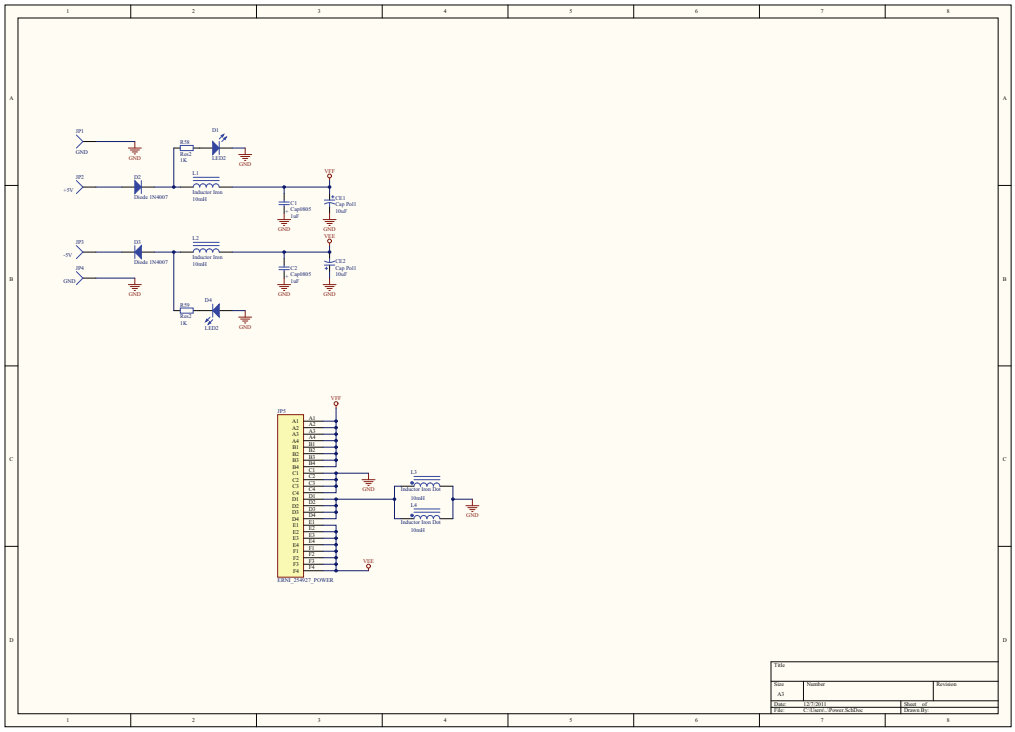

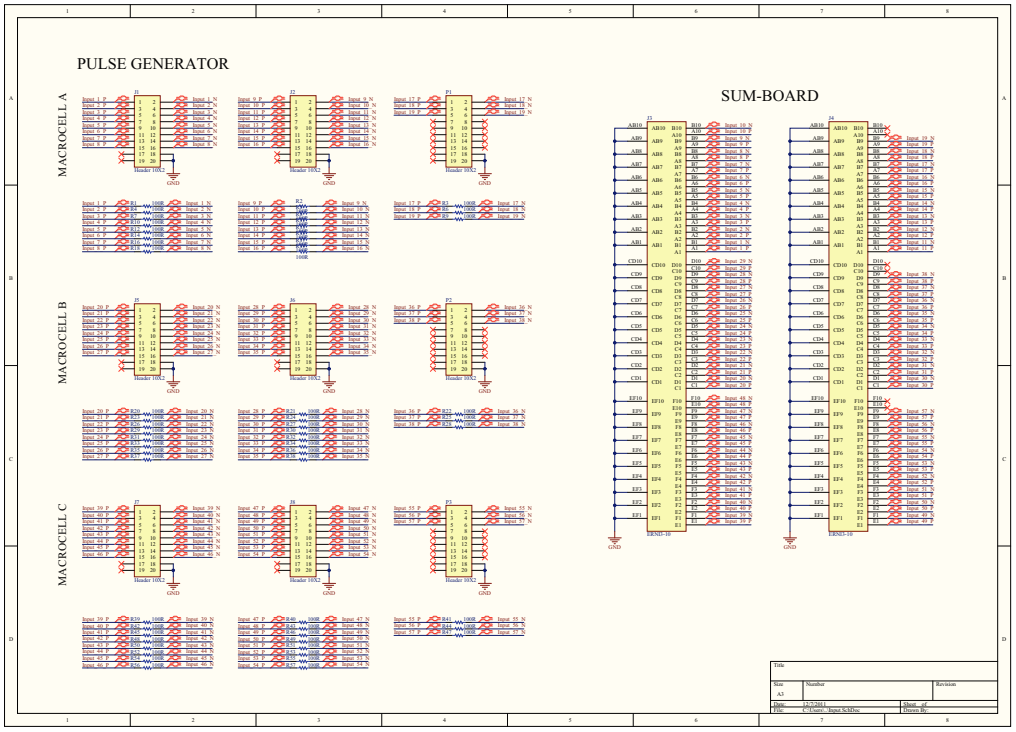
PULSE GENERATOR
SUM-BOARD
MACROCELL A
MACROCELL B
MACROCELL C

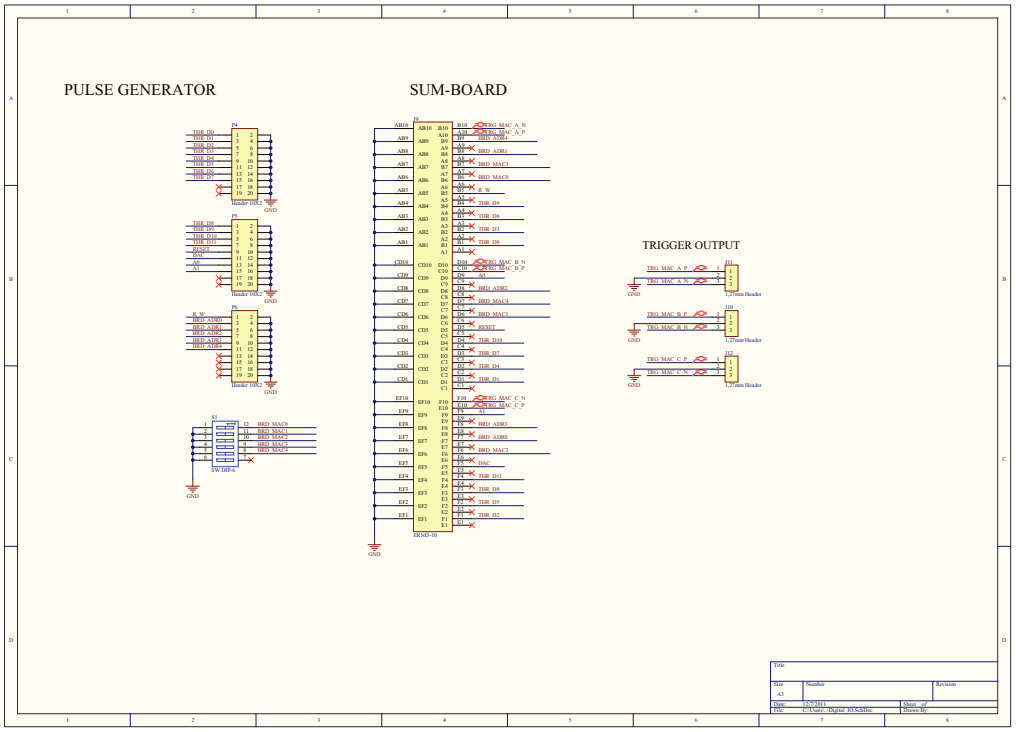
PULSE GENERATOR
SUM-BOARD
TRIGGER OUTPUT

E

MiniPulsar test-bench firmware

In this appendix, the original *VHDL* code of the *MiniPulsar* is reported.

E.1 The MiniPulsar test-bench code

This is the *VHDL* code uploaded in the *MiniPulsar* prototype board in order to check all the functionalities.

```
library ieee;
use ieee.std_logic_1164.all;
use ieee.std_logic_arith.all;
library altera;
use altera.altera_syn_attributes.all;

entity Testbench_MiniPulsar is
generic(Frequency_scale : integer := 40);       -- 40 means 1MHz (1 microsecond)
port(
-------------------------------------
--INPUTS--
-------------------------------------
MAIN_CLK:       in std_logic;                   -- Main clock
SDO_FPGA:       in std_logic;
SYSCLK:         in std_logic;                   -- Clock from VME controller
ASN:            in std_logic;                   -- VME address strobe
WRN:            in std_logic;                   -- VME write control
AM:             in std_logic_vector(5 downto 0);  -- Address modifier
GA:             in std_logic_vector(7 downto 0);  -- Geographical address
A:              in std_logic_vector(31 downto 1); -- VME address
L1IN:           in std_logic_vector(33 downto 0); -- Inputs on connector HONDA RPS-80LM
SVT_OUT_HOLD:   in std_logic;                   -- Command stop read FiFo
DSN:            in std_logic_vector(1 downto 0);  -- VME data strobe
SVT_IND:        in std_logic_vector(22 downto 0); -- Input from FiFo (From connector KEL-8831)
SVT_STATUS:     in std_logic_vector(4 downto 0);  -- 0 => FiFo1 full;
                                                  -- 1 => FiFo1 almost full;
                                                  -- 2 => FiFo1 empty;
                                                  -- 3 => FiFo2 empty;
                                                  -- 4 => Status SVT_DS (WCLK)
RESET :         in std_logic;                   -- Reset button

-------------------------------------
--OUTPUTS--
-------------------------------------
LCLK:           out std_logic;              -- Hola mezzanine clock
LCTRLN:         out std_logic;
LDERRN:         out std_logic;              -- Move to input
LDOWN_AN:       out std_logic;              -- Move to input
LED_ERR:        out std_logic;              -- Bottom red led
LED_RUN:        out std_logic;              -- Bottom green led
LED_SEL:        out std_logic;              -- Bottom yellow led
LWENN:          out std_logic;
SRAM_ADSCN:     out std_logic;              -- SRAM address strobe from controller
SRAM_ADSPN:     out std_logic;              -- SRAM addres strobe from processor
SRAM_ADVN:      out std_logic;              -- Increment address in SRAM burst cycle
SRAM_CE1n:      out std_logic;              -- SRAM chip enable 1
SRAM_CE2:       out std_logic;              -- SRAM chip enable 2
SRAM_CE3n:      out std_logic;              -- SRAM chip enable 3
SRAM_CLK:       buffer std_logic;           -- SRAM clock
```

```
SRAM_GWN:    out std_logic;                -- SRAM global write enable (all bytes written)
SRAM_OEN:    buffer std_logic;             -- SRAM output enable
SRAM_BWEN:   out std_logic;                -- SRAM byte enable
UDW0_A:      out std_logic;
UDW1_A:      out std_logic;
URESET_AN:   out std_logic;                -- Hola mezzanine reset
UTD0N:       out std_logic;
UXOFFN:      out std_logic;                -- Move to input
SVT_OUT_DS:  out std_logic;                -- FiFo clock distributor
DTACKn:      out std_logic;
BERRn:       out std_logic;
DIR_DATA:    out std_logic;                -- Data direction VME <--> FPGA
DATA_EN:     buffer std_logic;             -- VME data enable
CARD1_ID:    out std_logic_vector(3 downto 0);   -- Move to input
CARD2_ID:    out std_logic_vector(3 downto 0);   -- Move to input
D:           out std_logic_vector(31 downto 0);  -- VME data
F1CTRL:      out std_logic_vector(32 downto 0);  -- DRS1 controls
F1IO:        out std_logic_vector(45 downto 0);  -- DRS1 data
F2CTRL:      out std_logic_vector(32 downto 0);  -- DRS2 controls
F2IO:        out std_logic_vector(45 downto 0);  -- DRS2 data
L1OUT:       out std_logic_vector(33 downto 0);  -- Outputs on connector HONDA RPS-80LM
LD:          out std_logic_vector(31 downto 0);  -- Hola data
SRAM_ADDR:   out std_logic_vector(20 downto 0);  -- SRAM addresses
SRAM_BW:     out std_logic_vector(3 downto 0);   -- SRAM bytes selection
SRAM_DQ:     inout std_logic_vector(31 downto 0);-- SRAM data
SRAM_DP:     inout std_logic_vector(3 downto 0); -- SRAM data
SVT_CTRL:    out std_logic_vector(3 downto 0);   -- 0 => REN; 1 => RCLK;
                                                 -- 2 => FiFo reset/WEN;
                                                 -- 3 => FiFo write distributor
SVT_OUT:     out std_logic_vector(22 downto 0);  -- Outputs to connector KEL-8831
URL:         out std_logic_vector(3 downto 0);   -- Hola address
LED:         out std_logic_vector(3 downto 1)    -- 1 => Top red led;
                                                 -- 2 => Top yellow led;
                                                 -- 3 => Top green led;
);

end Testbench_MiniPulsar;


architecture Bhv of Testbench_MiniPulsar is
signal Scale_counter:     integer := 0;                  -- Count the frequency_scale cycles
signal Frequency_out:     std_logic := '0';              -- Frequency @ outputs
signal Led_time :         integer := 0;                  -- Counter timing for the LEDs
signal Led_scale:         integer := 1000000;            -- Timing for the LEDs
signal Led_out:           std_logic := '0';              -- LED_RUN output
signal SRAM_counter:      integer := 0;                  -- Counter timing for the SRAM FSM
signal SRAM_WR_RD_count:  integer := 0;                  -- Counter timing for the SRAM write
    and read
constant SRAM_scale:      integer := 8;                  -- Timing for the single SRAM cycle
constant SRAM_W_R_scale:  integer := 524286;             -- Timing for the SRAM (default
    1048574)
signal SRAM_DQ_in:        std_logic_vector(31 downto 0); -- Signal input connected to SRAM_DQ
signal SRAM_DQ_out:       std_logic_vector(31 downto 0); -- Signal output connected to SRAM_DQ
signal SRAM_DP_in:        std_logic_vector(3 downto 0);  -- Signal connected to SRAM_DP
type STATE is (RESET_SRAM,
               WAIT_SRAM,
               PRE0_WRITE_SRAM,
               PRE1_WRITE_SRAM,
               WRITE_SRAM,
               PRE0_READ_SRAM,
               PRE1_READ_SRAM,
               READ_SRAM);
signal State_pres, State_fut: STATE := WAIT_SRAM;


begin

Led_scale <= (Frequency_scale * 2000000);        -- 2000000 means 2 sec

Output_freq: process (MAIN_CLK)
begin
if MAIN_CLK'event and MAIN_CLK = '1' then
  if ((Scale_counter < Frequency_scale) and (Scale_counter < (Frequency_scale/2))) then
             -- First half duty cycle (50%)
    Scale_counter <= Scale_counter + 1;          -- Increase counter
    Frequency_out <= '0';                        -- Output @ '0'
  elsif ((Scale_counter < Frequency_scale) and (Scale_counter >= (Frequency_scale/2))) then
           -- Second half duty cycle
    Scale_counter <= Scale_counter + 1;          -- Increase counter
    Frequency_out <= '1';                        -- Output @ '1'
  else                                           -- Scale_counter @ end of cycle
    Frequency_out <= '0';                        -- Output @ '0'
    Scale_counter <= 0;                          -- Reset counter
  end if;
end if;
end process Output_freq;


Output_LEDs: process (MAIN_CLK)
begin
if MAIN_CLK'event and MAIN_CLK = '1' then
  if ((Led_time < Led_scale) and (Led_time < (Led_scale/2))) then-- First half duty cycle
      (50%)
    if Led_time = (Led_scale/4) then                             -- Blink each 1 sec
      LED_SEL <= '1';                                            -- 1 means ON
```

```
      --LED(2) <= '1';-- Uncomment if you want to check the upper LEDs & comment in FiFo
          status
    else
      LED_SEL <= '0';                                          -- 0 means OFF
      --LED(2) <= '0';-- Uncomment if you want to check the upper LEDs & comment in FiFo
          status
    end if;
    Led_time <= Led_time + 1;                                  -- Increase LEDs counter
    Led_out <= '0';
    LED_ERR <= '0';
    --LED(3) <= '0';-- Uncomment if you want to check the upper LEDs & comment in FiFo status
  elsif ((Led_time < Led_scale) and (Led_time >= (Led_scale/2))) then-- Second half duty
      cycle
    if Led_time = 3*(Led_scale/4) then
      LED_SEL <= '1';                                          -- LED_SEL ON
      --LED(2) <= '1';-- Uncomment if you want to check the upper LEDs & comment in FiFo
          status
    else
      LED_SEL <= '0';                                          -- LED_SEL OFF
      --LED(2) <= '0';-- Uncomment if you want to check the upper LEDs & comment in FiFo
          status
    end if;
    Led_time <= Led_time + 1;
    Led_out <= '1';
    LED_ERR <= '0';                                            -- LED_ERR OFF
    --LED(3) <= '0';-- Uncomment if you want to check the upper LEDs & comment in FiFo status
  else
    Led_out <= '0';
    Led_time <= 0;
    LED_ERR <= '1';                                            -- LED_ERR ON (Blink each 2
        sec)
    --LED(3) <= '1';-- Uncomment if you want to check the upper LEDs & comment in FiFo status
  end if;
end if;
end process Output_LEDs;


-----------------------------------
-- FiFos commands--
-----------------------------------
FiFo_status: process (SVT_STATUS)
begin
  case SVT_STATUS(0) is
    when '0' => LED(1) <= '1';                                 -- FiFo1 full (Red led ON)
    when others => LED(1) <= '0';
  end case;

  case SVT_STATUS(1) is
    when '0' => LED(2) <= '1';                                 -- FiFo1 almost full (Yellow led)
    when others => LED(2) <= '0';
  end case;

  if (SVT_STATUS(2) or SVT_STATUS(3)) = '0' then               -- FiFos empty (Green led ON)
    LED(3) <= '1';
  elsif (SVT_STATUS(2) xor SVT_STATUS(3)) = '1' then           -- FiFo1 or FiFo2 empty (Green led
      blink)
    LED(3) <= Led_out;
  else
    LED(3) <= '0';
  end if;
end process FiFo_status;


-----------------------------------
-- FiFos controls--
-----------------------------------
FiFo_controls: process (RESET, Frequency_out, SVT_STATUS(4), SVT_OUT_HOLD)
begin
  if RESET = '0' then                          -- Reset activated
    SVT_CTRL(0) <= '1';                        -- FiFo read deactivated
    SVT_CTRL(1) <= '0';                        -- FiFo read clock deactivated
    SVT_CTRL(2) <= '0';                        -- FiFo reset & write deactivated
    SVT_CTRL(3) <= '0';                        -- FiFo write check deactivated
  elsif SVT_OUT_HOLD = '0' then
    SVT_CTRL(0) <= '1';                        -- FiFo read deactivated
    SVT_CTRL(1) <= '0';                        -- FiFo read clock deactivated
    SVT_CTRL(2) <= '1';                        -- FiFo write activated
    SVT_CTRL(3) <= SVT_STATUS(4);              -- FiFo write check activated for desy chain
  else
    SVT_CTRL(0) <= '0';                        -- FiFo read activated
    SVT_CTRL(1) <= Frequency_out;              -- FiFo read clock @ "Frequency out"
    SVT_CTRL(2) <= '1';                        -- FiFo write activated
    SVT_CTRL(3) <= SVT_STATUS(4);              -- FiFo write check activated for desy chain
  end if;
end process FiFo_controls;


-----------------------------------
-- SRAM commands--
-----------------------------------
SRAM_CLK <= MAIN_CLK;
LD <= SRAM_DQ_in;          -- Map SRAM_DQ into LD when data read from SRAM
URL <= SRAM_DP_in;

SRAM_FSM_clk: process (SRAM_CLK, RESET)          -- SRAM State machine clk & counter
begin
```

```
  if SRAM_CLK'event and SRAM_CLK = '0' then
    if RESET = '0' then                              -- Reset SRAM
      State_pres <= RESET_SRAM;
      SRAM_counter <= 0;
      SRAM_WR_RD_count <= 0;
    else
      State_pres <= State_fut;
    end if;
    if (SRAM_counter > SRAM_scale) then
      SRAM_counter <= 0;
      if (SRAM_WR_RD_count > SRAM_W_R_scale) then
        SRAM_WR_RD_count <= 0;
      else
        SRAM_WR_RD_count <= SRAM_WR_RD_count + 1;        -- Increase SRAM data counter
      end if;
    else
      SRAM_counter <= SRAM_counter + 1;          -- Increase SRAM cycle counter
    end if;
  end if;
end process SRAM_FSM_clk;

SRAM_FSM: process (State_pres, SRAM_counter, SRAM_OEN)  -- SRAM State machine function
begin
  case State_pres is
    when RESET_SRAM =>                      -- State 0 => RESET
      State_fut <= WAIT_SRAM;
      SRAM_DP <= (others => '0');
    when WAIT_SRAM =>                       -- State 1 => WAIT
      if (SRAM_counter /= 1) and ((SRAM_counter /= 6)) then
        State_fut <= WAIT_SRAM;
      elsif (SRAM_counter = 6) then
        State_fut <= PRE0_READ_SRAM;
      else
        State_fut <= PRE0_WRITE_SRAM;
      end if;
    when PRE0_WRITE_SRAM =>                 -- Load address into registers for writing
      State_fut <= PRE1_WRITE_SRAM;
    when PRE1_WRITE_SRAM =>                 -- Load address into memory for writing
      State_fut <= WRITE_SRAM;
    when WRITE_SRAM =>                      -- Write memory
      State_fut <= WAIT_SRAM;
    when PRE0_READ_SRAM =>                  -- Load address into registers for reading
      State_fut <= PRE1_READ_SRAM;
    when PRE1_READ_SRAM =>                  -- Load address into memory for reading
      State_fut <= READ_SRAM;
    when READ_SRAM =>                       -- Read memory
      State_fut <= WAIT_SRAM;
    when others =>
      State_fut <= RESET_SRAM;
end case;

  -- Bidirectional function
  if SRAM_OEN = '1' then
    SRAM_DQ(31 downto 0) <= SRAM_DQ_out(31 downto 0);            -- SRAM data 0-31
    SRAM_DP <= conv_std_logic_vector(SRAM_WR_RD_count, 4);       -- SRAM data 32-36
    SRAM_DQ_in <= (others => 'Z');
    SRAM_DP_in <= (others => 'Z');
  else
    SRAM_DQ_in (31 downto 0) <= SRAM_DQ (31 downto 0);           -- Map SRAM_DQ into LD
    SRAM_DP_in <= SRAM_DP;                                       -- Map SRAM_DP into URL
    SRAM_DQ <= (others => 'Z');
    SRAM_DP <= (others => 'Z');
  end if;
end process SRAM_FSM;

with State_pres select
  SRAM_BW <= B"1111" when RESET_SRAM,
  B"1111" when WAIT_SRAM,
  B"1111" when PRE0_WRITE_SRAM,
  B"1111" when PRE1_WRITE_SRAM,
  B"0000" when WRITE_SRAM,
  B"1111" when PRE0_READ_SRAM,
  B"1111" when PRE1_READ_SRAM,
  B"1111" when READ_SRAM,
  B"1111" when others;
with State_pres select
  SRAM_BWEN <= '1' when RESET_SRAM,
   '1' when WAIT_SRAM,
   '1' when PRE0_WRITE_SRAM,
   '1' when PRE1_WRITE_SRAM,
   '0' when WRITE_SRAM,
   '1' when PRE0_READ_SRAM,
   '1' when PRE1_READ_SRAM,
   '1' when READ_SRAM,
   '1' when others;
with State_pres select
  SRAM_GWN <= '1' when RESET_SRAM,
   '1' when WAIT_SRAM,
   '1' when PRE0_WRITE_SRAM,
   '1' when PRE1_WRITE_SRAM,
   '0' when WRITE_SRAM,
   '1' when PRE0_READ_SRAM,
   '1' when PRE1_READ_SRAM,
   '1' when READ_SRAM,
   '1' when others;
with State_pres select
```

```
   SRAM_CE1n <= '1' when RESET_SRAM,
    '1' when WAIT_SRAM,
    '0' when PRE0_WRITE_SRAM,
    '0' when PRE1_WRITE_SRAM,
    '0' when WRITE_SRAM,
    '0' when PRE0_READ_SRAM,
    '0' when PRE1_READ_SRAM,
    '0' when READ_SRAM,
    '1' when others;
SRAM_CE2  <= '1';
SRAM_CE3n <= '0';
with State_pres select
   SRAM_OEN <=   '1' when RESET_SRAM,
    '1' when WAIT_SRAM,
    '1' when PRE0_WRITE_SRAM,
    '1' when PRE1_WRITE_SRAM,
    '1' when WRITE_SRAM,
    '1' when PRE0_READ_SRAM,
    '1' when PRE1_READ_SRAM,
    '0' when READ_SRAM,
    '1' when others;
SRAM_ADVN <= '1';
with State_pres select
   SRAM_ADSPN <= '1' when RESET_SRAM,
    '1' when WAIT_SRAM,
    '0' when PRE0_WRITE_SRAM,
    '0' when PRE1_WRITE_SRAM,
    '1' when WRITE_SRAM,
    '0' when PRE0_READ_SRAM,
    '0' when PRE1_READ_SRAM,
    '1' when READ_SRAM,
    '1' when others;
with State_pres select
   SRAM_ADSCN <= '1' when RESET_SRAM,
    '1' when WAIT_SRAM,
    '0' when PRE0_WRITE_SRAM,
    '0' when PRE1_WRITE_SRAM,
    '1' when WRITE_SRAM,
    '0' when PRE0_READ_SRAM,
    '0' when PRE1_READ_SRAM,
    '1' when READ_SRAM,
    '1' when others;
with State_pres select
   SRAM_ADDR <= (others => '0') when RESET_SRAM,
    (others => '0') when WAIT_SRAM,
    conv_std_logic_vector(SRAM_WR_RD_count,SRAM_ADDR'length) when PRE0_WRITE_SRAM,
    conv_std_logic_vector(SRAM_WR_RD_count,SRAM_ADDR'length) when PRE1_WRITE_SRAM,
    (others => '0') when WRITE_SRAM,
    conv_std_logic_vector(SRAM_WR_RD_count,SRAM_ADDR'length) when PRE0_READ_SRAM,
    conv_std_logic_vector(SRAM_WR_RD_count,SRAM_ADDR'length) when PRE1_READ_SRAM,
    (others => '0') when READ_SRAM,
    (others => '0') when others;
with State_pres select
   SRAM_DQ_out(18 downto 0) <=   (others => '0') when RESET_SRAM,
    (others => '0') when WAIT_SRAM,
    (others => '0') when PRE0_WRITE_SRAM,
    (others => '0') when PRE1_WRITE_SRAM,
    conv_std_logic_vector(SRAM_WR_RD_count, 19) when WRITE_SRAM,
    (others => '0') when PRE0_READ_SRAM,
    (others => '0') when PRE1_READ_SRAM,
    (others => '0') when READ_SRAM,
    (others => '0') when others;
with State_pres select
   SRAM_DQ_out(31 downto 19) <= (others => '0') when RESET_SRAM,
    (others => '0') when WAIT_SRAM,
    (others => '0') when PRE0_WRITE_SRAM,
    (others => '0') when PRE1_WRITE_SRAM,
    conv_std_logic_vector(SRAM_WR_RD_count, 13) when WRITE_SRAM,
    (others => '0') when PRE0_READ_SRAM,
    (others => '0') when PRE1_READ_SRAM,
    (others => '0') when READ_SRAM,
    (others => '0') when others;


-------------------------------------
-- General I/O--
-------------------------------------
LED_RUN <= Led_out;
LCLK <= Frequency_out;
LCTRLN <= GA(0);                    -- Map GA(0) into LCTRLN
LDERRN <= GA(1);                    -- Map GA(1) into LDERRN
LDOWN_AN <= GA(2);                  -- Map GA(2) into LDOWN_AN
LWENN <= GA(3);                     -- Map GA(3) into LWENN
UDW0_A <= GA(4);                    -- Map GA(4) into UDW0_A
UDW1_A <= GA(5);                    -- Map GA(5) into UDW1_A
URESET_AN <= GA(6);                 -- Map GA(6) into URESET_AN
UTD0N <= GA(7);                     -- Map GA(7) into UTD0N
UXOFFN <= ASN;                      -- Map UXOFFN into ASN
DTACKn <= Frequency_out;
BERRn <= Frequency_out;


DATA_EN <= '1' when RESET = '0' else '0';       -- Enable the VME tranceivers (Active low)
DIR_DATA <= '0' when DATA_EN = '0' else 'Z';    -- Enable VME tranceiver direction ('0' from
    FPGA to VME)
```

```
SVT_OUT <= SVT_IND;                                  -- Map the SVT_IND into SVT_OUT
SVT_OUT_DS <= Frequency_out;                         -- Map Frequency_out in the FiFo clock
L1OUT(33 downto 0) <= L1IN(33 downto 32) &           -- Map the L1IN into L1OUT
                      Frequency_out &                -- Map L1IN31 for WCLK of FiFo
                      L1IN(30 downto 0);             -- Map the L1IN into L1OUT
F1IO <= (0 => DSN(0), 1 => DSN(1), 2 => WRN, others => Frequency_out);
F1CTRL(5 downto 0) <= AM(5 downto 0);                -- Map F1CTRL[32..28] into AM[5..0]
F1CTRL(32 downto 6) <= (others => Frequency_out);
CARD1_ID <= (others => Frequency_out);
F2IO <= (others => Frequency_out);
F2CTRL <= (others => Frequency_out);
CARD2_ID <= (others => Frequency_out);
D(31 downto 0) <= A(31 downto 1) & SYSCLK;           -- Map VME address into VME data + Sysclk

end Bhv;
```

F

MiniPulsar schematics

In this appendix, the schematics of the *MiniPulsar* are presented.

F.1 MiniPulsar schematics sheets

These schematics refer to the *MiniPulsar* version 2.1.

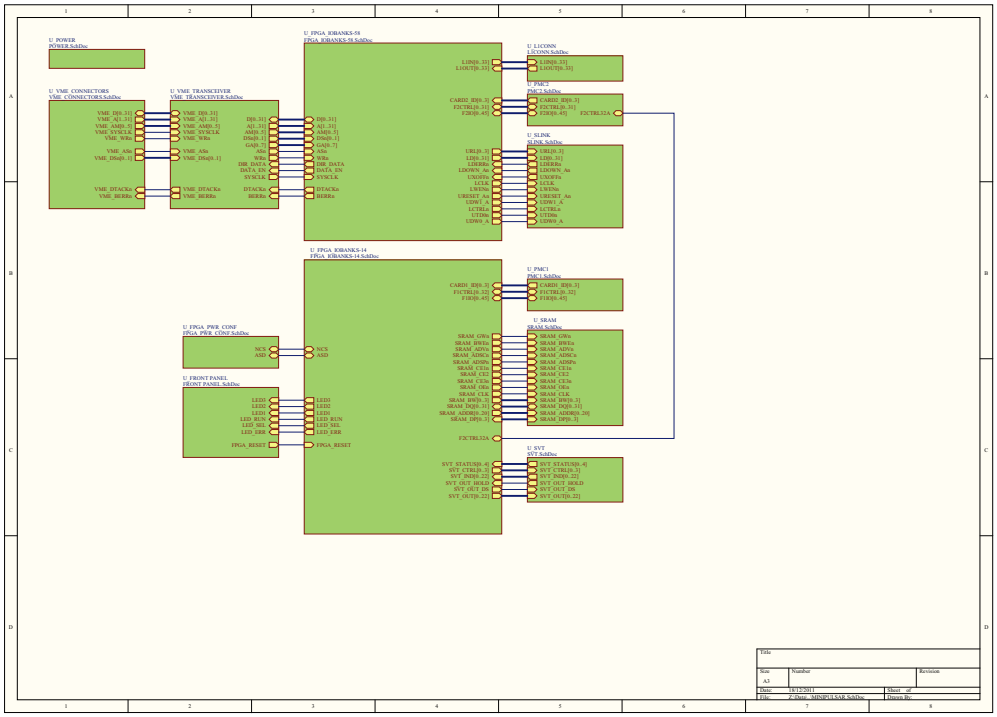

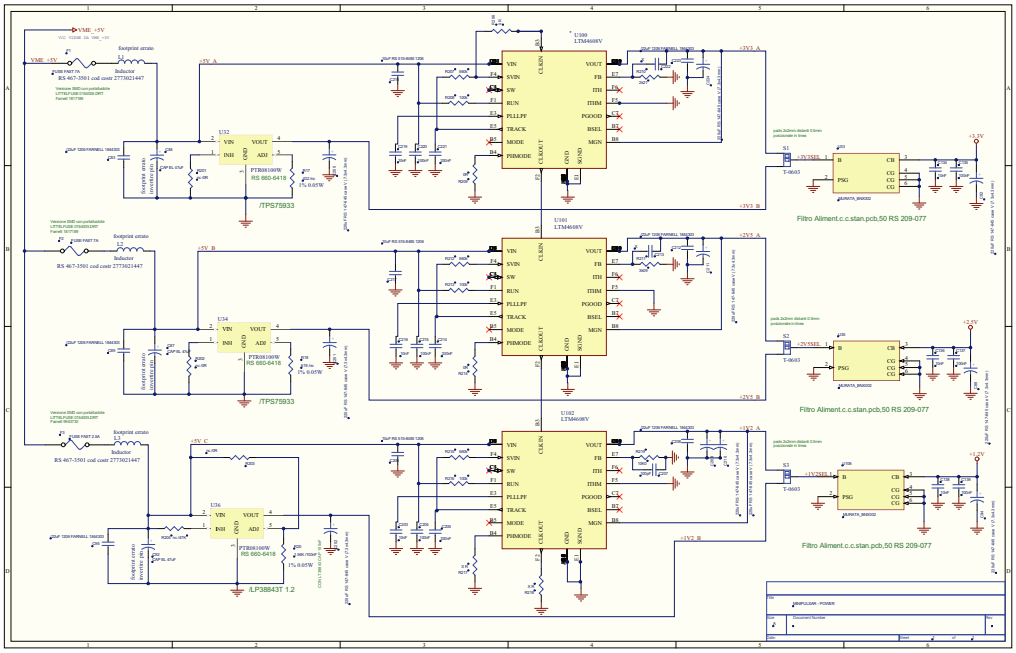
VME_+5V
+5V_A
+5V_B
+5V_C
LTM4608IV
PTB98106W
RS 660-6418
/TPS75933
ILP38843T 1.2
Filtro Aliment.c.c.stan.pcb,50 RS 209-077

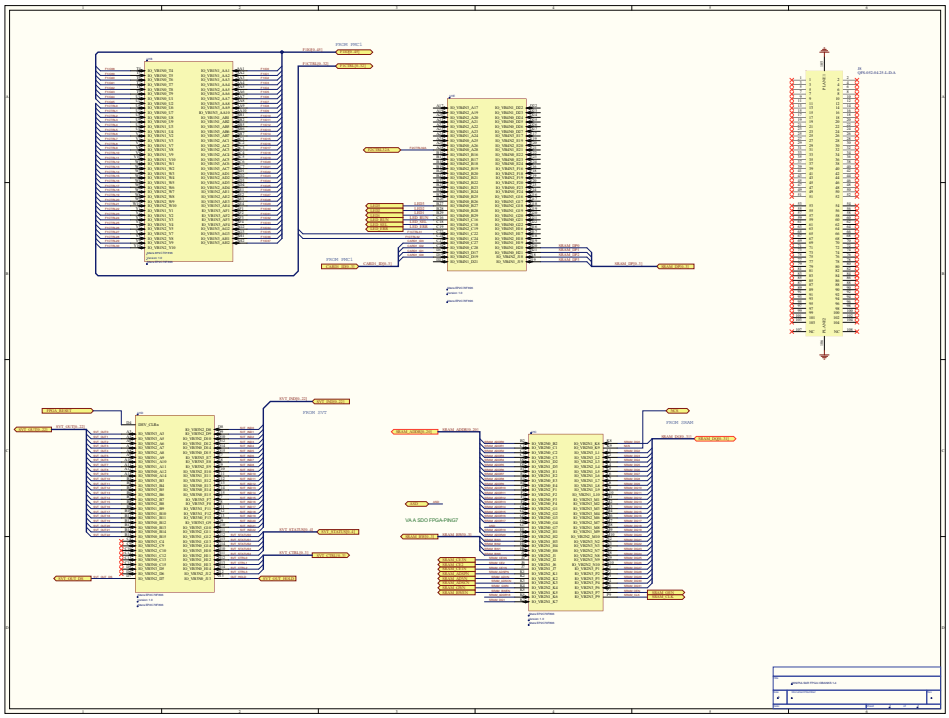

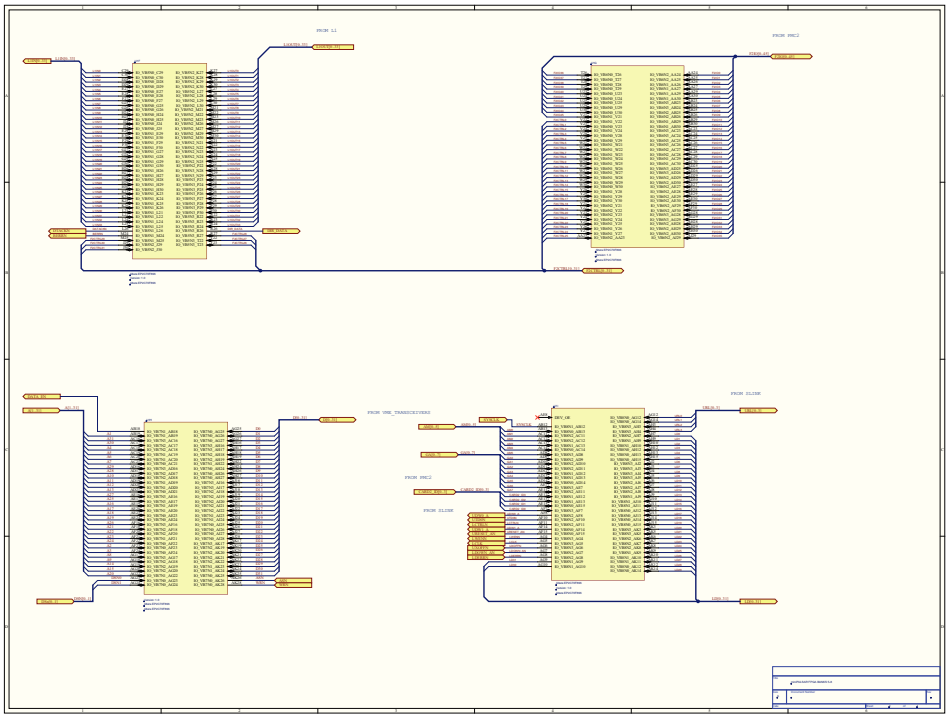

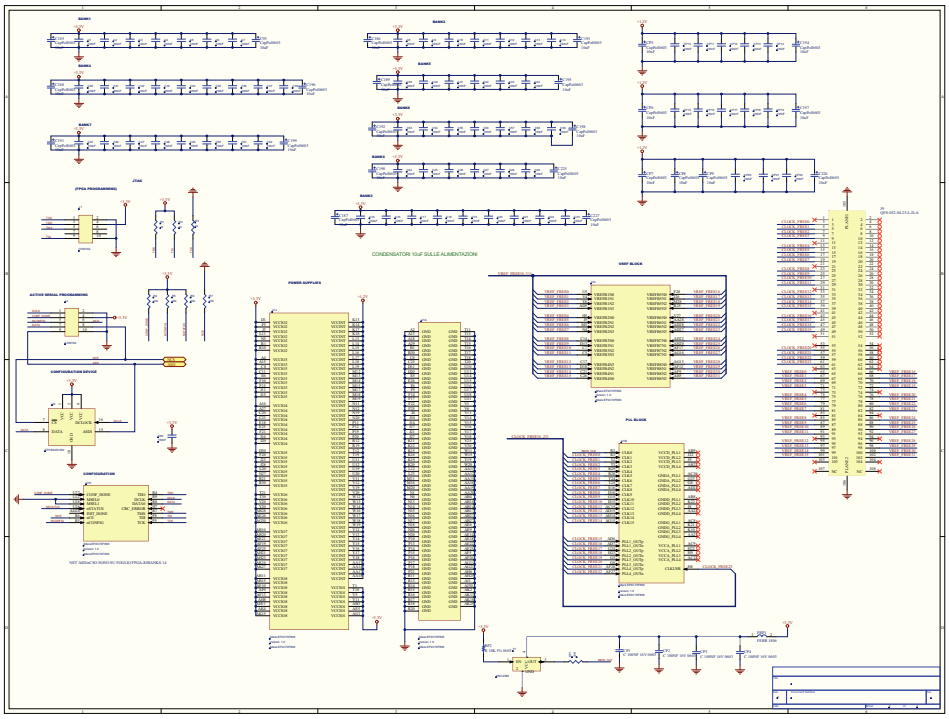

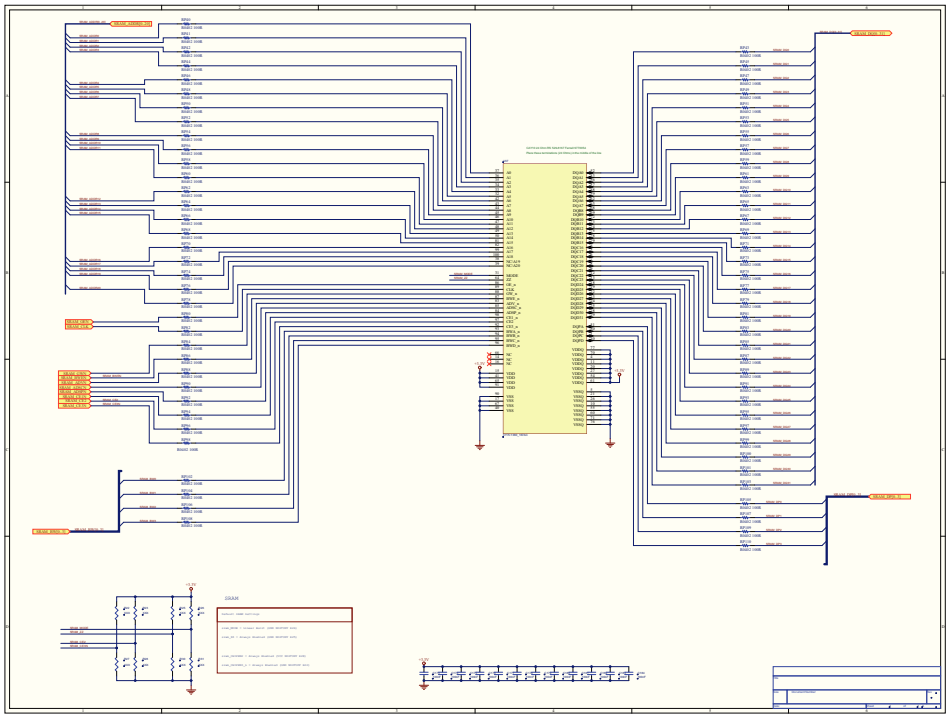

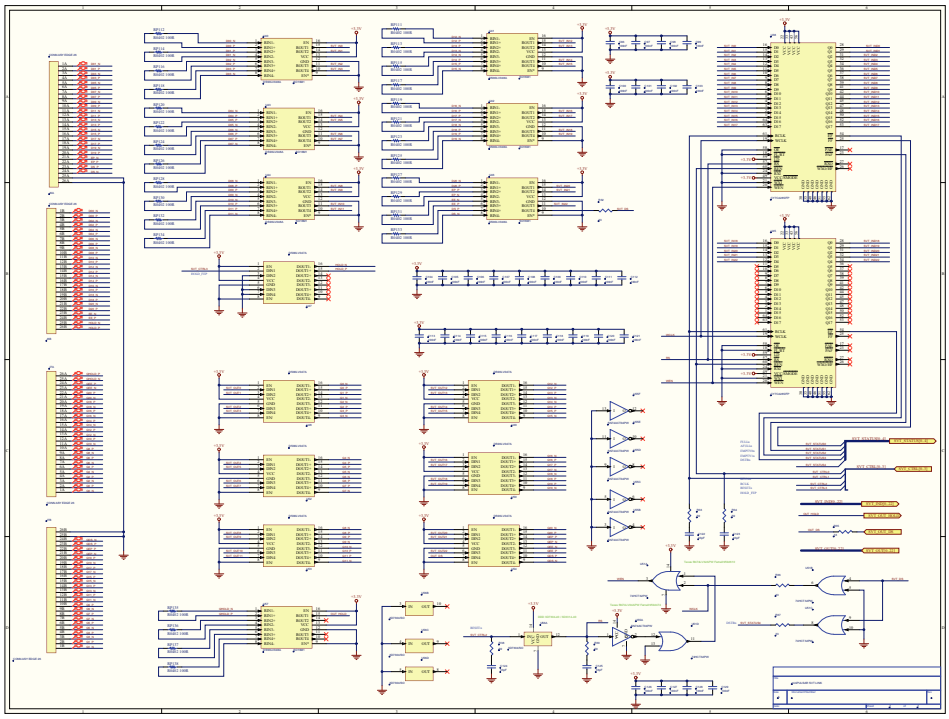

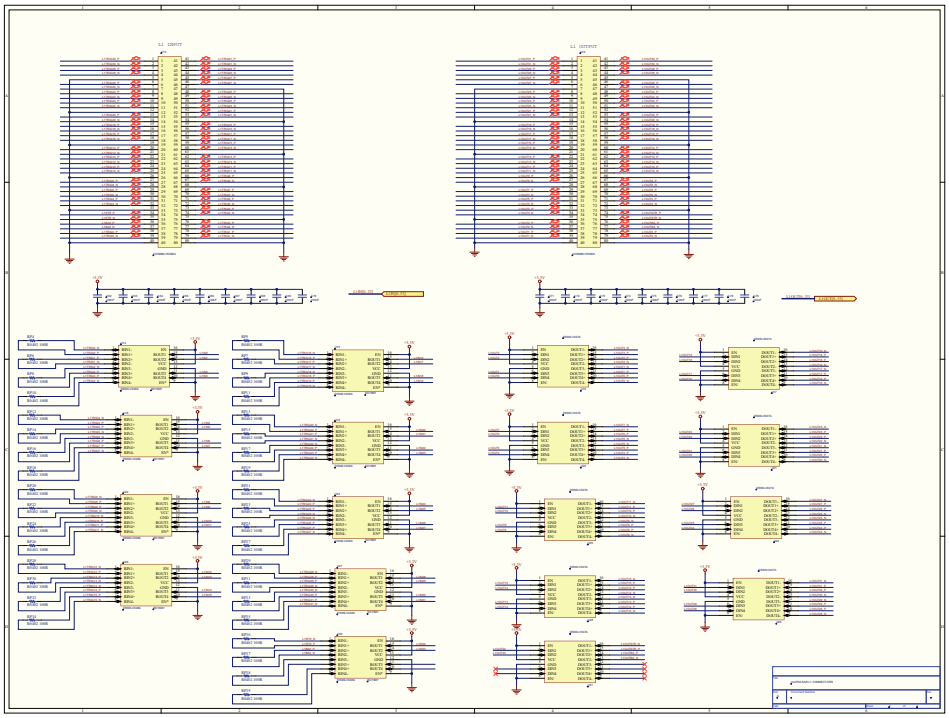

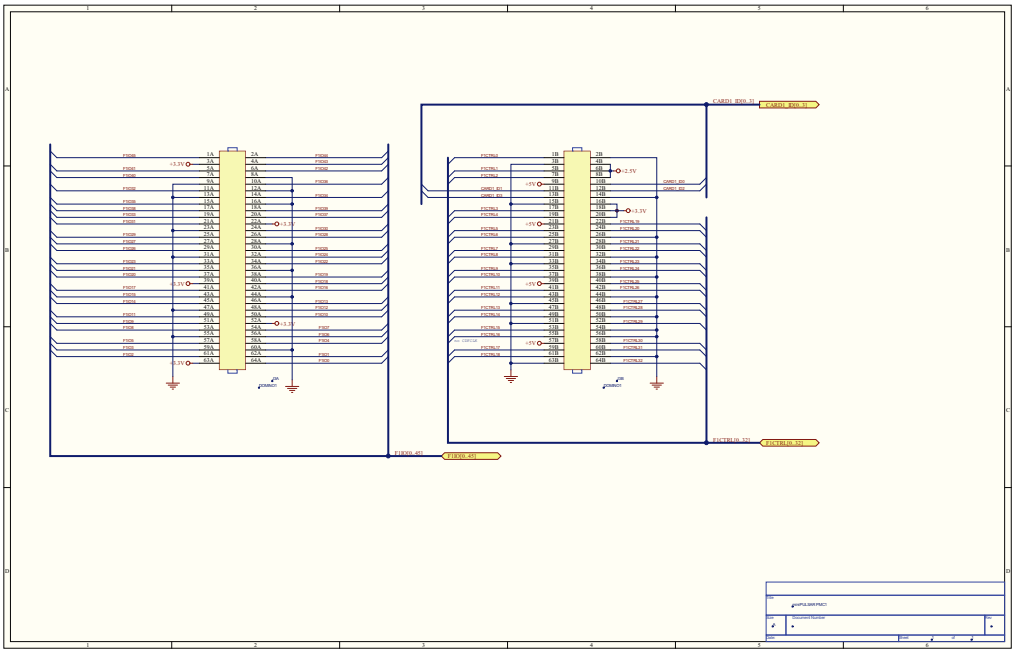

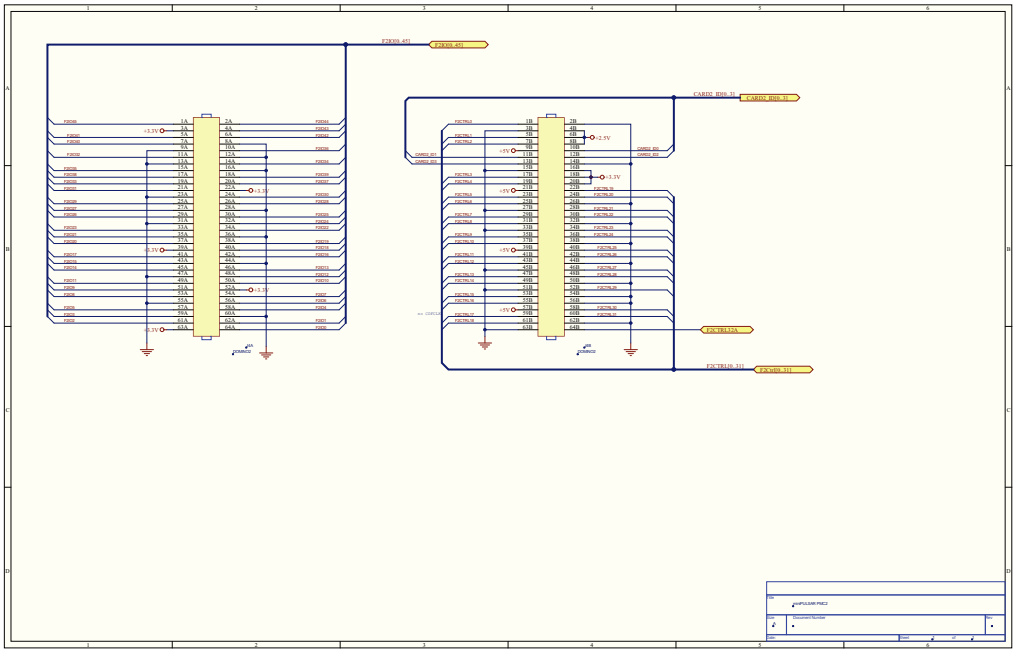

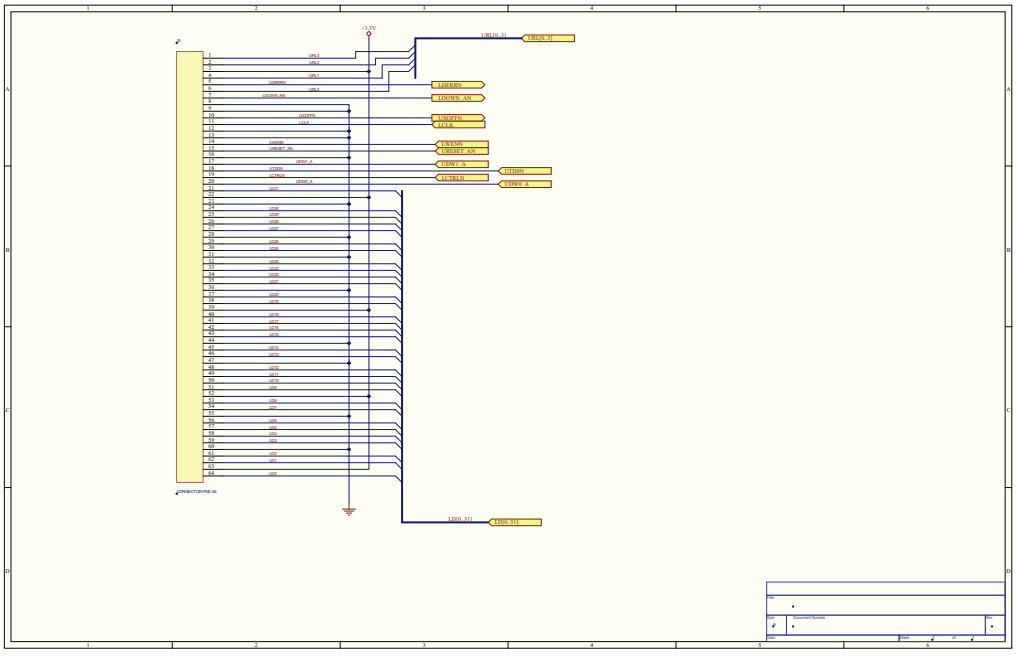

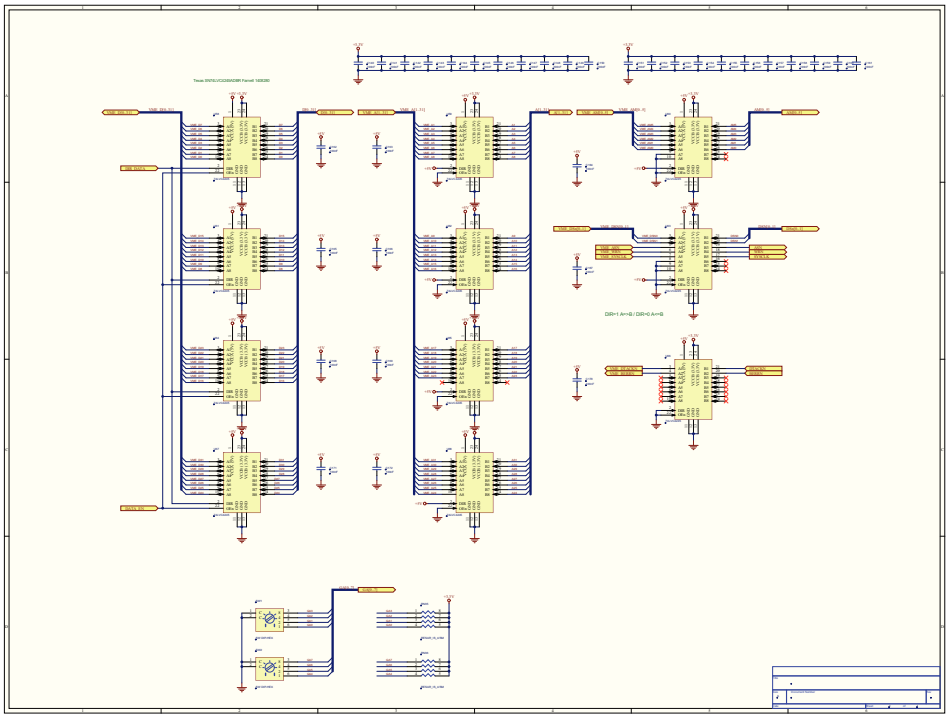

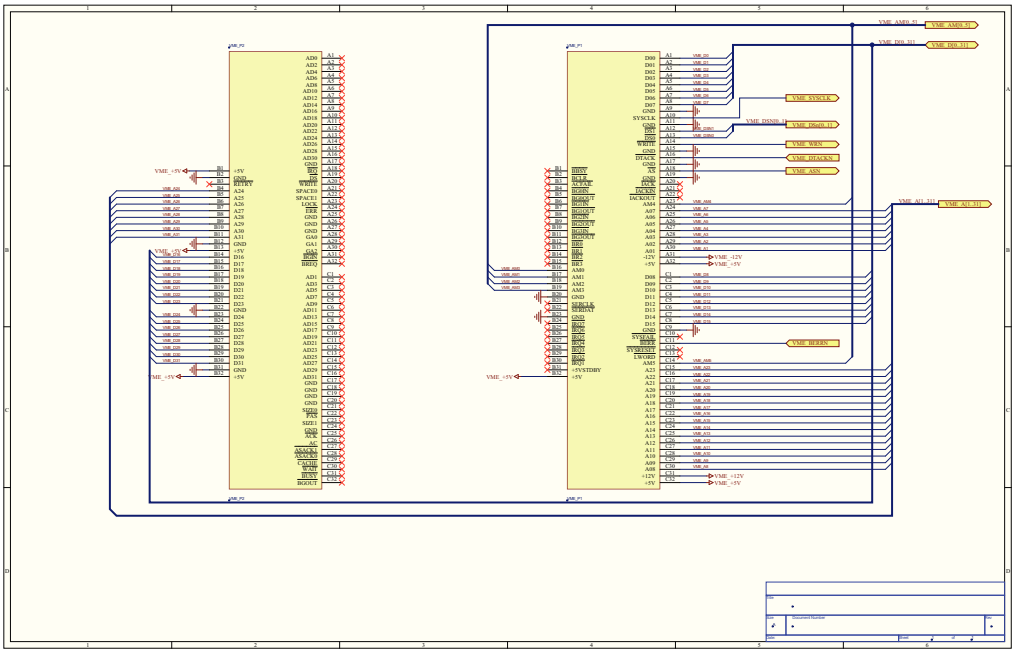

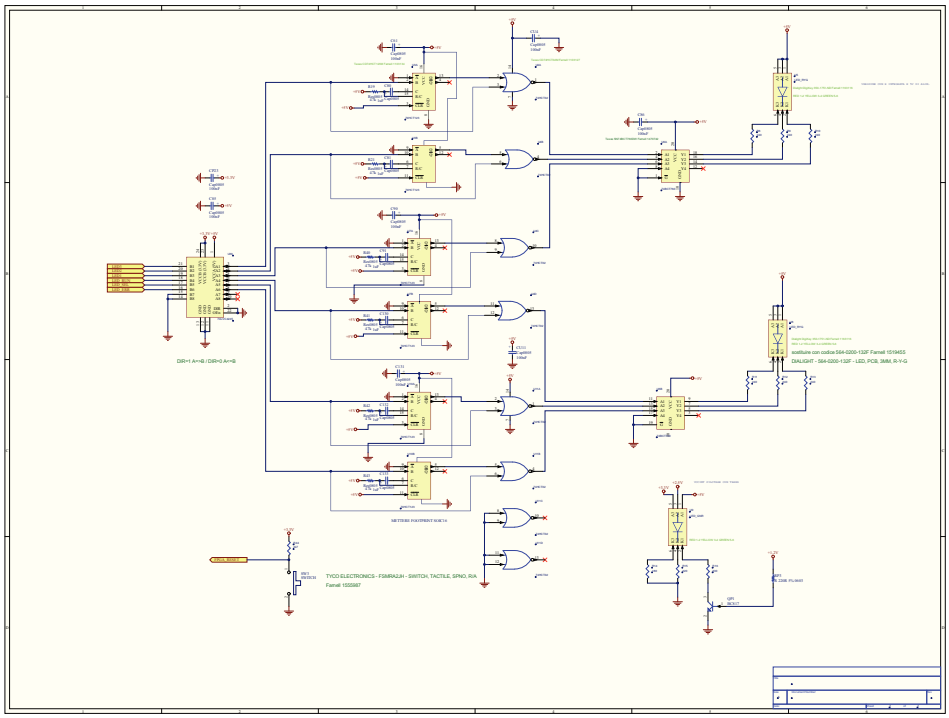

Bibliography

[1] Felix Aharonian and Alexander Konopelko. Stereo imaging of VHE gamma-ray sources. In *Kruger Park International Workshop on TeV Gamma-Ray Astrophysics*, page p.15. Wesprint - Potchefstroom, December 1997.

[2] Felix Aharonian, Werner Hofmann, Alexander Konopelko, and Heinrich Völk. The potential of ground based arrays of imaging atmospheric Čherenkov telescopes. Determination of shower parameters. *Astroparticle Physics*, 6(3):343–368, April 1997. doi: 10.1016/S0927-6505(96)00069-2.

[3] Carl David Anderson. The positive electron. *Physical Review*, 43(6):491–494, March 1933. doi: 10.1103/PhysRev.43.491.

[4] Carl David Anderson and Seth Henry Neddermeyer. Note on the nature of cosmic-ray particles. *Physical Review*, 51(10):884–886, May 1937. doi: 10.1103/PhysRev.51.884.

[5] Pierre Victor Auger, Roland Maze, P. Ehrenfest, J. Daudin, and Robley A. Freon. Extensive cosmic-ray showers. *Reviews of modern physics*, 11(3-4):288–291, July 1939. doi: 10.1103/RevModPhys.11.288.

[6] Walter Baade. The resolution of Messier 32, NGC 205, and the central region of the Andromeda nebula. *Astrophysical Journal*, 100:137–146, September 1944. doi: 10.1086/144650.

[7] Walter Baade. The Period-Luminosity relation of the Cepheids. *Publications of the Astronomical Society of the Pacific*, 68(400):5–16, February 1956.

[8] J. A. Barrio, F. Lucarelli, P. Antoranz, M. Asensio, M. Camara, J. L. Contreras, M. V. Fonseca, M. Lopez, J. M. Miranda, I. Oya, R. de los Reyes, R. Firpo, N. Sidro, F. Goebel, and N. Otte. The central pixel of the MAGIC telescope for optical observations. *Nuclear Instruments and Methods in Physics Research A*, 589(3):415–424, March 2008. doi: 10.1016/j.nima.2008.03.007.

[9] D. Bastieri, D. Agguiaro, J. Arnold, C. Bigongiari, F. Dazzi, M. Doro, N. Galante, M. Garczarczyk, E. Lorenz, D. Maniero, M. Mariotti, R. Mirzoyan, A. Moralejo, D. Pascoli, A. Pepato, L. Peruzzo, M. Rebeschini, A. Saggion, P. Sartori, V. Scalzotto, D. Tescaro, and N. Tonello for the MAGIC collaboration. The mirrors for the MAGIC telescopes. In *29th International Cosmic Ray Conference*, volume 5, pages 283–286, August 2005.

[10] Gianfranco Bertone, Dan Hooper, and Joseph Silk. Particle dark matter: evidence, candidates and constraints. *Physics Reports*, 405(5-6):279–390, January 2005. doi: 10.1016/j.physrep.2004.08.031.

[11] Hans A. Bethe. Energy production in stars. *Physical Review*, 55(1):103, January 1939. doi: 10.1103/PhysRev.55.103.

[12] Homi Jehangir Bhabha and Walter Heitler. The passage of fast electrons and the theory of cosmic showers. *Proceedings of the Royal Society of London series A: mathematical, physical and engineering sciences*, 898(A):432–458, 1937. doi: 10.1098/rspa.1937.0082.

[13] C. Bigongiari, D. Bastieri, N. Galante, E. Lorenz, M. Mariotti, R. Mirzoyan, A. Moralejo, A. Pepato, L. Peruzzo, A. Saggion, V. Scalzotto, and N. Tonello. The MAGIC telescope reflecting surface. *Nuclear Instruments and Methods in Physics Research A*, 518(1-2):193–194, February 2004. doi: 10.1016/j.nima.2003.10.058.

[14] A. Biland, M. Garczarczyk, H. Anderhub, V. Danielyan, D. Hakobyan, E. Lorenz, and R. Mirzoyan on behalf of the MAGIC collaboration. The active mirror control of the MAGIC telescope. In *30th International Cosmic Ray Conference*, volume 3, pages 1353–1356. Provided by Cornell University, July 2007.

[15] Massimiliano Bitossi. *Ultra-fast sampling and readout for the MAGIC-II telescope Data Acquisition system*. PhD thesis, University of Pisa, February 2009.

[16] P. M. S. Blackett. A possible contribution to the night sky from the Čerenkov radiation emitted by cosmic rays. In *The emission spectra of the night sky and aurorae. Papers read at an international conference held under the auspices of the Gassiot Committee of the Royal Society in London in July 1947*, volume Report 1, pages 34–35. The Physical Society, 1948.

[17] R. D. Blandford and J. P. Ostriker. Supernova shock acceleration of cosmic rays in the galaxy. *Astrophysical Journal*, 237(1):793–808, May 1980. doi: 10.1086/157926.

[18] Craig F. Bohren and Donald R. Huffman. *Absorption and scattering of light by small particles*. Wiley, 1983. ISBN 9780471293408.

[19] Hermann Bondi and Thomas Gold. The Steady-State theory of the expanding Universe. *Monthly Notices of the Royal Astronomical Society*, 108(3):252–270, July 1948.

[20] Markus Böttcher. Modeling the emission processes in blazars. *Astrophysics and Space Science*, 309(1):95–104, April 2007. doi: 10.1007/s10509-007-9404-0.

[21] Thomas Bretz, Daniela Dorner, Robert M. Wagner, and Peter Sawallisch. The drive system of the major atmospheric gamma-ray imaging Čerenkov telescope. *Astroparticle Physics*, 31(2):92–101, March 2009. doi: 10.1016/j.astropartphys.2008.12.001.

[22] G. A. Camelia, J. Ellis, N. E. Mavromatos, , D. V. Nanopoulos, and S. Sarkar. Tests of quantum gravity from observations of big gamma-ray bursts. *Nature*, 393 (6687):763–765, June 1998. doi: 10.1038/31647.

[23] K. S. Cheng, C. Ho, and M. Ruderman. Energetic radiation from rapidly spinning pulsars. I. Outer magnetosphere gaps. II. VELA and Crab. *Astrophysical Journal*, 300(2):500–539, January 1986. doi: 10.1086/163829.

[24] Marshall Clagett. *Ancient Egyptian science, Volume 1*. American Philosophical Society, Philadelphia (USA), 1999.

[25] Jacob Clay. Penetrating radiation. In *Proceeding of the Royal Academy of Science, 31*, pages 1091–1097, 1928.

[26] P. Colin, D. Borla Tridon, E. Carmona, F. De Sabata, M. Gaug, S. Klepser, S. Lombardi, P. Majumdarand, A. Moralejo, V. Scalzotto, and J. Sitarek for the MAGIC collaboration. Performance of the MAGIC telescopes in stereoscopic mode. In *31th International Cosmic Ray Conference*, pages 1–4. Provided by Cornell University, July 2009.

[27] AGILE collaboration. The Crab nebula super-flare in April 2011: extremely fast particle acceleration and gamma-ray emission. *The Astrophysical Journal Letters*, 741(1):L5 (4pp), November 2011. doi: 10.1088/2041-8205/741/1/L5.

[28] AGILE collaboration. Discovery of powerful gamma-ray flares from the Crab Nebula. *Science*, 331(6018):736–739, February 2011. doi: 10.1126/science.1200083.

[29] Fermi-LAT collaboration. The first Fermi Large Area Telescope catalog of gamma-ray pulsars. *The Astrophysical Journal Supplement Series*, 187(2):460–494, April 2010. doi: 10.1088/0067-0049/187/2/460.

[30] Fermi-LAT Collaboration. Fermi Large Area Telescope second source catalog. *ArXiv e-prints*, August 2011. URL http://lanl.arxiv.org/abs/1108.1435. Provided by Cornell University.

[31] Fermi-LAT Collaboration. Gamma-ray flares from the Crab Nebula. *Science*, 331 (6018):739–742, February 2011. doi: 10.1126/science.1199705.

[32] MAGIC collaboration. VHE γ–ray observation of the Crab Nebula and its Pulsar with the MAGIC telescope. *The Astrophysical Journal*, 674(2):1037–1055, February 2008. doi: 10.1086/525270.

[33] MAGIC collaboration. FADC signal reconstruction for the MAGIC telescope. *Nuclear Instruments and Methods in Physics Research A*, 594(3):407–419, September 2008. doi: 10.1016/j.nima.2008.06.043.

[34] MAGIC collaboration. Implementation of the Random Forest method for the imaging atmospheric Čerenkov telescope MAGIC. *Nuclear Instruments and Methods in Physics Research Section A*, 588(3):424–432, April 2008. doi: 10.1016/j.nima.2007.11.068.

[35] MAGIC collaboration. Observation of pulsed γ–rays above 25 GeV from the Crab Pulsar with MAGIC. *Science*, 322(5905):1221–1224, October 2008. doi: 10.1126/science.1164718.

[36] MAGIC collaboration. Observation of pulsed γ–rays above 25 GeV from the Crab pulsar with MAGIC. *Science*, 322(5905):1221–1224, November 2008. doi: 10.1126/science.1164718.

[37] MAGIC collaboration. Improving the performance of the single-dish Čerenkov telescope MAGIC through the use of signal timing. *Astroparticle Physics*, 30(6): 293–305, January 2009. doi: 10.1016/j.astropartphys.2008.10.003.

[38] MAGIC collaboration. Phase-resolved energy spectra of the Crab Pulsar in the range of 50-400 GeV measured with the MAGIC telescopes. *ArXiv e-prints*, January 2011. URL http://arxiv.org/abs/1109.6124v2. Provided by Cornell University.

[39] MAGIC collaboration. Observations of the Crab Pulsar between 25 and 100 GeV with the MAGIC I telescope. *Astrophysical Journal*, 742(1):id. 43, November 2011. doi: 10.1088/0004-637X/742/1/43.

[40] MAGIC collaboration. Performance of the MAGIC stereo system obtained with Crab nebula data. *Astroparticle Physics*, 35(7):435–448, February 2012. doi: 10.1016/j.astropartphys.2011.11.007.

[41] Pierre AUGER Collaboration. Correlation of the highest-energy cosmic rays with nearby extragalactic objects. *Science*, 318(5852):938–943, November 2007. doi: 10.1126/science.1151124.

[42] Pierre AUGER Collaboration. Measurement of the energy spectrum of cosmic rays above 10^{18} eV using the *Pierre AUGER* observatory. *Physics Letters B*, 685 (4-5):239–246, March 2010. doi: 10.1016/j.physletb.2010.02.013.

[43] VERITAS collaboration. Detection of pulsed gamma rays above 100 GeV from the Crab Pulsar. *Science*, 334(6052):69–72, October 2011. doi: 10.1126/science.1208192.

[44] S.C. Commichau, A. Biland, J.L. Contreras, R. de los Reyes, A. Moralejo, J. Sitarek, and D. Sobczynska on behalf of the MAGIC collaboration. Monte Carlo studies of geomagnetic field effects on the imaging air Čerenkov technique for the MAGIC telescope site. *Nuclear Instruments and Methods in Physics Research*, 595(Section A):572–586, October 2008. doi: 10.1016/j.nima.2008.07.144.

[45] Nicolaus Copernicus. *De revolutionibus orbium coelestium*. J. Petreium, Nuremberg (Holy Roman Empire of the German Nation), 1543.

[46] J. Cortina and J.C. Gonzalez. The cosmic electron background in low energy imaging atmospheric Čerenkov telescopes: effect of the geomagnetic field. *Astroparticle Physics*, 15(2):203–210, April 2001. doi: 10.1016/S0927-6505(00)00147-X.

[47] Juan Cortina. Influence of the geomagnetic field on the electron background of low energy iacts. In *17th European Cosmic Ray Conference*, July 2000.

[48] Charles Coulomb. Troisième mémoire sur l'électricité et le magnétisme. de la quantité d'électricité qu'un corps isolé perd dans le temps donné, soit par le contact de l'air plus ou moins humide, soit le lond des soutiens plus ou moins idio-électriques, avec 1 planche. *Mémoires de l'Académie royale des sciences*, 88: 612–638, 1785.

[49] Francesco Dazzi. Realizzazione ed analisidel trigger di livello 1 del telescopio MAGIC. Master thesis, Università degli Studi di Padova - Dipartimento di Fisica G. Galilei, June 2001.

[50] M. Doro, D. Bastieri, A. Biland, F. Dazzi, L. Font, M. Garczarczyk, M. Ghigo, E. Giro, F. Goebel, R. Kosyra, E. Lorenz, M. Mariotti, R. Mirzoyan, L. Peruzzo, G. Pareschi, and J. Zapatero. The reflective surface of the MAGIC telescope. *Nuclear Instruments and Methods in Physics Research A*, 595(1):200–203, September 2008. doi: 10.1016/j.nima.2008.07.073.

[51] Arthur Stanley Eddington. *Stellar movements and the structure of the Universe*. Macmillan and Co. Limited, London (England), 1914.

[52] Albert Einstein. Zur elektrodynamik bewegter körper. *Annalen der Physik*, 322 (10):891–921, June 1905. doi: 10.1002/andp.19053221004.

[53] Albert Einstein. Die grundlage der allgemeinen relativitätstheorie. *Annalen der Physik*, 354(7):769–822, March 1916. doi: 10.1002/andp.19163540702.

[54] R. C. Hartman et al. The third EGRET catalog of high-energy gamma-ray sources. *Astrophysical Journal*, 123(1):79–202, July 1999. doi: 10.1086/313231.

[55] Riccardo Paoletti et al. The trigger system of the MAGIC telescope. *IEEE Transactions Nuclear Science*, 54(2):404–409, April 2007. doi: 10.1109/TNS.2007.892649.

[56] Trevor C. Weekes et al. Observation of TeV gamma rays from the Crab nebula using the atmospheric Čerenkov imaging technique. *Astrophysical Journal*, 342 (1):379–395, July 1989. doi: 10.1086/167599.

[57] G. G. Fazio and F. W. Stecker. Predicted high energy break in the isotropic gamma ray spectrum: a test of cosmological origin. *Nature*, 236(5241):135–136, April 1970. doi: 10.1038/226135a0.

[58] Eugene Feenberg and Henry Primakoff. Interaction of cosmic-ray primaries with sunlight and starlight. *Physical Review*, 73(5):449–469, March 1948. doi: 10.1103/PhysRev.73.449.

[59] Pepe Flix and Eva Domingo. Topological defects. Software MAGIC meeting, September 2004.

[60] CERN European Organization for Nuclear Research. CERN S-link homepage, July 2003. URL http://hsi.web.cern.ch/HSI/s-link/.

[61] J.A Hinton for the HESS collaboration. The status of the HESS project. *New Astronomy Reviews*, 48(5-6):331–337, April 2004. doi: 10.1016/j.newar.2003.12.004.

[62] Galileo Galilei. *Sidereus Nuncius*. Baglioni, Venice (Italy), 1610.

[63] Markus Gaug. *Calibration of the MAGIC telescope and observation of gamma ray bursts*. PhD thesis, Universitat Autonoma de Barcelona Departament de Fisica, March 2006.

[64] Florian Goebel, Hendrik Bartko, Emiliano Carmona, Nicola Galante, Tobias Jogler, Razmik Mirzoyan, Jose Antonio Coarasa, and Masahiro Teshima. Upgrade of the MAGIC telescope with a multiplexed fiber-optic 2GSamples/s FADC Data Acquisition System system. In *30th International Cosmic Ray Conference*, volume 3, page 1481âĂŞ1484. Provided by Cornell University, July 2007.

[65] Dennis Häfner. Development of a new analog Sum-Trigger for the MAGIC experiment with a continuously adjustable analog delay line and automatic calibration. Diploma thesis, Ludvig Maximilians Universität München, November 2010.

[66] William F. Hanlon. *The energy spectrum of ultra high energy cosmic rays measured by the high resolution Fly's Eye observatory in stereoscopic mode*. PhD thesis, University of Utah, December 2008.

[67] Alice K. Harding, Julie V. Stern, Jaroslaw Dyks, and Michal Frackowiak. High-altitude emission from pulsar slot gaps: The crab pulsar. *Astrophysical Journal*, 680(2):1378–1393, March 2008. doi: 10.1086/588037.

[68] Sachio Hayakawa. Propagation of the cosmic radiation through intersteller space. *Progress of Theoretical Physics*, 8(5):571–572, November 1952. doi: 10.1143/PTP.8.571.

[69] Walter Heitler. *The quantum theory of radiation*. International series of monographs on physics. Dover Publications, 1954. ISBN 9780486645582.

[70] William Herschel. Account of the changes that have happened, during the last twenty-five years, in the relative situation of double-stars; With an investigation of the cause to which they are owing. *Philosophical Transactions of the Royal Society of London*, 93:339–382, January 1803. doi: 10.1098/rstl.1803.0015.

[71] Victor Hess. Über beobachtungen der durchdringenden strahlung bei sieben freiballonfahrt. *Physikalische Zeitschrift*, 13:1084–1091, 1912.

[72] Anthony M. Hillas. Čerenkov light images of EAS produced by primary gamma. In *19th International Cosmic Ray Conference*, volume 3, pages 445–448. SAO/-NASA Astrophysics Data System, August 1985.

[73] Werner Hofmann. Data analysis techniques for stereo IACT systems. *AIP conference proceedinds*, 515:318–322, June 2000. doi: 10.1063/1.1291386.

[74] Edwin Hubble. A relation between distance and radial velocity among extra-galactic nebulae. *Proceedings of the National Academy of Sciences*, 15(3):168–173, January 1929. doi: 10.1073/pnas.15.3.168.

[75] William Huggins and W. A. Miller. On the spectra of some of the fixed stars. *Philosophical Transactions of the Royal Society of London*, 154:413–435, May 1864. doi: 10.1098/rstl.1864.0012.

[76] William Huggins and W. A. Miller. On the spectra of some of the nebulae. *Philosophical Transactions of the Royal Society of London*, 154:437–444, September 1864. doi: 10.1098/rstl.1864.0013.

[77] Karl Jansky. Electrical disturbances apparently of extraterrestrial origin. *Proceedings of the Institute of Radio Engineers*, 21(10):1387–1398, October 1933. ISSN 0731-5996. doi: 10.1109/JRPROC.1933.227458.

[78] J. V. Jelley. *Čerenkov radiation and its applications*. Pergamon Press, Oxford (UK), 1958.

[79] J. V. Jelley and W. Galbraith. Light pulses from the night sky associated with cosmic rays. *Nature*, 171:349–350, February 1953. doi: 10.1038/171349a0.

[80] T. W. Jones, S. L. O'Dell, and W. A. Stein. Physics of compact nonthermal sources. Theory of radiation processes. *Astrophysical Journal*, 188(2):353–368, March 1974. doi: 10.1086/152724.

[81] Johannes Kepler. *Astronomia nova*. G. Voegelinus, Prague (Czech), 1609.

[82] Johannes Kepler. *Harmonices mundi*. Ioannes Plancus, sumptibus Godofredi Tampachii Bibl. Francof., 1619.

[83] T. M. Kneiske, K. Mannheim, and D. H. Hartmann. Implications of cosmological gamma-ray absorption i. evolution of the metagalactic radiation field. *Astronomy & Astrophysics*, 386(1):1–11, April 2002. doi: 10.1051/0004-6361:20020211.

[84] A. Konopelko. Altitude effect in Čerenkov light flashes of low energy gamma-ray-induced atmospheric showers. *Journal of Physics G: Nuclear and Particle Physics*, 30(12):1835–1846, October 2004. doi: doi:10.1088/0954-3899/30/12/006.

[85] John Kraus. A strange radiation from above. *Cosmic Search Issue: 5*, 2(1):20–23, Winter 1980. URL http://www.bigear.org/CSMO/HTML/CS05/cs05p20.htm.

[86] William Kraushaar and George Whipple Clark. Gamma ray astronomy. *Scientific American*, 206(5):52–61, May 1962.

[87] J. I. Latorre, P. Pascual, and R. Tarrach. Speed of light in non-trivial vacua. *Nuclear Physics B*, 437(1):60–82, March 1995. doi: 10.1016/0550-3213(94)00490-6.

[88] Cesar Mansueto Giulio Lattes, Hugh Muirhead, Giuseppe Occhialini, and Cecil Frank Powell. Processes involving charged mesons. *Nature*, 159:694–697, May 1947. doi: 10.1038/159694a0.

[89] Henrietta S. Leavitt and Edward C. Pickering. Periods of 25 variable stars in the small Magellanic cloud. *Harvard College Observatory circular*, 173:1–3, March 1912.

[90] Georges Lemaître. Un Univers homogène de masse constante et de rayon croissant rendant compte de la vitesse radiale des nébuleuses extra-galactiques. *Annales de la Societe Scientifique de Bruxelles*, 47(A):49–59, 1927.

[91] Georges Lemaître. The beginning of the world from the point of view of quantum theory. *Nature*, 127(3210):447, May 1931. doi: 10.1038/127706b0.

[92] Marvin Leventhal, Crawford J. MacCallum, Scott D. Barthelmy, Neil Gehrels, Bonnard J. Teegarden, and Jack Tueller. Reappearance of the annihilation line source at the galactic centre. *Nature*, 339:36–38, May 1989. doi: 10.1038/339036a0.

[93] T. P. Li and Y. Q. Ma. Analysis methods for results in gamma-ray astronomy. *Astrophysical Journal*, 272(1):317–324, September 1983. doi: 10.1086/161295.

[94] Tiehui Ted Liu, Mircea Bogdan, and Burkard Reisert et al. Pulsar project, September 2004. URL http://hep.uchicago.edu/~thliu/projects/Pulsar/.

[95] Saverio Lombardi. *Development of analysis tools for the MAGIC telescopes and observation of the Segue 1 satellite galaxy with the MAGIC-I telescope*. PhD thesis, University of Padova, July 2010.

[96] M. Lopez, N. Otte, M. Rissi, T. Schweizer, M. Shayduk, and S. Klepser for the MAGIC collaboration. Detection of the Crab pulsar with MAGIC. *ArXiv e-prints*, July 2009. URL http://arxiv.org/abs/0907.0832. Provided by Cornell University.

[97] R. Mirzoyan and E. Lorenz. Measurement of the night sky light background at la palma. R - Report MPI-PhE/94-35, Max-Planck-Institut für physik München, December 1994.

[98] Razmik Mirzoyan and Eckart Lorenz. On the calibration accuracy of light sensors in atmospheric ČerenkovôŔřĎ fluorescence and neutrino experiments. In *25th International Cosmic Ray Conference*, volume 5, pages 265–268. World Scientific, July 1997.

[99] A. Moralejo, M. Gaug, E. Carmona, P. Colin, C. Delgado, S. Lombardi, D. Mazin, V. Scalzotto, J. Sitarek, and D. Tescaro for the MAGIC collaboration. MARS, the MAGIC analysis and reconstruction software. In *31th International Cosmic Ray Conference*, pages 1–4. Provided by Cornell University, July 2009.

[100] Philip Morrison. On gamma-ray astronomy. *Il Nuovo Cimento*, 7(6):858–865, March 1958. doi: 10.1007/BF02745590.

[101] Jernej Mrovlje and Damir Vrančic. Distance measuring based on stereoscopic pictures. In *Proceeding of the 9th international PhD workshop on wystems and control: a young generation viewpoint*, page 18, October 2008.

[102] Juan E. Naya, Scott D. Barthelmy, Lyle M. Bartlett, Neil Gehrels, Marvin Leventhal, Ann Parsons, Bonnard Teegarden, and Jack Tueller. Detection of high-velocity ^{26}Al towards the galactic centre. *Nature*, 384:44–46, November 1996. doi: 10.1038/384044a0.

[103] Isaac Newton. *Philosophiæ naturalis principia mathematica*. Josephi Streater, London (England), 1687.

[104] Rolf Buehler on behalf of the Fermi-LAT collaboration. Fermi LAT detection of a new enhanced gamma-ray emission from the Crab Nebula region. *The Astronomer's Telegram*, ATELs #3276, April 2011.

[105] A. Ostankov, , E. Lorenz, M. Martinez, and R. Mirzoyan. A study of the new hemispherical 6-dynodes pmt from electron tubes. *Nuclear Instruments and Methods in Physics Research A*, 442(1-3):117–123, March 2000. doi: 10.1016/S0168-9002(99)01208-5.

[106] Domenico Pacini. La radiazione penetrante alla superficie ed in seno alle acque. *Il Nuovo Cimento*, Series VI 3:93–100, 1912. doi: 10.1007/BF02957440.

[107] D. Paneque, H. J. Gebauer, E. Lorenz, M. Martinez, K. Mase, R. Mirzoyan, A. Ostankov, and T. Schweizer. A method to enhance the sensitivity of photomultipliers for air Čerenkov telescopes. *Nuclear Instruments and Methods in Physics Research A*, 504(1-3):109–115, May 2003. doi: 10.1016/S0168-9002(03)00805-2.

[108] D. Paneque, H. J. Gebauer, and E. Lorenz R. Mirzoyan. A method to enhance the sensitivity of photomultipliers for air Čerenkov telescopes by applying a lacquer that scatters light. *Nuclear Instruments and Methods in Physics Research A*, 518(1-2):619–621, February 2004. doi: 10.1016/j.nima.2003.11.101.

[109] Riccardo Paoletti, Ciro Bigongiari, Massimiliano Bitossi, Roberto Cecchi, and Raffaello Pegna. The global trigger system of the MAGIC telescope array. In *IEEE - Nuclear Science Symposium Conference Record, 2008*, pages 2781–2783. IEEE, October 2008. doi: 10.1109/NSSMIC.2008.4774948.

[110] G. Pareschi, E. Giro, R. Banham, S. Basso, D. Bastieri, R. Canestrari, G. Ceppatelli, O. Citterio, M. Doro, M. Ghigo, F. Marioni, M. Mariotti, M. Salvati,

F. Sanvito, and D. Vernani. Glass mirrors by cold slumping to cover 100 m^2 of the MAGIC II Čerenkov telescope reflecting surface. In *Society of Photo-Optical Instrumentation Engineers (SPIE) conference series*, volume 7018, pages 70180W–70180W–11. SPIE, 2008 June. doi: 10.1117/12.790404.

[111] Michael Thomas Rissi. *Detection of pulsed very high energy gamma-rays from the Crab pulsar with the MAGIC telescope using an analog sum trigger*. PhD thesis, Institute for Particle Physics, ETH Zürich, October 2009.

[112] Michael Thomas Rissi, Nepomuk Otte, Thomas Schweizer, and Maxim Shayduk. A new trigger provides a lower energy threshold for the MAGIC Čerenkov telescope. *Nuclear Science Symposium Conference Record 2008*, pages 1472–1475, October 2008. doi: 10.1109/NSSMIC.2008.4774693.

[113] Bruno Rossi. Method of registering multiple simultaneous impulses of several Geiger's counters. *Science*, 125:636, April 1930. doi: 10.1038/125636a0.

[114] Bruno Rossi. I risultati della missione scientifica in Eritrea per lo studio della radiazione penetrante. Misure della distribuzione angolare di intensità della radiazione penetrante all'Asmara. *La ricerca scientifica supplemento*, 1(9-10):579–589, 1934.

[115] Bruno Rossi and Kenneth Greisen. Cosmic-ray theory. *Reviews of modern physics*, 13(4):240–309, October 1941. doi: 10.1103/RevModPhys.13.240.

[116] Marcel Schein, William P. Jesse, and Ernest Omar Wollan. The nature of the primary cosmic radiation and the origin of the mesotron. *Physical Review*, 59(7): 615, April 1941. doi: 10.1103/PhysRev.59.615.

[117] Pietro Angelo Secchi. *Sugli spettri prismatici delle stelle fisse, Memoria del A. P. Secchi*, volume Atti dell'Accademia Nazionale delle Scienze detta dei XL, Serie III - Tomo I - Parte I. Stamperia Reale, Firenze (Italy), 1867.

[118] Pietro Angelo Secchi. *Sugli spettri prismatici delle stelle fisse, Memoria II del A. P. Secchi*, volume Atti dell'Accademia Nazionale delle Scienze detta dei XL, Serie III - Tomo II. Stamperia Reale, Firenze (Italy), 1869.

[119] Pietro Angelo Secchi. *Sugli spettri prismatici de' corpi celesti, Memoria III*, volume Atti dell'Accademia Nazionale delle Scienze detta dei XL, Serie III - Tomo II. Stamperia Reale, Firenze (Italy), 1869.

[120] Harlow Shapley. Globular clusters and the structure of the galactic system. *Publications of the Astronomical Society of the Pacific*, 30(173):42–54, February 1918. doi: 10.1086/122686.

[121] Harlow Shapley and Heber D. Curtis. The scale of the Universe. In *Bulletin of the National Research Council*, volume 2, pages 171–217. National Research Council of the National Academy of Sciences, May 1921.

[122] Dorota Sobczyńska. Limits to the energy resolution of a single air Čerenkov telescope at low energies. *Journal of Physics G: Nuclear and Particle Physics*, 36 (4):045201, February 2009. doi: 10.1088/0954-3899/36/4/045201.

[123] Bonnard J. Teegarden, Scott D. Barthelmy, Neil Gehrels, Jack Tueller, and Marvin Leventhal. Resolution of the 1238 keV gamma-ray line from supernova 1987A. *Nature*, 339:122–123, May 1989. doi: 10.1038/339122a0.

[124] D. Tescaro, J. Aleksic, M. Barcelo, M. Bitossi, J. Cortina, M. Fras, D. Hadasch, J. M. Illa, M. Martinez, , D. Mazin, R. Paoletti, and R. Pegna on behalf of the MAGIC collaboration. The readout system of the MAGIC-II Čerenkov telescope. In *31th International Cosmic Ray Conference*, pages 1–4. Provided by Cornell University, July 2009.

[125] Edwin Tjandranegara. Distance estimation algorithm for stereo pair images. ECE technical reports TR-ECE-05-10, Purdue University, August 2005.

[126] Gerald J. Toomer. *Ptolemy's Almagest*. Princeton University Press, Princeton (USA), 1998. ISBN 978-0-691-00260-6.

[127] D. Borla Tridon, F. Goebel, D. Fink, W. Haberer, J. Hose, C.C. Hsu, T. Jogler, R. Mirzoyan, R. Orito, O. Reimann, P. Sawallisch, J. Schlammer, T. Schweizer, B. Steinke, M. Teshima, and for the MAGIC collaboration. Performance of the camera of the MAGIC II telescope. In *31th International Cosmic Ray Conference*, pages 1–4. Provided by Cornell University, July 2009.

[128] Daniela Borla Tridon. *A study of cosmic electrons between 100 GeV and 2 TeV with the MAGIC telescopes*. PhD thesis, Physik Department der Technische Universität München, June 2011.

[129] V. Vittorini, M. Tavani, G. Pucella, E. Striani, I. Donnarumma, P. Caraveo, A. Giuliani, S. Mereghetti, A. Pellizzoni, A. Trois, A. Ferrari, G. Barbiellini, A. Bulgarelli, P. W. Cattaneo, S. Colafrancesco, E. Del Monte, Y. Evangelista, F. Lazzarotto, L. Pacciani, M. Pilia, , and C. Pittori. Spectral evolution of the 2010 september gamma-ray flare from the Crab Nebula. *The Astrophysical Journal Letters*, 732(2):L22 (5pp), April 2011. doi: 10.1088/2041-8205/732/2/L22.

[130] Heinrich Völk and Konrad Bernlöhr. Imaging very high energy gamma-ray telescopes. *Experimental astronomy*, 25(1):173–191, March 2009. doi: 10.1007/s10686-009-9151-z.

[131] Robert M. Wagner. *Measurement of VHE γ–ray emission from four blazars using the MAGIC telescope and a comparative blazar study*. PhD thesis, Physik Department der Technische Universität München, November 2006.

[132] T. C. Weekes, H. Badran, S.D. Biller, I. Bond, S. Bradbury, J. Buckley, D. Carter-Lewis, M. Catanese, S. Criswell, W. Cui, P. Dowkontt, C. Duke, D. J. Fegan, J. Finley, L. Fortson, J. Gaidos, G. H. Gillanders, J. Grindlay, T. A. Hall, K. Harris, A. M. Hillas, P. Kaaret, M. Kertzman, D. Kieda, , F. Krennrich, M. J. Lang, S. LeBohec, R. Lessard, J. Lloyd-Evans, J. Knapp, B. McKernan, J. McEnery, P. Moriarty, D. Muller, P. Ogdenc, R. Ong, D. Petry, J. Quinn, N. W. Reay, P. T. Reynolds, J. Rose, M. Salamon, G. Sembroski, R. Sidwell, P. Slane, N. Stanton, S. P. Swordy, V. V. Vassiliev, and S. P. Wakel. VERITAS: the Very Energetic Radiation Imaging Telescope Array System. *Astroparticle Physics*, 17(2):221–243, May 2002. doi: 10.1016/S0927-6505(01)00152-9.

[133] Trevor C. Weekes. The atmospheric Čerenkov imaging technique for very high energy gamma-ray astronomy. *ArXiv e-prints*, August 2005. URL http://arxiv.org/abs/astro-ph/0508253. Provided by Cornell University.

[134] Trevor C. Weekes. Revealing the dark TeV sky: the atmospheric Čerenkov imaging technique for very high energy gamma-ray astronomy. *ArXiv e-prints*, June 2006. URL http://arxiv.org/abs/astro-ph/0606130. Provided by Cornell University.

[135] Andrew T. Young. 3. Observational technique and data reduction. In N. Carleton, editor, *Astrophysics: Optical and infrared*, volume 12 of *Methods of experimental physics*, pages 123–192. Academic Press, 1974. doi: 10.1016/S0076-695X(08)60495-0.

[136] R. Zanin, D. Mazin, E. Carmona, P. Colin, J. Cortina, T. Jogler, S. Klepser, A. Moralejo, J. Sitarek for the MAGIC collaboration, D. Horns, and M. Meyer. MAGIC measurement of the Crab Nebula spectrum over three decades in energy. In *32th International Cosmic Ray Conference*, volume 7/11, pages 71–74. IHEP, August 2011.

[137] Roberta Zanin and Juan Cortina for the MAGIC collaboration. The central control of the MAGIC telescopes. In *31th International Cosmic Ray Conference*, pages 1–4. Provided by Cornell University, July 2009.

Useful units

The basic units used in this thesis are listed and briefly explained in this section.

A : ampere, unit of current. By definition, $1\,\mathrm{mA} = 10^{-3}\,\mathrm{A}$.

a.u. : arbitrary units.

b : bit.

B : byte. By definition, $1\,\mathrm{byte} = 8\,\mathrm{bit}$.

Crab nebula unit is an integral flux unit. It is the fraction of *Crab* nebula flux above a certain energy threshold, which corresponds to the measured or reported flux.

dB : decibel.

erg unit of energy, used in astronomy. $1\,\mathrm{erg} = 10^{-7}\,\mathrm{J}$.

eV means electronvolt. It is a unit of energy often used in particle and astroparticle physics. It is equal to approximately $1.602{\times}10^{19}\,\mathrm{J}$. By definition, $1\,\mathrm{keV} = 10^{3}\,\mathrm{eV}$, $1\,\mathrm{MeV} = 10^{6}\,\mathrm{eV}$, $1\,\mathrm{GeV} = 10^{9}\,\mathrm{eV}$, $1\,\mathrm{TeV} = 10^{12}\,\mathrm{eV}$, and $1\,\mathrm{PeV} = 10^{15}\,\mathrm{eV}$.

Gbps giga bits per second.

gr : gram, unit of weight. By definition, $1\,\mathrm{kg} = 1000\,\mathrm{gr}$.

Gsample/s : giga sample per second.

h : hour.

Hz : hertz, unit of frequency. By definition, $1\,\mathrm{kHz} = 10^{3}\,\mathrm{Hz}$, $1\,\mathrm{MHz} = 10^{6}\,\mathrm{Hz}$ and $1\,\mathrm{GHz} = 10^{9}\,\mathrm{Hz}$.

KiB : kibibyte. By definition, $1\,\mathrm{KiB} = 2^{10}\,\mathrm{byte} = 1024\,\mathrm{byte}$.

Kib : kibibit. By definition, $1\,\mathrm{Kib} = 2^{10}\,\mathrm{bit} = 1024\,\mathrm{bit}$.

light year is a unit of length. Corresponds to $9{,}461{\times}10^{15}\,\mathrm{m}$.

m : metre, unit of space. By definition, $1\,\mathrm{km} = 1000\,\mathrm{m}$, $1\,\mathrm{cm} = 10^{-2}\,\mathrm{m}$, $1\,\mathrm{mm} = 10^{-3}\,\mathrm{m}$, $1\,\mu\mathrm{m} = 10^{-6}\,\mathrm{m}$ and $1\,\mathrm{nm} = 10^{-9}\,\mathrm{m}$.

$\mathbf{M}_{\odot}$ is the mass of the Sun.

Mbps mega bits per second.

MJD stands for Modified Julian Date. Is a time unit corresponding to the number of days elapsed since midnight of November 17, 1858.

parsec is a length unit, corresponding to $30.857{\times}10^{15}\,\mathrm{m}$.

pc : parsec.

pF : picoFarad.

phe stands for number of photo-electrons and is a unit that characterizes the images size collected by a *IACT*. It represents the sum of the calibrated charge of a triggered event collected by each *PMT* of the telescope camera.

redshift (z) is the ratio decreased by a unit between the radiation wavelength emitted by an object in Doppler motion with respect to an observer, λ_{em}, and that observed, λ_{ob}: $1 + z = \frac{\lambda_{ob}}{\lambda_{em}}$. In astronomy it is used as a distance or time unit.

s : second, unit of time. By definition, $1\,\mathrm{ms} = 10^{-3}\,\mathrm{s}$, $1\,\mu\mathrm{s} = 10^{-6}\,\mathrm{s}$, $1\,\mathrm{ns} = 10^{-9}\,\mathrm{s}$ and $1\,\mathrm{ps} = 10^{-12}\,\mathrm{s}$.

sr : steradian.

U In electronics, U means dimensional unit. When the subject is the *PCB* height, the minimum dimension is 3U, which corresponds to 100 mm. Then each increment is made by 44.45 mm steps. A 6U board is height 233.35 mm, while 9U are 366.79 mm. When the subject is a mechanical rack, the single unit is always 44,45 mm, so 3U are 133.35 mm. The starting different is introduced to allows the insertion of the boards.

V : volt, unit of voltage. By definition, $1\,\mathrm{mV} = 10^{-3}\,\mathrm{V}$ and $1\,\mu\mathrm{V} = 10^{-6}\,\mathrm{V}$.

W : watt, unit of power. By definition, $1\,\mathrm{kW} = 10^{3}\,\mathrm{W}$.

yr : year.

Ω : ohm, unit of resistance.

Acknowledgements

This work of thesis and the associated research activity are the result of more than three years of scientific collaboration with many people, whom I would like to thank.
To Daniele Corti for the incessant and patient collaboration to design, realize and test the *Sum-Trigger-II* project. As the "sandwich" method reveals, you are for sure the number one. It does not matter if it is impossible to dialogue and share a different idea with you. You sit on the right side of God... You are the number one! Without you this project would have remained unfulfilled.
To Elisa Prandini for the camera homogeneity study, the *Sum-Trigger-II* simulations and the work concerning the low energy events. The beginning was a complete different political point of view. So divergent, that we met passing through the infinity. The final result is a homogeneous understanding that the telescopes does not work properly.
To Marcos Lopez for the Monte Carlo simulations performed with *CameraSim* and the fundamental contribution about the performance of different trigger layouts. Now, Marcos, *Geminga* is waiting us.
To Barbara De Lotto as doctorate tutor. She was always available and ready to give me the right solution, although my situation was never easy to manage.
To Riccardo Paoletti for some electronic tests, the support during the development of the *MiniPulsar* board and the valued technical suggestions. I cannot forget your sharp statement during a hard moment: «*You hypocrite, first take the log out of your own eye, and then you will see clearly to take the speck out of your brother's eye.*».
To Alessandro De Angelis as assistant supervisor and for the awful lot of helpful documentation about the cosmic rays' discovery. Last but not least, I cannot forget the excellent cup of wine at the end of my last seminary.
To Mosé Mariotti as funds coordinator of the project. He always strongly believed in this innovative system and he promoted it everywhere, finding the economic support for both the engineering and the realization.
To Giuseppe Galeazzi for the electronic simulations and the planning of some relevant parts of the system.
To Antonio Saggion for the interesting discussions about the atmospheric shower theory. However, I prefer to talk about rugby...
To Bagdat Baibussinov for the choice of some components of the system and the design of the *Sum-test-board* prototype.
To the MPI group for the collaboration in the realization of the *Sum-Trigger-II* project. A special thanks is direct to Dennis Häfner and Thomas Schweizer. They have supported me in every moment, with a real, sincere and transparent collaborative approach.
To Croatian group and Villi Scalzotto for the New Event Display in *Mars* program and the help in the study of events at low energies. Especially I would like to mention Iva, Nikola, Ivica and Tomislav.
To Jeffery Wyss for the corrections of the abstract, the outline and the chapter 4.
To Massimo Persic for the improving of the English style in chapters 1 and 2.
To Roberta Zanin for the suggestions regarding the analysis chain in chapter 2.

To Rudolf Bock for the improving of the English style in chapters 2 and 3.
To Oscar Blanch for the discussions on the trigger strategies at low energies, examined in chapter 3.
To Markus Garczarczyk for the corrections of chapter 4.
To José Luis Lemus for the corrections of chapters 5 and 6.
To Karsten Berger, the first one who has read the whole thesis.
To all the *MAGIC* colleagues, with whom I shared the exciting experience to work in close contact, especially the Padova group and the three Charlie's y–angels (Ely, Symo & Corny).

To my small brother Alberto for the inestimable and continuous affection. During all this period, he has supported me as Chris Ashton... Staying relaxed on the white sofa and watching the Rugby World Cup 2011, he has been a strong stimulus to write about γ-astronomy. Then, moving very slowly to the magic loft, he has provided me a perfect atmosphere for the concentration, mixing perfectly amazing House music.
To my girlfriend Angela for the several designs made with AutoCAD and the understanding of the difficult period. Now it is time to get married, so we become a couple of unemployed. Don't be sad, we can always plant a field with beans.
I got the main support from outside the work environment. There are no words to explain the loving and continuous presence of dad Antonio and mum Santina. They are a perfect and tireless logistic machine. Now it is time to get a serious job to compensate for 36 years of heavy efforts!

The author would like to thank the University of Udine, the INFN Sezione di Padova and the Altera Inc. for supporting the project through the Altera University Program.